# Simulation of the $D_s$ Semileptonic Decay with the $\bar{\text{P}}$ANDA Detector and Experimental Verification of the Micro-Vertex-Detector Pixel Readout ASIC with Proton Test Beam

DISSERTATION

zur
Erlangung des Grades
"Doktors der Naturwissenschaften"
an der Fakultät für Physik und Astronomie
der Ruhr-Universität Bochum

von
Lu Cao

aus
Guiyang, China

Bochum 2016

**Versicherung gemäß §7 Abs. 2 Nr. 6 PromO 2011**
Hiermit versichere ich, dass ich meine Dissertation selbstständig und ohne unerlaubte fremde Hilfen angefertigt und verfasst habe und keine anderen als die angegebenen Hilfsmittel und Hilfen benutzt habe. Meine Dissertation habe ich in dieser oder ähnlicher Form noch bei keiner anderen Fakultät der Ruhr-Universität Bochum oder bei einer anderen Hochschule eingereicht.

| | |
|---|---|
| 1 Gutachter: | Prof. Dr. James Ritman |
| 2 Gutachter: | Prof. Dr. Ulrich Wiedner |

Tag der Disputation: 14.07.2016

## Abstract

The $\bar{\text{P}}$ANDA experiment will study a wide range of physics topics with beams of antiprotons incident on fixed proton or complex nuclear targets. One issue is the $D_s$ semileptonic decay, which is governed by both the weak and strong forces. The interaction can be parameterized by a transition form factor. The performance of $\bar{\text{P}}$ANDA to measure the decay form factor of $D_s^+ \rightarrow \eta e^+ \nu_e$ is evaluated via Monte Carlo simulation. This thesis concentrates on describing the software development and the evaluation of the expected resolution. A preliminary estimate of the expected count rate is obtained. In this measurement, it is essential to reconstruct the $D_s$ semileptonic decay with high efficiency and purity in order to overcome the many orders of magnitude higher background. The Micro-Vertex-Detector plays an import role in the whole tracking system. The rate capability and tracking performance of the recent ASIC prototype for the readout of the MVD is tested using a beam of high-energy protons.

Das $\bar{\text{P}}$ANDA Experiment nutzt die Wechselwirkung zwischen einem Antiprotonenstrahl und einem Wasserstoff-Target um ein breites Spektrum an physikalischen Fragestellungen zu untersuchen. Eine davon ist die Messung des semileptonischen Zerfalls des $D_s$, der sowohl durch die schwache wie auch die starke Wechselwirkung beeinflusst wird. Der komplexe Zerfall kann durch einen Übergangsformfaktor parametrisiert werden. Im Rahmen dieser Arbeit wurde mit Hilfe von Monte-Carlo-Simulationen untersucht, wie gut $\bar{\text{P}}$ANDA den Übergangsformfaktor des Zerfalls $D_s^+ \rightarrow \eta e^+ \nu_e$ bestimmen kann. Um das Signal des Zerfalls vom Untergrund, der mehrere Größenordnungen größer ist, trennen zu können, ist es notwendig den Zerfallspunkt des $D_s$ mit hoher Präzision zu messen. Dabei spielt der Mikro-Vertex-Detektor des $\bar{\text{P}}$ANDA Experimentes eine entscheidende Rolle. In dieser Arbeit sind die Eigenschaften eines Prototyps der Front-End-Elektronik des Pixelteils des MVD mit Hilfe eines Protonenteststrahls untersucht worden.

# Preface

In the past decade, detailed and comprehensive analyses of open charm transitions have provided insights into nonperturbative dynamics of Quantum Chromo Dynamics (QCD), but they are still not sufficient. The semileptonic $\mathrm{D_s}$ decays are governed by both weak and strong interactions. The strong interaction dynamics can be described by a transition form factor $f(q^2)$, where $q^2$ is the squared invariant mass of the lepton-neutrino system. Various theoretical calculations provide predictions on this transition form factor based on different scenario assumptions. A precise experimental observation is required to corroborate the theoretical models and provide clues to understand the mechanism. There is no existing experimental determination of the $\mathrm{D_s}$ semileptonic decay form factor yet because of low statistics for this decay. Compared to electron-positron collisions, antiproton-proton interactions are expected to a much higher cross section for $\mathrm{D_s}$ production. Therefore, in the full version of the Facility for Antiproton Ion Research (FAIR) (high luminosity mode) the $\overline{\mathrm{P}}$ANDA experiment will have the opportunity to measure the $\mathrm{D_s}$ semileptonic decay form factor.

The $\overline{\mathrm{P}}$ANDA experiment is one of the major projects of the FAIR in Darmstadt, Germany. It

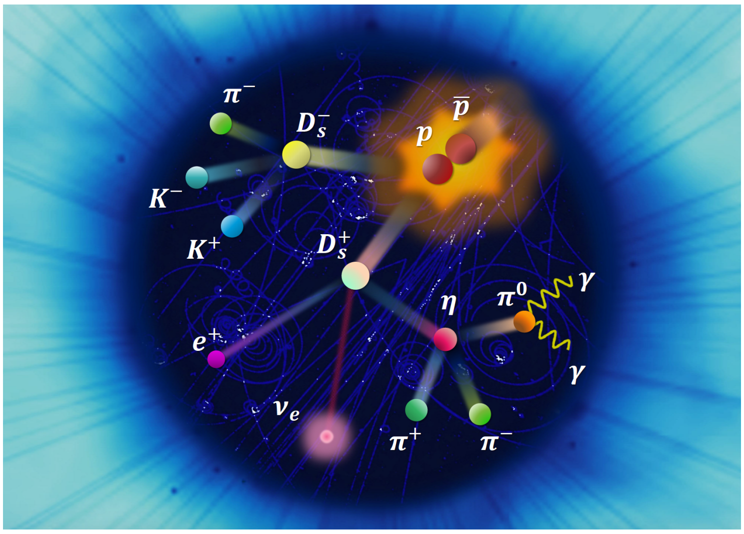

**Figure 1:** Artistic view of the $\mathrm{D_s}$ meson semileptonic decay in antiproton proton annihilation.

will study the interactions between an intense, phase space cooled beam of antiprotons in the momentum range of $1.5 \sim 15$ GeV/$c$ provided by the High-Energy Storage Ring (HESR) and hydrogen or heavier nuclear targets. In order to serve the wide physics potential with antiprotons, $\bar{\text{P}}$ANDA is designed as a general purpose detector covering nearly the complete solid angle for both neutral and charged particles with good momentum and particle identification capabilities as well as an excellent vertex determination. By performing resonance and threshold scans with the high precision antiproton beam, $\bar{\text{P}}$ANDA will achieve more than an order of magnitude higher mass resolution compared to existing facilities, e.g. the B-factories.

In the semileptonic decay of $\text{D}_\text{s}$ meson, there is one neutrino in the event. The achievable performance of the $\bar{\text{P}}$ANDA detector to measure these types of reactions has not yet been studied in detail. However, it is expected to work very well based upon the design performance and experience with other detector systems due to the kinematic constraints, which allow these events to be completely reconstructed despite one particle not being measured. The goal of this study is to evaluate and optimize the physics performance of the $\bar{\text{P}}$ANDA detector to measure the form factor of semileptonic $\text{D}_\text{s}$ meson decays.

To study the $\text{D}_\text{s}$ semileptonic decay form factor it is essential to select those events out of the huge background with high efficiency and purity. For this purpose, high quality tracking and a precise reconstruction of the decay vertices are needed. As the most central sub-detector of the $\bar{\text{P}}$ANDA, the Micro Vertex Detector (MVD) plays an import role in the whole tracking system. Validating the recent MVD readout Application-Specific Integrated Circuit (ASIC) prototype on the rate capability and tracking performance is done with a proton beam. The analyses of the test-beam data is presented in this thesis.

The thesis is structured as below.

Chapter 1 is a brief review of the Standard Model of particle physics with the most essential ideas.

Chapter 2 introduces the form factor of hadrons in both theoretical and experimental views, where a summary of the recent studies on $\text{D}_\text{s}$ semileptonic decays are presented.

Chapter 3 is an overview of the $\bar{\text{P}}$ANDA experiment, including the physics program, the accelerator facility, the components of the $\bar{\text{P}}$ANDA detector and the software framework.

Chapter 4 presents a detailed study of the simulations of $\text{D}_\text{s}$ semileptonic decay. The estimated cross sections of this decay are briefly summarized. The tuning of the selection parameters and reconstruction strategy is described, and followed by the reconstruction results for two different tag modes. After that the estimated event rate and the beam momentum dependence of the reconstruction efficiencies are presented.

Chapter 5 introduces the recent ASIC prototype for the Micro-Vertex-Detector readout and the test-beam setup. Detailed analyses of test-beam data is given.

Chapter 6 summarizes the results obtained in this thesis, and provides a outlook for further investigations.

# Contents

# The Standard Model of Particle Physics

# 1

The Standard Model of particle physics was proposed around 1970 and the main elements of it were experimentally confirmed culminating with the discovery of the Higgs boson in 2012. The modern era of questing for the fundamental building blocks of matter that started with Rutherford at the beginning of the 20th century has now been going on for more than 100 years. This chapter provides a review of the essential concepts of the Standard Model.

## 1.1 Fundamental Forces

There are four fundamental forces in nature. They are the strong, electromagnetic, weak and gravitational force (see Fig. 1.1). These forces can be classified by their distance dependences. In general, a long-range force decreases only as an inverse power of the distance. A short-range force, on the other hand, is a force whose strength diminishes exponentially with the distance [1].

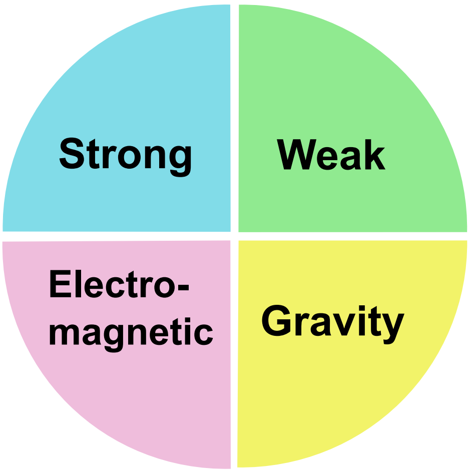

**Figure 1.1:** Four forces of Nature.

**Long-Range Forces: Gravity and Electromagnetic Force** The gravitational force, or gravity, is negligibly weak at the elementary particle level: between the proton and electron is $10^{-42}$ times the electromagnetic force [2]. The force's strength becomes comparable to that of the others only on an extremely small scales, i.e. the Planck scale of $10^{-35}$ m, or equivalently at an extremely high energy, i.e. the Planck energy of $10^{19}$ GeV. Indeed, galaxies that are hundreds million light years apart are known to be mutually attracted by the gravitational force. The strength of the force decreases inversely proportional to the distance squared, but it also scales as the mass, and concentration of the mass more than compensates the distance even on a cosmic scale. Gravity is not a part of the Standard Model, but it is thought that there may be particles called *gravitons*, which are the excitations of gravitational waves. One hundred years after Albert Einstein predicted the general theory of relativity, the gravitational waves were observed for the first time by the LIGO detectors [3]. The detected gravitational waves were considered to have been produced during the final fraction of a second of two black holes' merging to produce a single, more massive spinning black hole. Based on the observed signals, it was estimated that the black holes for this event were about 29 and 36 times the mass of the sun, and this event took place 1.3 billion years ago. This discovery opens an unprecedented new window onto the cosmos.

The behaviour of the electromagnetic force is similar to and far stronger than gravity, but, in general, the positive and negative charges compensate each other. However, its long-distance effect manifests itself in the form of the galactic magnetic field, which spans hundreds or possibly millions of light years. It binds nuclei and electrons to form atoms, atoms to form molecules, and molecules to form matter as we observe it. Atomic, molecular, and condensed matter physics need only consider the electromagnetic force. There, the theory of Quantum Electro-Dynamics (QED) is used to describe the dynamical behaviour of point-like charged particles (notably electrons), the electromagnetic field, and their interactions. Mathematically, it is a combination of quantized Maxwell equations and relativistic quantum mechanics. The electromagnetic force, though playing an essential role at the microscopic level, can also act at the macroscopic distance. The reason is that its strength is proportional to the inverse square of the distance (*Coulomb's law*).

**Short-Range Forces: Strong and Weak Force** In the ultramicroscopic world of the nuclei at scales less than $10^{-15}$ m, the strong and the weak force gain in importance. The reason why they are important only at such a small scale is that they are short ranged, e.g. the strong force reaches only a few hadron diameters, and accumulation of the mass does not help to make it stronger. The strong force (referred to as the *color force* at the most fundamental level) acts between quarks to bind them to form hadrons. Historically, the strong force was first discovered as the nuclear force to bind protons and neutrons [1, 4]. But as they were found to be composites of the quarks, the nuclear force is recognised as a kind of molecular force (*van der Waals force*) that can be derived from the more fundamental color force.

In 1935, Yukawa predicted the existence of the $\pi$ meson as the carrier of the nuclear force [5]. The idea that the force is transmitted by a *force carrier particle* was revolutionary and laid the foundation for present gauge theories. Later, it was clarified that the pion was a composite particle and cannot be a fundamental force carrier, but the basic idea remains valid. The weak force is known to act in the decay of hadrons, notably in nuclear decays. It is also known to control the burning rate of the sun and to play a decisive role in the explosion of type II supernovae. The weak force can be described by a gauge theory that contains one charge, i.e. weak isospin, which plays the same role in the weak interaction as color charge in the strong interaction.

**Unification of the Forces** In 1979, it was found that the electromagnetic and weak interaction can be unified as the *electroweak interaction* [6]. The unification is accomplished under an SU(2) × U(1) gauge group. Its existence was experimentally established later. Considering that the electromagnetic and weak forces are unified and all four fundamental forces work in the same mathematical framework, it is natural to consider that all the forces are unified but show different aspects in different environments. The *Grand Unified Theory*, to unify the electroweak and strong interactions, and the *Super Grand Unified Theory* to combine all the forces, including gravity, are currently active research areas. Among them, *supergravity* [7] and *superstring* [8] theories are the most popular. But only the electroweak theory and Quantum Chromo Dynamics (QCD) are experimentally well established and are called collectively the *Standard Model* of elementary particles. The history and current situation of force unification are shown in Fig. 1.2.

## 1.2 Elementary Particles

In the search for the fundamental building blocks of matter physicists have found smaller and smaller constituents. Force-carrying particles have been seen in experiments for all fundamental forces except for gravitation. There, the mediating particles, the graviton, is still hypothetical [2]. Fig. 1.3 shows the elementary particles in the Standard Model grouped to quarks, leptons, gauge bosons, and the recently discovered Higgs boson.

**Quarks** Experiments at particle accelerators in the 1950s and ’60s showed that protons and neutrons are merely representatives of a large family of particles now called *hadrons*. More than 100 hadrons, sometimes called the *hadronic zoo*, have thus far been detected [1]. These hadrons, like atoms, can be systematically classified in groups with similar properties. It led to the assumption that they cannot be understood as fundamental constituents of matter. In 1964, the *quark model* was independently proposed by physicists Murray Gell-Mann [11] and George Zweig [12]. It should be possible to reconstruct and explain the properties (charge, mass, magnetic moment, isospin, etc.) of the nucleons from the quantum numbers of these constituents.

The quark model consists of six types of quarks, known as *flavors*: up, down, strange, charm, top, and bottom (labeled in purple in Fig. 1.3). Table 1.1 lists the quantum numbers of quarks. Quarks are strongly interacting fermions with spin 1/2 and, by convention, positive parity. *Antiquark*, the antiparticle of a quark, has negative parity. Quarks have the additive baryon number 1/3, antiquarks -1/3. They are related to the charge $Q$ (in units of the elementary charge $e$) through the generalized Gell-Mann-Nishijima formula [9]

$$Q = I_3 + \frac{b + S + C + B + T}{2}, \tag{1.1}$$

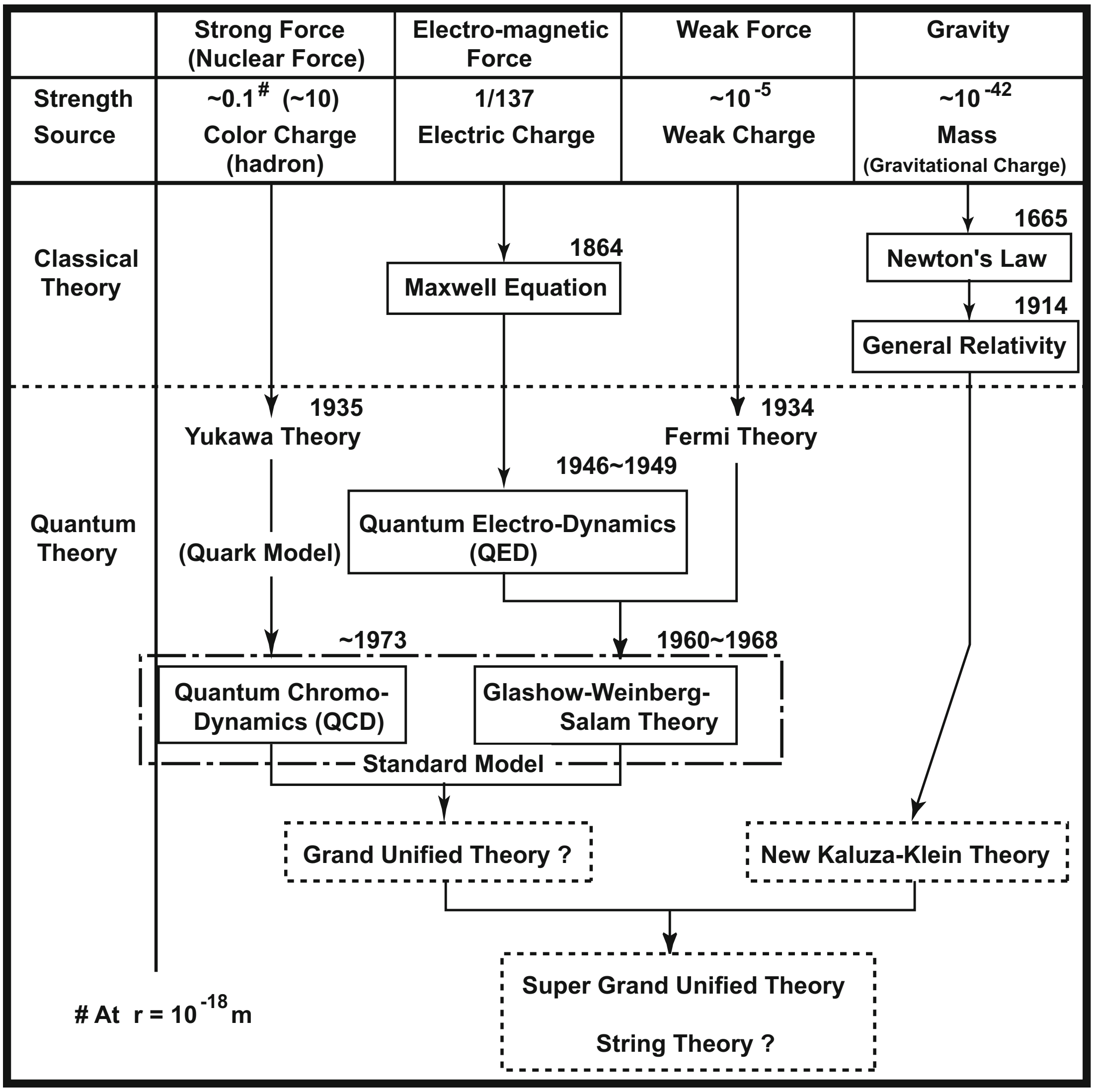

**Figure 1.2:** Unification of the forces. The theories enclosed in dashed lines are not yet established. The strong force changes its strength appreciably within currently available energy ranges or, equivalently, distances. This is why the distance of the strong force is specified. Figure and description cited from Ref. [1].

where $b$ is the baryon number (see Sec. 1.4.2); $S$, $C$, $B$ and $T$ are strangeness, charm, bottomness and topness, respectively. The convention is that the flavor of a quark ($I_3$, $S$, $C$, $B$, or $T$) has the same sign as its charge $Q$. Antiquarks have the opposite flavor signs. The hypercharge $Y$ is defined as

$$Y = b + S + C + B + T = 2(Q - I_3). \tag{1.2}$$

The concept of hypercharge combines and unifies isospin and flavor into a single charge operator. Isospin is defined in the SU(2) model while the SU(3) model defines hypercharge.

The quarks that determine the quantum numbers of nucleons are called *valence quarks*. In

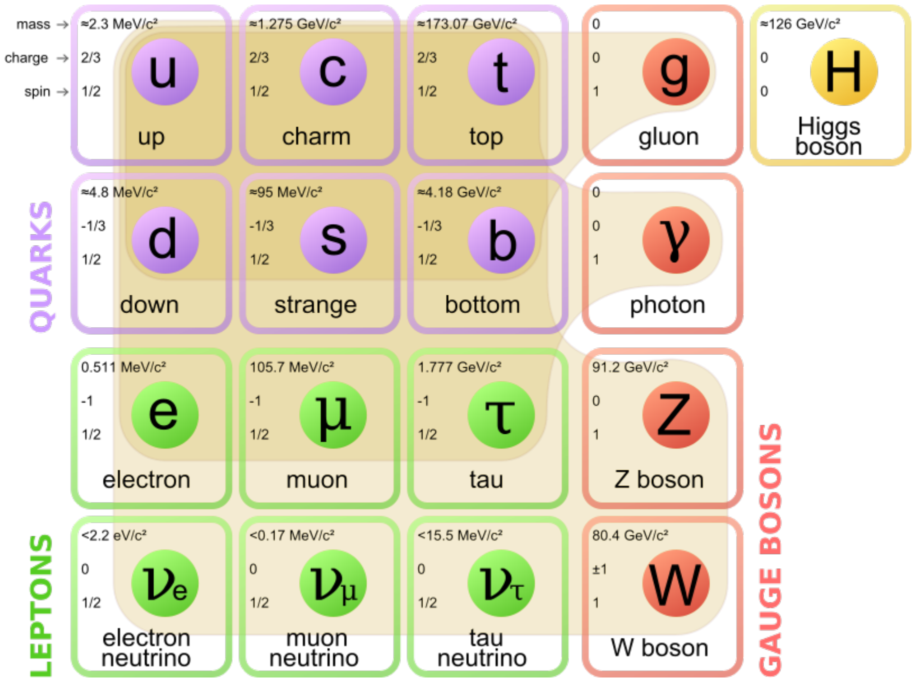

**Figure 1.3:** Fundamental particles in the Standard Model. The Standard Model consists of elementary particles, with the three generations of fermions in the first to third column, gauge bosons in the fourth column (red), and the Higgs boson in the fifth. Brown loops indicate which bosons couple to which fermions. The masses for the u-, d-, s-quark are current-quark masses, and for c- and b-quark are the running mass in the $\bar{M}S$ scheme. The mass of the t-quark is from direct measurements [9]. Picture cited from [10].

addition to these, virtual quark-antiquark pairs, *sea quarks*, also exist in the nucleon. Their effective quantum numbers average out to zero and do not alter those of the nucleon. Because of their non-zero electrical charge, they are visible in deep inelastic scattering. However, they carry only very small fractions of the nucleons momentum. Only about half of the momentum of a nucleon is carried by valence and sea quarks. In dealing with the spectroscopic properties of nucleons, sea quarks and intermediate bosons, *gluons*, need not be explicitly handled. They can be combined with the valence quarks. One then acts as though there were only three valence quarks, with enlarged masses but unchanged quantum numbers. These *effective valence quarks* are called *constituent quarks*. In interpreting deep inelastic scattering, the rest masses of the bare quarks were neglected. These masses are commonly called *current quark masses*. However, these are not the masses obtained from hadron spectroscopy; for instance, from calculations of magnetic moments and hadron excitation energies. The constituent masses are mainly due to the cloud of gluons and sea quarks. The constituent quark masses are much larger for the light-flavor quarks and there is almost no difference for the heavy-flavor. The last two columns of Table 1.1 list these two masses for the six quarks. Note that these estimates of the quark masses are model dependent.

Quarks have another important property called *color*, which is needed to ensure that quarks in hadrons obey the Pauli principle. The color charge of quarks and gluons has three dimensions: red, green and blue, and antiparticles have the anti-version of each color. Particles in nature are

**Table 1.1:** Quantum numbers and masses of the quarks. Here the notations are defined as $I$: isospin, $I_3$: isospin 3rd-component, $S$: strangeness, $C$: charm, $B$: bottomness, $T$: topness, $b$: baryon number, $Y$: hyercharge and $Q$: electric charge. $M_{eff}$ stands for the constitute quark mass, and $M_{bare}$ is the current-quark mass.

| | $I$ | $I_3$ | $S$ | $C$ | $B$ | $T$ | $b$ | $Y$ | $Q[e]$ | $M_{eff}[\mathrm{MeV}/c^2]$ | $M_{bare}[\mathrm{MeV}/c^2]$ |
|---|---|---|---|---|---|---|---|---|---|---|---|
| u | 1/2 | 1/2 | 0 | 0 | 0 | 0 | 1/3 | 1/3 | 2/3 | 336 [13] | 2.3 [9] |
| d | 1/2 | -1/2 | 0 | 0 | 0 | 0 | 1/3 | 1/3 | -1/3 | 340 [13] | 4.8 [9] |
| s | 0 | 0 | -1 | 0 | 0 | 0 | 1/3 | -2/3 | -1/3 | 486 [13] | 95 [9] |
| c | 0 | 0 | 0 | 1 | 0 | 0 | 1/3 | 4/3 | 2/3 | 1550 [13] | 1300 [13] |
| b | 0 | 0 | 0 | 0 | -1 | 0 | 1/3 | -2/3 | -1/3 | 4730 [13] | 4200 [13] |
| t | 0 | 0 | 0 | 0 | 0 | 1 | 1/3 | 4/3 | 2/3 | 177,000 [13] | 174,000 [13] |

colorless, due to the QCD confinement [14]. In addition, because the mass eigenstates are not equal to the flavor eigenstates, different flavors of quarks can change via the weak interaction. The mixing scheme is introduced later in the Sec. 1.3.

**Leptons** The leptons either carry integer electric charge or are neutral. The charged leptons are: the electron ($\mathrm{e}^-$), the muon ($\mu^-$), and the tau ($\tau^-$) as well as their antiparticles ($\mathrm{e}^+$, $\mu^+$ and $\tau^+$), which have the same masses as their partners but have opposite electric charge. The electron is the lightest of these particles. The neutral leptons are called *neutrinos*. A different flavor of neutrino ($\nu_\mathrm{e}$, $\nu_\mu$, $\nu_\tau$) is paired with each flavor of charged lepton. The leptons are fermions and thus have half-integer spin. The antiparticles of charged leptons have opposite electric charge, while antineutrinos are neutral. Because antineutrinos and neutrinos are electrically neutral particles, it is possible that they are actually the same particle. Particles that have this property are known as *Majorana particles*. If neutrinos are indeed Majorana particles, then neutrinoless double beta decay as well as a range of other lepton number violating phenomena, would be allowed [15]. Many experiments contribute to this issue, such as IGEX [16] and NEMO [17]. The research on the nature of neutrino is ongoing.

Different flavor neutrinos can mix or oscillate. In Eq. 1.3, the eigenstates of the weak interaction, i.e. ($\nu_\mathrm{e}$, $\nu_\mu$, $\nu_\tau$), are a complete, orthonormal basis for the Standard Model neutrino. The eigenbasis can also be constructed out of three neutrino states of definite mass, $\nu_1$, $\nu_2$ and $\nu_3$. These two eigenbases are not the same but a transition matrix $U_{\alpha i}$ allows for each flavor state to be written as a superposition of mass eigenstates. This transition matrix is the Pontecorvo-Maki-Nakagawa-Sakata matrix (PMNS) matrix. It is a unitary matrix and contains information on the mixing of quantum states of neutrinos when they propagate freely and when they take part in the weak interactions. The PMNS matrix was introduced in 1962 by Ziro Maki, Masami Nakagawa and Shoichi Sakata [18] to explain the neutrino oscillations predicted by Bruno Pontecorvo [19]. Fig. 1.4 illustrates the relative sizes of the PMNS matrix elements. Larger matrix elements imply more of mixing.

$$\begin{pmatrix} \nu_e \\ \nu_\mu \\ \nu_\tau \end{pmatrix} = \begin{pmatrix} U_{e1} & U_{e2} & U_{e3} \\ U_{\mu1} & U_{\mu2} & U_{\mu3} \\ U_{\tau1} & U_{\tau2} & U_{\tau3} \end{pmatrix} \begin{pmatrix} \nu_1 \\ \nu_2 \\ \nu_3 \end{pmatrix} \tag{1.3}$$

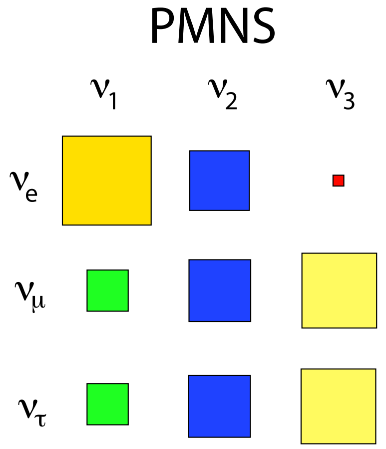

**Figure 1.4:** The sizes of the the PMNS matrix elements for neutrino mixing. The area of the boxes represents the square of the matrix elements. Picture taken from Ref. [20].

Neutrinos are electrically neutral leptons and, as such, do not feel the electromagnetic or strong forces. Since neutrinos interact only weakly, they can only be detected indirectly in processes where charged particles are produced. Typically the energy, momentum and spin carried away or brought in by the neutrino is determined by measuring the other particles involved in the reaction and applying conservation laws. Experiments with solar, atmospheric, reactor and accelerator neutrinos have provided compelling evidences for oscillations of neutrinos caused by nonzero neutrino masses and neutrino mixing. Two outstanding experimentalist, Takaaki Kajita and Arthur B. McDonald were rewarded the Nobel Prize in 2015 for their contributions [21]. Neutrino oscillation, in which a neutrino of one kind is transformed to another while it propagates, does not happen if the mass of the neutrino vanishes, as is assumed in the simplest form of the Standard Model [1]. Neutrino oscillation has been studied by a variety of experiments, e.g. SNO, Super-Kamiokande, OPERA, Double Chooz, Daya Bay, RENO, MINOS and T2K [9]. Investigation on oscillating and the mass of neutrinos is of fundamental importance for making progress in our understanding of the origin of neutrino masses and mixing and of the symmetries governing the lepton sector of particle interactions.

**Gauge Bosons** According to the Standard Model, interactions between the particles mentioned above are mediated by the exchange of vector bosons, i.e. particles with spin one. These are photons in electromagnetic interactions, gluons in strong interactions and the $W^+$, $W^-$, and $Z^0$ bosons in weak interactions.

For the strong interaction, gluons are the exchange particles that couple to the color charge. This is analogous to the electromagnetic interaction in which photons are exchanged between electrically charged particles. The potential between two quarks has an unusual behaviour (illustrated in Fig. 1.5): it is very small when the quarks are at a close distance and increases as the distance grows and the force remains constant even if the quarks are removed further and further from each other. If one attempts to separate a quark-antiquark pair, the energy of the gluon field becomes larger and larger, until a new quark-antiquark pair can be created. As a result, one does not end up with two isolated quarks but with new quark-antiquark pairs instead. These behaviours are described by the two essential properties of QCD, the *asymptotic freedom* and *confinement*. One of the greatest intellectual challenges of modern physics is to understand confinement not just as a phenomenon but to comprehend it quantitatively from the theory of the strong force. For this, physicists need a better understanding of the behaviour of the strong force at medium and larger distances.

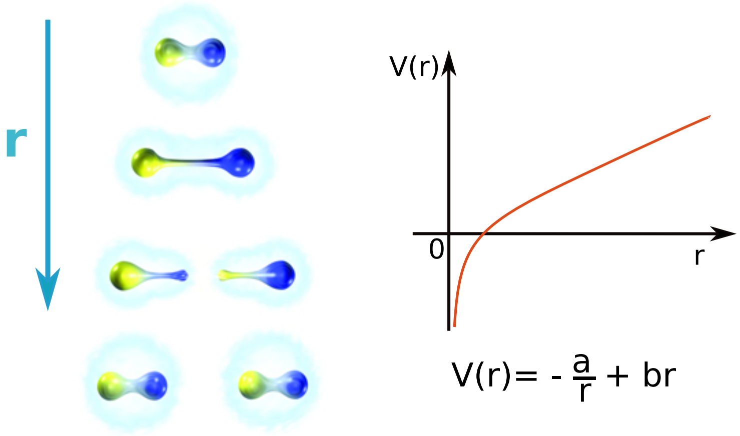

**Figure 1.5:** Left: a quark-antiquark pair is stretched apart until a new $q\bar{q}$ pair is produced due to the color confinement. Figure adapted from Ref. [22]. Right: a sketch of the non-relativistic $q\bar{q}$ potential $V(r)$, where the strong coupling constant is embodied in the parameter $a$ as $a = 4\alpha_s/3$ and $b$ represents the strength of the linear confinement.

The weak interaction is mediated by exchange of $W^{\pm}$ and $Z^0$ bosons and is responsible for e.g. the decay of quarks and leptons. The $W^{\pm}$ and $Z^0$ bosons are very heavy particles, masses $M_W \approx 80\,\text{GeV}/c^2$ and $M_Z \approx 91\,\text{GeV}/c^2$, in contrast to the strong, electromagnetic, and gravitational interaction that are mediated by massless bosons. According to the Heisenberg uncertainty principle, they can be produced as virtual, intermediate particles in scattering processes for extremely short times. Therefore, the weak interaction is of very short range. The rest mass of the photon is zero. Therefore, the range of the electromagnetic interaction is infinite. Even though the exchange bosons of the weak interaction couple to the quarks and leptons with approximately equal strength as the photons to the charges, at low energies (low compared to 100 GeV) the interaction appears point-like and weak, due to the masses of the exchange boson. The charged W boson plays an important role in quark flavor changing, as the weak quark decays only proceed through $W^{\pm}$ exchange. Neutral currents which change the quark flavor (e. g. $c \to u$) have thus far not been observed [9].

**Higgs Bosons** The basic equations of the unified theory correctly describe the electroweak force and its associated force-carrying particles, namely the photon, and the W and Z bosons, except for a major glitch. All of these particles emerge without a mass. While this is true for the photon, we know that the W and Z have mass, nearly 100 times that of a proton. Fortunately, theorists Robert Brout, Francois Englert, and Peter Higgs made a proposal to solve this problem [23, 24]. What we now call the Brout-Englert-Higgs mechanism gives a mass to the gauge boson W and Z when they interact with an invisible field, now called the *Higgs field*. The world average mass of the Higgs boson is $125.09\,\mathrm{GeV}/c^2$ [9]. The presence of this field explains why some fundamental particles have mass when, based on the symmetries controlling their interactions, they should be massless. The existence of the Higgs field would also resolve several other long-standing puzzles, such as the reason for the weak force's extremely short range.

On 4th July, 2012, the ATLAS [25] and CMS [26] experiments at CERN's Large Hadron Collider (LHC) announced they had each observed a new particle in the Standard Model predicted mass region of the Higgs boson. Since the Higgs field is scalar, the Higgs boson has zero spin. It is very unstable, decaying into other particles almost immediately. The Higgs boson couplings to the fundamental particles are set by their masses. This is a new type of interaction, very weak for ordinary particles, such as up and down quarks, and electrons, but strong for heavy particles such as the W and Z bosons and the top quark. More precisely, the Higgs boson couplings to fundamental fermions are linearly proportional to the fermion masses, whereas the couplings to bosons are proportional to the square of the boson masses [9]. Since it interacts with all the massive elementary particles of the Standard Model, the Higgs boson has many different processes through which it can decay, for example, into a fermion-antifermion pair, or a pair of massive gauge bosons. Higgs bosons can possibly also decay into gluons or photons but requires an intermediate loop of virtual heavy quarks (top or bottom) or massive gauge bosons [27].

The Standard Model predicts that Higgs bosons could be formed in a number of ways [28], although the probability of producing a Higgs boson in any collision is always expected to be very small [29], for instance, only one Higgs boson per ten billion collisions in the LHC. The main production mechanisms at the Tevatron and the LHC are gluon fusion, weak-boson fusion, associated production with a gauge boson and associated production with top quarks [9].

The search for the Higgs boson has been carried out in the particle physics community for the last 50 years. The properties of the Higgs boson still need further studies, both theoretically and experimentally. These investigations start off a new era of precision Higgs boson measurements and pave the way for studying new physics by means of the Higgs boson.

## 1.3 CKM Quark-Mixing Matrix

This Cabibbo-Kobayashi-Maskawa (CKM) matrix describes quark mixing in three generations. The masses and mixings of quarks have a common origin in the Standard Model: they arise from the Yukawa interactions of the quarks with the Higgs condensate. When the Higgs field acquires a vacuum expectation value, quark mass terms are generated [27]. The physical states are obtained by diagonalizing the up and down quark mass matrices by four unitary matrices, $V_{L,R}^{u,d}$. The charged current $\mathrm{W}^{\pm}$ interactions couple to the physical up and down-type quarks with couplings given by [9]

$$V_{CKM} \equiv V_L^u V_L^{d\dagger} = \begin{pmatrix} V_{ud} & V_{us} & V_{ub} \\ V_{cd} & V_{cs} & V_{cb} \\ V_{td} & V_{ts} & V_{tb} \end{pmatrix}. \tag{1.4}$$

This is similar to the neutrino sector, in fact, the PMNS scheme was modelled in accordance to the Cabibbo-Kobayashi-Maskawa matrix (CKM) one. The CKM matrix is a 3 × 3 unitary matrix containing the information on the strength of flavor-changing weak decays as

$$\begin{pmatrix} d' \\ s' \\ b' \end{pmatrix} = \begin{pmatrix} V_{ud} & V_{us} & V_{ub} \\ V_{cd} & V_{cs} & V_{cb} \\ V_{td} & V_{ts} & V_{tb} \end{pmatrix} \begin{pmatrix} d \\ s \\ b \end{pmatrix}. \tag{1.5}$$

The square of the magnitude of the matrix element $|V_{qq'}|^2$ is proportional to the probability from a quark $q$ going over to a quark $q'$. Fig. 1.6 shows a pictorial description of the magnitudes of the CKM matrix elements. The diagonal elements of this matrix describe transitions within a family; they deviate from unity by only a few percent. The values of the matrix elements $V_{cb}$ and $V_{ts}$ are nearly one order of magnitude smaller than those of $V_{us}$ and $V_{cd}$. Accordingly, transitions from the third to the second generation (t → s, b → c) are suppressed by nearly two orders of magnitude compared to transitions from the second to the first generation. This applies to an even higher degree for transitions from the third to the first generation. The direct transition b → u was detected in the semileptonic decay of B mesons into non-charmed mesons.

The CKM matrix elements are fundamental parameters of the Standard Model, so their precise determination is important. The magnitude of $V_{cs}$ is involved in the measurement of the $\mathrm{D_s}$ semileptonic decay form factor presented in the course of this thesis, thus its determination is presented with more details here. The experimental measurement of $|V_{cs}|$ is possible using semileptonic D or leptonic $\mathrm{D_s}$ decays, with unquenched Lattice Quantum Chromodynamics (LQCD) calculations of the semileptonic D form factor or the $\mathrm{D_s}$ decay constant as the input parameter. Leptonic decays are studied by several experiments independently, the average value is $|V_{cs}| = 1.008 \pm 0.021$ [9], where the error is dominated by the LQCD determination of the $\mathrm{D_s}$ decay constant. On the other hand, for the semileptonic D decays, unquenched LQCD calculations of the $\mathrm{D} \to \mathrm{K}\ell\nu$ form factor are available [30]. Thus CLEO-c [31], Belle [32], and BaBar [33] measured this channel, forming a combined value of $|V_{cs}| = 0.953 \pm 0.008 \pm 0.024$, where the first error is experimental and the second is dominated by the theoretical uncertainty of the form factor. The averaged value of these two methods is given as $|V_{cs}| = 1.006 \pm 0.0023$ in PDG 2012 [27], and $|V_{cs}| = 0.986 \pm 0.0016$ in PDG 2014 [9] with a lower uncertainty.

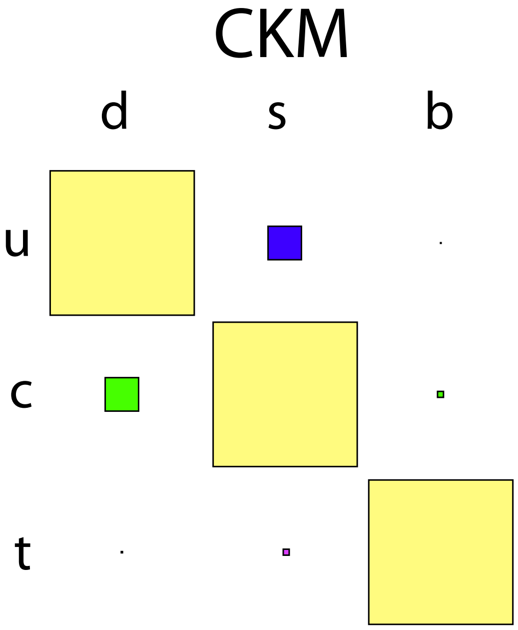

**Figure 1.6:** Illustration of magnitudes of the CKM matrix elements for quark mixing. The area of the squares represents the square of the matrix elements. Figure taken from Ref. [20].

## 1.4 Hadrons

By the end of the 19th century, it was known that all matter is composed of atoms. However, the existence of close to 100 elements showing periodically recurring properties was a clear indication that atoms themselves must have an internal structure and are not indivisible as the name would suggest. The modern concept of the structure of atom emerged at the beginning of the 20th century, in particular as a result of Rutherford's experiments [34]. Hadrons can be classified in two groups: the baryons, fermions with half-integer spin, and the mesons, bosons with integerl spin.

### 1.4.1 Mesons

Hadrons composed of quark-antiquark pairs are called *mesons*. There is no "meson number conservation", in contrast to baryon number conservation. This is understood in the quark model: mesons are quark-antiquark combinations $q\bar{q}$ and so the number of quarks minus the number of antiquarks is a conserved quantity and equal to zero in this case.

Mesons have baryon number $b = 0$. In the quark model, they are $q\bar{q}$ bound states (the flavors of $q$ and $\overline{q}$ may be different). If the orbital angular momentum of the $q\bar{q}$ state is $L$, then the *parity* $P$ is $(-1)^{L+1}$. The *meson spin* $J$ is given by the usual relation $|L-S| < J < |L+S|$, where $S$ is 0 (antiparallel quark spins) or 1 (parallel quark spins). For mesons with no net flavor, the charge conjugation or *C-parity* is $C = (-1)^{L+S}$, but flavored mesons have indefinite value of $C$. In addition, the C-parity can be generalized to the *G-parity* $G = (-1)^{I+L+S}$ for mesons made of quarks and their own antiquarks ($I_3 = 0$) and for the charged $c\bar{s}$ and $\bar{c}s$ states (isospin $I = 1$). The mesons are classified in $J^{PC}$ multiplets. The $L = 0$ states are the pseudoscalars ($0^{-+}$) and

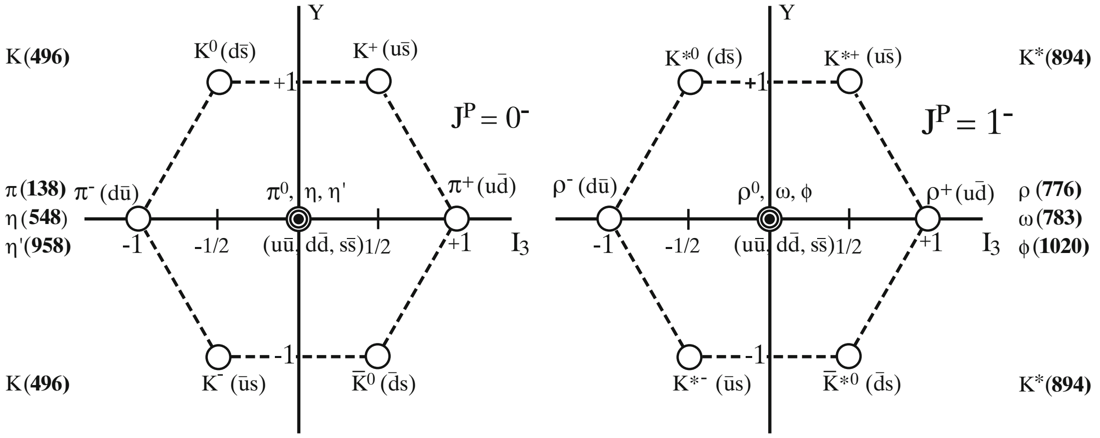

**Figure 1.7:** SU(3) meson nonet in the $I_3 - Y$ plane [1]. Numbers in parentheses are mass values in units of MeV/$c^2$, averaged within the isospin multiplet. Left: pesudoscalar mesons and $q\bar{q}$ combinations. Right: vector mesons.

the vectors ($1^{--}$). The orbital excitations $L = 1$ are the scalars ($0^{++}$), the axial vectors ($1^{++}$) and ($1^{+-}$), and the tensors ($2^{++}$). Radial excitations $n_r$ are denoted by the principal quantum number $n$ as $n = L + n_r + 1$. The very short lifetime of the $t$ quark makes it likely that bound state hadrons containing $t$ quarks and/or antiquarks do not exist.

One of the beautiful features of the quark models is its symmetries. The three light-flavor quarks (u, d, s) can be presented by the SU(3) group and the third component of its isospin $I_3$ and the hypercharge $Y$. If one wants to take the total six flavors into account, the representation of SU(6) symmetry is needed. Fig. 1.7 shows the representation of the quantum numbers $Y$ and $I_3$ for which the mesons form an nonet with spin $J = 0$ and $J = 1$. The combination of the quarks (u, d, s) and the antiquarks ($\bar{\text{u}}$, $\bar{\text{d}}$, $\bar{\text{s}}$) forms a singlet and an octet following the SU(3) Lie algebra. Note that a state vector with $I_3 = Y = 0$ is found in the octet ($\eta_8$) and singlet ($\eta_1$)

$$\eta_8 = \frac{1}{\sqrt{6}}(\text{u}\bar{\text{u}} + \text{d}\bar{\text{d}} - 2\text{s}\bar{\text{s}}), \qquad \eta_1 = \frac{1}{\sqrt{3}}(\text{u}\bar{\text{u}} + \text{d}\bar{\text{d}} + \text{s}\bar{\text{s}}). \tag{1.6}$$

The physical states $\eta$ and $\eta'$ should be a mixture of these multiplet states

$$\eta = \cos\theta\,\eta_8 - \sin\theta\,\eta_1, \qquad \eta' = \sin\theta\,\eta_8 + \cos\theta\,\eta_1. \tag{1.7}$$

This SU(3) *mixing* is more dominant in the meson multiplet than in the baryon multiplets [35]. The $\eta$-$\eta'$ mixing angle is a long-standing problem and still under investigation [36, 37]. The semileptonic decay form factor of $\text{D}_\text{s} \to \eta^{(\prime)}\ell\,\nu_\text{e}$ is regarded as a useful probe to study the mixing mechanism.

The quark and antiquark forming a meson can have the same or different flavors. In the charm sector, *open-charm* mesons are defined for a charm quark bound with a non-charm quark, such as $\text{D}^+ = |c\bar{d}\rangle$, $\text{D}_\text{s}^+ = |c\bar{s}\rangle$ and $\text{D}_\text{s}^- = |\bar{c}s\rangle$. A $c\bar{c}$ pair is called a charmonium state, for example the J/$\psi$, which has *hidden-charm*.

States in the natural spin-parity series $P = (-1)^J$ must have $S = 1$ and hence, $CP = +1$. Thus, mesons with natural spin-parity and $CP = -1$ ($0^{+-}$, $1^{-+}$, $2^{+-}$, $3^{-+}$, ...) are forbidden in the $q\bar{q}$ model. The $J^{PC} = 0^{--}$ state is forbidden as well. Mesons with such *exotic* quantum numbers may exist, but would lie outside the $q\bar{q}$ model. The possible candidates for understanding the nature of such exotic mesons could be glueballs $|gg\rangle$, multiquark states $|q\bar{q}q\bar{q}\rangle$, and hybrid states $|q\bar{q}g\rangle$, or a mixture of above.

### 1.4.2 Baryons

The simplest description of baryons is that they are composed of three quarks. Since quarks have spin 1/2, baryons have half-integer spin. The lowest mass baryons are the proton and the neutron. When baryons are produced in particle reactions the same number of anti-baryons are simultaneously created. To describe this phenomenon a new additive quantum number is introduced: baryon number $b$. The baryon numbers of the quarks are included in Table 1.1. We assign $b = 1$ to baryons and $b = -1$ to anti-baryons. Accordingly, a baryon number +1/3 is attributed to quarks, and a baryon number -1/3 to antiquarks. All other particles have baryon number $b = 0$. Baryon number is regarded as conserved in all particle reactions and decays due to the long life time of baryons, e.g. $> 5.9 \times 10^{33}$ years for the proton [38].

So far all established baryons are 3-quark $|qqq\rangle$ configurations, although very recently the LHCb experiment observed a $J/\psi p$ resonance possibly forming a $|uudc\bar{c}\rangle$ pentaquark state [39]. In 2011, the WASA-at-COSY experiment found a possible multiquark state [40], which was interpreted as a hidden color six-quark state [41]. This experimental observation was confirmed in another process [42]. However, the nature of this state is still unclear. Besides the six-quark state, it also can be regarded as a di-baryon system, i.e. a $\Delta\Delta$ bound state, or a mixture of both configurations.

The ground state baryons with just up and down quarks are the nucleons (isospin $I = 1/2$) and the $\Delta$ particles ($I = 3/2$). Baryons containing at least one s-quark are collectively known as *hyperons*, for example the $\Sigma$, $\Xi$ or $\Omega$ states. Fig. 1.8 shows the eight $J^P = (1/2)^+$ ground state baryons and Fig. 1.9 shows the ten ground state $(3/2)^+$ baryons. These can be derived mathematically by multiplying three SU(3) groups together, which means a combination of three quarks in flavor SU(3) symmetry. One of the applications of the symmetries is the Gell-Mann-Okubo mass formula,

$$M = \alpha + \beta Y + \gamma[I(I+1) - Y^2/4], \tag{1.8}$$

where the coefficients $\alpha$, $\beta$, and $\gamma$ are constant in a SU(3) multiplet. This formula was first deduced by Okubo [43], and then applied by Gell-Mann [44] to predict the mass of the $\Omega^-$. If the SU(3) symmetry was an exact symmetry of the strong interaction, then all states of one SU(3) multiplet would be energetically degenerate, which means they should have exactly the same mass. However, experiments show that for the baryon octet the mass splitting is on the order of 10% [35], hence SU(3) symmetry is broken in nature.

The Standard Model is believed to be theoretically self-consistent and has demonstrated huge and continued successes in providing experimental predictions, but it does leave some

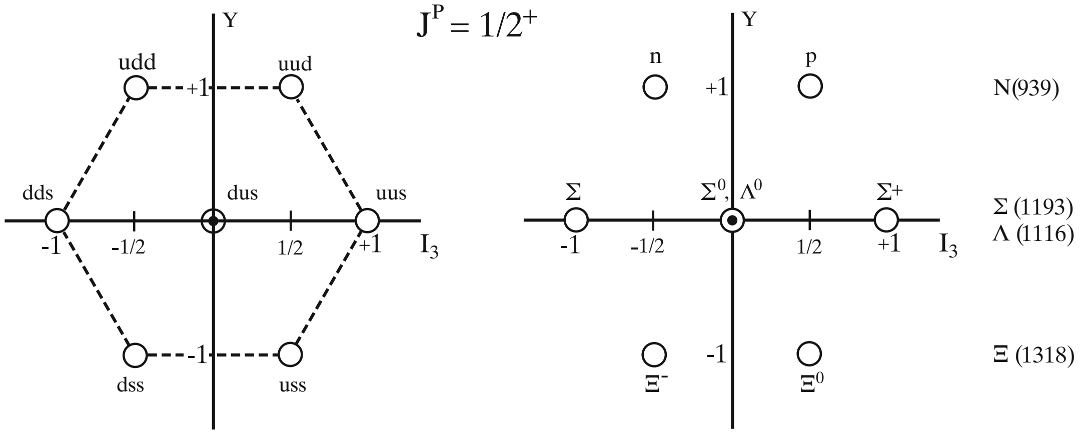

**Figure 1.8:** SU(3) baryon octet in the $I_3 - Y$ plane. Left: an octet made of three quarks. Right: observed $(1/2)^+$ baryons. Figures taken from Ref. [1].

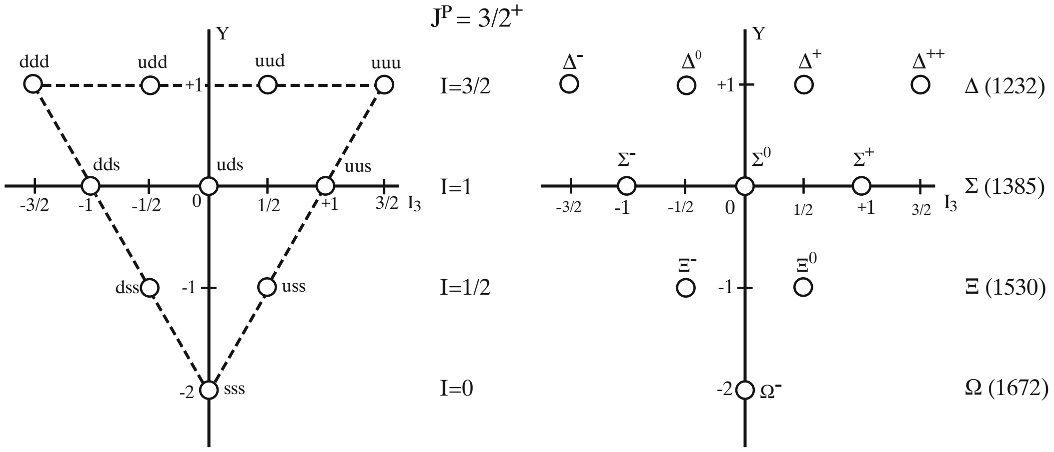

**Figure 1.9:** SU(3) baryon decuplet in $I_3 - Y$ plane. Left: ten states constructed as totally symmetric combinations of three quarks. Right: observed $(3/2)^+$ resonances. Figures taken from Ref. [1].

phenomena unexplained, e.g. dark matter and dark energy, neutrino oscillations, or the matter-antimatter asymmetry in the universe. Note that many theories beyond the Standard Model, including the extremely popular supersymmetry [45], double the number of elementary particles by hypothesizing that each known particle associates with a "shadow" partner far more massive [20]. Although the Standard Model provides an excellent description of electroweak and strong interactions, there are many reasons for us to expect new forces giving rise to new particles at larger masses than the known fermions or bosons. A large increase in accelerator energy and/or intensity and detector precision is required to find phenomena that go beyond the Standard Model and explore new physics.

# Form Factor of Hadrons 2

Since the quark model was proposed, we have known that baryons and mesons are all made up of quarks and antiquarks. One would therefore expect that by now we would have figured out exactly how quarks fit into the hadrons and lead to their observable properties, e.g. mass, size, spin, charges and currents. But nature is much more devious, and does not allow easy insight into its workings. One of the tools that has been successfully used to gain insight into the structure of hadrons is the measurement of form factors. This chapter starts from the electromagnetic form factor of the nucleon as an introductory example for the transition form factor of $\mathrm{D_s}$ semileptonic decay. An overview of recent theoretical studies on $\mathrm{D_s}$ semileptonic decay form factor and related measurements in this field is presented.

## 2.1 Space-Like Form Factor

Electromagnetic form factors of a hadron are the direct link to the structure of the hadron in terms of its constituents. They describe the coupling of a photon with a certain four-momentum to the distribution of charges and currents in the hadron. The nucleon space-like form factor can be measured in lepton-proton elastic scattering.

The Feynman diagram of electron-proton elastic scattering is shown in Fig. 2.1. The initial proton has the four-momentum $p$, and the recoil proton has $p'$. This electromagnetic interaction takes place by exchanging a *virtual photon*. A virtual photon has the quantum numbers of a photon, but it is called off-shell since the relation $E^2 = P^2 + M^2$ requires a non-zero value of $M_{\gamma^\star}$.

The lepton vertex is described completely within QED and on the nucleon vertex, the structure of the nucleon can be parameterised by two Lorentz scalar functions depending on the momentum transfer only. These scalar functions are the Dirac form factor $F_1$ and the Pauli form factor $F_2$, which describe the non-helicity-flip and the helicity-flip part of the hadronic current, respectively. Due to the recoil of the virtual photon, the energy loss of the electron is significant. Consequently, it is no longer possible to describe the scattering in terms of a three-momentum transfer. Instead, the Lorentz-invariant four-momentum square can be used to describe the scattering as:

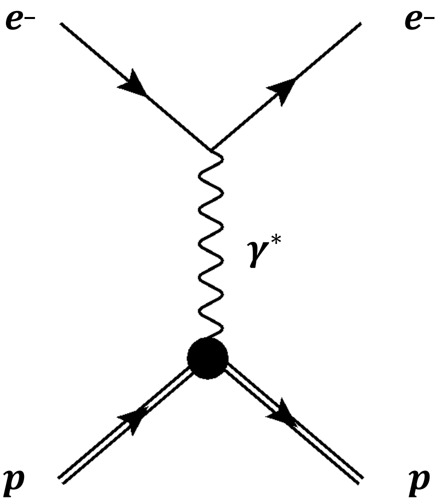

**Figure 2.1:** Feynman diagram of electron-proton elastic scattering $e^-p \to e^-p$. The initial proton (electron) has the four-momentum $p(k)$, and the final proton (electron) has $p'(k')$, thus the momentum of the photon $q$ is $q = p' - p = k' - k$.

$$\begin{aligned} q^2 &= \left(p-p'\right)^2 = 2m_e^2c^2 - 2\left(EE'/c^2 - \left|\mathbf{p}\right|\left|\mathbf{p}'\right|\cos\theta\right) \\ &\approx \frac{-4EE'}{c^2}\sin^2\frac{\theta}{2}. \end{aligned} \tag{2.1}$$

In order to work with positive quantities, $Q^2$ is defined as

$$Q^2 = -q^2. \tag{2.2}$$

For a four-momentum transfer $q^2 < 0$, or equivalently $Q^2 > 0$, the interaction is considered *space-like*. The Feynman amplitude for elastic electron-proton scattering in the framework of one-photon exchange is

$$M = \frac{e^2}{q^2}\left[\bar{u}(k')\gamma_\mu u(k)\right]\left[\bar{U}(p')\left(F_1(q^2)\gamma_\mu + i\frac{\sigma_{\mu\nu}q^\nu}{2m_p}F_2(q^2)\right)U(p)\right], \tag{2.3}$$

where $u$ and $U$ are the electron and proton Dirac spinors and $m_p$ is the mass of proton. With this amplitude, one can obtain the differential cross section of elastic electron-proton scattering, which is known as *Rosenbluth formula* [46]. It can be simplified by replacing the point-like coupling term with the cross section for elastic election-muon scattering, i.e. the Mott cross-section, as

$$\left(\frac{d\sigma}{d\Omega}\right) = \left(\frac{d\sigma}{d\Omega}\right)_{\text{Mott}} \times \left[\frac{G_E^2(Q^2) + \tau G_M^2(Q^2)}{1+\tau} + 2\tau G_M^2(Q^2)\tan^2\frac{\theta}{2}\right], \tag{2.4}$$

where $\tau = q^2/4m_p^2$. $G_E^2(Q^2)$ and $G_M^2(Q^2)$ are the *electric* and *magnetic form factors*, both of which depend on $Q^2$. They are linear combination of $F_1(Q^2)$ and $F_2(Q^2)$. The measured $Q^2$-dependence of the form factors embodies the information about the radial charge distributions and the magnetic moments [47]. In the Breit frame, space-like form factors are the Fourier transforms of the spatial charge ($G_E$) and magnetization distribution ($G_M$) of the proton, in non-relativistic approaches. Their slope at $q^2 = 0$ directly yields the charge and magnetisation radius of the proton.

The form factor idea is also applied to study the internal structure of mesons. Measurements of space-like form factors of mesons at large $Q^2$ are extremely difficult, if not impossible because meson targets do not exist. Measurements by means of either scattering of pion or kaon beams with electrons, or by electro-production of pions are largely confined to small momentum transfers [48].

## 2.2 Time-Like Form Factor

If one rotates the Feynman diagram on Fig. 2.1 to the horizontal direction, the four-momentum transfer $q$ is *time-like*: $q^2 \geq 0$, as shown in Fig. 2.2 for the interaction $\bar{p}p \rightarrow e^-e^+$ and the same diagram holds for $e^-e^+ \rightarrow \bar{p}p$. The annihilation process allows to access positive $q^2$ starting from the threshold of $q^2 = 4m_p^2$. Measurements of form factors for time-like momentum transfers can be at $e^-e^+$ colliders and $\bar{p}p$ annihilations. In principle, the $e^-e^+$ experiments can be used to measure form factors of any meson or baryon. On the other hand, a $\bar{p}p$ annihilation experiment like P̄ANDA, is designed to study the proton time-like form factor with high precision [49].

Here the virtual photon is the electromagnetic probe. The differential cross section for unpolarized initial and final states of the process $\bar{p}p \rightarrow e^+e^-$ is [49, 50]:

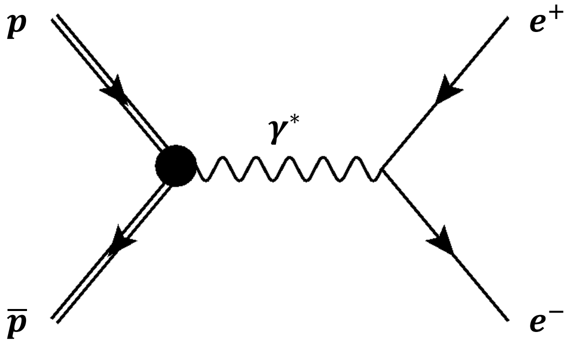

**Figure 2.2:** Feynman diagram of the $\bar{p}p \rightarrow e^+e^-$ process.

$$\frac{d\sigma}{d\cos\theta} = \frac{\pi\alpha^2(\hbar c)^2}{8m_p^2\sqrt{\tau(\tau-1)}}\left[|G_M|^2(1+\cos^2\theta) + \frac{|G_E|^2}{\tau}(1+\cos^2\theta)\right]. \tag{2.5}$$

Experimentally, this differential cross section can be measured over a wide range of $\cos\theta$ which allows an independent determination of the moduli $G_E(q^2)$ and $G_M(q^2)$. Unitarity of the S-matrix requires that space-like form factors are real functions of $q^2$, while for time-like $q^2$ they are complex functions. As mentioned in Sec. 2.1, space-like form factors, in the Breit frame, imply the information about the radial charge distributions and the magnetic moments; on the other hand, time-like form factors reflect the frequency spectrum of the electromagnetic response of the proton. That way two complementary aspects of proton structure can be studied and ask for a full and complete description of the electromagnetic form factors over the full kinematical range of $q^2$. Fig. 2.3 shows the world data until 2012 on proton form factors together with the model predictions by Ref. [51].

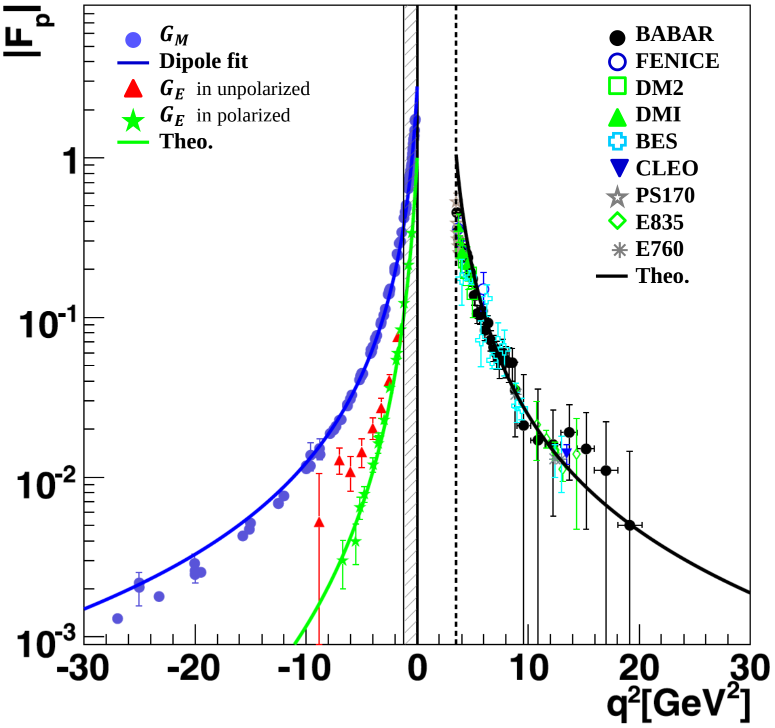

**Figure 2.3:** World data on proton form factors as function of $q^2$, in space-like ($q^2 < 0$) region and time-like ($q^2 > 0$) region. Space-like region: $G_M$ data (blue circles), dipole function (blue line); electric form factor, $G_E$, from unpolarized measurements (red triangles) and from polarization measurements (green stars). The green line is the model prediction. Time-like region: world data under the assumption $|G_E| = |G_M|$. Model prediction (black line), and the experimental results: BABAR [52], FENICE [53], DM2 [54, 55], DM1 [56], BES [57], CLEO [58], PS170 [59], E835 [60, 61] and E760 [62]. Figure taken from Ref. [51].

## 2.3 Transition Form Factor

Based on the same idea for understanding nucleon structure, the *transition form factor* is used to parameterize the transition amplitude as a function of momentum transfer $q^2$ for investigating the interaction governed by QCD effects and dynamics of the constitutes in hadrons. One of the applications is to study the strong interactions on coupling vertex between pseudoscalar meson $P$ ($P$=η, η′, π$^0$, etc.) and photons, in the transition $\gamma^*\gamma \to P$ as illustrated by Fig. 2.4.

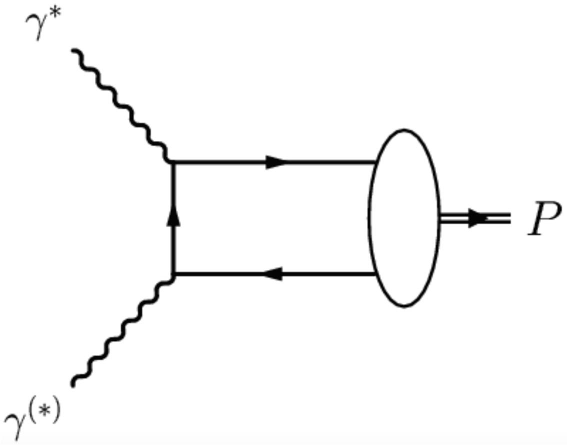

**Figure 2.4:** Feynman diagram of the $\gamma^*\gamma \to P$ process. $P$ is a pseudoscalar meson. Figure taken from [63].

The amplitude of the above process is

$$A = e^2 \upsilon_{\mu\nu\alpha\beta} e_1^\mu e_2^\nu q_1^\alpha \alpha_2^\beta F(q_1^2, q_2^2), \tag{2.6}$$

where the pseudoscalar meson $P$ is represented by a function $F(q_1^2, q_2^2)$ depending on the photon momentum transfer $q_1^2$ and $q_2^2$. This function $F$ is the so-called transition form factor, which embodies the hard scattering amplitude for the $\gamma^*\gamma \to q\bar{q}$ transition and nonperturbative meson distribution amplitude describing the transition $q\bar{q} \to P$. The latter plays an important role in understanding many QCD processes, e. g. $\chi_c \to \pi^+\pi^-$, $B \to \pi\ell\nu$ and so on.

Fig. 2.5 shows the measurement processes to study the transition form factor in the time- and space-like energy regions. The time-like region of the transition form factor can be accessed by the Dalitz decay $P \to \gamma e^+e^-$ (see Fig. 2.5(a)) in the momentum transfer range $0 < q^2 < m_P^2$. To complete the time-like region, the annihilation process $e^+e^- \to P\gamma$ (see Fig. 2.5(b)) allows access to the region with $q^2 > m_P^2$. In the space-like region, the form factor can be studied in the two-photon production process of the pseudoscalar meson $e^+e^- \to e^+e^-P$ (see Fig. 2.5(c)), where the virtual photon momentum transfers are $(-s + m_p^2) < q_1^2 < 0$ and $q_2^2 \approx 0$ with a center-of-mass energy $\sqrt{s}$.

Take one of the pseudoscalar mesons, η, for example, Fig. 2.6 shows the experimental data and theoretical analysis of the $\eta \to \gamma\gamma^*$ transition form factor in both space- and time-like regions. Besides the interests of understanding the transition form factor itself, the form factor parameters allow to examine the $\eta - \eta'$ mixing, the prediction of the $VP\gamma$ couplings etc., as studied in Ref. [64].

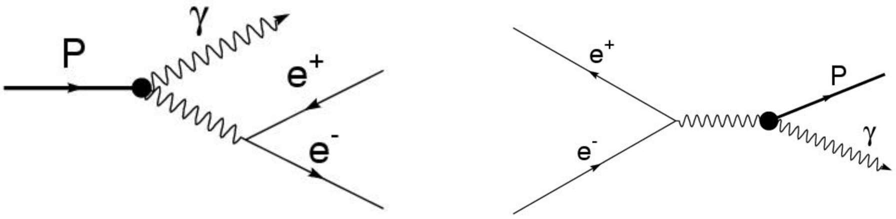

(a) $P \to \gamma e^+e^-$ (b) $e^+e^- \to P\gamma$

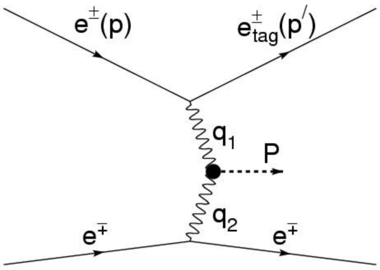

(c) $e^+e^- \to e^+e^-P$

**Figure 2.5:** Possible processes for measuring the pseudoscalar meson transition form factor. Figures taken from [63].

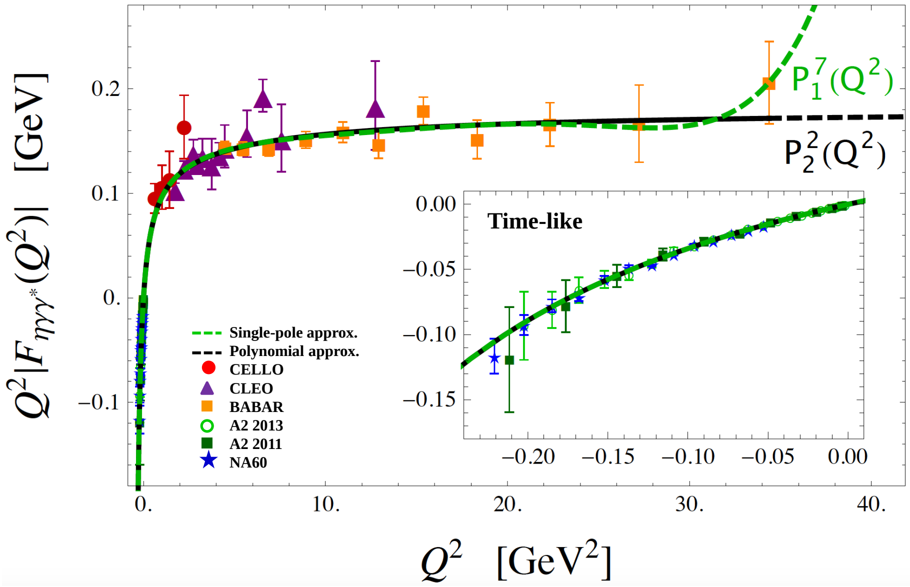

**Figure 2.6:** η transition form factors as a function of $Q^2$ ($Q^2 = -q^2$) in the space-like ($Q^2 > 0$) region and the time-like ($Q^2 < 0$) region. The green-dashed line and black line are the two different parameterizations described in [64]. Experimental data points in the space-like region are from the CELLO [65], CLEO [66], and BABAR [67] Collaborations. In the time-like region, the experimental data points are from NA60 [68], A2 2011 [69], and A2 2013 [70]. The inner plot shows a zoom into the time-like region. Figure taken from Ref. [64].

## 2.4 $\mathrm{D_s}$ Semileptonic Decay Form Factor

In particle physics, the *semileptonic decay* of a hadron refers to a decay through the weak interaction in which one lepton and the corresponding neutrino are produced in addition to one or more hadrons (shown in Fig. 2.7). The transition form factor of the $\mathrm{D_s}$ semileptonic decay is one of the main research objects of this thesis. The analysis of weak semileptonic decays, in which one meson changes into another and emits a W boson, provides a strong test of QCD. The test is complementary to that of comparing QCD predictions to experiment for the meson mass and leptonic decay constants, and in principle more stringent because, instead of just one number, the comparison involves the shape of a differential rate as a function of $q^2$. Another interesting aspect is that the singlet-octet mixing angle of the $\eta$ and $\eta'$ (see Sec. 1.4.1) should be reflected by the respective form factors, e.g. by a substantially different size of the gluonic contribution. The charmed semileptonic decays offer a very promising possibility to determine the leading Fock-state gluonic contribution of the $\eta'$. This section presents the recent theoretical studies on the form factors in the $\mathrm{D_s}$ semileptonic decay.

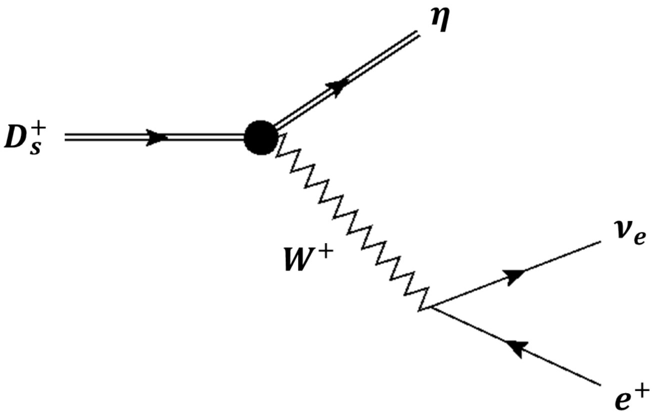

**Figure 2.7:** Feynman diagram of the $\mathrm{D_s^+} \to \eta e^+ \nu_e$ decay.

At the quark level, this process is induced by the semileptonic charm quark decay: $\mathrm{c} \to q \ell \nu_{\mathrm{e}}$, where q = d, s. The light d or s daughter quark is bound to the initial light quark of the charm meson by the strong interaction to form a new hadron. The momentum transfer $q$ is

$$q \equiv p_{\mathrm{W^+}} = p_{\mathrm{D_s^+}} - p_{\eta} = p_{\mathrm{e^+}} + p_{\nu_{\mathrm{e}}}. \tag{2.7}$$

Leptons are not involved in the strong interaction. Therefore, they can be factored out of the hadronic matrix element in the amplitude of the semileptonic decay process as [71]

$$A = \frac{G_F}{\sqrt{2}} V_{cq}^* \bar{\nu} \gamma_\mu l \langle \eta | \bar{q} \gamma^\mu c | \mathrm{D_s} \rangle, \tag{2.8}$$

where $G_F$ is the Fermi coupling constant. All strong interactions are included in the hadronic matrix element $\langle \eta | \bar{q} \gamma^\mu c | \mathrm{D_s} \rangle$. The amplitude depends both on the hadronic matrix element and the quark-mixing parameter, i.e. the CKM matrix element $V_{cq}$. Thus, the semileptonic process is a good laboratory for studying the quark-mixing mechanism and testing theoretical techniques developed for calculating the hadronic matrix element.

The hadronic matrix element can be decomposed into several form factors according to its Lorentz structure. The η is a pseudoscalar meson, thus the $\mathrm{D_s} \to \eta \ell \nu_\mathrm{e}$ semileptonic decay is generally characterized by the following two form factors, $f_0(q^2)$ and $f_+(q^2)$ [72]:

$$\langle \eta(k)|\bar{q}\gamma^\mu c|\mathrm{D_s}(p)\rangle = f_+(q^2)\left[(p+k)^\mu - \frac{m^2_{\mathrm{D_s}} - m^2_\eta}{q^2}q^\mu\right] + f_0(q^2)\frac{m^2_{\mathrm{D_s}} - m^2_\eta}{q^2}q^\mu, \tag{2.9}$$

where $m_{\mathrm{D_s}}$ and $m_\eta$ are the masses of $\mathrm{D_s}$ and η, respectively. Only $f_+(q^2)$ contributes the the experimental rate. The scalar form factor $f_0(q^2)$ is proportional to the squared lepton mass $m^2_{\mathrm{e^+}}$. Together with the CKM matrix element, and neglecting the lepton mass, one can relate the form factor to the differential decay width as:

$$\frac{\mathrm{d}\Gamma}{\mathrm{d}q^2} = \frac{G_F^2\left|V_{cs}\right|^2}{192\pi^3 m^3_{\mathrm{D_s}}}\left[\left(m^2_{\mathrm{D_s}} + m^2_\eta - q^2\right)^2 - 4m^2_{\mathrm{D_s}}m^2_\eta\right]^{3/2}\left|f_+^{\mathrm{D_s}\to\eta}(q^2)\right|^2. \tag{2.10}$$

In general, the form factor $f_+(q^2)$ can depend on all of the Lorentz scalars that are involved with the two momenta $p$ and $k$, i.e., $p^2$, $k^2$ and $p \cdot k$. However, $p^2$ and $k^2$ are not variables, they are the on-shell masses of the initial- and final-state particles. Therefore, the form factors can only depend on the Lorentz scalar $p \cdot k$, which can equivalently be represented by $q^2$, according to the relation $q^2 = p^2 - 2p \cdot k + k^2$. While the exact form of $f_+(q^2)$ is not calculable in QCD, it is expected to be an analytic function everywhere in the complex $q^2$ plane outside of a cut that extends along the positive $q^2$ axis from the mass of the lowest-lying vector meson $\mathrm{D_s^*}$ [31].

For the $q^2$ dependence of the form factor $f_+(q^2)$, several parameterizations have been suggested. The following is a review of these.

- Single pole model [73]:

$$f_+(q^2) = \frac{f_+(0)}{1 - \frac{q^2}{m^2_{\mathrm{pole}}}}, \tag{2.11}$$

  where the mass pole $m_{\mathrm{pole}}$ is predicted to be $\mathrm{D_s^*}$. The $f_+(q^2)$ can be normalized by its value at $q^2 = 0$ as $f_+(0)$.

- Modified pole model [73]:

$$f_+(q^2) = \frac{f_+(0)}{\left(1 - \frac{q^2}{m^2_{\mathrm{pole}}}\right)\left(1 - \alpha\frac{q^2}{m^2_{\mathrm{pole}}}\right)}, \tag{2.12}$$

where $m_{\text{pole}}$ is generally fixed to the $\mathrm{D_s^*}$ mass and $\alpha$ is a free parameter. This parameterization adds a second term to the expansion given in Eq. 2.11, thus assuming that all higher order poles can be modelled by a single effective pole. To reduce the number of free parameters, this model makes several simplifications including assuming the parameter for scaling violations is near unity and the one for hard scattering of gluons is near zero [31].

- ISGW2 parameterization [74]:

$$f_+(q^2) = \frac{f_+(q^2_{\text{max}})}{\left(1 + \frac{r^2_{\text{ISGW2}}}{12}\left(q^2_{\text{max}} - q^2\right)\right)^2}. \tag{2.13}$$

This parameterization is based on the quark model. $q^2_{\text{max}}$ is the upper limit on the physical range of $q^2$, i.e. $q^2_{\text{max}} = (m_{\mathrm{D_s}} - m_{\eta})^2$. This model was expected to be valid in the vicinity of $q^2_{\text{max}}$, a region of maximum overlap between the initial and final meson wave functions.

- Ball-Zwicky parameterization [75]:

$$f_+(q^2) = f_+(0)\left(\frac{1}{1-\frac{q^2}{m^2_{\mathrm{D_s^*}}}} + \frac{r\frac{q^2}{m^2_{\mathrm{D_s^*}}}}{\left(1-\frac{q^2}{m^2_{\mathrm{D_s^*}}}\right)\left(1-\alpha\frac{q^2}{m^2_{\mathrm{D_s}}}\right)}\right). \tag{2.14}$$

The idea of this model is basically to take the dispersive representation of the form factor, take out the known lowest-lying resonance and approximate the dispersion integral over many particle states, starting from $(m_{\mathrm{D_s}} + m_{\pi})^2$ by an effective pole. $r$ and $\alpha$ parametrize the radius and position of this pole, while $f_+(0)$ gives the overall normalization, similar to other models.

The form factors are generally controlled by nonperturbative dynamics, since perturbative QCD can not be applied directly. This form factor has been studied with several different theoretical tools. Recent calculations on $\mathrm{D_s} \to \eta^{(\prime)}\ell\,\nu_e$ form factors are briefly summarized in the following and prepared for comparison with future experimental determinations.

### 2.4.1 Calculations of QCD Sum Rules

In a nonperturbative theory, instead of a model-dependent treatment in terms of constituent quarks, hadrons are represented by their interpolating quark currents taken at large virtualities. The correlation function of these currents is introduced and treated in the framework of the Operator Product Expansion (OPE), where the short and long-distance quark-gluon interactions are separated. The expansion can be parametrized in terms of universal vacuum condensates which is known as QCD Sum Rules (QCDSR), or light-cone distribution amplitudes as in Light-Cone Sum Rules (LCSR). QCDSR was firstly introduced in 1979 [76]. Based on this framework, a recent calculation [77] proposed a parameterization of possible OZI rule suppressed contributions producing the $\eta'$ in the final state. It considered the semileptonic

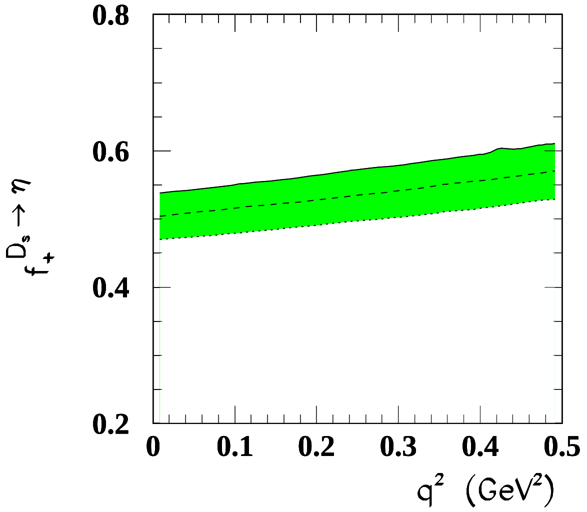

**Figure 2.8:** Form factor $f_+^{D_s\to\eta}(q^2)$ in QCD sum rules [77]. The shaded region represents the theoretical uncertainty due to the variation of input parameters. Figure taken from Ref. [77].

and nonleptonic $D_s$ decay modes to final states with $\eta$. The resulting form factor $f_+^{D_s\to\eta}(q^2)$ is shown by Fig. 2.8.

The form factor $f_+^{D_s\to\eta}(q^2)$ is obtained in the range of momentum transfer $0 \leq q^2 \leq 0.5$ GeV, which is not the complete physical region, and therefore the form factor for high momentum transfer $q^2$ is not calculated in this work. The $q^2$-dependence on Fig. 2.8 was fit by a linear expression, which is consistent in this momentum transfer range with a pole form, as Eq. 2.11 with a pole mass $m_{\text{pole}} \simeq 1.9$ GeV [77].

### 2.4.2 Calculations of Light-Cone Sum Rules

LCSR is another nonperturbative method, besides the previously mentioned QCDSR and later lattice technique. As these approaches are conceptually completely different, the ideal situation is reached if all give the same results. Recent LCSR studies [78, 79] offer increasingly precise calculations of these interesting form factors.

Ref. [78] presents an improved LCSR analysis of the decay form factors and branching fractions of the charmed mesons into $\eta$ and $\eta'$. Based on the calculated form factors, the ratios of $f_+^{\eta'}(q^2)/f_+^{\eta}(q^2)$ is used to access the $\eta-\eta'$ mixing scheme and the possible gluonic contribution. The $q^2$-dependence on the $D_s$ to $\eta$ decay form factor was fitted by the simple Ball-Zwicky parameterization ( see 2.14) with $r = 0.284^{+0.003}_{-0.002}$, $r = 0.252^{+0.107}_{-0.082}$ and $|f_+(0)| = 0.432^{+0.033}_{-0.033}$. Ref. [79] uses leading-order LCSR with chiral currents including meson mass corrections, while the normalization is $|f_+(0)| = 0.45 \pm 0.14$. Fig. 2.9 compares these results.

In these calculations, the form factors in the high momentum transfer region behaves significantly different within various phenomenological treatments. On the other hand, the gluonic contribution can not be determined yet since the experimental precision is not yet sufficient.

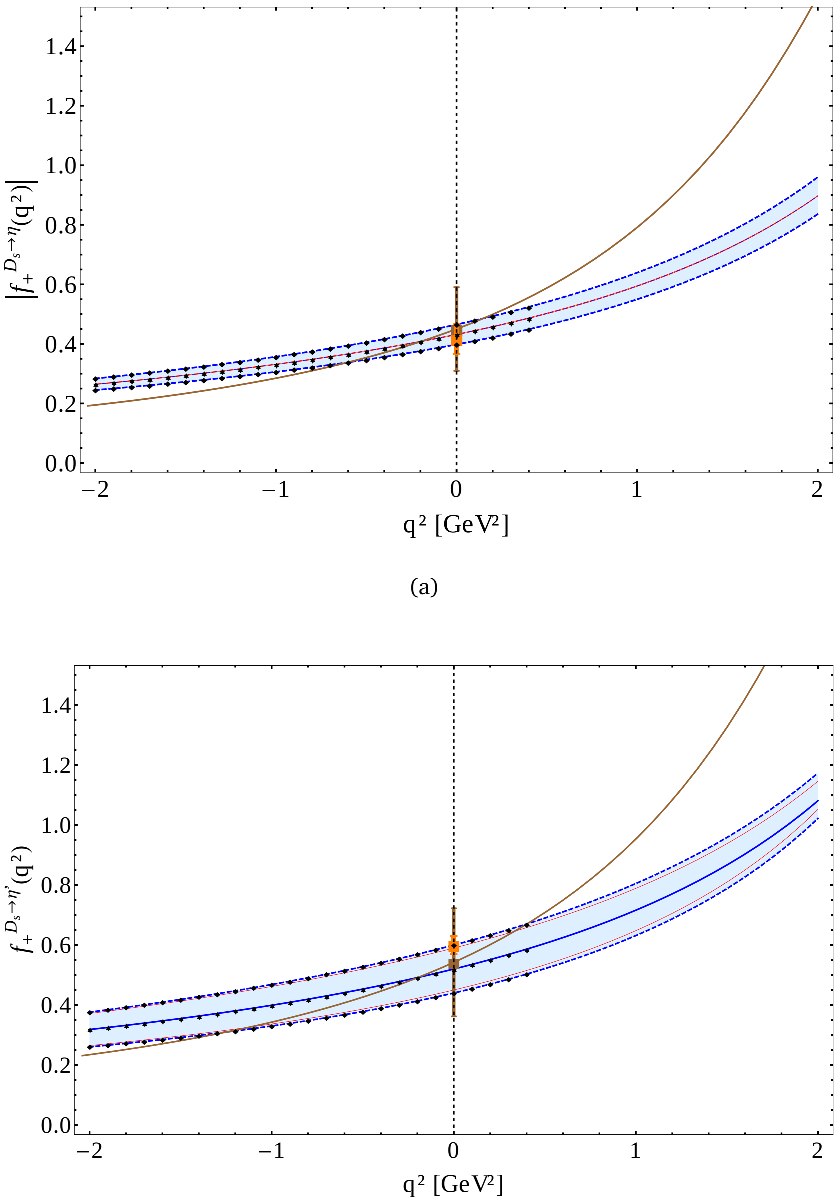

(a)

(b)

**Figure 2.9:** Form factor $f_+^{D_s\to\eta^{(\prime)}}(q^2)$ as a function of $q^2$. (a) is for $D_s^+ \to \eta$; (b) is for $D_s^+ \to \eta'$. The black dots are the calculated sum rule values. The solid blue line is the fit to the central values. Blue dashed band: Full uncertainties of the result in Ref. [78]. Red lines: Uncertainty coming from the gluonic contribution, which due to a very small impact nearly conceal the blue line. Brown line: results of another calculation of LCSR from Ref. [79]. Orange point: corrected lattice result from [72]. Figures taken from Ref. [78].

Future measurements with higher accuracy are needed to settle this long-standing issue and thereby make important steps towards understanding the nonperturbative dynamics of QCD.

### 2.4.3 Calculations of Lattice QCD

Lattice studies of the $D_s$ semileptonic decays are technically challenging due to the presence of disconnected quark-line contributions. So far only the form factor for the decay $D_s \to \phi \ell \nu_\ell$ has been computed, omitting the disconnected contributions [80]. For the channel with a $\eta$ meson, the scalar form factor $f_0(q^2)$ has been studied in Ref. [81], which contains the disconnected fermion loop diagrams. This is the first LQCD result of decay form factors including these contributions and it is found that the disconnected fermion loops give significant contributions to the form factor. Fig. 2.10 shows the results from Ref. [81].

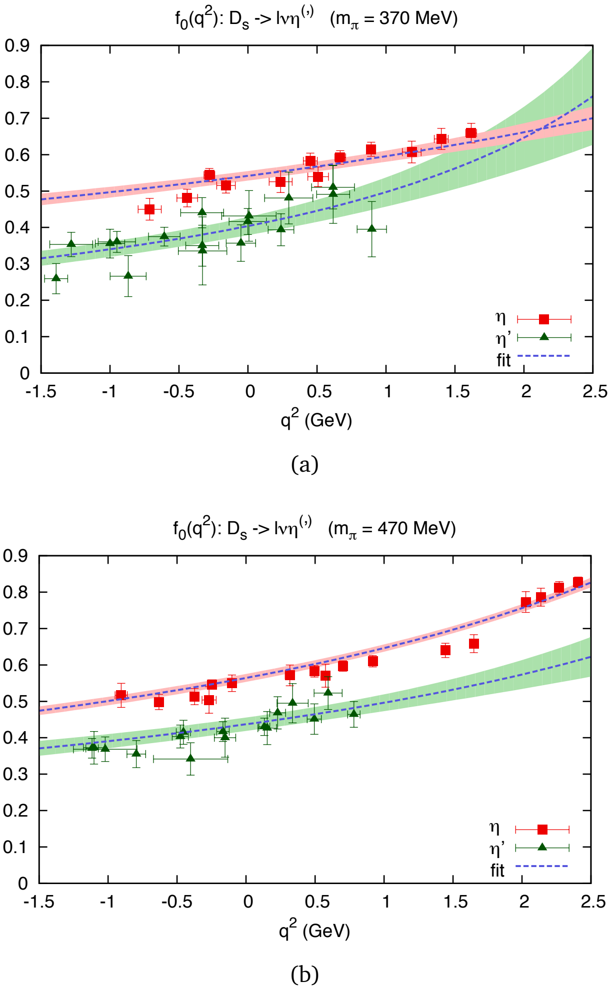

(a)

(b)

**Figure 2.10:** The scalar form factor $f_0(q^2)$ for $D_s \to \eta^{(\prime)} \ell \nu_\ell$ in LQCD. The errors are statistical only and the dashed lines indicate the fits to the form factors using the parameterizations $f_0(q^2) = f_0(0)/(1 - bq^2)$. (a) are the results with $M_\pi \approx 370$ MeV and (b) assumes $M_\pi \approx 470$ MeV. Figures taken from Ref. [81].

A first principles calculation of the form factors for $D_s \to \eta^{(\prime)} \ell \nu_\ell$ can serve as a cross-check on the assumptions of the sum rule approach and is of phenomenological interest in itself, providing information on the internal structure of the mesons in the final state. In terms of experimental results, there are no measurements of the form factors for these modes so far and only the branching fractions for $D_s \to \eta^{(\prime)}\ell\,\nu_\ell$ have been determined by the CLEO collaboration [82]. Therefore, P̄ANDA has strong motivation to perform the first measurement of the form factors.

## 2.5 Experiments on Semileptonic Decays of $D_s$ Meson

About 15% of the $D_s$ meson decays [9] (see Fig. 2.11) are semileptonic. They are by far dominated by decays with $\eta$, $\eta'$ and $\phi$ mesons in the final state. The exclusive $D_s$ decays to final states containing $\eta$ and $\eta'$ represent nearly 30% of the total decay rate. $D_s$ could be a suitable system where to gather information aspects of the $\eta - \eta'$ phenomoenology via measuring the transition form factors precisely.

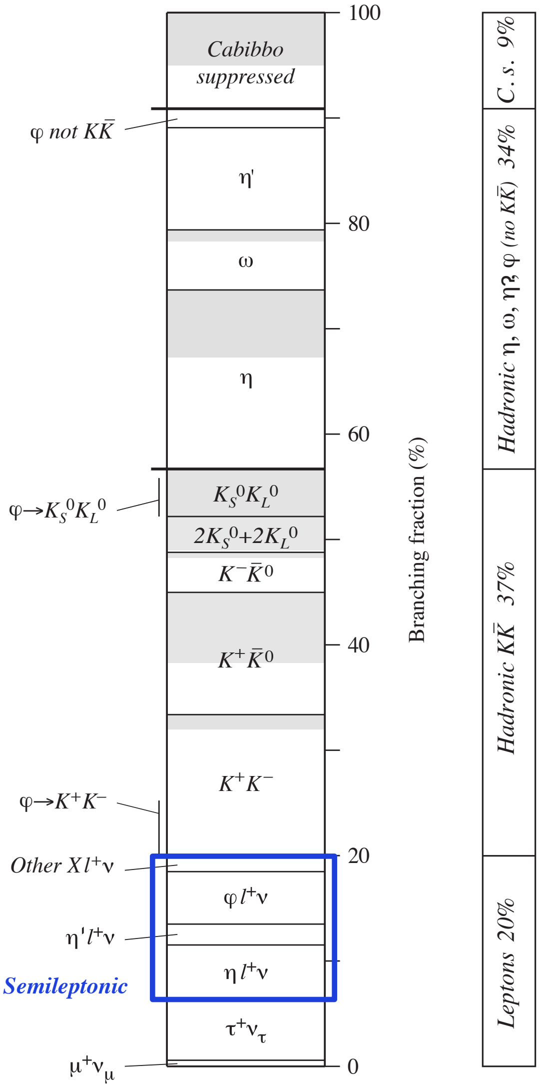

**Figure 2.11:** A partial breakdown of the $D_s^+$ branching fractions cited from Ref. [9]. Shading indicates parts of bins allotted to as-yet unmeasured exclusive modes. The blue box indicates the fraction of semileptonic decays. Figure adapted from Ref. [9].

Data on charm semileptonic decays exists since 1993, when the Fermilab E653 experiment first observed $\mathrm{D}_s^+ \to \eta^{(\prime)}\mu^+\nu_\mu$ and extracted the form factor parameters of $\mathrm{D}_s^+ \to \phi\mu^+\nu_\mu$ at $q^2 = 0$ [83]. In 2009 the first absolute measurement of the branching ratio (BR) $BR(\mathrm{D}_s^+ \to \eta^{(\prime)}\mathrm{e}^+\nu_\mathrm{e})$ [82] and the first observation of the $\mathrm{D}^+ \to \eta\mathrm{e}^+\nu_\mathrm{e}$ decay [84] were reported by the CLEO collaboration. Improved branching fraction measurements, together with the observation of the decay mode $\mathrm{D}^+ \to \eta'\mathrm{e}^+\nu_\mathrm{e}$ and the first form factor determination for $\mathrm{D}^+ \to \eta\mathrm{e}^+\nu_\mathrm{e}$, followed in 2011 [85]. Table 2.1 summarizes the measurements on $\mathrm{D}_s$ semileptonic decays up to 2015 [9].

**Table 2.1:** Summary on available experiments measuring branching ratios (BR) and decay form factors of $\mathrm{D}_s$ semileptonic decays. "$\surd$" indicates that the corresponding data exist and have been published. Only at momentum transfer $q^2 = 0$ are the form factor parameters of $\mathrm{D}_s \to \phi\ell\nu_\ell$ determined in all relevant experiments.

| Decay mode | Events | BR | Form Factor | Collaboration | Year | Ref. |
|---|---|---|---|---|---|---|
| $\mathrm{D}_s^+ \to \phi\mu^+\nu_\mu$ | 793 | | $\surd$ | FOCS | 2004 | [86] |
| | 127 | | $\surd$ | E791 | 1999 | [87] |
| | 90 | | $\surd$ | E687 | 1994 | [88] |
| | 19 | | $\surd$ | E653 | 1993 | [83] |
| $\mathrm{D}_s^+ \to \phi\mathrm{e}^+\nu_\mathrm{e}$ | 106 | $\surd$ | | CLEO | 2009 | [89] |
| | 45 | $\surd$ | | CLEO | 2009 | [82] |
| | 25000 | $\surd$ | $\surd$ | BaBar | 2008 | [90] |
| | 144 | | $\surd$ | E791 | 1999 | [87] |
| | 308 | | $\surd$ | CLEO | 1994 | [91] |
| $\mathrm{D}_s^+ \to \omega\mathrm{e}^+\nu_\mathrm{e}$ | - | $\surd$ | | CLEO | 2011 | [92] |
| $\mathrm{D}_s^+ \to \mathrm{K}^0\mathrm{e}^+\nu_\mathrm{e}$ | 14 | $\surd$ | | CLEO | 2009 | [82] |
| $\mathrm{D}_s^+ \to \mathrm{K}^*(892)\,\mathrm{e}^+\nu_\mathrm{e}$ | 8 | $\surd$ | | CLEO | 2009 | [82] |
| $\mathrm{D}_s^+ \to f_0(980)\,\mathrm{e}^+\nu_\mathrm{e}$ | 44 | $\surd$ | | CLEO | 2009 | [89] |
| | 13 | $\surd$ | | CLEO | 2009 | [82] |
| $\mathrm{D}_s^+ \to \eta\mathrm{e}^+\nu_\mathrm{e}$ | 82 | $\surd$ | | CLEO | 2009 | [82] |
| $\mathrm{D}_s^+ \to \eta'\mathrm{e}^+\nu_\mathrm{e}$ | 8 | $\surd$ | | CLEO | 2009 | [82] |

As shown in Table 2.1, no experimental result on the form factor $f_+^{\mathrm{D}_s\to\eta}(q^2)$ exist, and the branching ratio for this channel has only been measured by CLEO in 2009 with insufficient statistics to study the form factors. Note that most of the previous measurements used $\mathrm{e}^+\mathrm{e}^-$ annihilation for producing charm meson pairs. Fig. 2.12 shows the charm production cross section in $e^+e^-$ interactions [93]. The maximum cross section for a $D_s$ pair is found to be ~0.3 nb. In the future $\bar{P}$ANDA experiment, a higher cross section is expected using antiproton-proton as the production process [94] (see Sec. 4.1.1).

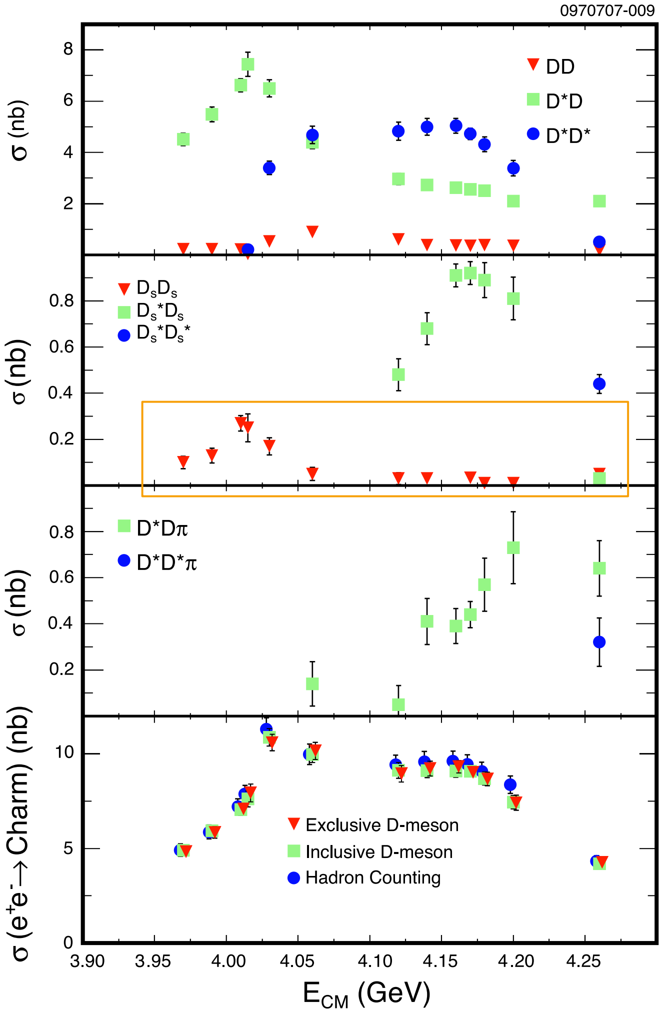

**Figure 2.12:** CLEO measurement of charm production cross sections in $e^+e^-$ annihilation at energies between 3.97 and 4.26 GeV [93]. This histogram shows the exclusive cross sections for two-body and multi-body charm-meson final states, and total observed charm cross section with combined statistical and systematic uncertainties. The orange box highlights the cross section $\sigma(e^+e^- \rightarrow D_s^+D_s^-)$. Figure adapted from Ref. [93].

# $\bar{\text{P}}$ANDA Experiment at FAIR 3

The $\bar{\text{P}}$ANDA experiment (AntiProton ANnihilation at DArested) will be one of the key experiments at the Facility for Antiproton and Ion Research (FAIR) (**F**acility for **A**ntiproton and **I**on **R**esearch), which is under construction adjacent to GSI Helmholtz Centre for Heavy Ion Research (GSI) in Darmstadt, Germany. $\bar{\text{P}}$ANDA studies interactions between antiprotons and fixed target protons or other nuclei in the momentum range of 1.5 GeV/$c$ to 15 GeV/$c$ [49] using the high energy storage ring High-Energy Storage Ring (HESR). This chapter gives a comprehensive overview of the $\bar{\text{P}}$ANDA experiment, including the FAIR accelerator complex (in Sec. 3.1) and the $\bar{\text{P}}$ANDA detector: the envisioned physics topics (in Sec. 3.2), the sub-detector designs (in Sec. 3.3) and analysis software (in Sec. 3.4).

## 3.1 Overview of FAIR Facility

FAIR will be an international accelerator facility of the next generation. The GSI facility is being upgraded, and together with a new proton linear accelerator will serve as pre-accelerator and injector for the new complex. FAIR is a unique international accelerator facility for the research with antiprotons and ions. It allows several physics programs to be carried out in parallel, covering four major fields:

- Antiproton Annihilation at Darmstadt ($\bar{\text{P}}$ANDA)
- Compressed Baryonic Matter (CBM)
- Atomic, Plasma Physics and Applications (APPA)
- Nuclear Structure, Astrophysics and Reactions (NUSTAR)

An overview of the complex is shown in Fig. 3.1, where the existing GSI facility is denoted in blue and the new facility is in red. Latest technological concepts will enable the construction of a state-of-the-art, multipurpose accelerator facility. Its core, a double-ring accelerator (SIS100/300 heavy ion synchrotron) with a circumference of 1100 m, will be associated with a complex system of cooler and storage rings and experimental setups. The synchrotron will

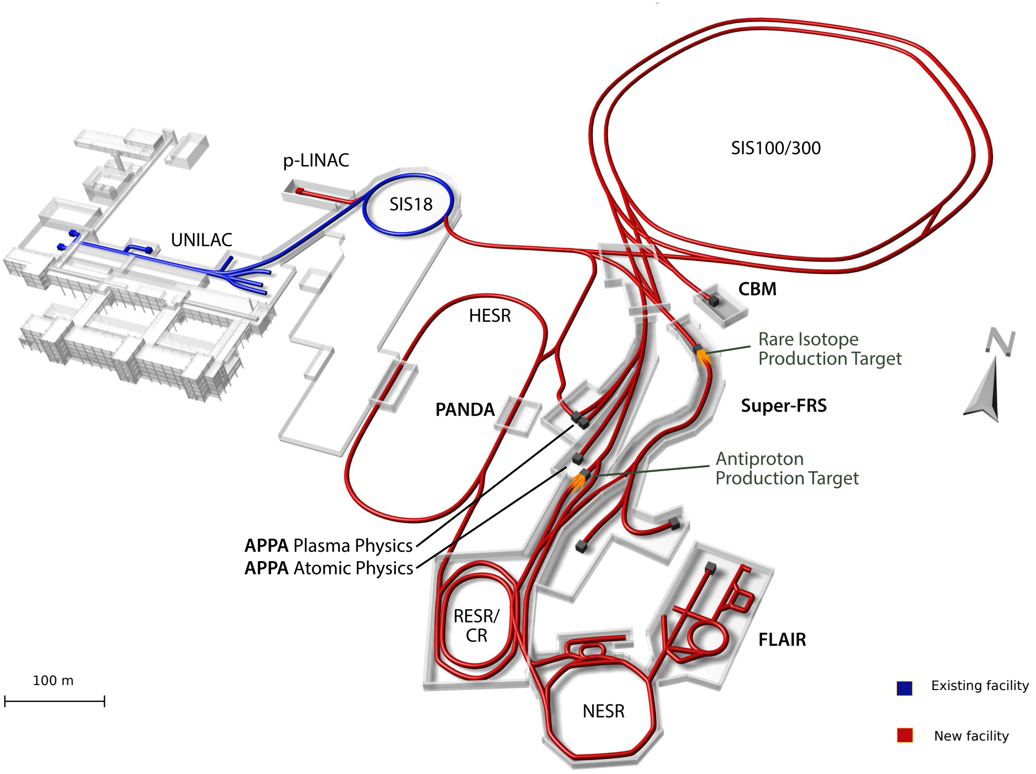

**Figure 3.1:** The full FAIR complex facility. The existing accelerators of the GSI are displayed in blue, and the new systems are displayed in red, which belong to the FAIR facility. Figure adapted from Ref. [95].

deliver ion beams of unprecedented intensities. Thus, also intensive secondary beams can be produced, providing antiprotons and exotic nuclei for groundbreaking experiments. The system of storage and cooler rings allows to drastically improve the quality, for instance of the energy spread and emittance of the secondary beams, in order to use them for high precision experiments. Moreover, in connection with the SIS100/300 synchrotron an efficient parallel operation of all four scientific programs can be realized.

The central part of FAIR is a synchrotron complex providing intense pulsed ion beams. Antiprotons are produced by inelastically colliding the accelerated protons of 29 GeV with a metal target. The protons are provided by the SIS100 synchrotron. After the antiprotons are produced, they have to be collected in a magnetic horn and separated from collision residue particles in a subsequent 58 m beam line. Antiprotons of 3 GeV with a momentum spread $\Delta p/p = \pm 3\%$ are transferred into the collector ring (CR), where the antiprotons are collected and cooled. Approximately $2 \times 10^5$ protons are required to collect one antiproton. Considering a high collection efficiency provided by high density (i.e. high Z) materials, and avoiding target melting due to the deposited energy of the proton beam, an about 11 cm long copper or nickel target is chosen [96, 97].

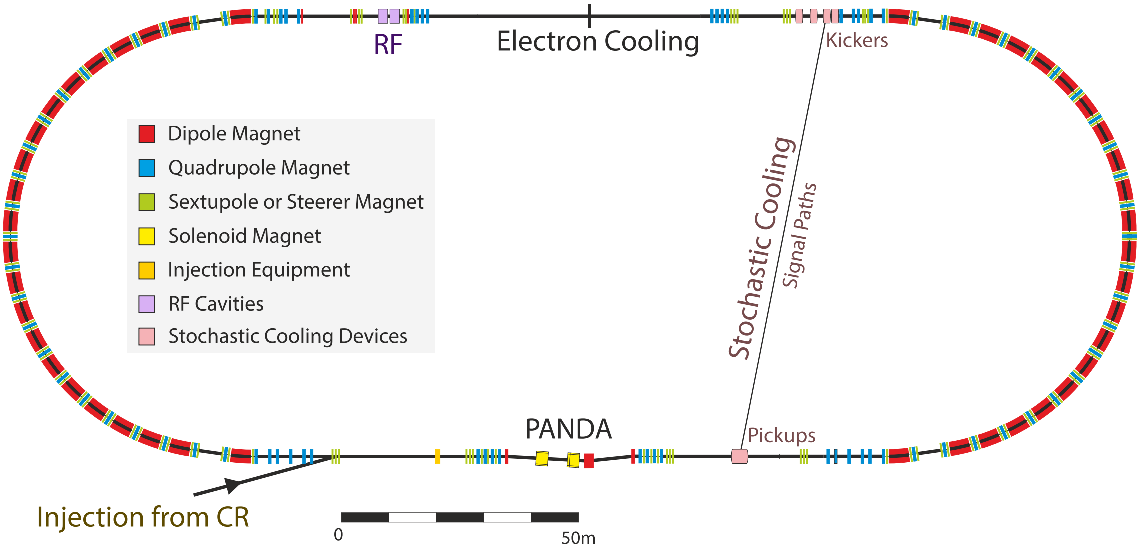

**Figure 3.2:** Schematic drawing of the HESR. The $\overline{\text{P}}$ANDA experiment will be located in the lower straight section. The electron cooling will be located in the upper straight section. Figure taken from Ref. [49].

The produced antiprotons will then be filled into the HESR, and then will collide with a fixed target inside the $\overline{\text{P}}$ANDA detector. A schematic view of the HESR is shown in Fig. 3.2. The HESR is dedicated to supply $\overline{\text{P}}$ANDA with high intensity and high quality antiproton beams over a broad momentum range from 1.5 GeV/$c$ to 15 GeV/$c$. An important feature of this new facility is the combination of phase-space cooled beams and dense internal targets, comprising challenging beam parameters in two operation modes: the High Luminosity (HL) mode and the High Resolution (HR) mode [98]. The HR mode is defined in the momentum range from 1.5 GeV/$c$ to 9 GeV/$c$. To reach a relative momentum spread down to the order of $3 \sim 4 \times 10^{-5}$, only $10^{10}$ circulating $\bar{\text{p}}$ in the ring are anticipated, where the luminosity is $2 \times 10^{31}\,\text{cm}^{-2}\text{s}^{-1}$. The HL mode requires an order of magnitude higher beam intensity with reduced momentum resolution on the order of $10^{-4}$ to reach a peak luminosity of $2 \times 10^{32}\,\text{cm}^{-2}\text{s}^{-1}$ in the full momentum range up to 15 GeV/$c$. Very powerful phase-space cooling will be needed to obtain these beam parameters. Therefore, high-energy electron cooling and high-bandwidth stochastic cooling will be utilized for these two modes [99].

The HESR lattice is designed as a racetrack shaped ring, consisting of two 180° arc sections connected by two long straight sections [49]. One straight section will mainly be occupied by the electron cooler. The other section will host the experimental installation with an internal $H_2$ pellet or cluster target, radio-frequency (RF) cavities, injection kickers and septa (see Fig.3.2). For stochastic cooling pickup and kicker tanks are also located in the straight sections, opposite to each other. Special requirements for the lattice are dispersion free straight sections and small betatron amplitudes in the range of a few meters at the internal interaction point. In addition the betatron amplitudes at the electron cooler are adjustable within a large range.

The realization of the whole FAIR project will be approached in a few stepwise modules [100]. In the Modularised Start Version (MSV) Phase A, the SIS100 synchrotron will be constructed and applied for the scientific studies planed in the MSV modules 0-3, for instance, the physics of

CBM and the low-luminosity required topics in $\bar{\text{P}}$ANDA. The remaining program of $\bar{\text{P}}$ANDA will be carried out in Phase B as modules 4-5, when the Recuperated Experimental Storage Ring (RESR) is available.

## 3.2 Physics Program of $\bar{\text{P}}$ANDA

Experimental studies of hadron structure can be performed with different probes such as electron, pion, kaon, proton or antiproton beams. Each of them has its specific advantages. In antiproton-proton annihilation, particles with gluonic degrees of freedom as well as particle-antiparticle pairs are copiously produced. In addition, a good performance of beam cooling and high luminosity allows spectroscopic studies with unprecedented statistics and precision at $\bar{\text{P}}$ANDA. The $\bar{\text{P}}$ANDA scientific program addresses fundamental questions of QCD, and in particular the interest is centered on the non-perturbative regime, where first-principle calculations are not applicable. Fig. 3.3 indicates the antiproton momenta required to cover a wide range of physics topics, including charmonium spectroscopy, the search for charmed hybrids and glueballs, open-charm physics and hypernuclear studies. This section gives a brief introduction for each main topics, and more details can be found in Ref. [49].

### 3.2.1 Hadron Spectroscopy

Essential predictions of QCD and the Standard Model are embodied in hadron spectroscopy. Due to the recent discovery of states with unexpected properties, hadron spectroscopy has received revitalised interest. $\bar{\text{P}}$ANDA will study hadron spectroscopy up to the mass region of charm quarks. From the experimental point of view, the main goal is to identify the physical states, their quantum numbers, and measure their masses, widths. Based on this we can determine their decay modes and branching ratios, as well as study the underlying dynamics of production and decay. The unique advantage of $\bar{\text{P}}$ANDA is that the antiproton-proton interaction allows to produce states of all quantum numbers, which opens a wide view to explore the hadron spectrum. The subtopics of $\bar{\text{P}}$ANDA will be introduced in the following.

**Charmonium Spectrum** A detailed and precise spectroscopy of the charmonium states will provide new insights into the behaviour of the strong force and the origin of QCD confinement. In this regime, the recent discoveries of new charmonium-like mesons have attracted much interest both in the theoretical and experimental communities, since the new states do not fit well into the quark model predictions in contrast to the previously known states.

Here the search for exotic states like glueballs, hybrids and multiquark states in the light quark domain and in the hidden and open charm region is in the focus of interest. The charmonium spectrum can be calculated within the framework of non-relativistic potential models (see Ref. [103] and references therein), LQCD calculation [104], Effective Field Theory (EFT) and Quark Potential Model (QPM). All eight charmonium states below the open charm ($D\bar{D}$) threshold are known, but the measurement of their parameters and decays is far from complete. A study of experimental data from the Belle, BaBar, BES, CLEO, CDF, and D0 collaborations concludes that eleven of the recently discovered states can be interpreted as $S$, $P$, $D$-wave charmonium states (two singlet $^1S_0$, two singlet $^1D_2$ , three triplet $^3S_1$ , three triplet $^3P_J$ , and one triplet $^3D_2$) charmonium states [105]. As shown in Fig. 3.4, copious $J^{PC} = 1^{--}$ states have

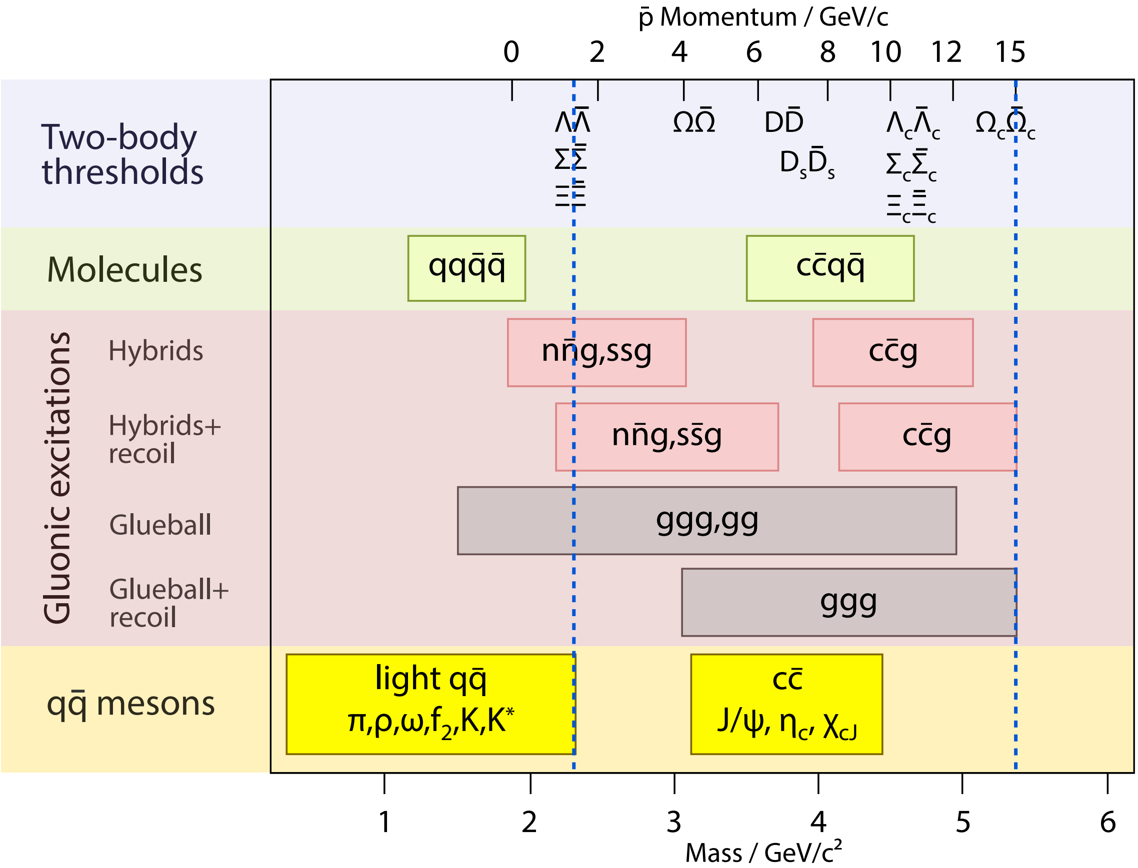

**Figure 3.3:** Mass range of hadrons accessible with antiproton beams at the HESR. The corresponding beam momentum is shown by the upper X axis. The dashed lines indicate the momentum range of the P̄ANDA experiment, 1.5 GeV/$c$ to 15 GeV/$c$. Figure taken from Ref. [101, 102].

been seen in $e^+e^-$ collisions, while only a few high-$L$ states, i.e. $P$, $D$-wave, are measured due to the limitations of the single photon production scheme. P̄ANDA will explore the energy region below and above the open charm threshold, to look for the missing $D$ and $F$-wave states. In addition, by means of fine scans it will be possible to re-examine the "understood" charmonium sector with higher precision.

Besides the conventional $c\bar{c}$ bound states, a plethora of narrow charmonium-like resonances, known as the XYZ states, have been discovered in recent years (see Fig. 3.4). Here "X" stands for all unassigned particles in general. For a finer classification, "Y" is used to specify the $J^{PC} = 1^{--}$ states which are found in $e^+e^-$ mode and "Z" labels the charged states. Some of the XYZ states have exotic quantum numbers, which are forbidden in $q\bar{q}$ picture (see Sec. 1.4.1). While the nature of these states remains hitherto unexplained, many interesting assumptions have been put forward. With its high-quality antiproton beam, the P̄ANDA experiment will be in the position to make decisive contribution to the understanding of these states. Antiproton-proton interactions can form all allowed fermion-antifermion quantum states in direct resonant formation. Therefore, a strong indication of a state $X$ with exotic quantum numbers not allowed in $q\bar{q}$ would be observed in a production process, e.g. $\bar{p}p \rightarrow X\pi^0$ but unobserved in direct

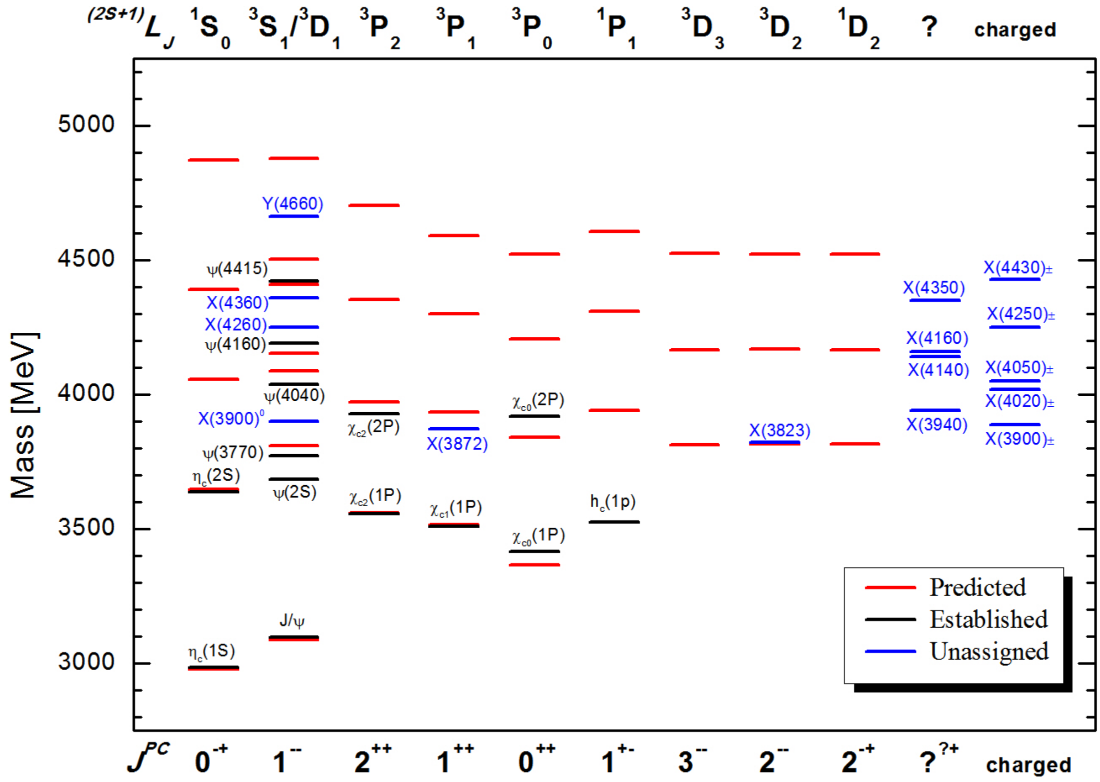

**Figure 3.4:** The status of charmonium spectrum. The red bars indicate the theoretical predictions [103], which are based on a potential model calculation with a scalar-vector mixing linear confinement. The recently updated experimental data of the PDG (2014) [9] are listed: the black bars are well established $c\bar{c}$ states, and the blue bars stand for the newly found charmonium-like XYZ particles. Here the particle names follow the labels on the PDG list. Not confirmed particles are not listed, e.g. Y(4008), Y(4274), Z(4200)$^{\pm}$ etc..

formation $\bar{p}p \rightarrow X$. P̄ANDA is able to find more clues about the number of the XYZ states, and brings a possibility to search for glueballs, hybrids and multiquark states, which are theoretically possible candidates for the exotic states.

**Open-Charm Spectra** Similar to the hidden-charm sector presented above, the spectra of open-charm mesons (see Fig. 3.5) contain a number of experimentally well-established states, while a number of states remains unexplained. Suggestions such as hybrid mesons (in which the gluonic field is excited), molecular mesons and tetraquarks (with four valence quarks) have been proposed, but no clear picture has emerged. In particular, the masses and widths of the enigmatic $D^*_{s0}(2317)^{\pm}$ and $D_{s1}(2460)^{\pm}$ are lighter and narrower than in quark models [106].

So far only experimental upper limits of a few MeV on the full width exist, limited by the detector resolution. With the excellent definition of the HESR antiproton beam, P̄ANDA will be able to reach a mass resolution about 20 times better than that obtained at B factories, and can study these widths down to values of better than 100 keV [22] by measuring the excitation function close to threshold, which is sensitive to the resonance width. P̄ANDA plans to do a mass scan in 100 keV steps for the $D^*_{s0}(2317)$, $D_{s1}(2460)$ and $D_{s1}(2536)$. Recent simulation work

[107] estimates a $D^*_{s0}(2317)$ production rate on the order of $(3 \sim 300) \times 10^3$ reconstructed events per day with the $\bar{\text{P}}$ANDA detector in the high luminosity mode.

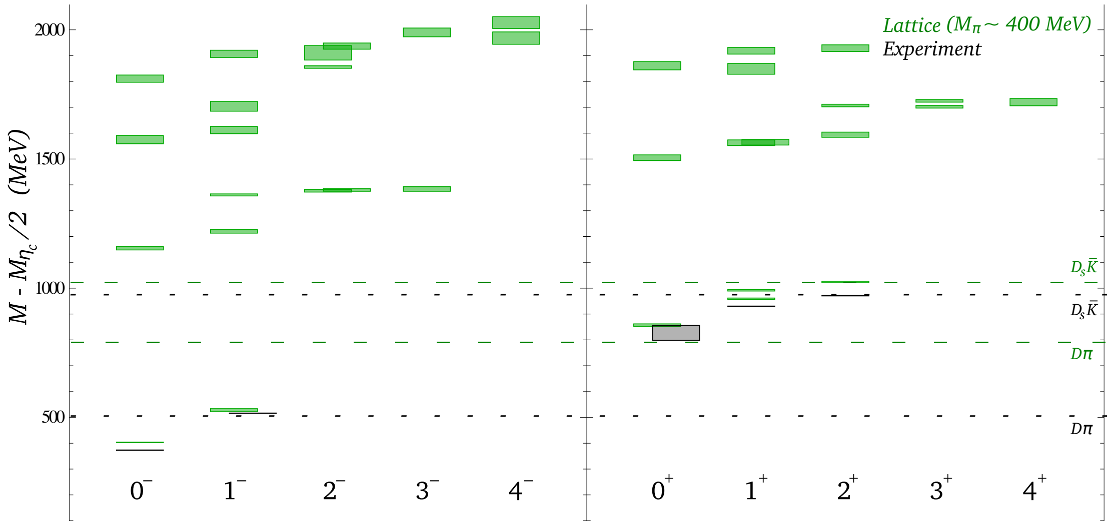

(a) Charm-light spectrum.

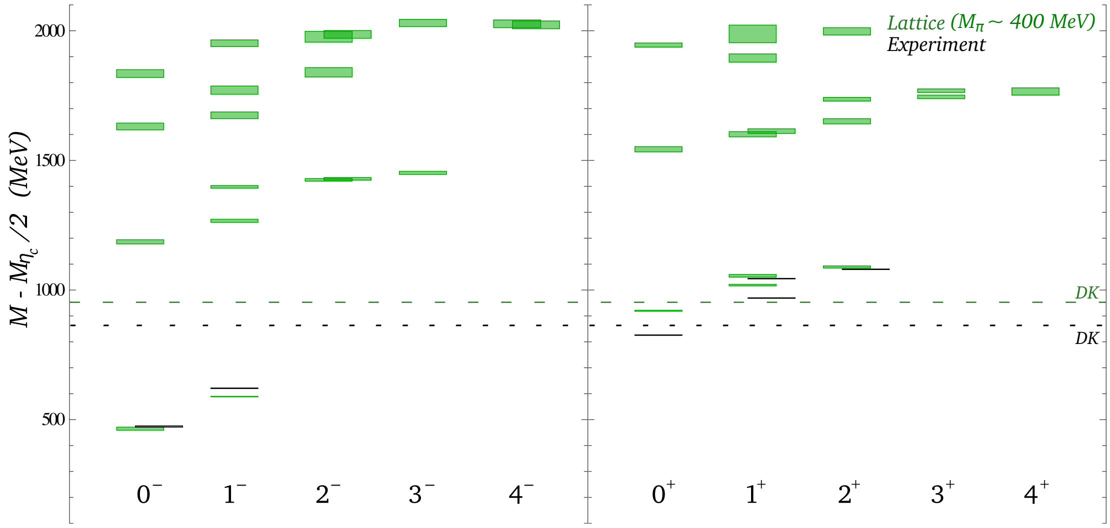

(b) Charm-strange spectrum.

**Figure 3.5:** LQCD calculations of open-charm spectra labelled by $J^P$ [108]. The plot shows the calculated (experimental) masses with half the calculated (experimental) $\eta_c$ mass subtracted to reduce the uncertainty from tuning the bare charm-quark mass. The green boxes/lines are calculated values, while the black ones correspond to experimental values from the PDG 2012 [27]. The vertical size of each box represents the one sigma statistical uncertainty region.

**Gluonic Excitations** Gluonic excitations will be accessible with unprecedented accuracy, thereby allowing high-precision tests of the strong interaction. Gluonic hadrons are classified in two main categories: glueballs, i.e. states where only gluons contribute to the overall quantum

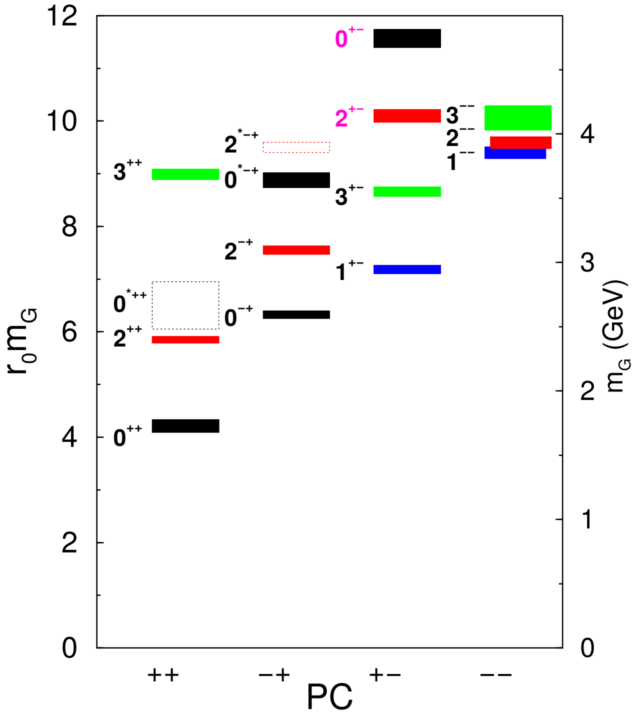

**Figure 3.6:** Glueball spectrum from QCD calculation [109, 110]. Figure cited from Ref. [102].

numbers, and hybrid hadrons, which consist of valence quarks and antiquarks as hadrons plus one or more excited gluons which contribute to the overall $J^{PC}$ quantum numbers. Non-exotic glueballs and hybrids can be identified by measuring an overpopulation of the experimental meson spectrum and by comparing properties, like masses, quantum numbers, and decay channels, with predictions from phenomenology models or LQCD. The properties of glueballs and hybrids are determined by the long-distance features of QCD and their study will yield fundamental insight into the structure of the QCD vacuum.

Fig. 3.6 shows the LQCD prediction of the glueball spectrum. The most promising candidates for gluonic hadrons are the observations of the Crystal Barrel collaboration, $\pi_1(1400)$ first seen with antiprotons stopped in liquid deuterium [111], and $\pi_1(1600)$ found in $\bar{\text{p}}\text{p}$ annihilation [112]. Both of them have the exotic $J^{PC} = 1^{-+}$ quantum number. While the region of the ground-state glueball was investigated in the Crystal Barrel experiment, the tensor glueball and the spin exotic glueballs with $J^{PC} = 0^{+-}, 2^{+-}$ are the important research topics for $\bar{\text{P}}$ANDA.

Furthermore, as shown Fig. 3.6, the predicted mass of the lightest (scalar) glueball is around 1.6 GeV in the quenched LQCD approximation [109]. Flux-tube models imply that if there is a $q\bar{q}$ nonet nearby, with the same $J^{PC}$ as the glueball, then glueball-quarkonium mixing will dominate the decay [113]. The possible candidates in this scenario are the $0^{++}$ states $a_1(1400)$, $f_0(1370)$, $K(1430)$, $f_0(1500)$ and $f_0(1710)$. The interest now centers on clarifying the details and extent of such mixing.

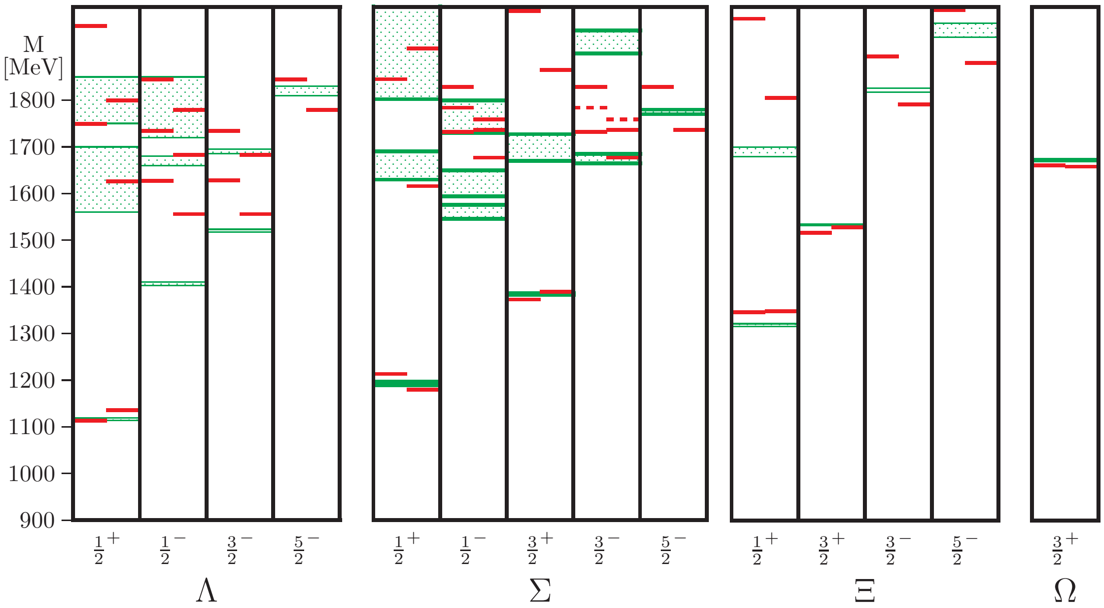

**Figure 3.7:** Spectrum for the lowest Λ, Σ, Ξ, Ω states with total angular momentum and parity $J^P$ for the two relativistic constituent quark models, i.e. One-Gluon-Exchange (left bars) and Goldstone-Boson-Exchange (right bars), in comparison to experimental values with uncertainties [114] shown as green shadowed boxes. The dashed lines in the $J^P = 3/2^-$ Ξ spectrum represent (decuplet) eigenstates, for which there is no experimental counterpart yet. Figure taken from Ref. [115].

**Baryon Spectrum** An understanding of the baryon spectrum is one of the primary goals of non-perturbative QCD. In the nucleon sector, where most of the experimental information is available, the agreement with quark model predictions is astonishingly poor, and the situation is even worse in the strange baryon sector.

Fig. 3.7 shows the spectrum of the lightest strange baryons, where the relativistic constituent quark models were applied. Experimental evidence for some Σ-states and above all in the Ξ-sector is lacking for phenomenology studies. Since 1988 nothing of significance on Ξ resonances has been added in the PDG. Moreover, for a complete assignment of states in the flavor octets additional information also on Λ resonances is urgently needed.

The $\overline{\text{P}}$ANDA experiment is well suited for a comprehensive baryon spectroscopy program, in particular the spectroscopy of the double-strange (Ξ) and triple-strange (Ω) baryon sectors. It is also possible to explore the charmed baryon sector. Besides large cross sections, a particular benefit of using antiprotons in these studies is that in $\bar{p}p$ collisions no production of extra mesons is required to balance strangeness or charm. This reduces the energy threshold and thus the number of background channels. Strange baryons are characterized by their or their daughters' displaced decay vertices. For reconstructing the vertex information, the $\overline{\text{P}}$ANDA trackers are designed to also achieve a good tracking performance for displaced vertices.

### 3.2.2 Hadrons in the Nuclear Medium

Antiproton-nucleus collisions at $\overline{\text{P}}$ANDA offer a very promising opportunity to study the properties of hadrons inside the nuclear environment and the properties of the nuclear medium itself. $\bar{\text{p}}$A collisions are sensitive to the nuclear potential of produced hadrons at low momentum, thus allow to explore the nuclear potential of antibaryons and $\bar{K}$, and test the configuration of the $\bar{K}NN$ system. The high-intensity $\bar{\text{p}}$ beam of up to 15 GeV/$c$ will allow an extension of this program to the charm sector both for hadrons with hidden and open charm. Another study, which can be carried out by $\overline{\text{P}}$ANDA, is the measurement of charmonium production cross sections in antiproton annihilations on a series of nuclear targets. The comparison of the resonant J/$\psi$ yield obtained from $\bar{\text{p}}$ annihilation on protons and different nuclear targets allows to deduce the J/$\psi$-nucleus dissociation cross section, a fundamental parameter to understand $J/\psi$ suppression in relativistic heavy ion collisions interpreted as a signal for quark-gluon plasma formation [116]. The theoretical study on the charmonium production in $\bar{\text{p}}$A reactions presented in Ref. [117] estimates an optimistic rate for the $\overline{\text{P}}$ANDA experiment.

### 3.2.3 Nucleon Structure in Electromagnetic Processes

The virtual photon is an excellent tool to investigate the structure of the nucleon. $\overline{\text{P}}$ANDA offers the unique possibility to make a precise determination of the time-like form factors (see Sec. 2.2). The form factors measured in electron scattering ($\text{e}^-\text{p} \to \text{e}^-\text{p}$) are intimately connected with those measured in the annihilation process ($\bar{\text{p}}\text{p} \to \text{e}^+\text{e}^-$). These observables can probe our understanding of the nucleon structure in the regime of non-perturbative QCD as well as at higher energies where perturbative QCD applies.

In studies of deeply virtual Compton scattering, the high energy region (hard part) can be described by perturbative QCD and QED, and the soft part is described by Generalized Parton Distributions (GPDs). The non-perturbative object allows to interpret hadronic structure information in terms of quark and gluon degree of freedom. GPDs are currently seen as a tool to study the nature and origin of the nucleon spin. For studies of the nucleon structure in the $\bar{\text{p}}\text{p} \to \gamma\gamma$ process at $\overline{\text{P}}$ANDA, the expected count rate based on a simple model is a few thousand $\gamma\gamma$ events per month for a luminosity of $2 \times 10^{32}\,\text{cm}^{-2}\text{s}^{-1}$ at an energy of $\sqrt{s} = 3.2\,\text{GeV}/c^2$ [49]. The comparison of the differential cross sections for the various processes and the comparison with GPDs based models will allow new insights into the annihilation process in terms of quark models and QCD. Further development of the GPDs approach introduces baryon-to-meson Transition Distribution Amplitudes (TDAs), which probe partonic correlations between states. A feasibility study for $\overline{\text{P}}$ANDA has been done to measure the nucleon-to-pion TDAs in $\bar{\text{p}}\text{p} \to \text{e}^+\text{e}^-\pi$ [118].

In addition, $\overline{\text{P}}$ANDA has a chance to study the Transverse Parton Distributions (TPDs) in the dilepton Drell-Yan process $\bar{\text{p}}\text{p} \to \ell^+\ell^- X$ [49, 119]. The Drell-Yan production of muon pairs is a useful tool to access transverse spin effects within the nucleon.

### 3.2.4 Hypernuclei

A hyperon is any baryon containing one or more strange valence quarks. A hypernucleus is a nucleus which contains at least one hyperon. The hyperon bound in a nucleus offers a

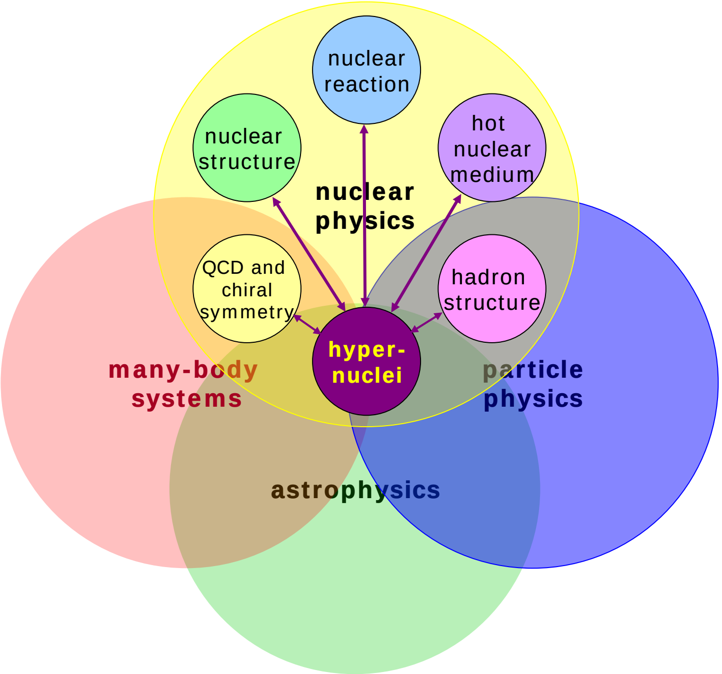

**Figure 3.8:** Hypernuclei and their link to other fields of physics. Figure cited from Ref. [49].

selective probe of the nuclear many-body problem, as it is not restricted by the Pauli principle in populating all possible nuclear states, in contrast to neutrons and protons. Since hyperons have a different value of the strangeness quantum number, they share space and momentum with the usual nucleons that can only differ from each other in spin and isospin. A comparison of ordinary nuclei and hypernuclei may reveal new insights in key questions in nuclear physics like for example the origin of the nuclear spin-orbit force [120]. Therefore, a nucleus may serve as a laboratory offering a unique possibility to study basic properties of hyperons and strange exotic objects. Thus, as shown in Fig. 3.8, hypernuclear physics represents an interdisciplinary science linking many fields of particle, nuclear and many-body physics.

An important goal is to measure the level spectra and decay properties of hypernuclei for testing the energies and wave functions from microscopic structure models [121]. Detailed information on excitation spectra of hypernuclei and their structure will provide unique clues on the hyperon-nucleon and double hypernuclei interactions. To study double hypernuclei physics, in $\overline{\text{P}}$ANDA, bound states of $\Xi$ hypernuclei will be used as a gateway to form double-$\Lambda$ hypernuclei [122]. The two-step production scheme is illustrated in Fig. 3.9, where the reactions $\bar{p}p \rightarrow \Xi^-\bar{\Xi}^+$ and $\bar{p}n \rightarrow \Xi^-\bar{\Xi}^0$ followed by re-scattering of the $\Xi^-$ within the primary target nucleus are employed. After stopping the $\Xi^-$ in an external secondary target composed of silicon detectors and $^9$Be,$^{10,11}$B or $^{12,13}$C absorbers, the formed $\Xi$ hypernuclei are converted into double-$\Lambda$ hypernuclei. The $\gamma$ rays from the excited double hypernuclei can be detected.

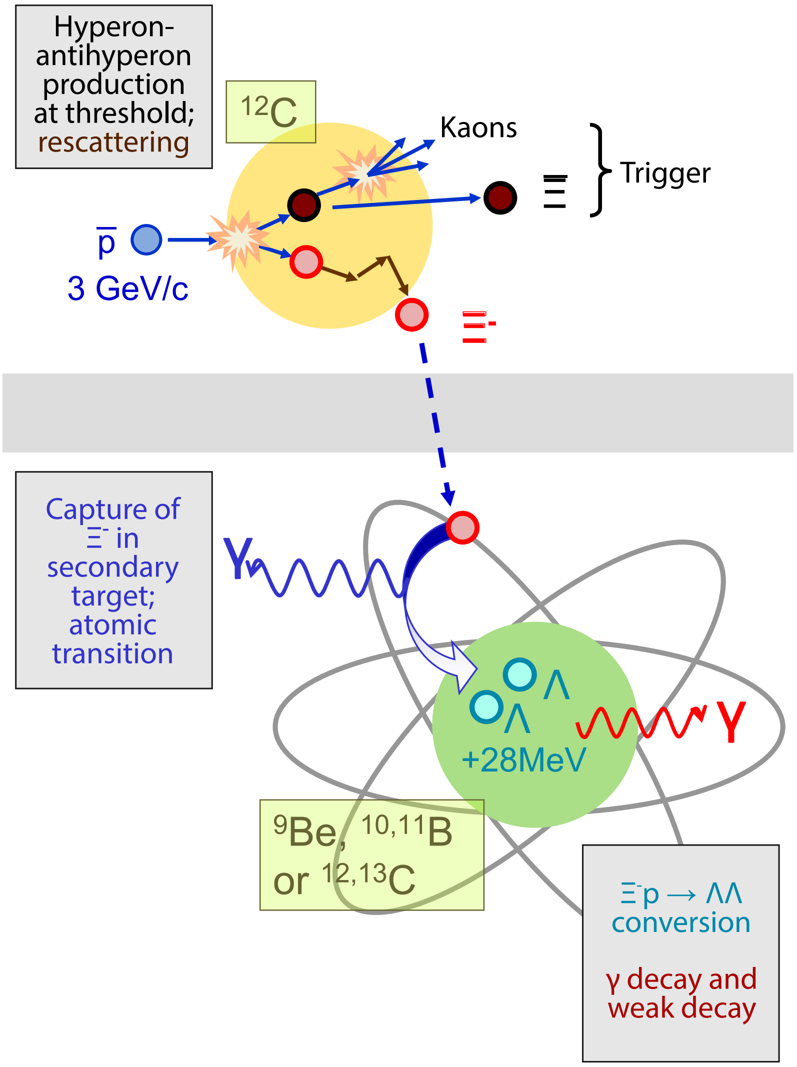

**Figure 3.9:** Illustration of double hypernucleus production in $\bar{\text{P}}$ANDA. Figure cited from Ref. [49].

### 3.2.5 Electroweak Physics

In the full MSV 0-5 of the FAIR project, with the high-intensity antiproton beam available at HESR a large number of D meson can be produced. This gives the possibility to observe rare weak decays of these mesons, allowing to study electroweak physics by probing predictions of the Standard Model and searching for enhancements introduced by processes beyond the Standard Model. There are several interesting topics in this field, e.g. CP (Charge-Parity symmetry) violation and $D^0$-$\bar{D}^0$ mixing, CP violation in hyperon decays and violation of fundamental symmetries in rare decays.

Since the electroweak processes are very rare and small deviations are looked for, the statistics is a main factor in these measurements. This implies that they must be performed at the highest possible luminosity. Even better would be to extend the antiproton production rate beyond the anticipated $2 \times 10^7$/s [49]. However, a long-term parasitic measurement in parallel to spectroscopy and other topics, whenever D mesons are produced can also provide an interesting amount of statistics over some years of operation. The value of the production cross section for $\bar{\text{p}}\text{p} \to \text{D}\bar{\text{D}}$ is an open question. Ref. [49] (and references therein) indicates that the cross section is some where between 3 nb and 200 nb. This same range is estimated for the production cross section of the $\text{D}_\text{s}$ meson. Sec. 4.1.1 gives a detailed discussion on the cross section of $\bar{\text{p}}\text{p} \to \text{D}_\text{s}^+\text{D}_\text{s}^-$, and the electroweak process $\text{D}_\text{s}^+ \to \eta \text{e}^+ \nu_\text{e}$ is systematically simulated in this thesis.

## 3.3 $\bar{\text{P}}$ANDA Detector

The physics program, as described in Sec. 3.2, poses significant challenges for the $\bar{\text{P}}$ANDA detector. For the envisaged experimental program a nearly full $4\pi$ coverage of the solid angle together with a high resolution for tracking, particle identification and calorimetry, high rate capabilities and a versatile readout and event selection are mandatory. To obtain a good momentum resolution the detector will be composed of two magnetic spectrometers: the Target Spectrometer (TS), based on a superconducting solenoid magnet surrounding the interaction region, which will be used to measure at large polar angles and the Forward Spectrometer (FS), based on a dipole magnet, for particles emitted at small polar angles.

The Target Spectrometer will surround the interaction region and measure charged tracks in a homogeneous solenoidal magnetic field. In the manner of a collider detector it will contain detectors in an onion-shell like configuration. Pipes for the injection of target material will have to cross the spectrometer perpendicular to the beam pipe. The Target Spectrometer will be arranged in three parts: the barrel covering polar angles between 22° and 140°, the forward end cap extending the polar angle range down to 5° and 10° in the vertical and horizontal planes, respectively, and the backward end cap, covering the polar angular region between about 145° and 170° [123]. An artistic view of the TS is shown in Fig. 3.10.

The Forward Spectrometer will cover all particles emitted in vertical and horizontal angles below 5° and 10°, respectively. Charged particles will be momentum analyzed by a dipole field. Fig. 3.11 gives an overview to the instrumentation of the Forward Spectrometer.

In the following, an overview of the complex detector system is presented, including the target and the sub-detectors categorized by their functions, e.g. tracking and particle identification. Fig. 3.12 shows the basic detection concepts of the detector system.

### 3.3.1 Target Systems

The design of the solenoid magnet allows for an implementation of different target systems. $\bar{\text{P}}$ANDA will use both gaseous and non-gaseous targets. A very precise positioning of the target is crucial for the exact definition of the primary interaction vertex. Hydrogen target systems will be used for the study of antiproton-proton reactions. A high effective target density of up to $4 \times 10^{15}$ hydrogen atoms per square centimeter must be achieved to fulfil the design goals of the high luminosity mode. Besides using hydrogen as the target material, an extension to heavier gases such as deuterium, nitrogen or argon is planned for complementary studies with nuclear targets.

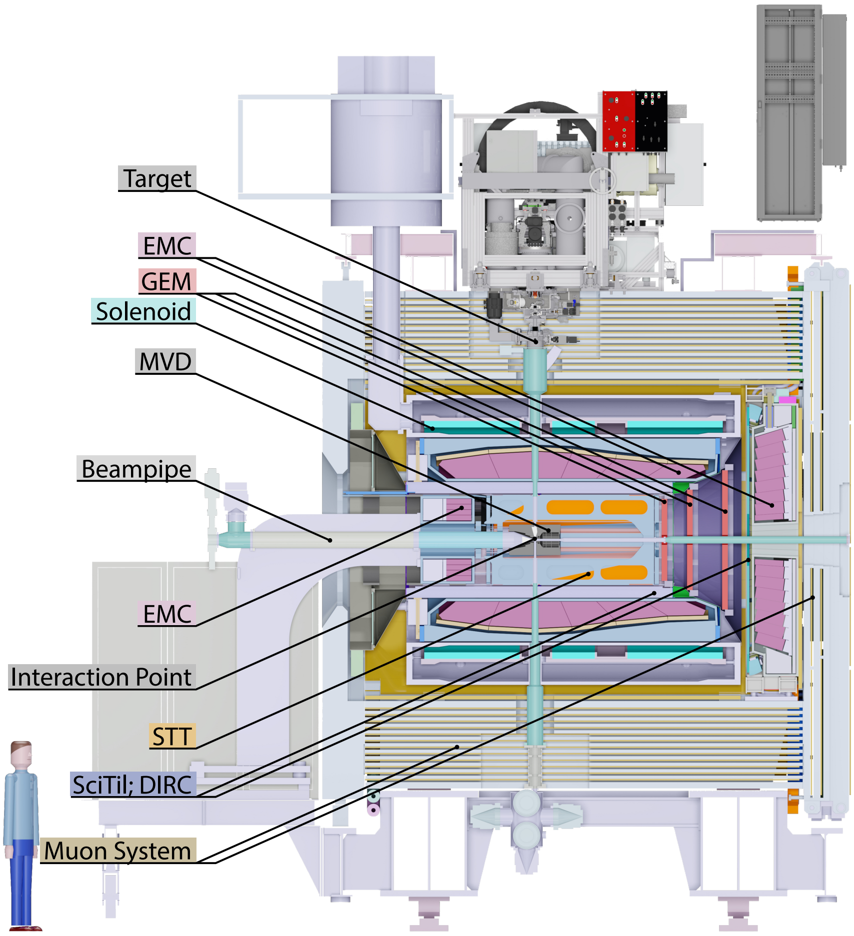

**Figure 3.10:** Artistic view of the $\bar{\text{P}}$ANDA Target Spectrometer (TS) with all sub-detectors. The antiproton beam approaches from the left. Figure taken from Ref. [49, 101]. The Forward Spectrometer (FS) follows to the right of this, which is illustrated in Fig. 3.11.

### 3.3.2 Tracking Detectors

Due to the fixed-target kinematics, a very good spatial resolution is particularly needed in the forward direction, and slightly lower precision for the backward hemisphere. The charged particle tracking system must handle the high particle fluxes that are anticipated for a luminosity of up to several $10^{32}\,\text{cm}^{-2}\text{s}^{-1}$. The central trackers, including the Micro Vertex Detector (MVD), Straw Tube Tracker (STT) and Gas Electron Multiplier (GEM) (as listed in Fig. 3.12), should have good detection efficiency for secondary vertices. The Forward Tracking System (FTS) will allow to track particles in the field of the dipole magnet with highest momenta as well as very low momentum where tracks will curl up inside the magnetic field. The tracking detectors are briefly introduced in the following.

**Micro Vertex Detector (MVD)** The central task of the MVD is a precise measurement of the location of both the primary interaction vertex and secondary decay vertices of short-lived particles. For this purpose the detection of a first track point very close to the nominal vertex is

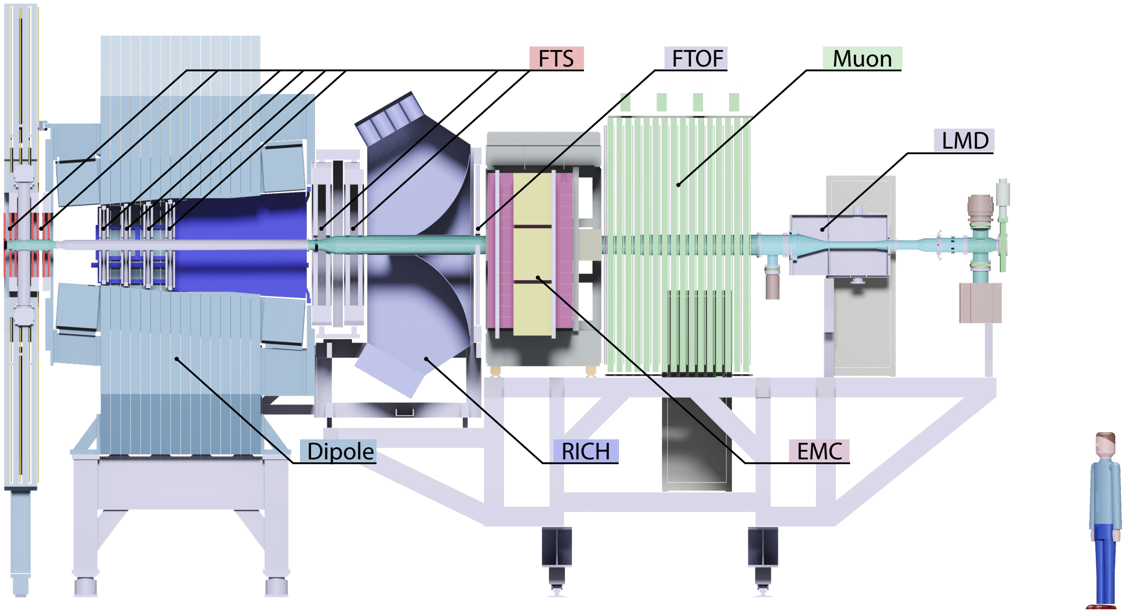

**Figure 3.11:** Side view of the $\overline{\text{P}}$ANDA Forward Spectrometer (FS) with its sub-detectors. The antiproton beam approaches from the left. Figure taken from Ref. [49, 101].

mandatory. Moreover, the obtained track information from the vertex detector also results in an improved transverse momentum resolution. The general detection concept of $\overline{\text{P}}$ANDA requests nearly full solid angle coverage. The boundary conditions of adjacent detector subsystems define a polar angular range of approximately 3° to 150° to be covered by the MVD.

The setup is depicted in Fig. 3.13. The concept of the MVD is based on radiation hard, silicon pixel detectors with fast individual pixel readout circuits and silicon strip detectors. The layout foresees a four layer barrel detector with an inner radius of 2.5 cm and an outer radius of 13 cm. The two innermost layers will consist of pixel detectors and the outer two layers will be equipped with double-sided silicon strip detectors. Six detector wheels arranged perpendicular to the beam will achieve the best acceptance for the forward emitted particles. While the inner four layers will be made entirely of pixel detectors, the following two will be a combination of strip detectors for the outer radii and pixel detectors closer to the beam pipe as shown in Fig. 3.13.

As shown in Fig. 3.14, due to the geometry of the different layers, the pixel sensor modules have a rectangular shape with four different lengths. For sufficient granularity, a pixel size of $100 \times 100\ \mu\text{m}^2$ is chosen. The hybrid pixel detector (top right in in Fig. 3.14) is a combination of sensor and readout Application-Specific Integrated Circuit (ASIC). The top right figure in

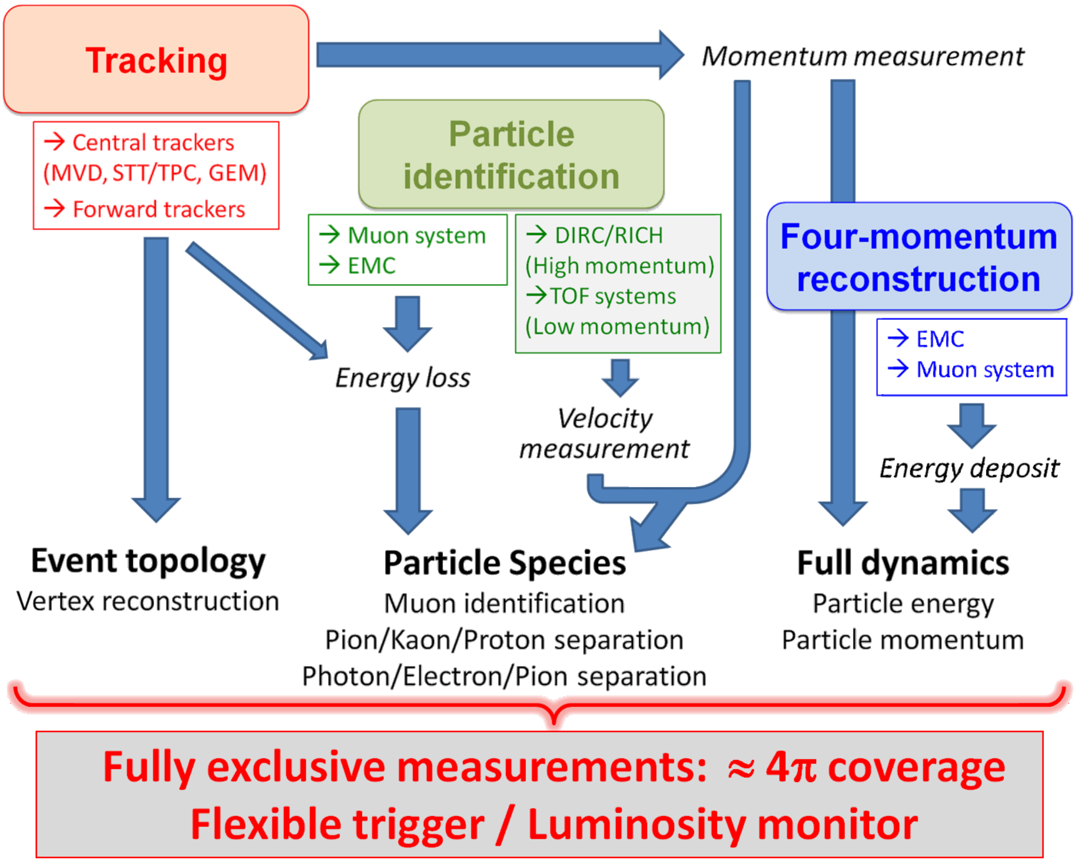

**Figure 3.12:** Basic detection concept of the $\overline{\text{P}}$ANDA detector. Figure taken from Ref. [123].

Fig. 3.14 shows a schematic profile of a hybrid pixel sensor with readout, support structure and cooling pipe. Concerning the sensor material, the silicon epitaxial layer grown on a Czochralski substrate is selected to satisfy the expected radiation hardness. The two main parts, i.e. sensor and readout electronics, are connected by solder-lead or indium bumps. Since the MVD is close to the $\bar{p}p$ interaction point, it has to take care of the data coming from a large flux of particles. A very high interaction rate up to $2 \times 10^7$ interactions/s will be processed at $\overline{\text{P}}$ANDA, and for the "hottest" MVD chip an average rate of $2.9 \times 10^6$ counts/s is assumed. Due to the requirements of the $\overline{\text{P}}$ANDA triggerless Data Acquisition (DAQ) concept, a powerful front-end readout ASIC is required to deal with the full data stream of the MVD. The Torino Pixel (ToPix), a readout ASIC connected to the pixel is being developed to measure a two-dimensional spatial position, a precise time stamp and information on the deposited energy. A study of the performance of a front-end prototype is part of this thesis, and the related details are presented in Chap. 5.

**Straw Tube Tracker (STT)** This detector will consist of aluminized Mylar tubes called straws. These will be stiffened by operating them at an overpressure of 1 bar, which makes them self-supporting. The straws are to be arranged in planar layers which are mounted in a hexagonal shape around the MVD as shown in Fig. 3.15 . In total there are 27 layers of which the 8 central

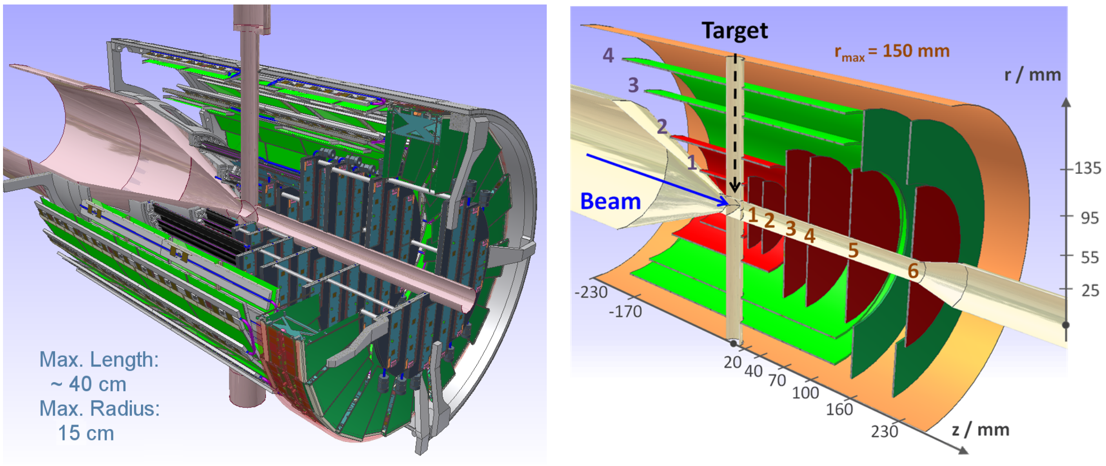

(a) (b)

**Figure 3.13:** The Micro-Vertex Detector (MVD) of the Target Spectrometer surrounding the beam and target pipes seen from downstream. (a) A look inside a three-quarters portraits of the detector. (b) Basic layout of the MVD. The red inner parts are equipped with silicon hybrid pixel sensors. Double-sided silicon micro-strip detectors employed in the outer layers are indicated in green. Figures cited from Ref. [124].

layers are skewed to achieve an acceptable resolution of 3 mm also in z (parallel to the beam). The gap to the surrounding detector systems will be filled with further individual straws. In total there will be 4636 straws around the beam pipe at radial distances between 15 cm and 41.8 cm with an overall length of 150 cm. All straws have a diameter of 10 mm and are made of a 27 µm thick Mylar foil. Each straw tube is constructed with a single anode wire in the center that is made of 20 µm thick gold plated tungsten. The gas mixture used will be argon (90%) and $CO_2$ (10%) as quencher. With these parameters, a resolution in the X and Y coordinates of better than 150 µm is expected. A thin and light space frame will hold the straws in place, the force of the wires however is maintained solely by the overpressure in the straws themselves. This overall design results in a material budget of 1.2% of one radiation length [123].

**Gas Electron Multiplier (GEM)** Particles emitted at polar angles below 22°, which are not covered fully by the STT will be tracked by three planar stations placed approximately 1.1 m, 1.4 m and 1.9 m downstream of the target. Each station consists of double planes with two projections per plane. The stations will be equipped with gaseous micro-pattern detectors based on GEM foils as amplification stages. The chambers have to sustain a high counting rate of particles peaked at the most forward angles due to the relativistic boost of the reaction products as well as due to the small angle $\bar{p}p$ elastic scattering. The maximum expected particle flux in the first chamber in the vicinity of the 5 cm radius opening for the beam pipe will be about $3 \times 10^4\,\text{cm}^{-2}\text{s}^{-1}$ [49].

**Forward Tracking System (FTS)** The tracking detectors mentioned above are the central trackers. In the forward region the deflection of particles trajectories will be measured with three pairs of tracking drift detectors (labeled in Fig. 3.11). Each pair will contain two autonomous

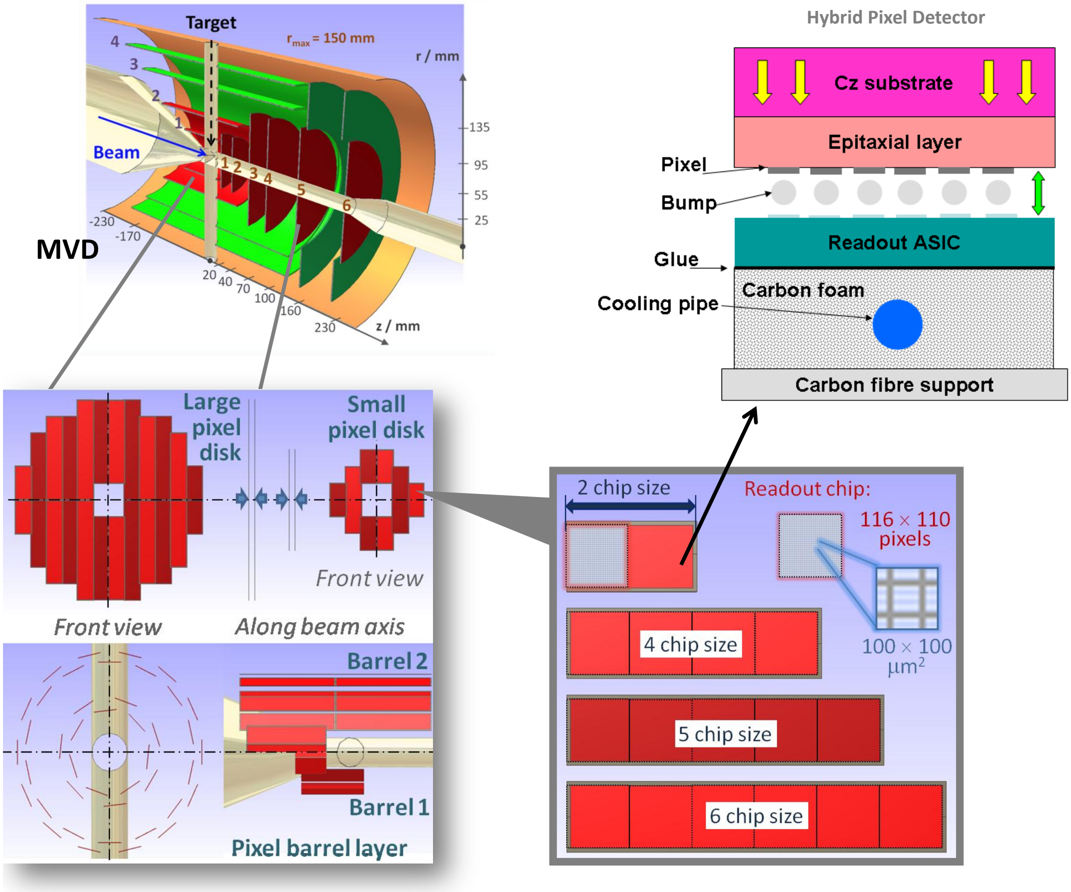

**Figure 3.14:** Schematic overview of the hybrid detector utilized in the MVD. Figures cited from Ref. [124].

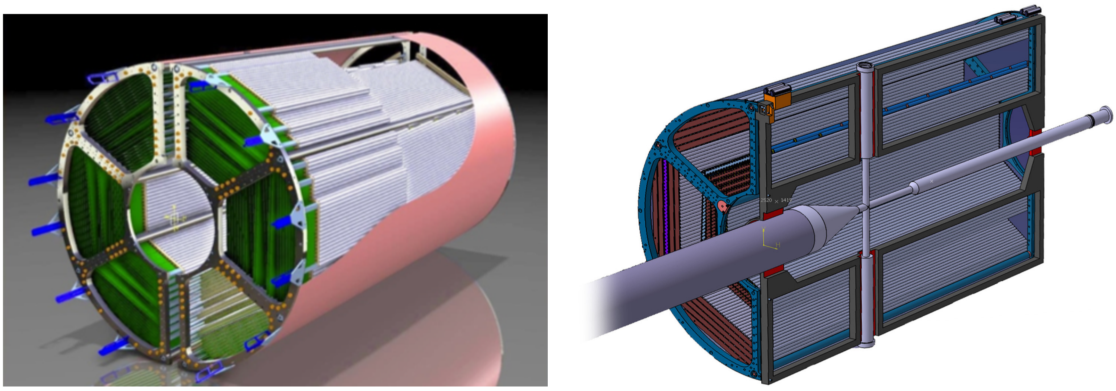

(a)

(b)

**Figure 3.15:** (a) Artistic view of the STT with the mechanical frame and supporting structure seen from upstream. (b) A semi-cylinder view of STT with the target-beam cross pipe. Figures taken from Ref. [101, 123].

detectors, thus in total 6 independent detectors will be mounted. Each tracking detector will consist of four double-layers of straw tubes [123]. The planned configuration of double-layers of straws will allow to reconstruct tracks in each pair of tracking detectors separately, which is especially important in case of multi-track events.

### 3.3.3 Particle Identification Detectors

Charged particle identification of hadrons and leptons over a large range of angles and momenta is an essential requirement to meet the physics objectives of P̄ANDA. There will be several dedicated systems that are complementary to the other detectors and will provide means to identify particles. The main part of the momentum spectrum above 1 GeV/$c$ will be covered by Cherenkov detectors. Below the Cherenkov threshold of kaons several other processes will be employed for particle identification: the tracking detectors are able to provide specific energy loss measurements, as illustrated in Fig. 3.12. In addition, the time-of-flight barrel and forward wall can identify slow particles.

**Detection of Internally Reflected Cherenkov Light (DIRC)** Charged particles in a dielectric medium with index of refraction $n$, propagating with velocity $\beta c > 1/n$, emit radiation at an angle $\theta_C = \arccos(1/n\beta)$. Therefore, the mass of the detected particles can be determined by combining the velocity information determined from $\theta_C$ with the momentum information from the tracking detectors [49]. In the barrel part, i.e. at polar angles between 22° and 140°, particle identification will be performed by Detection of Internally Reflected Cherenkov Light (DIRC). At P̄ANDA, it is intended to focus the images by lenses onto micro-channel plate photomultiplier tubes (MCP PMTs) which are insensitive to magnetic fields [49]. This fast light detector type allows a more compact design and the readout of two spatial coordinates [123]. In the forward direction for particles at polar angles between 5° and 22°, the same radiator, fused silica, is to be employed, however in the shape of a disk. It will be placed directly upstream of the forward end cap calorimeter.

**Ring-Imaging Cherenkov Detector (RICH)** In the Forward Spectrometer, for separating the π/K and K/p at very high momenta Ring-Imaging Cherenkov (RICH) detector is proposed. The favored design is a dual radiator RICH detector [49] using silica aerogel and $C_4F_{10}$ gas, which can separate π/K/p from 2 GeV/$c$ to 15 GeV/$c$.

**Time-Of-Flight System (TOF)** This system consists of a barrel part inside the Target Spectrometer, a forward wall far away from the target and a side part placed inside the dipole magnet opening. The barrel Time Of Flight (TOF) positioned outside the Barrel DIRC, will provide particle identification for slow particles at large polar angles in the solenoid magnetic field. The detector is based on scintillator tiles of $28.5 \times 28.5\ \text{mm}^2$ [124], individually read out by two Silicon Photo Multipliers per tile. The full system consists of 5760 tiles in the barrel part and can be augmented also by approximately 1000 tiles in the forward direction just in front of the end cap disc DIRC. The expected time resolution of 100 ps will allow precision timing of tracks for event building and fast software triggers. The detector also provides well timed input with a good spatial resolution for online pattern recognition.

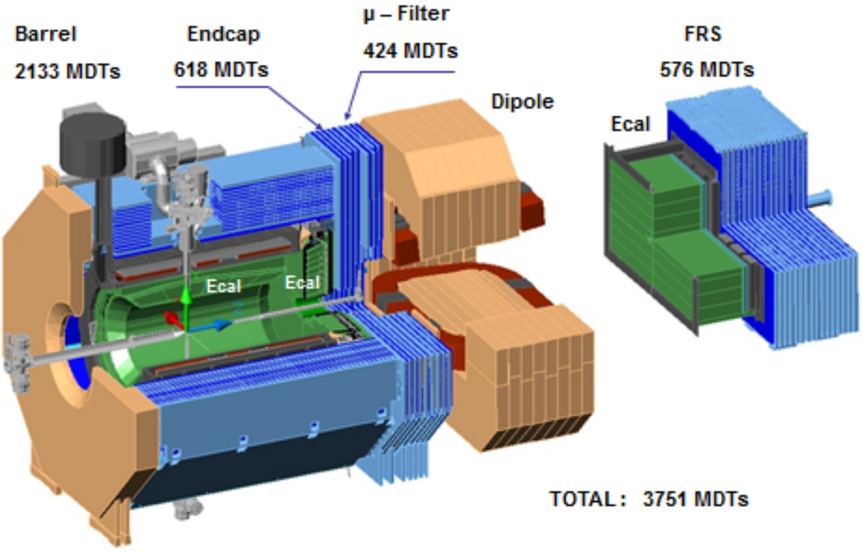

**Figure 3.16:** The layout of Muon System (blue) using the technique of Range System with the number of MDT detectors for each particular subsystem. Figure taken from Ref. [125].

In the Forward Spectrometer, a TOF wall is proposed for particle identification, in addition to the RICH. This wall of plastic scintillator slabs read out on both ends by fast photo-tubes will be placed at about 7 m from the target. Similar detectors placed inside the dipole magnet opening (labled as *Side TOF* in Fig. 3.11), are used to detect low momentum particles, which do not exit the dipole magnet. The time resolution is expected to be in the order of 50 ps, thus allowing for a good $\pi/\text{K}$ and K/p separation up to momenta of 2.8 GeV/$c$ and 4.7 GeV/$c$, respectively [49].

**Muon System** The main task of the Muon System is the muon identification via pattern recognition and matching of the track segments to the tracks inside the magnets. The precise muon momentum measurement is performed by the trackers of the magnetic spectrometers. The Mini Drift Tubes (MDT) are proposed as detectors for the Muon System, which is a type of Iarocci tubes (steamer tubes). The technology for detecting muons in $\bar{\text{P}}$ANDA is a Range System (RS) with granularity chosen to be close to the muon straggling in the iron absorber. Fig. 3.16 shows the layout of the Muon System with the number of MDT detectors for each particular subsystem. All together, the Muon System will be instrumented with 3751 MDTs.

In the Target Spectrometer, the Muon System consists of the barrel part, the forward end cap and the additional muon filter. In the barrel there are 13 sensitive layers, each 3 cm thick. They alternate with 3 cm thick iron absorber layers (first and last iron layers are 6 cm thick), introducing enough material for the absorption of pions. In the forward end cap more material is needed due to the higher momenta of the incident particles. Therefore, six detection layers will be placed around five iron layers of 6 cm each within the downstream door of the return yoke, and a removable muon filter with additional five layers of 6 cm iron and corresponding detection layers will be located in the space between the solenoid and the dipole.

The Fragment Separator (FRS) of the Forward Spectrometer is similar to the muon system of

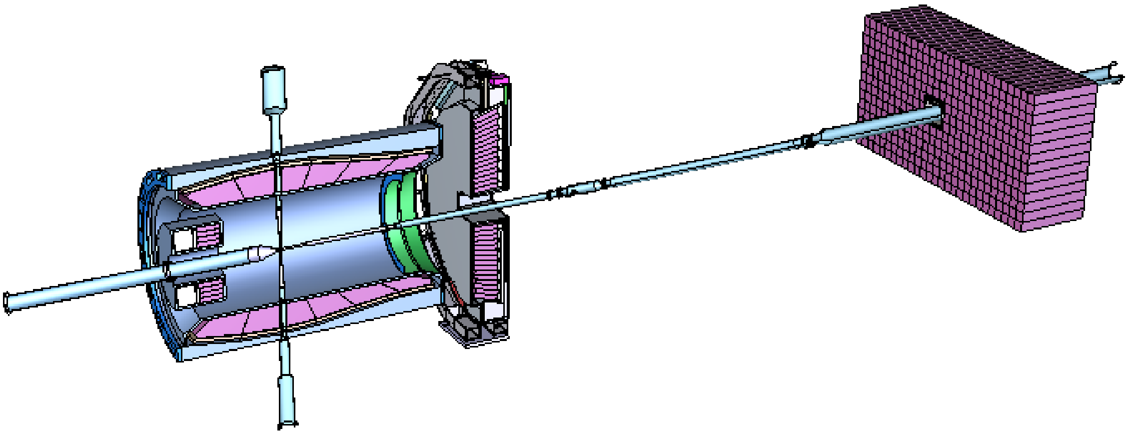

**Figure 3.17:** The electromagnetic calorimeter system of P̄ANDA. The EMC of the Target Spectrometer contains a backward endcap, barrel and forward endcap; a Shashlyk-like calorimeter (FSC) placed in the Forward Spectrometer. The target-beam cross pipe is included for a reference of position. Figure taken from Ref. [22].

the Target Spectrometer, but designed for higher momenta. The position of the FRS will be 9 m downstream from the target.

### 3.3.4 Electromagnetic Calorimeters

The basic function of an electromagnetic calorimeter is the efficient reconstruction of electrons, positrons and photons with high efficiency and low background. P̄ANDA will not have a threshold Cherenkov detector to discriminate pions from electrons and positrons. The complementary information of $E/p$ is required from calorimeters for identifying particles. Good identification and reconstruction of multi-photon and lepton-pair channels are essential for the success of the P̄ANDA experiment. In the Target Spectrometer a high precision Electromagnetic Calorimeter (EMC) will be built, and in the Forward Spectrometer a Shashlyk-type calorimeter (FSC) will be employed. Fig. 3.17 shows the layout of the calorimeters with the target and beam pipe.

The Target Spectrometer EMC contains three parts: backward endcap, barrel part and forward endcap. The barrel part and the forward end cap are depicted in Fig. 3.18. The scintillator material is lead tungstate ($PbWO_4$), which is a high density inorganic scintillator with sufficient energy and time resolution for photon, electron and hadron detection even at intermediate energies [127, 128]. The crystals are designed to be 20 cm long, thereby having a tolerable energy loss due to longitudinal leakage of the shower in order to achieve a relative energy resolution better than 2% at 1 GeV. Fig. 3.19 shows the crystal arrangement of the barrel. The crystals are grouped into packs of $4 \times 10$ leading to 16 sectors of 22.5° coverage in azimuthal angle each. With an inner radius of 57 cm the barrel part of the calorimeter requires 11,360 crystals, with a front face of $2.1 \times 2.1$ cm$^2$ each. The length of each crystal is 22 times the radiative length of $PbWO_4$, $X_0 = 7.39\,\mathrm{g/cm^2}$. The presented geometry foresees that the crystals do not point towards the target position. The focal axis of the slice is tilted by 4° to reduce the dead zone effect. This means, that tracks originating at the target never pass through gaps between crystals, but always cross a significant part of a crystal.

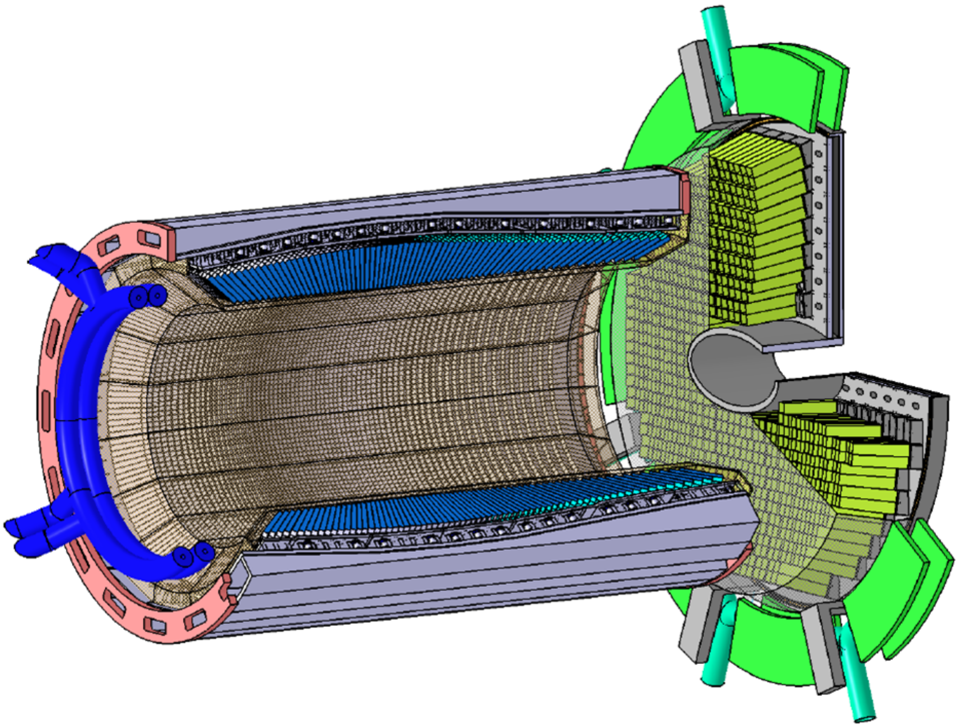

**Figure 3.18:** The barrel and forward endcap EMC with support and cooling structures. Figure taken from Ref. [126].

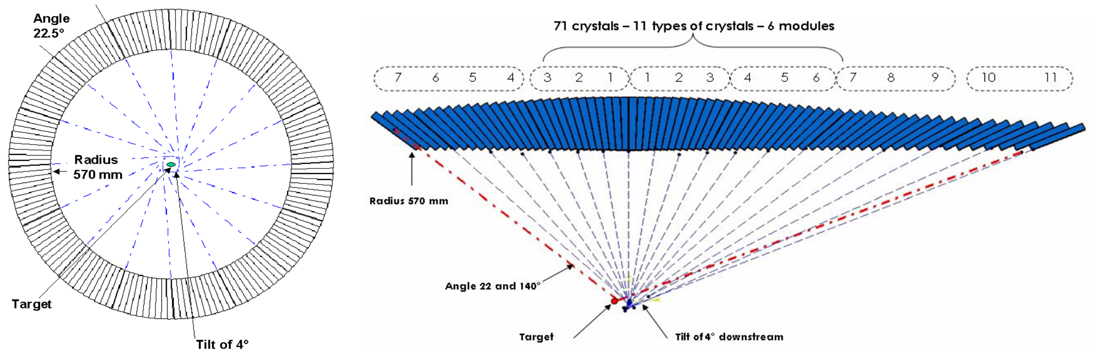

(a) (b)

**Figure 3.19:** Geometrical arrangement of the crystals of the barrel EMC. (a) The segmentation of the calorimeter along the circumference of the barrel part. The 160 crystals are grouped into 16 subunits named slices. (b) Geometrical arrangement of the crystals of the barrel in a cut along the beam axis. The definition of subgroups by pack of 4 and by module is indicated. Figures taken from Ref. [126].

The backward and forward endcaps require 592 and 3600 crystals, respectively. A total of 15,552 $PbWO_4$ crystals will be required. A fast signal will be derived for the first level trigger. The readout of the crystals will be done by large area avalanche photodiodes. The energy threshold is expected to be $E_{thres} < 20\,\mathrm{MeV}$ in order to achieve the physics goals of P̄ANDA. The highest energies are in the forward direction, while backward particles are relatively low in energy. The designed energy range for the backward endcap is from the $E_{thres}$ to 0.7 GeV, for the barrel EMC is up to 7.3 GeV, and for the forward endcap the maximum is 14.6 GeV.

The Forward Shashlyk-type Carlorimeter (FSC) is designed to cover the forward acceptance with high resolution and efficiency. It will contain 26 rows and 54 columns with a cell size of 55 mm×55 mm. The detection is based on lead-scintillator sandwiches read out with wavelength shifting fibers passing through the block and coupled to photomultipliers [126]. The position of the FSC will be 7 m to 8 m downstream of the target, as shown in Fig. 3.17.

### 3.3.5 Other Components

**Solenoid and Dipole Spectrometer Magnets** In the Target Spectrometer region, a superconducting solenoid will deliver a homogeneous solenoid field of 2 T with fluctuations of less than ±2% [129]. The yoke is 4.9 m long and its outer radius is 2.3 m. As the target requires vertical feed pipes the superconducting coil of the solenoid will be split at this point and the cryostat will exhibit two warm bores of 100 mm diameter, one above and one below the target position (see Fig. 3.10). All barrel detectors, except the muon chambers, will be hosted inside the warm bore of the solenoid cryostat with a diameter of 1.9 m. The flux return yoke will operate as a range system for the muon detection.

A large-aperture dipole magnet with bending power of 2 t·m will be used for the reconstruction of charged particle tracks in the Forward Spectrometer. The momentum resolution is designed to be better than ≤ 1%. In the current planning, the magnet yoke will be 2.5 m long in beam

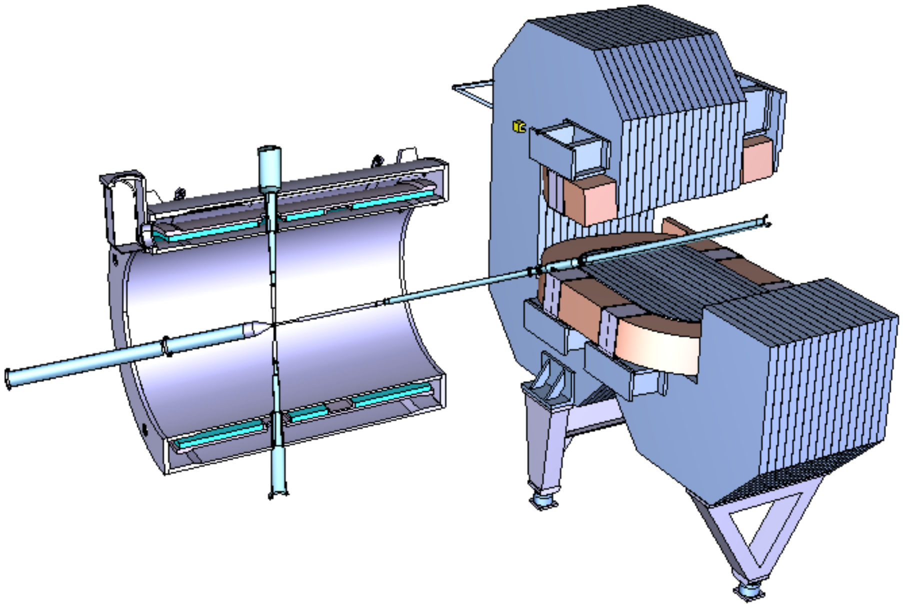

**Figure 3.20:** The solenoid and dipole spectrometer magnet of P̄ANDA shown with the target-beam cross pipe. Figure adapted from Ref. [22].

direction starting at 3.9 m downstream of the target, and the overall hight and width are 3.9 m and 5.3 m, respectively [124]. It will cover the entire angular acceptance of the Forward Spectrometer of $\pm 10^{\circ}$ and $\pm 5^{\circ}$ in the horizontal and in the vertical direction, respectively. This opening aperture is about $1 \times 3$ m. The dipole magnet will be part of the HESR lattice and ramped during the acceleration cycle of about 60 s [124].

**Luminosity Detector** In order to determine the cross section for physical processes, it is essential to determine the time integrated luminosity $L$ at the $\bar{\text{P}}$ANDA interaction region that was available while collecting a given data sample. The absolute cross section can be determined from the measured count rate of a specific process with known cross section. The luminosity at $\bar{\text{P}}$ANDA will be determined by using elastic antiproton-proton scattering as a reference channel [123]. At very small momentum transfer, corresponding to small polar angles, the elastic cross section is dominated by the Coulomb component, which is exactly calculable. Taking the beam divergence into account, the angular distribution of scattered antiprotons will be measured in the range of $3 \sim 8$ mrad, corresponding to the Coulomb-nuclear interference region. The angle of each scattered antiproton will be measured by four layers of double-sided High Voltage Monolythic Active Pixel Sensors (HVMAPS) modules placed about 11 m downstream from the interaction point, behind the Forward Spectrometer (see in Fig. 3.11). The planes are positioned as close to the beam axis as possible and separated by 10 cm to 20 cm along the beam direction. The current design foresees that every plane consists of 8 sensors in trapezoidal shape, covering the whole azimuthal angle, in order to suppress systematic effects from e.g. the forward dipole magnet and potential misalignment of the beam. The silicon sensors will be located inside the vacuum to minimize scattering of the antiprotons before traversing the tracking planes. The design goal of the proposed detector setup is to reach an absolute precision of 3% for the time integrated luminosity.

This design concept requires a knowledge about the physics parameters describing the dependence of the antiproton-proton elastic cross section on the squared four-momentum transfer in the Coulomb-nuclear interference region. An independent experiment, Key experiment fOr PANDA Luminosity determinAtion (KOALA), has been proposed to study the antiproton-proton elastic scattering in-depth and alleviate the lack of existing data in the momentum region of $\bar{\text{P}}$ANDA [130].

### 3.3.6 Data Acquisition

In the $\bar{\text{P}}$ANDA experiment, due to the $\bar{p}p$ high interaction rate of up to $2 \times 10^7$events/s and the very wide physics objectives with different event selection criteria, a new DAQ concept is being developed. Instead of a traditional hardware-level trigger, $\bar{\text{P}}$ANDA will employ a software trigger system, which allows to collect the incoming data stream continuously in real time and store the complete data set of selected events of interest. The initial 200 GB/s raw data from the front-ends will be reduced to 100-200 MB/s after the event selection for long-term storage.

Fig. 3.21 illustrates the DAQ scheme of $\bar{\text{P}}$ANDA. In this approach, every sub-detector system is a self-triggering entity. Hit signals are detected autonomously by the frontend electronic devices of sub-systems and are converted to digital data. In addition, a time-stamp will be assigned for each hit. Time information for every hit is defined by a global clock based on

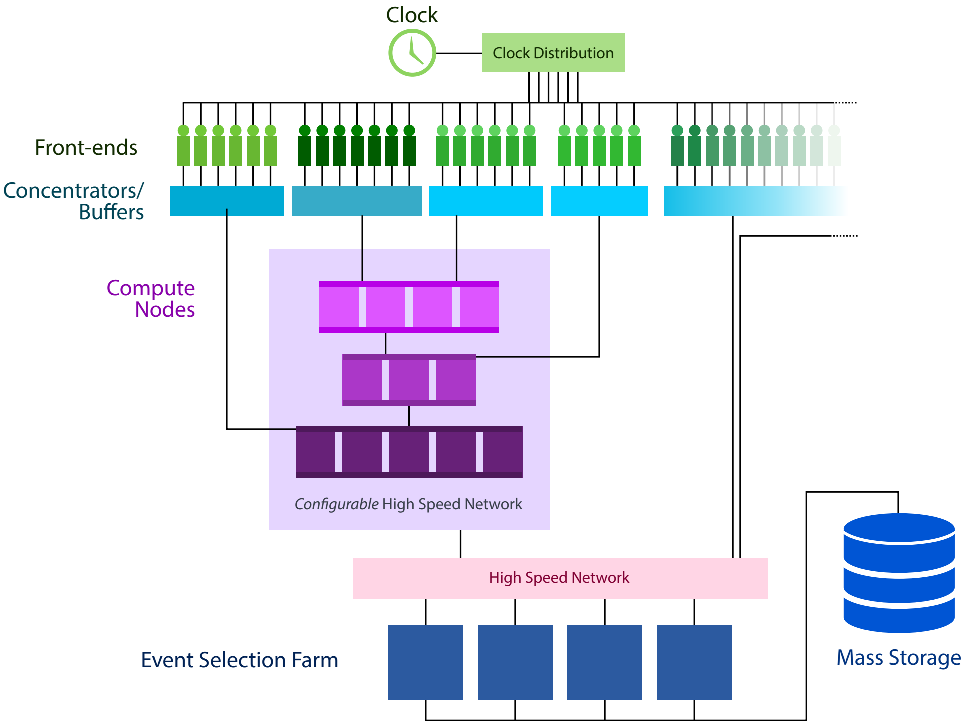

**Figure 3.21:** Schematic overview of the $\bar{\text{P}}$ANDA data acquisition scheme described in Ref. [49]. Figure cited from Ref. [101].

the Synchronization Of Data Acquisition (SODA) architecture. The time precision is better than 20 ps [131]. The data from the frontends of the same sub-detector are fed into data concentrators, where the continuous data streams are chopped into the data blocks of 500 µs. Data concentrators transmit data blocks to compute nodes, where the data from different detectors are assembled. Compute nodes offer a large computing power for online processing track reconstruction and preliminary Particle Identification (PID). Fast algorithms will be employed in this step to build event candidates. A high-speed network for event selection will select event candidates with a software trigger, where the results of online tracking and online PID are essential information and variables for discrimination. The complete raw data flow of selected events will be stored on the mass storage system. The required storage space will be a few PB per year. Then the process of DAQ is done and the stored data has been prepared for further offline analysis with higher-precision algorithms.

To facilitate the association of data fragments to events, the beam structure of the accelerator is exploited: every 1.8 µs there is a gap of about 400 ns needed to compensate the mean energy loss of the beam in the target with a bucket barrier cavity [49]. This time gap provides a clean division between consecutive data blocks, which can be processed independently. An important requirement for this scheme is that all detectors perform a continuous online calibration with data. The normal data taking is interleaved with special calibration runs. For the monitoring of the quality of data, calibration constants and event selection a small fraction of unfiltered raw data is transmitted to mass storage.

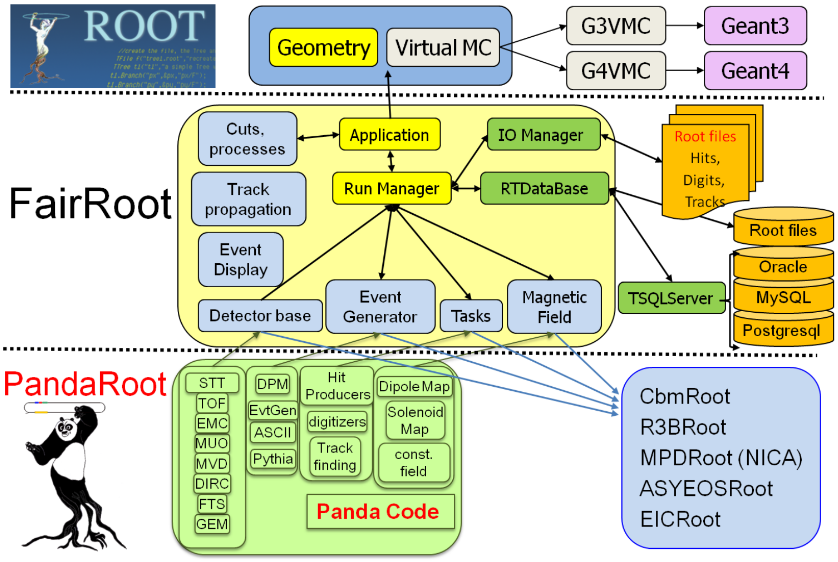

**Figure 3.22:** Code design of the P̄ANDA analysis software framework. Figure cited from Ref. [132].

This new concept provides a high degree of flexibility in the choice of trigger input parameters. It makes trigger conditions available, which are outside the capabilities of the standard approach. In this scheme, sub-detectors can contribute to the trigger decision on the same footing without restrictions due to hard-wired connectivity. Different physics can be accessed either in parallel or via software reconfiguration of the trigger system. High speed serial (10 Gb/s per link and beyond) and high-density Field-Programmable Gate Array (FPGA) with large numbers of programmable gates as well as more advanced embedded features are key technologies to be exploited within the DAQ framework [49].

## 3.4 P̄ANDA Analysis Software Framework

During the preparation of the P̄ANDA experiment, a software framework of data processing is under development for studying the performance of detectors and the feasibility of physics topics. It contains three major components of code: external packages, FairRoot and PandaRoot, as shown in Fig. 3.22. This section presents an overview of the framework and the analysis tools employed in this thesis.

### 3.4.1 External Packages and FairRoot

The external packages compose the collection of the third-party software, which is specified as part of FairSoft for the experiments carried on FAIR. The ROOT package [133, 134] is written in C++ and developed at CERN. It was firstly introduced in 1997 and now commonly used in the high energy physics community. ROOT provides a large set of functionalities and many applications are implemented for P̄ANDA, for example CINT (a macro interpreter with an interactive shell), PROOF (parallel processing) and so on. Geometry and Virtual Monte Carlo (VMC) are employed for defining the geometry information and accessing various Monte Carlo (MC) software packages. GEANT3 and GEANT4 are particle transport codes, which simulate the passage of particles through the matter of the complete P̄ANDA detector. The GEANT4 [135, 136] package was re-developed in C++ from the Fortran version GEANT3 physics models. By using the VMC concept it is possible to perform the simulations using either GEANT3 or GEANT4, without changing the user code or the geometry description.

FairRoot [137] is a common framework for many experiments at FAIR and beyond. As listed in Fig. 3.22, it provides run-task managing classes, which drive the execution of a simulation or reconstruction session, and handles the Input/Output (IO) files, as well as the parameter IO used in building the geometry for a simulation from different sorts of input files. On the other hand the framework delivers base classes for detector handling, magnetic field definition, event generators for simulation sessions as well as tasks, which are used for the analysis sessions. Additionally, it provides buffers and tasks which are needed for the time-based simulation.

### 3.4.2 PandaRoot

The P̄ANDA offline analysis and simulation framework is *PandaRoot*, which is an extension of the FairRoot framework. It is written in C/C++. The components of P̄ANDA are defined in the framework, including all sub-detector geometries, HESR beam pipe and target, as well as magnetic fields. Moreover, the tools for event reconstruction are implemented. To validate specific algorithms is one task of this thesis, as well as for possible improvement.

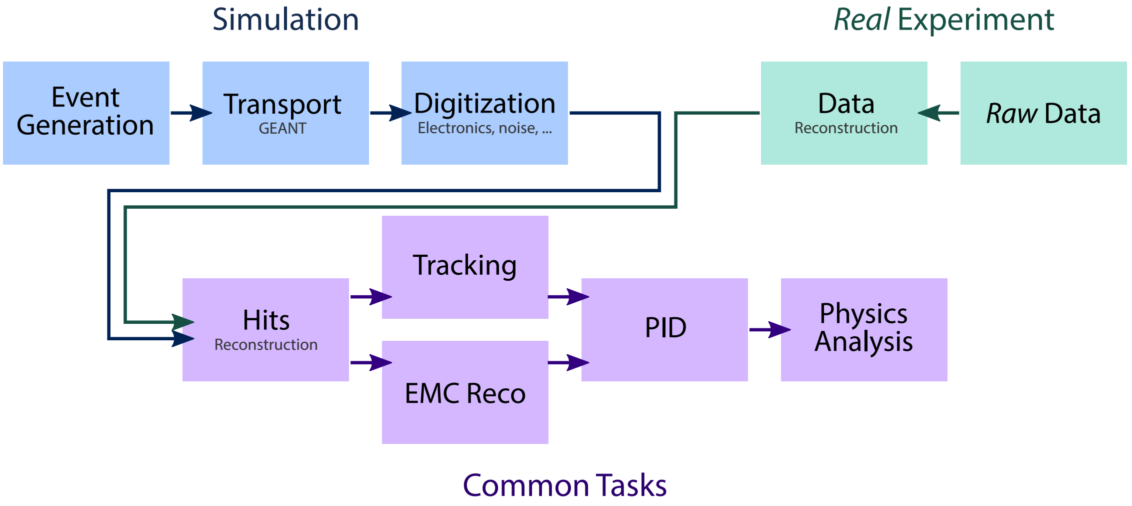

**Figure 3.23:** Workflow of data analysis in PandaRoot. The framework includes the analysis of simulation data and experiment data. Figure cited from Ref. [101, 138].

Fig. 3.23 illustrates the workflow within the framework of PandaRoot both for simulated data and actual measurements. The first two steps of data processing in the real experiment are handled by the online software trigger system (see Sec. 3.3.6). The following will focus on the workflow regarding simulation analysis in the framework.

#### 3.4.2.1 Event Generation

In the first step in the workflow of the simulations, events are produced by one of several different event generators according to the physics case, such as EvtGen, DPM, Pythia, UrQMD or also by generators developed within the collaboration for specifics physics scenario (i.e. for electromagnetic form factors, Drell-Yan, HyperNuclei, etc.) [132]. In this thesis, three generators are employed: EvtGen, DPM and Box Generator.

**EvtGen** The EvtGen project has been developed to study B physics [139]. Since it covers a wide range of high energy physics, it is employed in many particle physics experiments, like BaBar. EvtGen is used for producing signal events of the channels indicated by an input decay file. Each decay channel can be reproduced by a decay model. More than 150 decay models are defined for well known particle decays. It allows to generate the resonances of interest (called *signal*), taking into account the known decay properties, including angular distributions, polarization, etc., and allows user defined decay models. A stable release is available to all the particle physics experiments. The version used in this thesis is R01-03-00. The latest release (R01-05-00) was issued in Oct. 2015 [140]. The functionality related to this thesis has no changes in the updated version. A validation study of the related decay models has been done and is presented in Sec. 4.1.2.

**DPM** For the simulation of the generic annihilation background, the Dual Parton Model (DPM) [141] based generator is used for $\bar{p}p$ interactions. It is based on a synthesis of the Regge theory, topological expansions of QCD $1/N_f$ or $1/N_c$, and ideas from the parton model [49]. The energy dependence of cross sections is given by the Regge theory. Inelastic and elastic $\bar{p}p$ scattering processes are implemented. For P̄ANDA, DPM generates the "signal + background" exclusive events, which allows the study of background channels with comparing the net signal events obtained from EvtGen.

**Box Generator** In PandaRoot, the Box Generator is used as a *particle gun*, which allows to generate specified number and species of particles with a seleted momentum and angle range. This generator is used to investigate the performance of detectors and algorithms, for example, a single charged pion was used to study the EMC cluster correlation algorithm (Sec. 3.4.2.6).

#### 3.4.2.2 Particle Transport and Digitization

The propagation of generated particles through the P̄ANDA detector is taken care of by the GEANT [135, 136] transport code with a geometry description of the detector. As introduced previously in Sec. 3.4.1, GEANT3 and GEANT4 are available for PandaRoot. These versions of code take into account the full variety of interactions and decays that the different kinds of particles may undergo. The output of this step is a collection of MC Hits, which contain mainly the intersection point, energy loss and particle type of all decay products in the individual sub-detector.

Based on this output the digitization step follows, which models the electronic signals and corresponding digitized response of the front-end-electronics. The MC Hit is processed to Digi. This step makes the simulation data set as similar as possible to the real experimental data. Since this step starts before systematic PID, the particle species is assumed. Therefore, the following reconstruction algorithms developed with simulation data can be subsequently used for the beam data in the future.

#### 3.4.2.3 Track Reconstruction

The hits collected from each tracking sub-detector with global information on position and the associated time, are processed in this step to find the group of nearby hits possibly belonging to one trajectory. Each hit knows about the residual of the hit to a given reference trajectory and the precision of the measurement.

*Track finding* and *tracking fitting* is the task of the track reconstruction. For track finding, different algorithms of pattern recognition are implemented for the tracking detectors, e.g. Conformal Mapping and Hough Transformation. There the track finder searches for hits created by a common particle and associates the hits on sub-detectors to a trajectory in a given magnetic field. The global tracking, MVD + STT + GEM, is based on the Kalman Filter technique in PandaRoot, where the GENFIT package [142] and GEANE [143] are used. GENFIT is an experiment-independent track-fitting toolkit that combines fitting algorithms, track representations, and measurement geometries into a modular framework. The recent updated version is known as GENFIT2 with significant improvements in Kalman fitters, tracking algorithms and several additional aspects [144]. Both versions are available in PandaRoot. GEANE [143] is used as a track follower to propagate track parameters and error covariance matrices from one detector plane to another.

Besides the normal tracking process, an idealised pattern recognition is implemented for building tracks based on MC information to assign reconstructed hits to their original tracks. It adds hits from MVD + STT + GEM + FTS using the MC information, and give a gaussian smeared seed to the Kalman Filter. Since the pattern recognition in the Forward Spectrometer is currently under developing, the idealised algorithm is employed temporarily.

#### 3.4.2.4 Energy Reconstruction

As introduced in Sec. 3.3.4, 20 cm long $PbWO_4$ crystals with a front face of $2.1 \times 2.1$ cm$^2$ will be used to measure the deposited energy of particles. On the scintillator modules of the EMC and FSC (see Sec. 3.3.4) a photon or charged particle entering one element deposits energy in several nearby elements. Therefore, the task of energy reconstruction is clustering of the elements and separating showers caused by different incident particles.

The first step is *cluster reconstruction*, in which a contiguous area of crystals with deposited energy is found, as illustrated in Fig. 3.24(a). For each crystal, there is an energy threshold $E_{xtl}$. The deposited energy of individual crystals belonging to one cluster are added up as the total energy deposited of one cluster. The energy threshold for a cluster is $E_{cl}$. A cluster can be formed by more than one particle if the angular distance between the particles is small. Dividing the clusters caused by more than one particle is processed in the second step, *bump splitting*. A bump is defined by a local maximum inside the cluster, shown by Fig. 3.24(b). This local maximum has to be above a threshold $E_{max}$ otherwise the bump will not be accepted, but nevertheless it remains a cluster. The spatial position of a bump is calculated via a center-of-gravity method. The energy resolution of the EMC can achieve $0.3\% + 1.54\%/\sqrt{E/\text{GeV}}$ [145], and for the FSC it will be around $(2-3)\%/\sqrt{E/\text{GeV}}$ [146].

The energy thresholds, $E_{xtl}$, $E_{cl}$ and $E_{max}$, on one hand have to be as low as possible for detecting low energy particles and achieving a good energy resolution, on the other hand need to

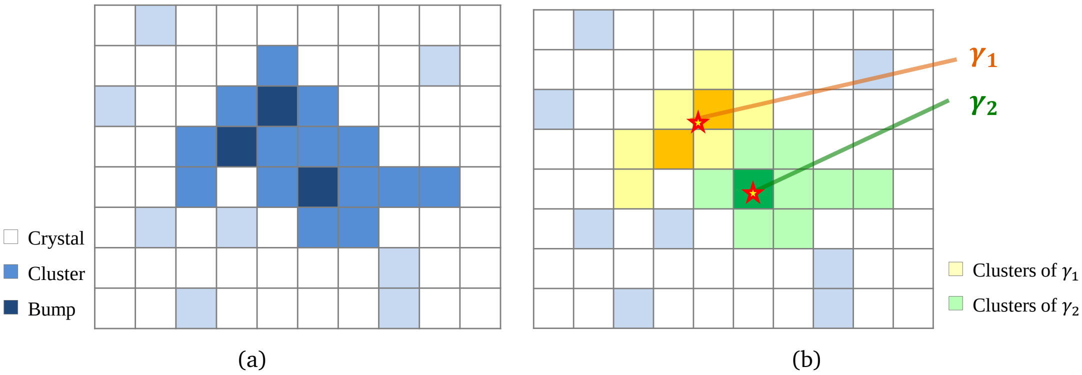

(a) (b)

**Figure 3.24:** Illustration of energy reconstruction with the EMC. The grid is a map of EMC crystals. (a) Cluster reconstruction. (b) Bump splitting.

be sufficiently high to suppress noise from readout, and statistical fluctuations of electromagnetic showers. Table 3.1 lists the planed energy thresholds for the EMC and FSC.

**Table 3.1:** Energy thresholds for the EMC in the Target Spectrometer [126] and the FSC in the Forward Spectrometer [146].

| | EMC/FSC |
|---|---|
| $E_{xtl}$ | 3 MeV |
| $E_{cl}$ | 10 MeV |
| $E_{max}$ | 20 MeV |

#### 3.4.2.5 Charged Particle Identification

Investigating the P̄ANDA physics topics require a good particle identification for charged hadrons and leptons over a large momentum range from 200 MeV/$c$ up to approximately 10 GeV/$c$. The PID detectors (in Sec. 3.3.3) provide useful PID information for specific particle species and momenta. The energy loss of specific particles in thin layers of material directly provides an access to the d$E$/d$x$. MVD and STT contribute to PID by measuring d$E$/d$x$. For particles with momenta above the Cherenkov threshold, the DIRC provides information on the Cherenkov angle to identify particles. RICH and TOF can provide the information for separating π/K/p in the high momentum region. Moreover, the footprints of deposited energy in the calorimeter differ distinctly for electrons, muons and hadrons. Besides the shower shape, the ratio of the deposited energy in the EMC to the reconstructed track momentum ($E/p$) is also used for PID. The Muon system provides a good muon identification for momenta above approximately 1 GeV/$c$, where electrons can be completely suppressed, and a contamination rate of only a few percent can be achieved for hadrons.

Each sub-detector has its own algorithm to calculate the probability density functions for all five charged particle hypotheses (e, $\mu$, π, K and p). The best PID performance can be obtained

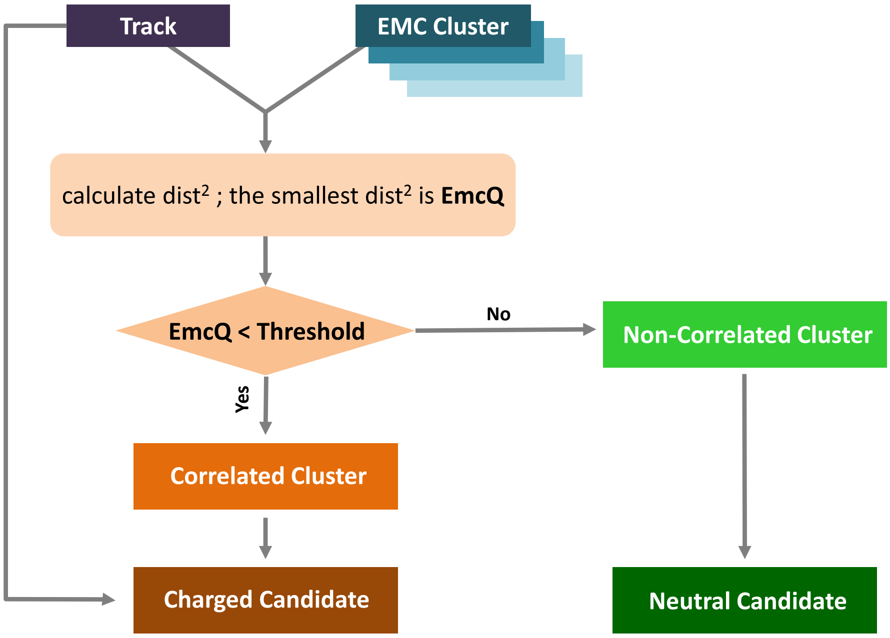

**Figure 3.25:** Sketch of the algorithms for the charged particle EMC correlation and the exclusion method of the neutral reconstruction.

by taking into consideration all available information from all sub-detectors. A gobal PID combines this information by applying a standard likelihood method, and a global probability is calculated. Due to the variety of requirements imposed by the different characteristics of the decay channels, the charged particle candidate lists depending on different selection criteria on the global probability are provided for the data analysis.

Besides the above conventional PID algorithms, there is an Ideal PID provided to study the best achievable performance of a detector. The idealised PID selector checks the particle type with MC truth, but not its charge. The charge identification follows the procedure of the non-ideal PID algorithm. For calculating the energy component, an ideal mass hypothesis is provided to use the mass of a MC true type particle replacing the default hypothesis of a charged pion.

#### 3.4.2.6 Neutral Particle Reconstruction

In contrast to the charged particles, neutral particles have no track information for PID, and they are only measured by the EMC with deposited energy and where the energy is deposited. However, both charged and neutral particles can interact with crystals of the EMC. The essential task for neutral particle reconstruction is distinguishing which clusters are caused by charged tracks and which ones are from neutral particles. Since parts of the PID for neutral particles has been developed in this thesis, a detailed description is presented in the following.

The common method for identifying photons is by associating charged tracks with reasonable EMC clusters, and then the remaining clusters, which are not correlated to charged tracks are considered to be photon candidates (see Fig. 3.25). There is a gap between the outer layer of tracking detectors and the EMC, thus the charged track needs to be extrapolated by GEANE [143] to the EMC surface. The algorithm loops through the track list, and finds the extrapolation point for each track. With the position information of the extrapolation point and the geometric center of the cluster, the distance squared from the extrapolated track to each cluster is calculated. Afterwards, for each track the smallest distance squared is stored as the *EMC quality*. If the EMC quality is below a given threshold, the EMC cluster related to the EMC quality is assigned as a charged cluster. Note that the cut parameter influences the PID efficiency, therefore it needs to be carefully selected.

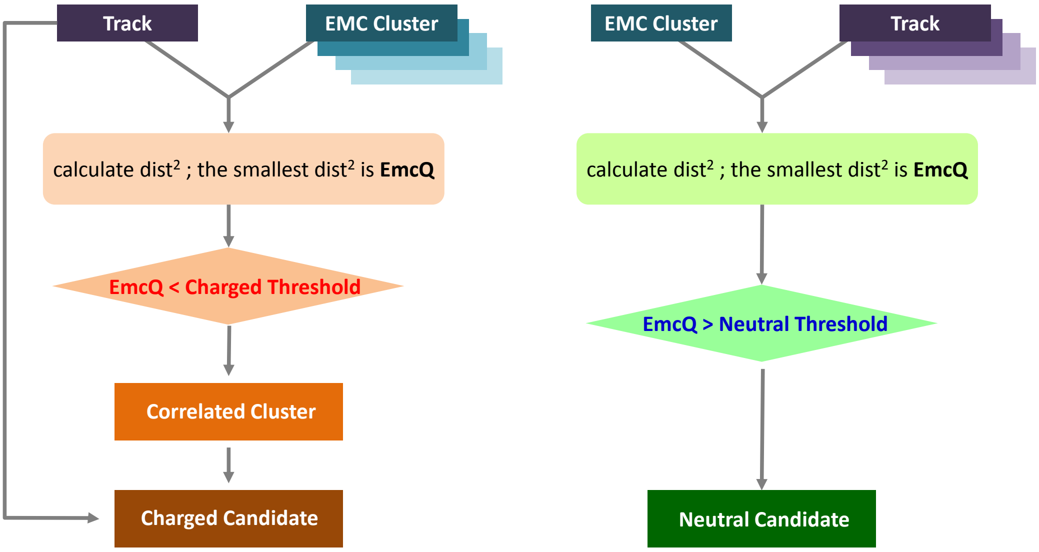

(a) Charged cluster correlation.

(b) Neutral candidate reconstruction.

**Figure 3.26:** Sketch of the independent algorithms for the charged and the neutral particle EMC correlation.

In order to find a reasonable parameter for the charged correlation and a possible way for cross checking, a new algorithm is implemented in PandaRoot for neutral PID. As shown in Fig. 3.26, in addition to the common charged correlation, this algorithm separates the neutral particle reconstruction as an independent procedure, where another parameter is employed for selecting neutral clusters. For each EMC cluster the distance squared to each extrapolated track point is calculated, and the smallest is taken as the EMC quality for this cluster. If the cluster's EMC quality is higher than a threshold, which means that no track point is nearby within a certain range, the cluster is reconstructed as a neutral candidate. The PID algorithm deals with the charged correlation first and the neutral correlation is the second but individual step. Two threshold parameters are employed in PandaRoot: for charged correlations `PndEMC12Cut` and for neutral correlations `PndEMCNeutralCut`.

Validating the correlation parameters is important for analysing decay channels containing one or more photons. Moreover, for different physics cases these parameters require different validation due to the influences of the charged tracks momentum and complexity of tracks. Sec. 4.2 shows how these parameters were selected within the simulated decay chain of this thesis.

#### 3.4.2.7 Physics Analysis Tools

After the PID procedure, charged and neutral particles have been prepared for analysis in order to reconstruct the events of interest. The standard operations include reconstructing composite particles, selecting reconstructed candidates and applying kinematic fitting, which are necessary to optimize the quality of the reconstructed objects and reject background. The main tools in PandaRoot are briefly introduced in the following.

**Rho Package** In the P̄ANDA analysis framework, Rho [147] has been implemented for managing candidates and candidate lists. It takes care of combining daughter particles to reconstruct the decay tree without double counting by indexing candidates. The properties of a candidate and the member of a candidate list are accessible by the functions provided by Rho, which significantly simplifies the programming work for analysis users. Moreover, storing event-wise reconstructed candidates with a bunch of useful information can be quickly done by using tuples and quality functions defined in Rho.

**Vertex Fit** The essential task for data analysis is to find a signal in a vast amount of background. Depending on the particular analysis under consideration, there are different kinds of constraints which are the most powerful. A very common situation is that the reconstructed particles originate from a common point in space-time. The spatial component is called the *vertex*, and it is possible during the reconstruction of the decay tree to take advantage of this by performing a *Vertex Fit*, which constrains the trajectories of charged particles to come from a common vertex. When applying a vertex fit on a composite candidate, the fitter modifies the track parameters within the errors in such a way, that the tracks come as close as possible to the hypothetical vertex. The returned information includes the modified track parameters, the $\chi^2$ value and its corresponding probability, which shows how well the tracks meet the hypothesis. It allows to remove those candidates with low probability or large $\chi^2$.

**Mass Constraint Fit** Requiring the tracks to come from a common point is not sufficient when two tracks are very close in space, but decay from different mother particles. A mass constraint fitter checks the kinematics of composite candidates to reject background combinations. It constrains the invariant mass of the fitted 4-vector to a certain fixed value, e.g. the PDG mass. Due to this strict constraint, it is suitable for resonances or particles with a width that is negligible compared to the detector's mass resolution. As for the vertex fitter the probability and $\chi^2$ are used to select events. In most cases, the fitted mass is located in a spike at the nominal mass. The mass resolution of the reconstructed candidates can not be evaluated after applying this fitting, since the masses in the acceptable $\chi^2$ range are forced to be in the spike.

**4-Vector Constraint Kinematic Fit** 4-vector constraint fit is an useful tool for analyzing an exclusive decay channel, i.e. reconstructing the complete event reaction, where all final state particles were reconstructed. In that case all components of the initial Lorentz vector ($E$, $p_x$, $p_y$, $p_z$) determined by the beam properties have to be conserved individually.

**Monte Carlo Truth Match** A MC truth match is a check whether a reconstructed decay tree resembles the original one created by the generator concerning mass hypothesis assignments and topology. It can only be applied for simulated data, where the MC truth for a certain decay is known. This match is of particular importance whenever the number of reconstructed signal particles in the data has to be determined precisely, since it might be the only way to access the reconstruction efficiency of the analysis procedure. Another useful feature of the MC truth match routine is that the match assigns a MC truth object also to the intermediate composite states.

# Simulation and Reconstruction of $\mathrm{D_s}$ Semileptonic Decay

# 4

In this chapter, the performance of the P̄ANDA detector to measure the semileptonic $\mathrm{D_s}$ decay is studied via Mote Carlo simulation. The framework to reconstruct the decay chain is presented in detail. The purpose of this simulation is to estimate the production rate of useful signal events and the available measurement precision of the form factor of the $\mathrm{D_s}$ semileptonic decay. An additional objective is the continuous development of the analysis tools of PandaRoot, necessary for the in-depth study of the detector's performance.

## 4.1 Production Reaction and Decay Chains

As illustrated in Fig. 4.1, the decay chain includes $\mathrm{\bar{p}p} \to \mathrm{D_s^+ D_s^-}$, $\mathrm{D_s^+} \to \eta \mathrm{e^+} \nu_\mathrm{e}$, $\eta \to \pi^0 \pi^+ \pi^-$, $\pi^0 \to \gamma\gamma$, and the decays of the tagged $\mathrm{D_s^-}$. Antiproton annihilation on a proton target is used to generate $\mathrm{D_s}$ meson pairs. One of the $\mathrm{D_s}$ mesons, e.g. $\mathrm{D_s^-}$, is used as a "trigger" and reconstructed via a decay branch that is relatively common and has a simple final state. In this work, two tagging channels are studied: $\mathrm{D_s^-} \to \mathrm{K^+ K^-} \pi^-$ and $\mathrm{D_s^-} \to \pi^+ \pi^- \pi^-$. Then the decays of the $\mathrm{D_s}$ with the opposite charge, $\mathrm{D_s^+}$, is studied in detail with minimal bias. In semileptonic decays of the $\mathrm{D_s^+}$ meson there is one neutrino in the event. The achievable performance of the P̄ANDA detector for these types of reactions has not been studied in detail yet; however, this is expected to work very well based upon the design performance and experience with other detector systems, which is due to the kinematic overconstraints that allows these events to be completely reconstructed despite one particle not being measured. After identifying the events and the branching fraction, the lepton-neutrino invariant mass will be determined in order to extract the form factor.

### 4.1.1 Theoretical Cross Section of $\mathrm{\bar{p}p} \to \mathrm{D_s^+ D_s^-}$

The center-of-mass energy threshold for generating a pair of $\mathrm{D_s}$ mesons is $\sqrt{s} = 3.936$ GeV, corresponding to an antiproton beam of 7.257 GeV/$c$ annihilating on a fixed proton target. Currently, very little is known about the interaction of charmed particles with conventional

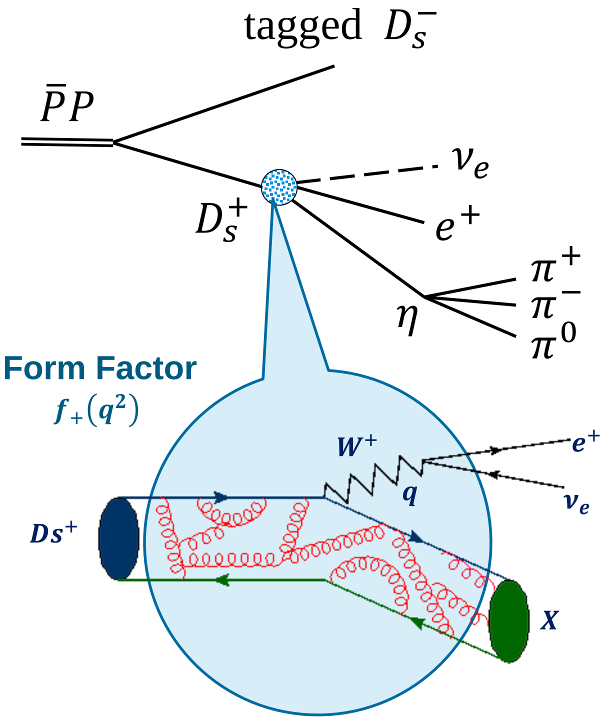

**Figure 4.1:** Simulated decay chain with single-tagged $D_s^-$. For the tagged $D_s^-$, two decay channels are considered: $D_s^- \to K^+K^-\pi^-$ and $D_s^- \to \pi^+\pi^-\pi^-$. The transition form factor of $D_s^+ \to \eta e^+ \nu_e$ is highlighted.

hadrons. The charm production of antiproton-proton interaction has not been measured yet. The available estimate on the cross section is from theoretical calculations. In the following, the recent calculation results are summarized.

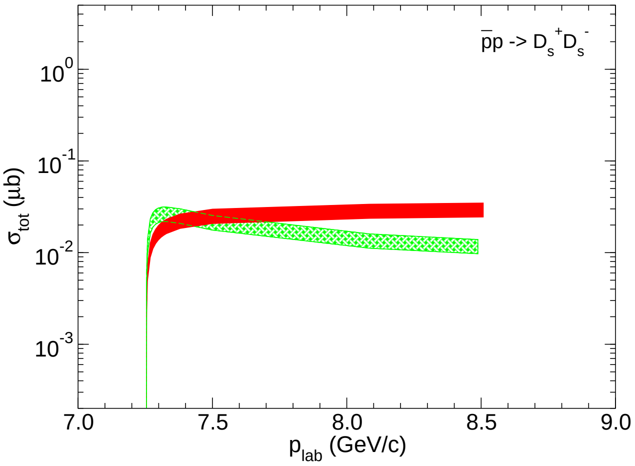

**Figure 4.2:** Total reaction cross sections for $\bar{p}p \to D_s^+D_s^-$ as a function of beam momentum $p_{lab}$, based on baryon-exchange (red shaded band) and the quark model (green band). Result of Ref. [94].

The direct $\overline{\mathrm{p}}\mathrm{p} \to \mathrm{D}_s^+\mathrm{D}_s^-$ transition requires the annihilation of three quark-antiquark pairs ($u$ or $d$) and a creation of two quark-antiquark pairs ($s$ and $c$). This process is OZI suppressed. Ref. [94] treats it as a two-step processes, i.e. $\overline{\mathrm{p}}\mathrm{p} \to \mathrm{D}^+\mathrm{D}^- \to \mathrm{D}_s^+\mathrm{D}_s^-$, where the elementary charm production process is described by baryon-exchange and in the constituent quark model, respectively. Additionally, the effects of the interactions in the initial and final states are taken into account, which are known to play an important role for energies near the production threshold [148]. In this framework, the production of D and $\mathrm{D}_s$ mesons are studied. The results for $\overline{\mathrm{p}}\mathrm{p} \to \mathrm{D}_s^+\mathrm{D}_s^-$ is shown in Fig. 4.2. It is found that the maximal cross section can roughly achieve 20 nb in the model based on baryon-exchange (red band in Fig. 4.2) with a $\overline{\mathrm{p}}$ beam of 8 GeV/$c$. The constituent quark model (green band) predicts a lower value. Overall, the possible range of the cross section estimated by Ref. [94] for a $\mathrm{D}_s$ pair is 5 ∼ 20 nb.

In the same theoretical framework, the authors of Ref. [94] also calculate the cross sections for $\mathrm{D}^0\,\overline{\mathrm{D}}^0$ and $\mathrm{D}^+\,\mathrm{D}^-$ in the two-step scenarios: $\overline{\mathrm{p}}\mathrm{p} \to \bar{N}N \to \mathrm{D}^+\mathrm{D}^-$ and $\overline{\mathrm{p}}\mathrm{p} \to \bar{N}N \to \mathrm{D}^0\overline{\mathrm{D}}^0$ respectively. Fig. 4.3(a) and Fig. 4.3(b) show the results, where the red band indicates the

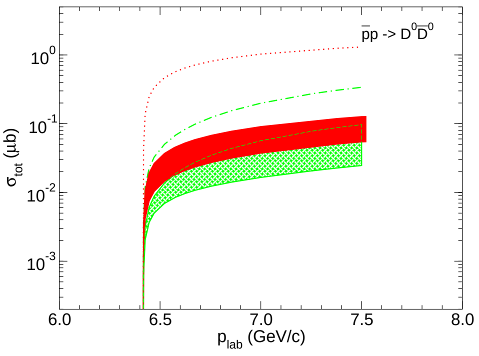

(a) Cross section of $\overline{\mathrm{p}}\mathrm{p} \to \mathrm{D}^0\overline{\mathrm{D}}^0$ [94].

(b) Cross section of $\overline{\mathrm{p}}\mathrm{p} \to \mathrm{D}^+\mathrm{D}^-$ [94].

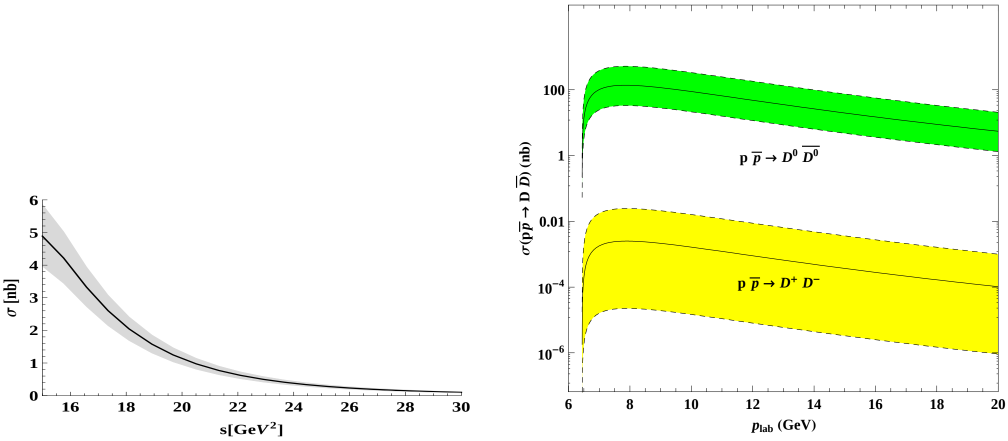

(c) Cross section of $\overline{\mathrm{p}}\mathrm{p} \to \mathrm{D}^0\overline{\mathrm{D}}^0$ [149].

(d) Cross section of $\overline{\mathrm{p}}\mathrm{p} \to \mathrm{D}\overline{\mathrm{D}}$ [150].

**Figure 4.3:** Theoretical calculations of non-stranged charm production with different techniques. See the text for further details.

estimate from the baryon-exchange based model and the green band is for the quark model. Results obtained in the Born approximation are indicated by the red dotted (baryon-exchange), and green dash-dotted (quark model) lines. The figures reveal that the quark model and the baryon-exchange transitions give similar final results, with those of the quark model being smaller on average by a factor of roughly 3 [94]. Comparing with Fig. 4.2, the cross section for a pair of $D_s$ mesons is found to be of the same order of magnitude as for D mesons, even though a two-step process is required in the case of $D_s$ mesons. The same situation is found in a similar framework for $\bar{p}p \rightarrow \bar{\Sigma}^+\Sigma^+$ and $\bar{p}p \rightarrow \bar{\Sigma}^-\Sigma^-$, which were of comparable magnitude [151], and then this prediction has been experimentally confirmed [152].

As mentioned above, the open-charm production cross section is far from being clear. For the cross section of D mesons in proton-antiproton interactions, there are several different theoretical approaches and models applied in studies [94, 149, 150, 153, 154]; however, the calculations produce a wide range of estimates (see Fig. 4.3). Fig. 4.3(c) shows the result from Ref. [149] using the double handbag approach, which is a perturbative QCD-motivated framework. Their cross section predictions are in accordance with the results of Ref. [155], where a quark-diquark model has also been used. However, these are one order of magnitude smaller than the hadronic interaction-model calculations of Refs. [94, 150]. On the other hand, it is promising to understand more about the charm production with the future P̄ANDA experiment to test the existing theoretical models.

In Fig. 4.3(d), the integrated cross section of charmed meson pairs is obtained with the Quark-Gluon String (QGS) model by Ref. [150], where the uncertainties shown by the dashed lines are introduced by the strong couplings obtained from LCSR. It is important to note that the QGS model is only applicable at sufficiently large energies [150]. These are beyond the upper limit of the P̄ANDA experiment; therefore, the cross section calculated can only be considered as an order of magnitude estimate. In addition, the adopted model is only valid at small momentum transfers, and the absorption factor is only taken in the first approximation [150]. Therefore, this estimate contains rather large uncertainties.

Considering all aspects discussed above, the cross section of $\bar{p}p \rightarrow D_s^+D_s^-$ is cited as 20 nb in this work to evaluate the production rate with a beam momentum of 8 GeV/$c$, according to the predictions of Ref. [94]. Due to the uncertainties, the simulation study has been carried out at various beam energy settings. The comparison of the reconstruction efficiency as a function of beam momentum is presented in Sec. 4.6.2.

### 4.1.2 Simulated Decay Chains and Decay Models

The form factor of the semileptonic decay $D_s^+ \rightarrow \eta e^+ \nu_e$ is a function of the momentum transfer squared between the $D_s^+$ and $\eta$, i.e. $q^2$, which equals to the total 4-momenta squared of the $e^+$ and $\nu_e$. The kinematics of the $\nu_e$ will not be directly measured with the P̄ANDA detector. Therefore, the $q^2$ has to be indirectly obtained by reconstructing the $D_s^-$ and $\eta$ mesons. The four-vector of the $D_s^+$ can be calculated with the initial $\bar{p}$ p system and the tagged $D_s^-$. Tagging the other $D_s$ meson, i.e. $D_s^-$, uses a decay mode which has a relatively high branching ratio and that can be efficiently reconstructed. The tagging modes $D_s^- \rightarrow K^+K^-\pi^-$ (called mode A in Fig. 4.4) and $D_s^- \rightarrow \pi^+\pi^-\pi^-$ (mode B) have been considered. This is done with the intention to

**Table 4.1:** Branching ratio of the simulated decay channels. Values in this table are from PDG2014 [9].

| Channel | BR |
|---|---|
| $D_s^+ \to \eta e^+ \nu_e$ | $(2.67 \pm 0.29)\%$ |
| $D_s^- \to K^+K^-\pi^-$ | $(5.39 \pm 0.21)\%$ |
| $D_s^- \to \pi^+\pi^-\pi^-$ | $(1.09 \pm 0.05)\%$ |
| $\eta \to \pi^0\pi^+\pi^-$ | $(39.41 \pm 0.20)\%$ |
| $\pi^0 \to \gamma\gamma$ | $(98.823 \pm 0.034)\%$ |

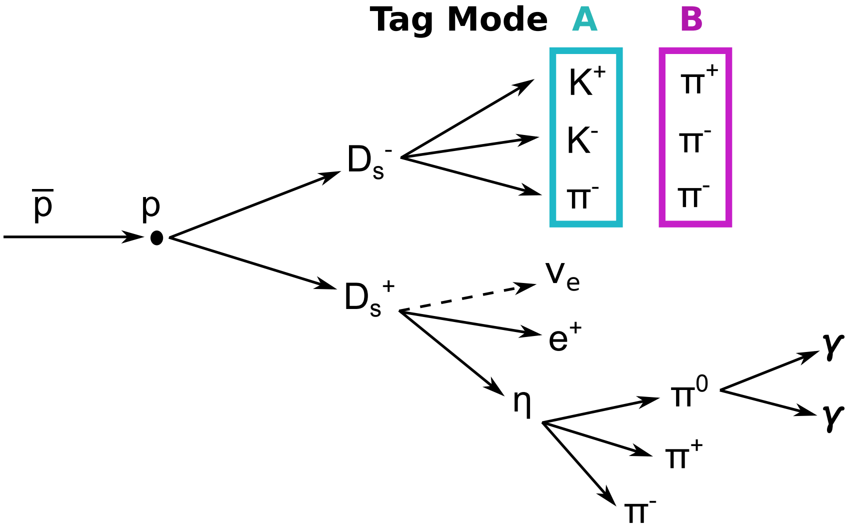

**Figure 4.4:** Decay tree of the simulation with two tagging modes of $D_s^-$: mode A is $D_s^- \to K^+K^-\pi^-$ and mode B is $D_s^- \to \pi^+\pi^-\pi^-$.

increase the usable statistics. The complete decay chain is illustrated in Fig. 4.4. The branching ratios of the simulated decay channels are summarized in Table 4.1.

The first task in this Monte Carlo simulation is to study the decay models used to simulate the signal events. For the processes $\bar{p}p \to D_s^+D_s^-$ and $\pi^0 \to \gamma\gamma$, the PHase SPace (PHSP) decay model is used. PHSP provides a generic phase space to n-bodies decay, where the spins of all particles in the initial and final states are averaged [139]. This mode is expected to be suitable to describe $\bar{p}p \to D_s^+D_s^-$ since the simulation energy is close to the production threshold, and all the valence quarks of $\bar{p}p$ are annihilated to generate charm and strange quarks to form the $D_s$ mesons. The $\pi^0$ has $J = 0$, thus it also should be simulated with PHSP (isotropic phase) in the decay $\pi^0 \to \gamma\gamma$. For the other channels, Dalitz plot analyses are applied to study the dynamics, in order to corroborate the correctness of the decay models by comparing with the available experimental measurements.

**Decay Model for $D_s^+ \to \eta e^+ \nu_e$** For the semileptonic decay $D_s^+ \to \eta e^+ \nu_e$, the ISGW2 model [74] is utilized for the simulation with the PandaRoot event generator. ISGW2 is an updated version of ISGW [156]. The updated model incorporates a number of features which should make it more reliable, including the constraints imposed by Heavy Quark Symmetry, hyperfine distortions of wave functions, and form factors with more realistic high recoil behaviours, e.g. describing the relations between form factors away from zero recoil and slopes near zero recoil [74].

The ISGW model is the first exclusive model to calculate rates to channels other than the pseudoscalar and vector ground states. The assumed pseudoscalar $\eta$-$\eta'$ mixing angle is $-20°$ in ISGW2. The individual decay rates of these two states are sensitive to this assumption, but the sum is relatively insensitive [74]. The Dalitz plot obtained in simulation is shown in Fig. 4.5.

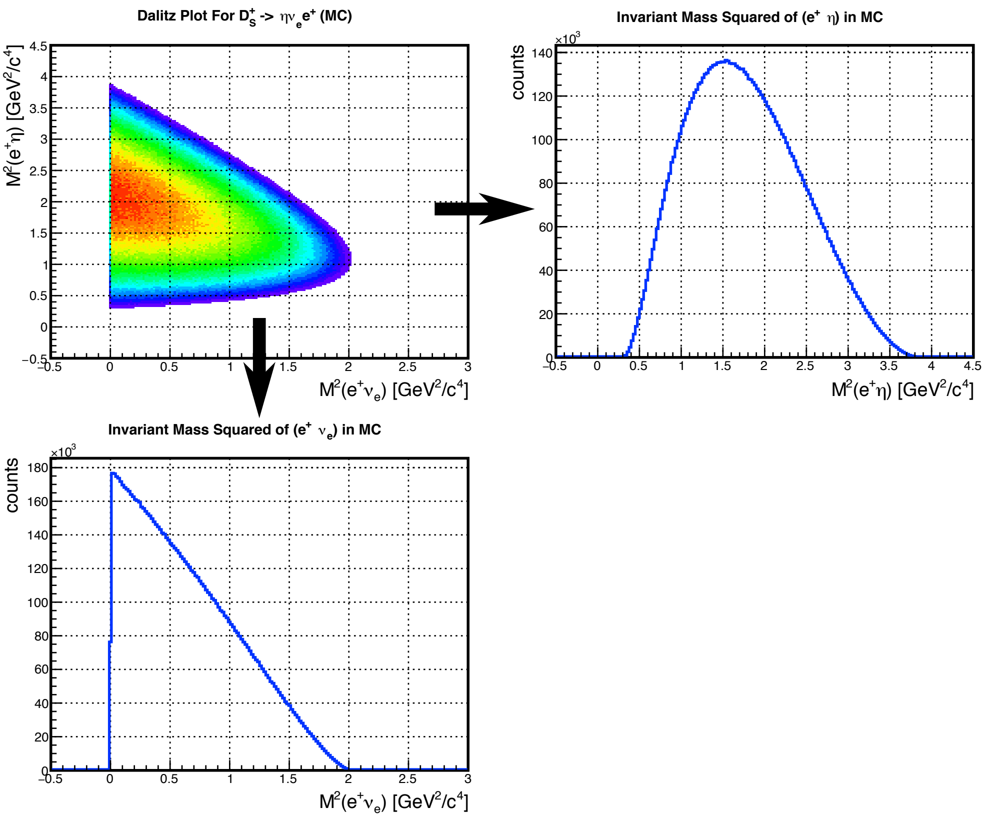

**Figure 4.5:** Dalitz plot of $D_s^- \to \eta e^+ \nu_e$ in ten million MC events with the ISGW2 decay model. The X and Y projections are shown.

**Decay Model for $D_s^- \to K^+K^-\pi^-$** The experimental results [157, 158] for this channel show that it is not described by the PHSP decay model. However, when the simulation of $D_s^- \to K^+K^-\pi^-$ was started at the end of 2012, an old version of the EvtGen [139] package (release number: alpha-00-09-42) was used within PandaRoot (release version: oct12). The package, at that moment, did not include a suitable decay model for $D_s \to KK\pi$. To attain a reasonable simulation a new decay model, DS_DALITZ, was introduced in PandaRoot. This was written in

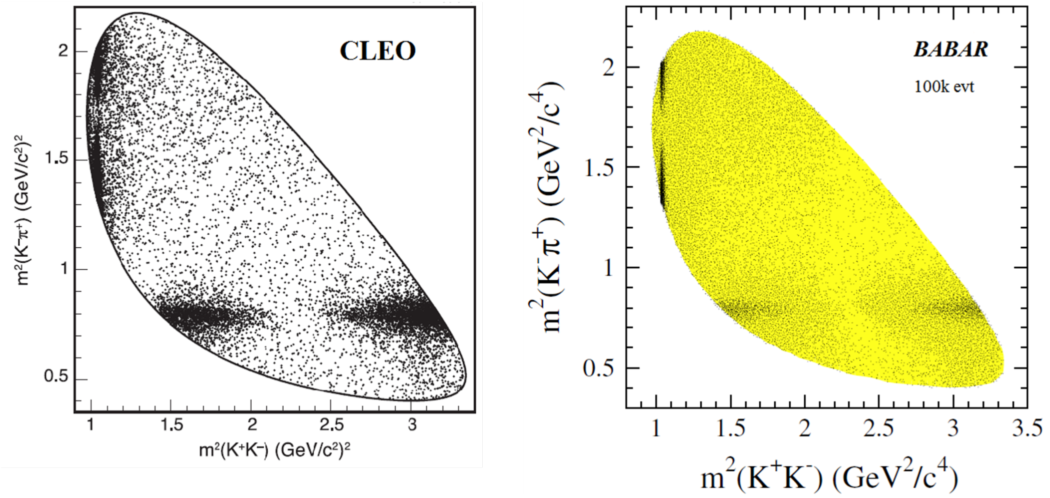

**Figure 4.6:** Experimental results of the Dalitz plots of $D_s^- \to K^+K^-\pi^-$. Left: Dalitz plot from CLEO with 14,400 events [157]. Right: Dalitz plot from BaBar with 100,000 events [158].

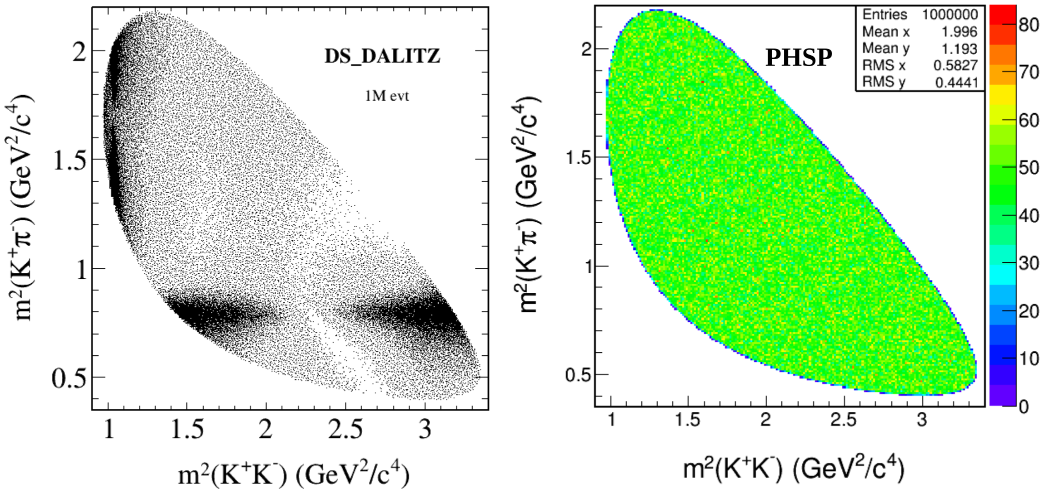

**Figure 4.7:** Comparison of the DS_DALITZ and PHSP on the Dalitz plot of $D_s^- \to K^+K^-\pi^-$. Left: Dalitz plot obtained from the DS_DALITZ decay model. Right: Dalitz plot obtained from the PHSP decay model.

addition to the existing code of the D_DALITZ model. The original code was obtained from a development version of EvtGen package, where the decay amplitude includes the contributions from the following resonances: $K^*(892)K^+$, $K_0^*(1430)K^+$, $f_0(980)\pi^+$, $\Phi(1020)\pi^+$, $f_0(1370)\pi^+$ and $f_0(1710)\pi^+$. One year later, PandaRoot was officially updated to include the new release of the EvtGen (release number: R01-03-00) in its release jan14. In this new EvtGen, there is a more powerful D_DALITZ implemented, which is expanded from D meson Dalitz decays to the $D_s$ meson. Therefore, both D_DALITZ and DS_DALITZ can be used to simulate $D_s \to KK\pi$ properly now. Furthermore, their codes and parameters are identical. The Dalitz amplitude parameters are from the BaBar experiment data [158].

Fig. 4.6 shows the experimentally measured Dalitz plots by the CLEO and BaBar collaborations. BaBar collected roughly 10 times more statistics than CLEO. Both of the plots clearly show the patterns caused by spin structures of intermediate resonances. Hence, the PHSP model in which the spin of final states are averaged is unable to reproduce the Dalitz plots obtained from experiments.

In Fig. 4.7, the comparison of the simulation results obtained with the implemented DS_DALITZ model and the PHSP model for $D_s^- \rightarrow K^+K^-\pi^-$ is shown. The result of DS_DALITZ agrees with the experiments as expected. Again, the PHSP has been proven to be not suitable for this decay channel.

**Decay Model for $D_s^- \rightarrow \pi^+\pi^-\pi^-$** The Dalitz plot analysis of approximately 13,000 $D_s^-$ decays to $\pi^+$ $\pi^-$ $\pi^-$ has been performed in Ref. [159]. The resonances contributions include the amplitude of $f_2(1270)\pi^+$, $\rho(770)\pi^+$, $\rho(1450)\pi^+$, and S-wave $\pi^+\pi^-$. This analysis is utilized to fit the amplitude parameters in the decay model D_DALITZ for this channel.

To compare with their Dalitz plot in the Monte Carlo simulation the same number of events are generated with the D_DALITZ decay model (see Fig. 4.8). This simulated Dalitz plot agrees well with the result from measurement.

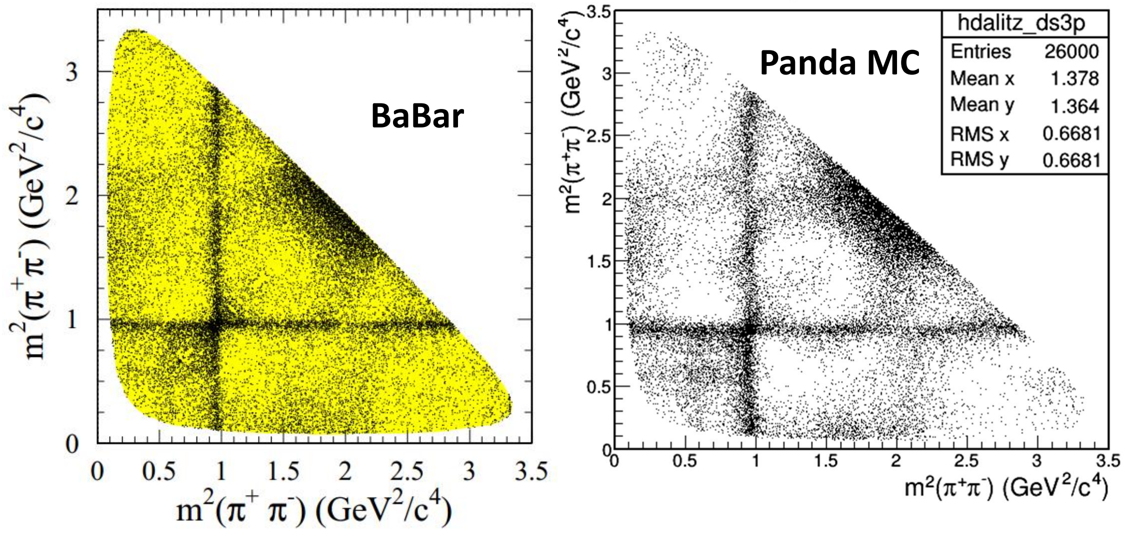

**Figure 4.8:** Dalitz plots of $D_s^- \rightarrow \pi^+\pi^-\pi^-$. Left: Dalitz plot obtained from BaBar experiment [159]. Right: Dalitz plot obtained from the simulation with PandaRoot.

**Decay Model for $\eta \rightarrow \pi^+\pi^-\pi^0$** The decay $\eta \rightarrow \pi^+\pi^-\pi^0$ violates isospin invariance. The KLOE collaboration measured this decay channel and extracted the parameters of the Dalitz plot density [160]. The decay model for simulating is the ETA_DALITZ model. Fig. 4.9 shows the good agreement of the $\eta \rightarrow \pi^+\pi^-\pi^0$ Dalitz plot distribution between the KLOE experiment and the PandaRoot simulation.

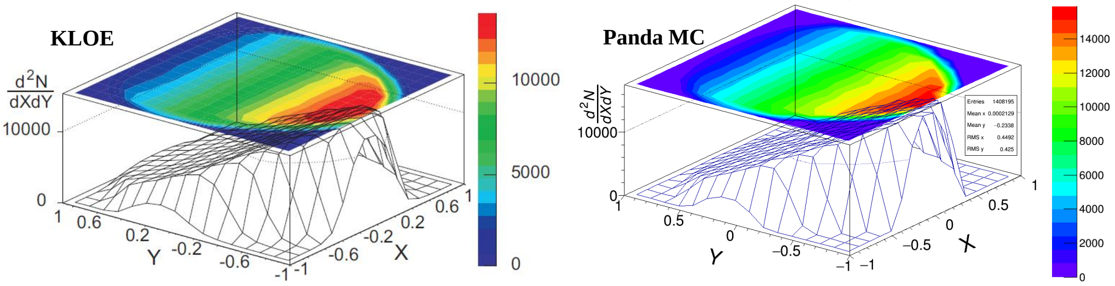

**Figure 4.9:** Dalitz plot distributions of $\eta \to \pi^+\pi^-\pi^0$ for the KLOE experiment [160] (left) and the PandaRoot simulations (right).

**Summary of the Decay Models** By comparing the available Dalitz plots for each decay, a suitable model was selected. Table 4.2 summarizes all the decay models utilized in this simulation.

**Table 4.2:** Decay models for simulated channels.

| Channel | Model |
|---|---|
| $\bar{p}p \to D_s^+ D_s^-$ | PHSP |
| $D_s^+ \to \eta e^+ \nu_e$ | ISGW2 |
| $D_s^- \to K^+K^-\pi^-$ | DS_DALITZ |
| $D_s^- \to \pi^+\pi^-\pi^-$ | D_DALITZ |
| $\eta \to \pi^0\pi^+\pi^-$ | ETA_DALITZ |
| $\pi^0 \to \gamma\gamma$ | PHSP |

### 4.1.3 Simulation Settings

A data set of one million signal events was simulated in order to obtain reasonable statistics for the $q^2$ distribution. In addition, 100 million background events were used for the signal-to-background study. Table 4.3 lists the main parameters of the simulations. These parameters have been introduced in Sec. 3.4.

Due to the uncertainties on the theoretical estimate of the cross section (as discussed in Sec. 4.1.1), three $\bar{p}$ beam momenta have been simulated in order to identify the one yielding the highest efficiency for the future data taking. The trunk 28748 version of PandaRoot was chosen for simulating the data set, which was implemented with the tested track fitting toolkit GENFIT2 [144]. To study the achievable best performance, the *ideal* algorithm for PID was applied. The details on tuning the EMC correlation parameters are presented by the following section Sec. 4.2.

**Table 4.3:** Simulation settings.

| Issue or Parameter | Setting |
|---|---|
| $\overline{p}$ beam momentum | 7.3 GeV/$c$, 7.7 GeV/$c$, 8 GeV/$c$ |
| PandaRoot software version | 28748 |
| PID algorithm | ideal (MC info) |
| Propagation package | GEANE4 |
| Tracking package | GENFIT2 |
| Charge particle EMC correlation parameter | 2500 cm$^2$ |
| Neutral particle EMC correlation parameter | 100 cm$^2$ |

## 4.2 Photon Reconstruction and Pre-Selection

Photon Reconstruction and Pre-Selection Reconstruction of neutral particles ($\pi^0$, $\eta$) requires a good identification and selection of photon candidates. This includes searching for the photon candidates among all the clusters detected by the EMC, and rejecting those low energy photons caused by bump split-offs and secondary interactions. The former issue is connected to the photon reconstruction efficiency and purity, which can be studied by looking at the neutral correlation parameter (see Sec. 3.4.2.6). The latter is an issue of significance in reconstructing the mother particles of the photons, i.e. $\pi^0$ and $\eta$, with an appropriate photon energy threshold. These studies are presented in detail in the following.

### 4.2.1 Efficiency Studies

As mentioned in Sec. 3.4.2.6, the algorithm for the EMC correlation of charged particle uses the correlation parameter PndEMC12Cut, which defines the maximum distance squared between the track extrapolation to the EMC and the nearest cluster. Similarly for the correlating neutral clusters, PndEMCNeutralCut is defined as the minimum distance squared between a cluster and the nearest point of any track extrapolation.

An efficiency study has been carried out with a particle gun using charged pions $\pi^-$. With the Box Generator (see Sec. 3.4.2.1), 10,000 $\pi^-$ each with 0.5 GeV/$c$ are generated in the angular range $\theta = 30°$ and $\phi = 0°\sim360°$. In this case, the total number of EMC clusters ($N_{all}$) and the number of the charged tracks ($N_{char}$) are known: $N_{all} = 23{,}102$ and $N_{char} = 9573$. These values are used to find the appropriate selection thresholds.

Fig. 4.10 shows the number of EMC correlated tracks $N'_{char}$ as a function of the correlation parameter PndEMC12Cut. When the parameter is higher than PndEMC12Cut $\approx$ 1600 cm$^2$, the distribution becomes nearly flat and $N'_{char}$ approaches the value of $N_{char}$. PndEMC12Cut=2500 cm$^2$

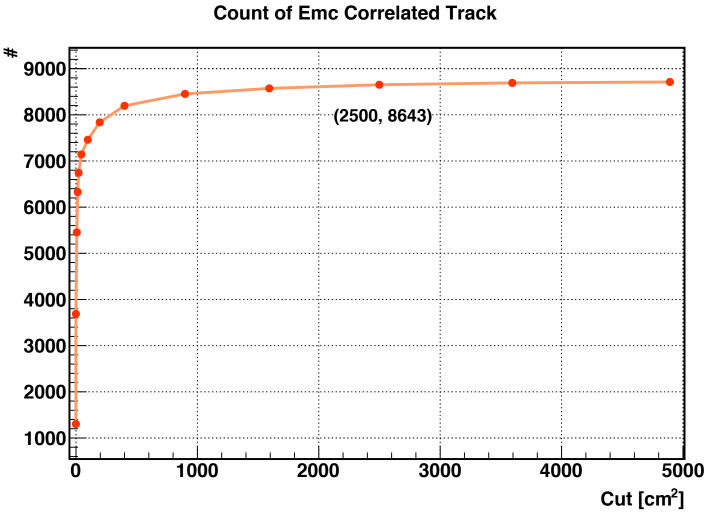

**Figure 4.10:** Number of EMC correlated tracks as a function of the correlation parameter PndEMC12Cut. The coordinates of the selected data point is indicated.

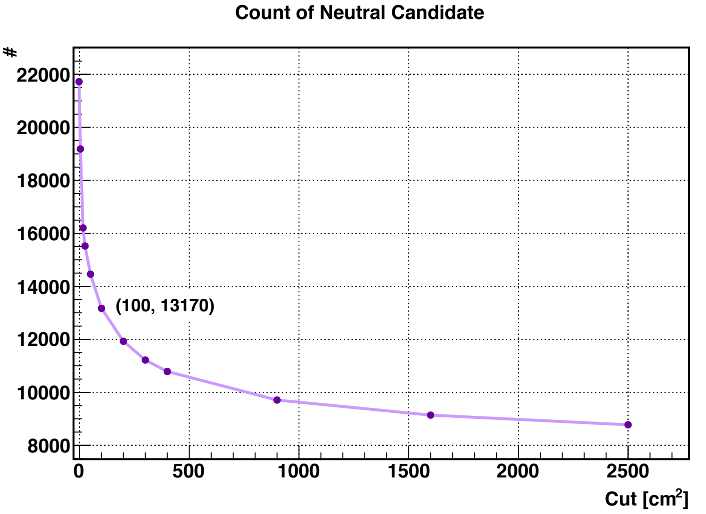

**Figure 4.11:** Number of EMC correlated neutral candidates as a function of the correlation parameter PndEMCNeutralCut. The coordinates of the selected data point is indicated.

is selected for the charged correlation for a stable and high efficiency, where the corresponding value of $N'_{char}$ is 8643. The correlation efficiency, defined as a ratio of $N'_{char}$ to $N_{char}$, is about 90% for this value of the cut.

On the other hand, the number of photon candidates $N_{neut}$ should approximately match the gap between the total number of clusters and the number of charged correlated clusters, i.e. $N_{neut} \approx N_{all} - N'_{char} = 14{,}459$. The distribution of $N_{neut}$ as a function of the neutral particle correlation parameter PndEMCNeutralCut is shown in Fig. 4.11. It is found that the number of neutral correlated clusters decreases when the cut parameter increases, $N_{neut}$ drops dramatically particularly in the low value region. Assuming the same correlation efficiency of charged particles in the correlation of neutral particles, the number of reconstructed neutral candidates is expected to be $N'_{neut} = 14{,}459 \times 90\% = 13{,}013$. Using this number as the criteria, the acceptable value of the neutral correlation parameter is around 100 cm$^2$.

### 4.2.2 Purity Studies

Besides the efficiency, the purity of the reconstructed neutral candidates is another issue for validating the correlation parameter PndEMCNeutralCut. High purity demands maximal correctness of the EMC cluster correlation. In contrast to the efficiency studies, where a particle gun was utilized, in the purity studies the value of PndEMCNeutralCut needs to be validated in the physical decay chain, due to the effect of charged particles with various momenta and multiplicity will have on the purity checking. In this step, MC truth matching (see Sec. 3.4.2.7) is used as a tool to discriminate the correct correlation by comparing to the topology of the decay tree.

A data sample of 2000 events has been simulated for the decay chain with tag mode B: $\bar{p}p \to D_s^+ D_s^-$, $D_s^+ \to \eta e^+ \nu_e$, $D_s^- \to \pi^+\pi^-\pi^-$, $\eta \to \pi^0\pi^+\pi^-$ and $\pi^0 \to \gamma\gamma$. Tag mode B has been chosen in order to study the situation with the highest complexity of the tracks, since pions have higher acceptance than kaons. The beam momentum is 8 GeV/$c$, and the photon energy threshold is 20 MeV. The charge correlation parameter PndEMC12Cut has been set to 2500 cm$^2$.

In the purity checking, the correlation parameter PndEMCNeutralCut was varied from (1, 100, 400, 900, 2500) cm$^2$. For each value of PndEMCNeutralCut, the numbers of MC truth matched $\pi^0$ and $\eta$ after all fits are shown in Fig. 4.12. As the cut parameter increases, the number of the MC truth matched $\pi^0$ continuously drops, however the number of the MC truth matched $\eta$ presents a peak at PndEMCNeutralCut= 100 cm$^2$. This result indicates that PndEMCNeutralCut= 100 cm$^2$ is the best choice considering the purity of reconstructed $\eta$.

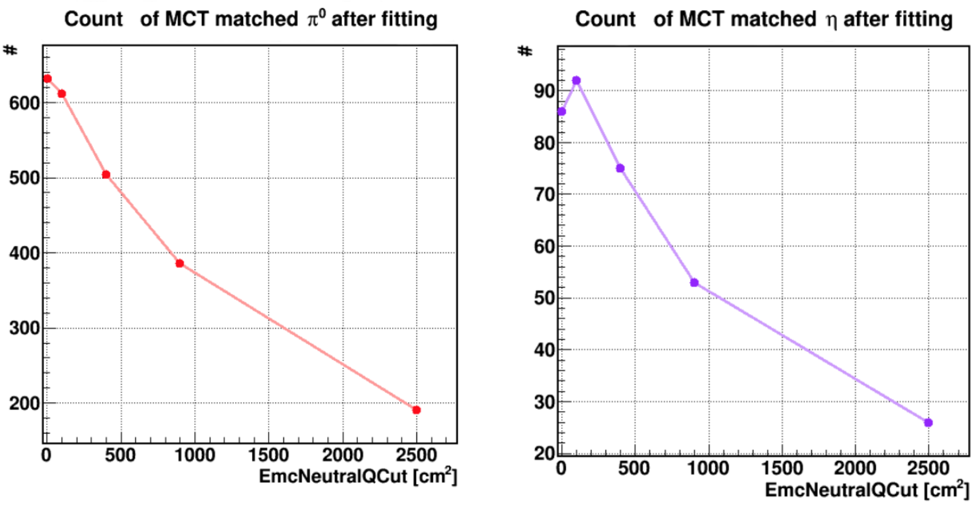

**Figure 4.12:** Number of MC truth matched neutral candidates as a function of the correlation parameter PndEMCNeutralCut. Left is for MC truth matched $\pi^0$, and right is for MC truth matched $\eta$.

### 4.2.3 Significance Studies

Low energy EMC clusters can be caused by bump split-off and secondary interaction, and lead to a high multiplicity of photon candidates, thus generating a high combinatorial background for the $\pi^0$ meson reconstruction. Therefore, it is necessary to pre-select photons by applying an energy threshold to achieve a good significance.

In order to select a reasonable energy threshold and cross check the neutral correlation parameter PndEMCNeutralCut, the significance of the reconstructed $\pi^0$ and $\eta$ has been studied with various energy thresholds for photons with the correlation parameter of $100\,\mathrm{cm}^2$ and $400\,\mathrm{cm}^2$, respectively. The significance is defined as

$$\text{significance} = \frac{N_{MCT}}{\sqrt{N_{all}}}, \tag{4.1}$$

where $N_{MCT}$ stands for the number of MC truth matched candidates, and $N_{all}$ symbolizes the total number of all candidates. This significance study is based on the same event sample generated for the previous purity study (see Sec. 4.2.2).

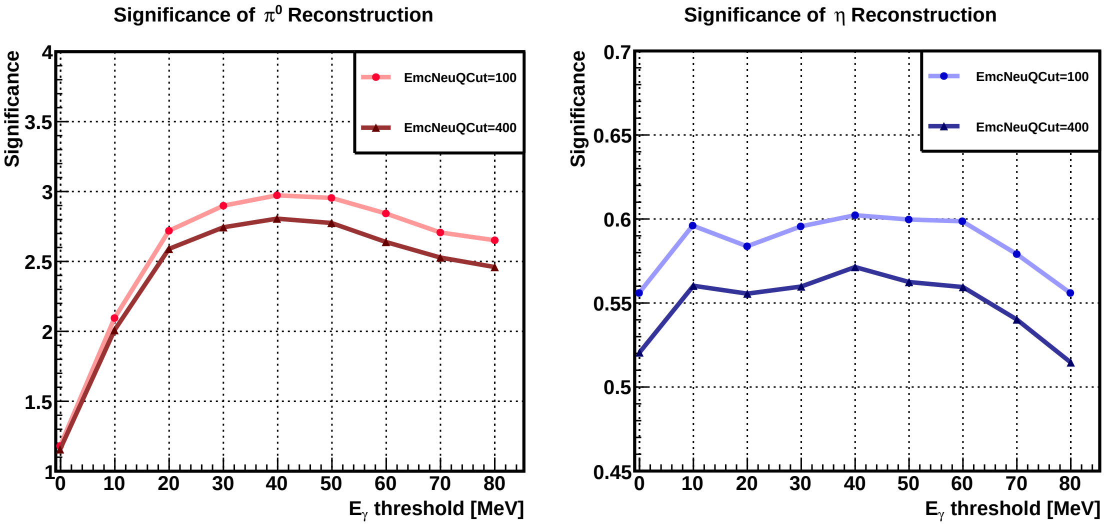

**Figure 4.13:** Significance of $\pi^0$ and $\eta$ reconstructions as a function of photon energy threshold. Left is for the reconstructed $\pi^0$, and right is for the reconstructed $\eta$. In both figures, the light color line (dot) indicates the results obtained with PndEMCNeutralCut= $100\,\mathrm{cm}^2$, and the dark color line (triangle) shows that of PndEMCNeutralCut= $400\,\mathrm{cm}^2$.

Fig. 4.13 shows the significance of $\pi^0$ and $\eta$ reconstructions as a function of the photon energy threshold. As expected, the $\pi^0$ significance is very low at $E_\gamma^{\mathrm{thr}} = 0\,\mathrm{MeV}$. This distribution continuously increases when the threshold increases to around 40 MeV, afterwards it drops. This implies the energy threshold is too high because a fraction of the signal photons have been rejected. In contrast to the distribution of the $\pi^0$ candidates, the significance for the $\eta$ candidates shows another peak at about 10 MeV. It is found that the significance with PndEMCNeutralCut= $100\,\mathrm{cm}^2$ is always higher than that of $400\,\mathrm{cm}^2$ in the whole tested range of the energy threshold.

This confirms the result obtained previously while investigating the efficiency (see Sec. 4.2.1). For the $\pi^0$ candidates, the difference between the results of two PndEMCNeutralCut values becomes larger when the energy threshold increases. Regarding to the various thresholds, both of the significances for $\pi^0$ and $\eta$ have a maximum at $E_\gamma^{\mathrm{thr}} = 40$ MeV. In summary, the highest significance can be achieved when the neutral correlation parameter is $100\,\mathrm{cm}^2$, and the photon energy threshold is 40 MeV.

## 4.3 Reconstruction Strategy

The reconstruction strategy is illustrated by Fig. 4.14 for both tag modes. For reconstructing the tagged $\mathrm{D_s^-}$, the procedure is generally the same for both modes: first determine the decay vertex of the combined daughters and then constrain its mass. In both of fits, a cut on the fit probability value was applied. In order to ensure the correct multiplicity, the "best" candidate with the smallest $\chi^2$ in the mass constraint fit was selected and stored.

The reconstruction of the neutral particals started with the $\pi^0$ meson, which decays into two photons. A photon energy threshold of 40 MeV was selected, as discussed in Sec. 4.2.3. Two photons (above the threshold) were combined to form a $\pi^0$ candidate. Then a mass constraint fit was applied and a probability cut was imposed to suppress the combinatorial background.

To determine the decay vertex of the $\eta$, the three charged particles $\pi^+$, $\pi^-$ and $\mathrm{e}^+$ were combined and fit by a vertex constrainer. This method was found to improve the $\eta$ vertex resolution by a factor of two compared to only combining the $\pi^+$ and $\pi^-$. More details on this issue will be presented in Sec. 4.4.3. After the vertex fit, the $\pi^+$ and $\pi^-$ were selected to combine with the reconstructed $\pi^0$. A fit with the mass constraint to $M_\eta$ was applied on this combination. In every event, the "best" $\eta$ candidate was selected as the candidate with the

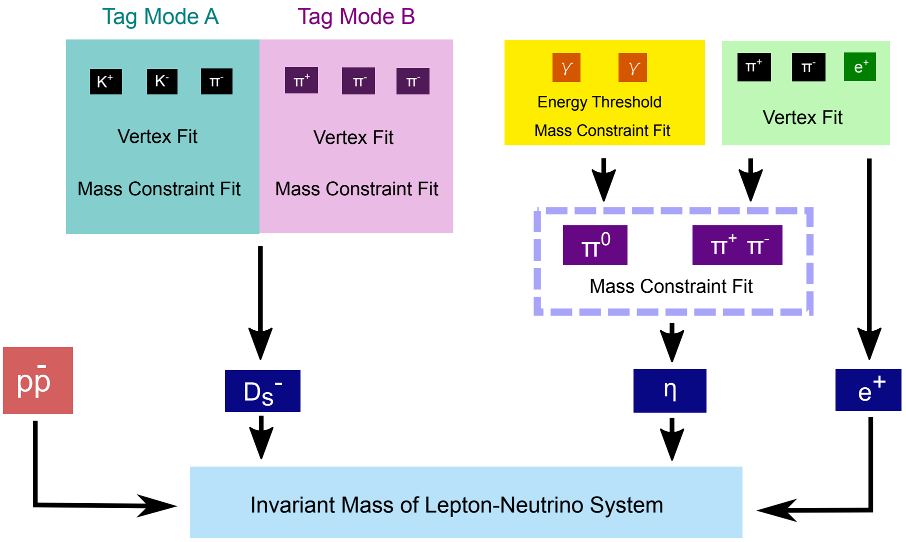

**Figure 4.14:** Reconstruction strategy with two tag modes: tag mode A is $\mathrm{D_s^-} \to \mathrm{K^+K^-}\pi^-$ and tag mode B is $\mathrm{D_s^-} \to \pi^+\pi^-\pi^-$. Independent of the tag mode, the reconstruction techniques for the other particles are the same.

smallest $\chi^2$ after the probability cut. With each selected $\eta$ candidates, the $e^+$ in the vertex fit combination ($\pi^+$, $\pi^-$, $e^+$) was chosen.

After reconstructing the intermediate particles, i.e. $D_s^-$, $\eta$ and $e^+$, the missing mass of the system can be calculated with the initial four-vector of the $\bar{p}p$ system. The missing mass is the mass of the unmeasured neutrino. The final goal is to determine the $M^2(e^+\nu_e)$ (as Eq. 4.2) distribution to study the semileptonic decay form factor of $D_s^+ \rightarrow \eta e^+ \nu_e$.

$$M^2(e^+\nu_e) = \left(E_{\bar{p}p} - E_{D_s^-} - E_\eta\right)^2 - \left|\mathbf{p}_{\bar{p}p} - \mathbf{p}_{D_s^-} - \mathbf{p}_\eta\right|^2, \tag{4.2}$$

where $E_{\bar{p}p}(\mathbf{p}_{\bar{p}p})$ is the energy (three-momentum) of the initial anti-proton beam and proton target system.

## 4.4 Simulation with the $D_s^- \rightarrow K^+K^-\pi^-$ Tag

The signal data set of one million events with the tag mode A, $D_s^- \rightarrow K^+K^-\pi^-$, was simulated with the settings as listed in Table 4.3. In the following, each reconstruction step with tag mode A is presented in detail; the study with tag mode B is described in Sec. 4.5.

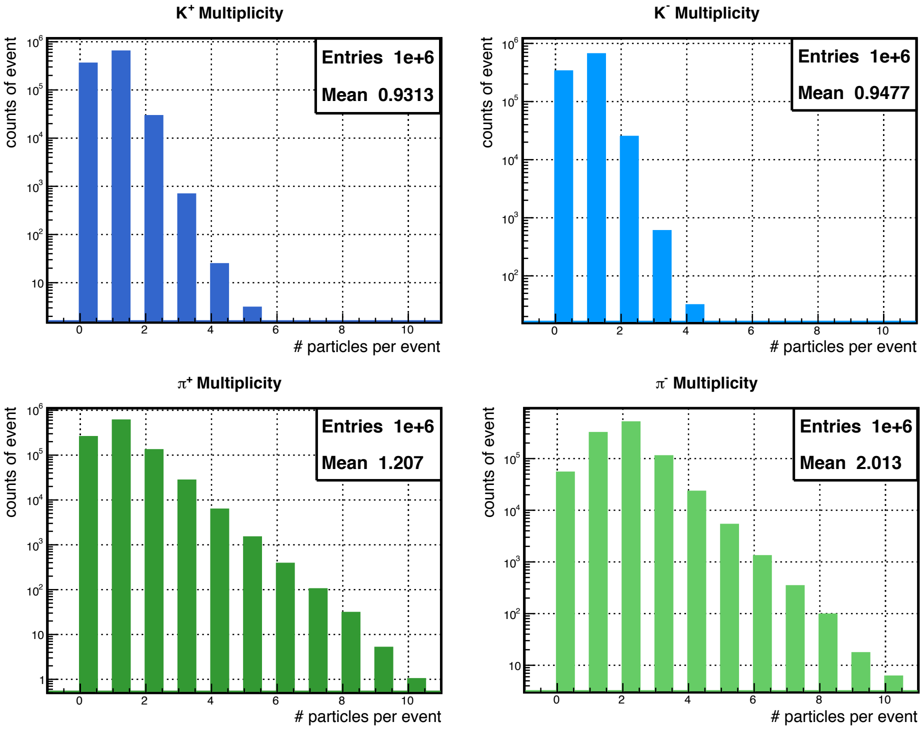

**Figure 4.15:** Multiplicity of reconstructed $K^\pm$ (upper row) and $\pi^\pm$ (lower row) in the complete decay tree with the $D_s^- \rightarrow K^+K^-\pi^-$ tagging mode. The Y-axis has a logarithmic scale.

### 4.4.1 Reconstruction of $D_s^- \to K^+K^-\pi^-$

For the tag mode A, the $D_s^-$ reconstruction was performed by combining the daughter particles: $K^+$, $K^-$, and $\pi^-$. In every event, there are six charged particles in the final products, including two $\pi^+$, one $\pi^-$, one $K^+$, one $K^\pm$ and one $e^+$. Fig. 4.15 shows the multiplicity of the $K^+$, $K^-$, $\pi^-$ and $\pi^+$. The number of entries corresponds to the total number of generated events $10^6$. The mean value indicates the average number of a certain particle per event. It is found that the detector acceptance for kaons is 30% lower than for pions. This is mostly because the pion decay length is more than double that for kaons, i.e. $c\tau(\pi^\pm) = 7.8\,\text{m}$ and $c\tau(K^\pm) = 3.7\,\text{m}$. Therefore, the kaons with low and forward directed momentum have a higher probability to decay before being detected. The acceptances of the decay products will affect the efficiency of raw $D_s^-$ candidates.

After combining the decay products of $D_s^-$, i.e. $K^+$, $K^-$, $\pi^-$, a series of fits were performed on the combination, to constrain them to a common decay vertex (vertex fit), and reproduce the invariant mass of the $D_s^-$ meson (mass constraint fit), as indicated in Fig. 4.14. The detailed

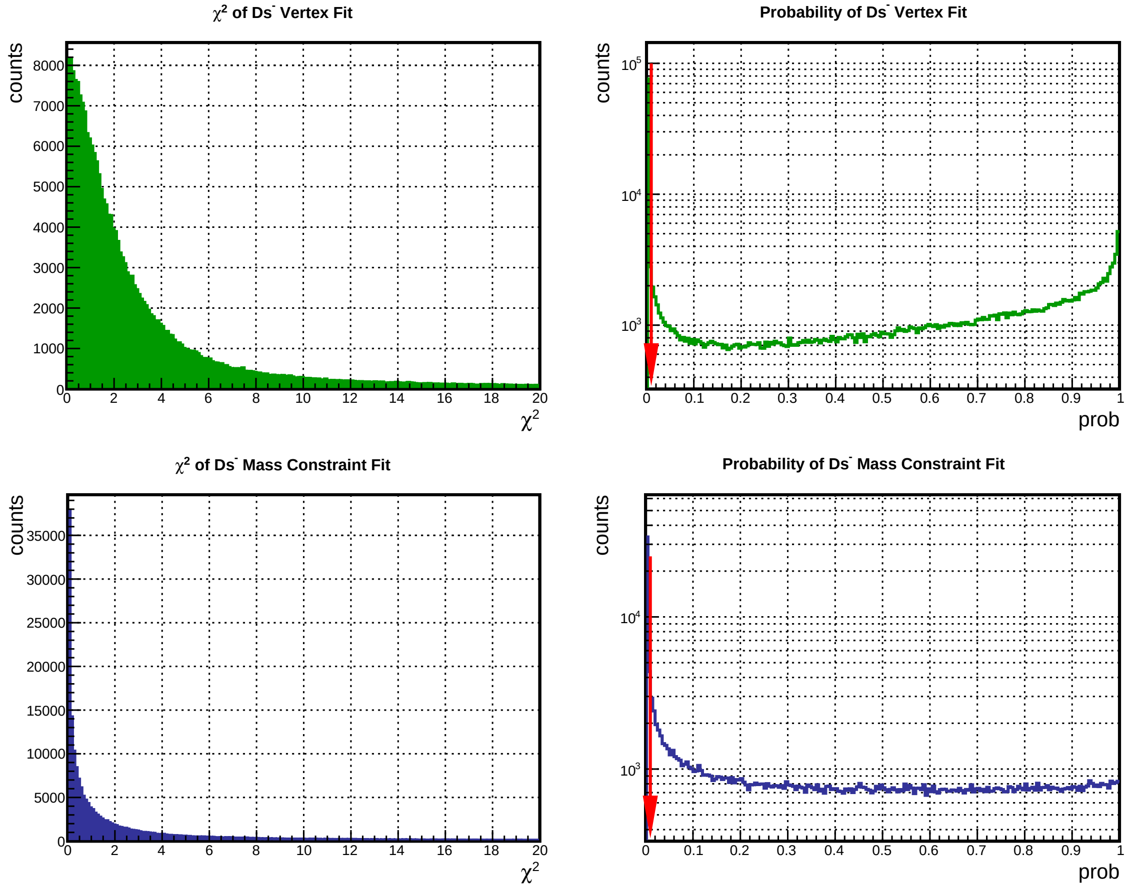

**Figure 4.16:** The $\chi^2$ (left column) and probability (right column) distributions of the $D_s^-$ vertex fit (upper row), and mass constraint fit (bottom row). In both cases the rejected candidates with probabilities lower than 1% are indicated by the red arrows.

selection cuts applied in this procedure are listed below:

- Mass window of raw $D_s^-$ candidates: $M = (1.968 \pm 0.08)\ \mathrm{GeV}/c^2$,
- Probability of the vertex fit: prob $> 1\%$,
- Probability of the mass constraint fit: prob $> 1\%$,
- After requiring prob $> 1\%$ in the mass constraint fit, the candidate with the smallest $\chi^2$ value for each event was selected.

The $\chi^2$ and probability distributions of the vertex fit and the mass constraint fit are shown in Fig. 4.16. In the vertex fit, the probability distribution has a sharp spike close to zero, and a rise when it approaches one, in contrast to the mass constraint fit, which shows a flat distribution above the spike. The reason for this unexpected distribution of the vertex fit is under investigation. The cut on probability was applied to suppress the combinatorial background. Here the criteria is to get rid off the sharp peak close to zero, which implies the fitting object is far from the aimed target, and should be rejected.

Fig. 4.17 shows the mass distribution of the $D_s^-$ candidates for various step of the reconstruction: all candidates before any fits (orange), after vertex fit (green), and after a further mass constraint fit (blue, pre-fit mass). The black arrows indicate the mass window, which includes the full signal peak. After the vertex fit, the mass resolution of the reconstructed $D_s^-$ is obtained via a polynomial-Gaussian fit, as shown in the right frame of Fig. 4.18. The mass resolution of

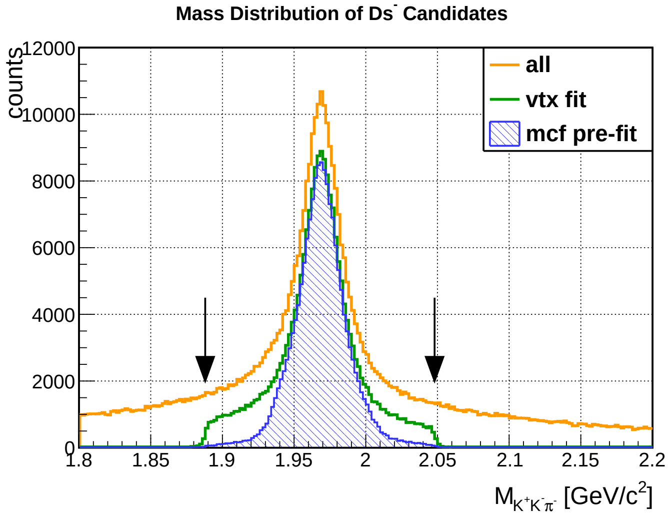

**Figure 4.17:** The mass distribution of the reconstructed $D_s^-$ candidates in tag mode A. The invariant mass distribution for all combinations of ($K^+$, $K^-$, $\pi^-$) is shown by the orange line; the distribution after the vertex fit is in green, and the striped blue area presents that of the pre-fit candidates, after the mass constraint fit. The black arrows indicate the mass window centered at the PDG listed mass value of the $D_s^-$ meson [9].

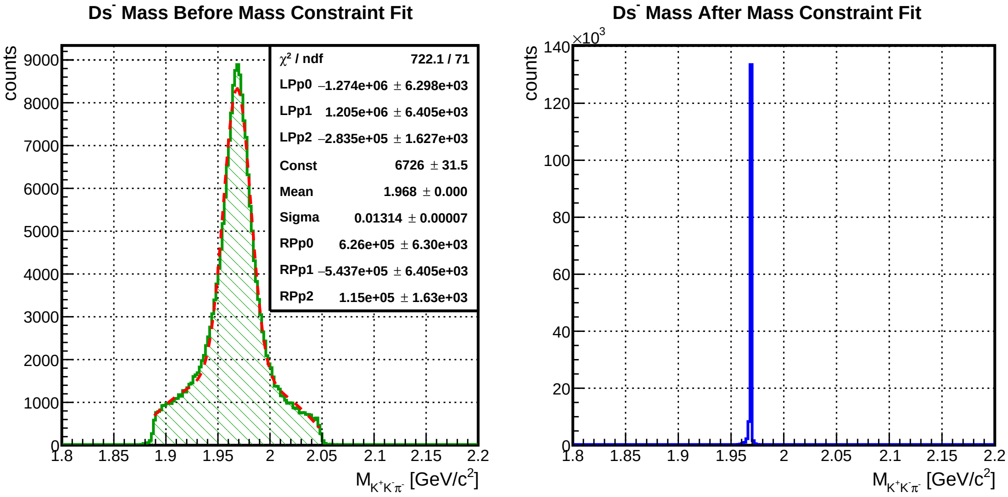

**Figure 4.18:** The invariant mass distribution of the reconstructed $\mathrm{D_s^-}$ candidates before the mass constraint fit (left) has been fit with a polynomial-Gaussian function to determine the resolution ($\sigma = 13.1\,\mathrm{MeV}/c^2$). The mass distribution after the mass constraint fit approaches a delta function (right).

the reconstructed $\mathrm{D_s^-}$ is about $13.1\,\mathrm{MeV}/c^2$ in this decay mode $\mathrm{D_s^-} \to \mathrm{K^+K^-\pi^-}$. After the mass constraint fit, the $\mathrm{D_s^-}$ mass becomes a sharp peak at the constraint $m_{PDG} = 1.968\,\mathrm{GeV}/c^2$ [9], as expected. It is not an exact delta function, due to the detector resolution.

After the vertex and mass constraint fits were performed, the best fitted candidates were selected if more than one $\mathrm{D_s^-}$ candidates was reconstructed in the event. After the probability cut was applied, only the one candidate with the smallest $\chi^2$ was selected. In this data set, approximately 15.1% of the $\mathrm{D_s^-}$ were reconstructed, and 13.8% were MC truth matched.

In Fig. 4.19, the left frame combining the vertex locations in the X and Y projections shows

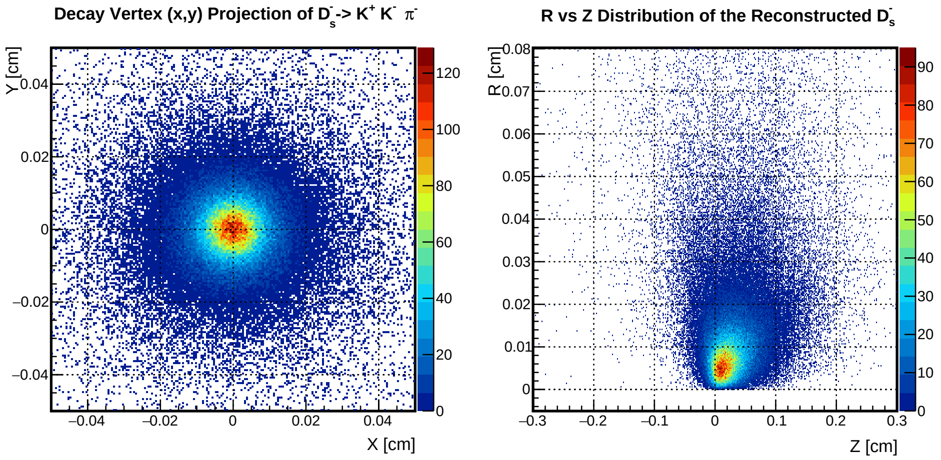

**Figure 4.19:** Decay vertex distributions of the decay $\mathrm{D_s^-} \to \mathrm{K^+K^-\pi^-}$. Left: the vertex projection on the X-Y plane. Right: the X-Y radius R versus Z distribution, where $R = \sqrt{X^2 + Y^2}$.

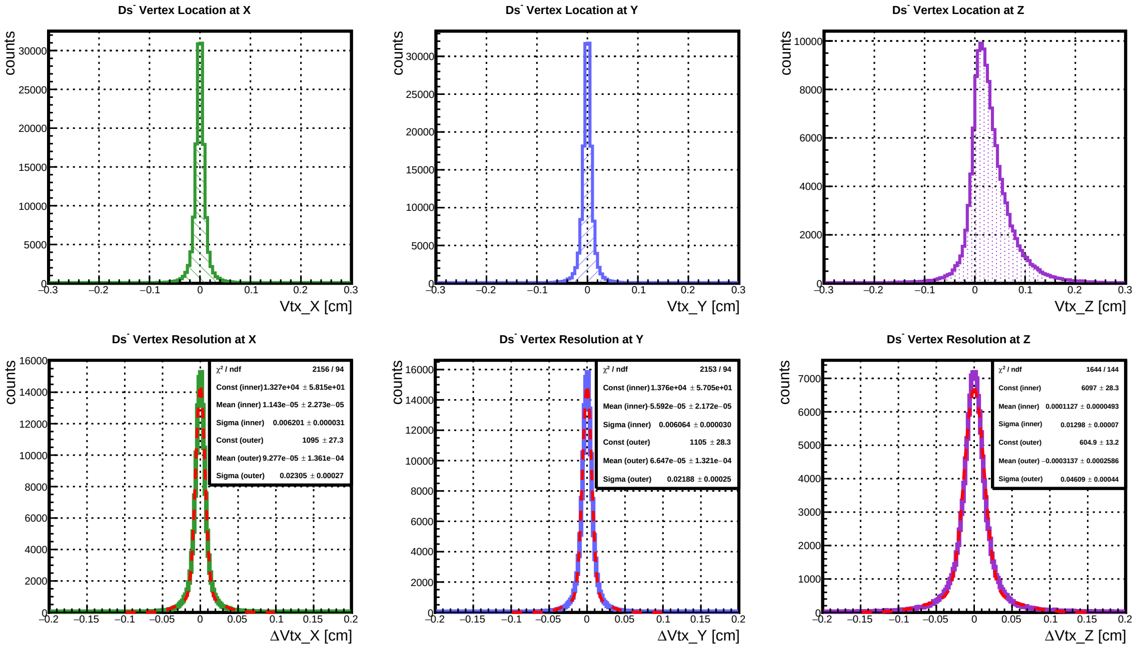

**Figure 4.20:** The vertex location distributions and resolutions of the reconstructed $D_s^-$ in $D_s^- \to K^+K^-\pi^-$. The upper three histograms are the reconstructed vertex distributions in the X, Y, Z projections, and the lower three (line) show the vertex resolutions $\Delta\text{Vtx} = \text{Vtx}_{\text{MC}} - \text{Vtx}_{\text{reco}}$, where the red dashed line presents a fit using a double-Gaussian function.

the decay points of the reconstructed $D_s^-$ normal to the beam direction, where the peak is symmetric and close to the center. The right frame shows the R-Z distribution of the $D_s^-$ decay vertex. In this figure the forward shift of the vertex location due to the finite life time of the $D_s$ meson is clearly visible. The $D_s^-$ vertex location distributions and resolutions are shown in Fig. 4.20. The vertex distributions in the X and Y projections are similar, and the Z coordinate vertex distribution is asymmetric and skewed in the forward direction. The vertex resolutions are determined via a double-Gaussian fit. Nearly two times better resolution is found in the transverse direction than in the longitudinal. In the X and Y projections the resolutions are around 61 μm, and in Z it is about 130 μm. This difference is due to the large forward boost of the daughter particles.

In this simulation, the $\bar{p}$ beam momentum is 8 GeV/$c$, which is roughly 0.7 GeV/$c$ higher than the production threshold of a $D_s^+D_s^-$ pair. Fig. 4.21 shows the momentum distribution of the reconstructed $D_s^-$, and the relative resolutions. The longitudinal momentum distribution is expected to be relative flat in the kinematically allowed region. However, an efficiency loss in the high $P_z$ region is found. In order to study the efficiency loss in detail, the decay chain with a higher and a lower beam momentum has been simulated, and the corresponding figures are shown in Appendix A and B . The relative momentum resolution is defined as $(P^{\text{reco}} - P^{\text{MC}})/P^{\text{MC}}$. A double-Gaussian fit was applied on the distribution. The sigma value of the inner Gaussian indicates the resolutions to be $\Delta P_t/P_t^{\text{MC}} = 2.2\%$ and $\Delta P_z/P_z^{\text{MC}} = 0.7\%$. In addition, the ratios of momenta between the reconstructed candidates and MC truth are shown in Fig. 4.22. It is found in both directions the ratios are peaked at $P^{\text{reco}}/P^{\text{MC}} = 1$ as expected. Comparing the

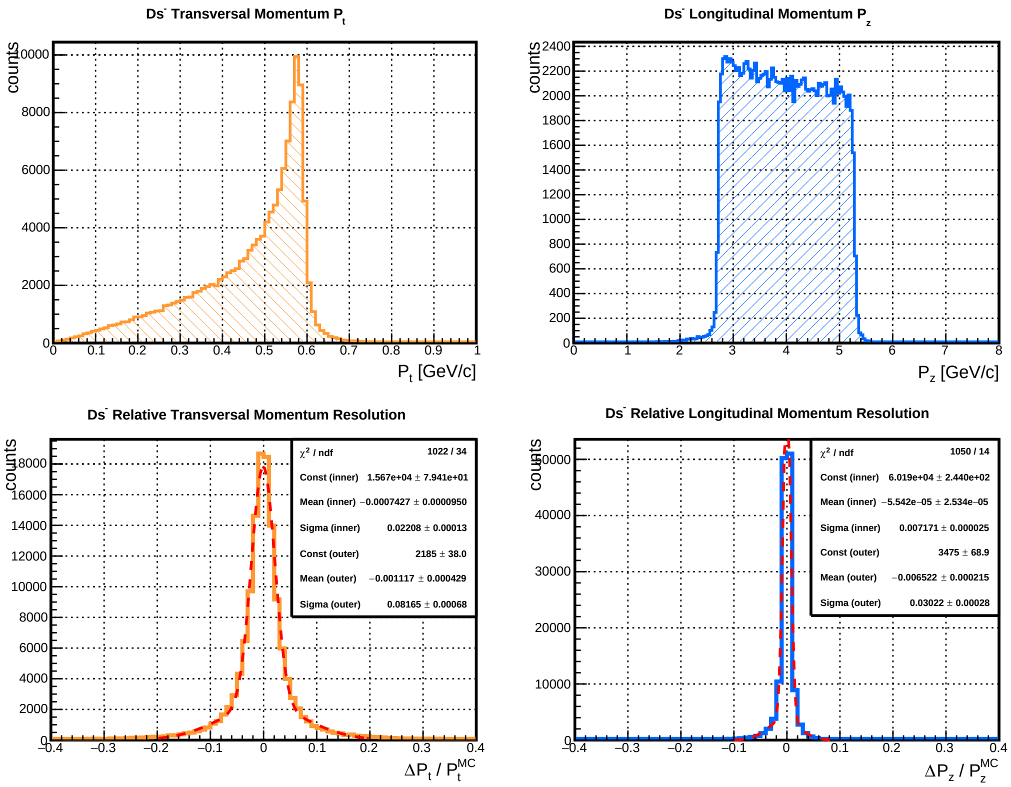

**Figure 4.21:** The reconstructed $D_s^-$ momentum distributions in the decay of $D_s^- \to K^+K^-\pi^-$. Transversal (orange) and longitudinal (blue) momentum distributions are shown. The relative resolutions are shown in the lower frame: the red dashed lines present double-Gaussian fits.

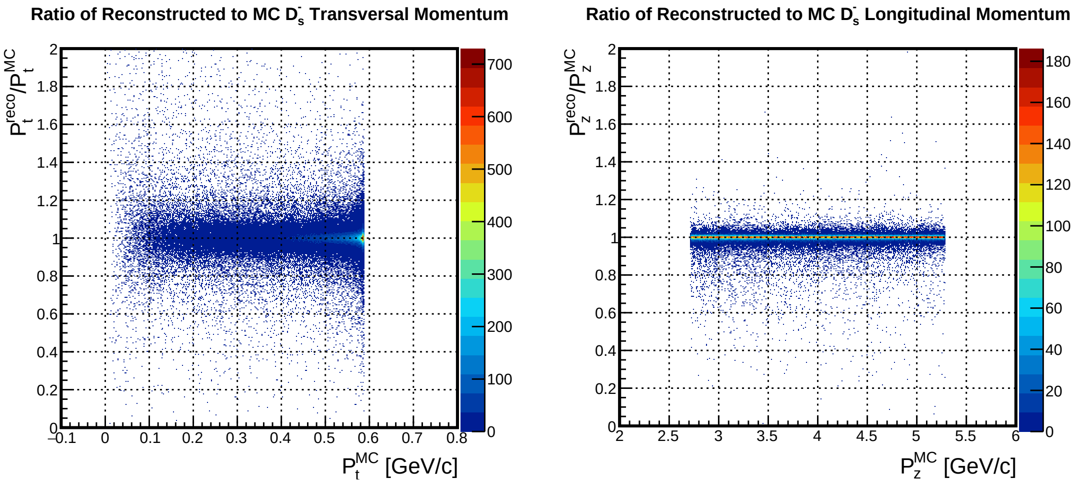

**Figure 4.22:** Ratio of the reconstructed to MC momentum of the $D_s^-$ in tag mode A. Left is the ratio as a function of the transversal momentum, and right is the ratio as a function of the longitudinal momentum.

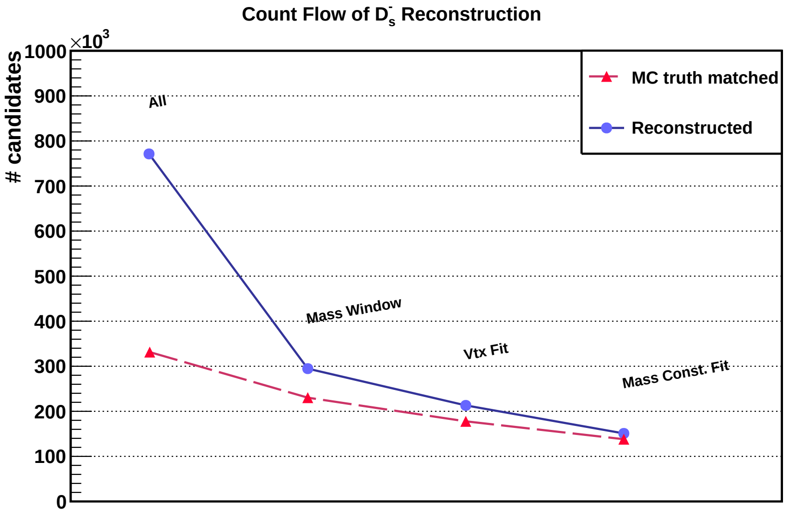

**Figure 4.23:** Count flow of $D_s^-$ reconstruction in the decay $D_s^- \to K^+K^-\pi^-$. The data points follow the order of the reconstruction procedure from left to right. Blue: the number of reconstructed candidates. Red: the number of MC truth matched candidates.

symmetric distribution for the transversal momentum, the longitudinal momentum of the $D_s^-$ is more often reconstructed to be lower than the truth $P_z^{MC}$.

**Table 4.4:** Summary of the $D_s^-$ reconstruction results for the decay $D_s^- \to K^+K^-\pi^-$.

| Reco eff. | MCT eff. | $\sigma_{mass}$ | $\sigma_{vtx}$ [μm] | | | $\sigma_P/P$ | |
|---|---|---|---|---|---|---|---|
| | | [MeV/$c^2$] | $X$ | $Y$ | $Z$ | $P_t$ | $P_z$ |
| 15.1% | 13.8% | 13.1 | 62 | 61 | 130 | 2.2% | 0.7% |

Fig. 4.23 shows the count flow in the $D_s^-$ reconstruction process, where every step is labeled. The Y-axis indicates the number of candidates found in the total simulated data set of one million events. The count rate of the reconstructed $D_s^-$ is found to be getting closer and closer to that of the MC truth matched with each reconstruction step. The number of the MC truth matched candidates drops more slowly than that of the reconstructed. It implies the combinatorial background has been effectively rejected after the reconstruction chain. The reconstruction efficiency and resolutions of the $D_s^-$ are summarized in Table 4.4.

**Background Events** In order to estimate the background contamination, 100 million background events were simulated by DPM generator with a $\bar{p}$ beam of 8 GeV/$c$. Except the beam momentum, all other settings are the same as in Table 4.3. The reconstruction of the background events was based on the same strategy as that for signal events (see Fig. 4.14).

The probability distribution of the vertex and mass constraint fits have an unexpected rise toward one, similar to the signal reconstruction (in Fig. 4.16). However, the problem is not

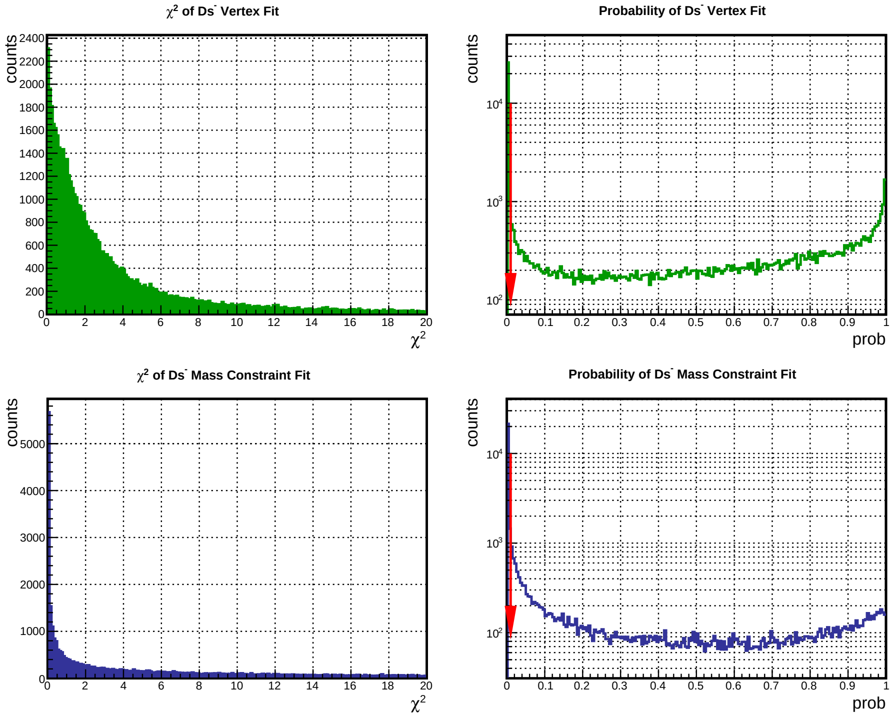

**Figure 4.24:** The $\chi^2$ (left) and probability (right; log scale) distributions for the $D_s^-$ vertex fit (top row) and mass constraint fit (bottom row) in the background study of tag mode A. The rejected candidates have probabilities lower than 1% (red arrows).

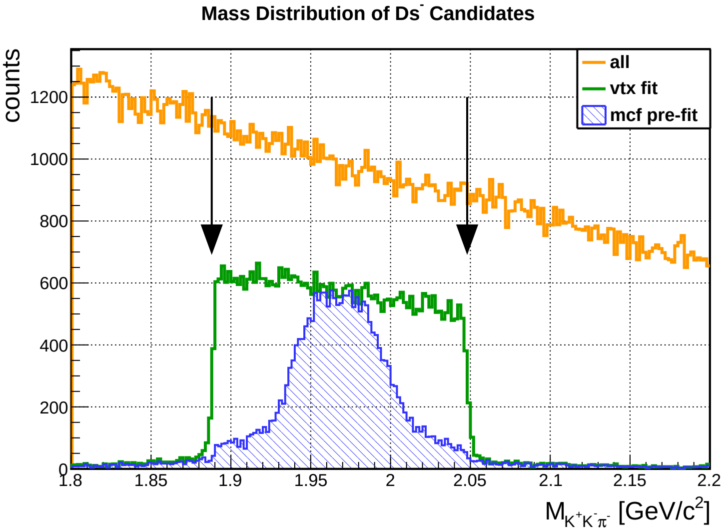

**Figure 4.25:** The mass distribution of the reconstructed $D_s^-$ candidates in the background study of tag mode A. Orange: the invariant mass distributions of all candidates. Green: the distribution after the vertex fit. Blue: the pre-fit mass distribution of the candidates after the mass constraint fit. The black arrows indicate the mass window.

seen in the mass constraint fit for the signal but exists here. A cut of prob > 1% was applied. The mass distribution is shown in Fig. 4.25. As expected, no peak structure can been seen without any cut, as shown by the orange line. This is because of the low branching ratio of $D_s^- \to K^+K^-\pi^-$. More than one third of the candidates inside the mass window are rejected due to the vertex fit. The width of the mass window is the same as that used in reconstructing the signal events, i.e. 160 MeV/$c^2$ centered at the PDG mass of the $D_s^-$ meson.

### 4.4.2 Reconstruction of $\pi^0 \to \gamma\gamma$

The reconstruction of the $\pi^0$ meson was performed by combining two photons. As shown in the first plot of Fig. 4.26, the mean multiplicity of photon candidates is about 16 photons per event, leading to a huge combinatorial background in the $\pi^0$ invariant mass distribution. In the raw signal data set, a lot of low energy photons are caused by split-offs, and some are from secondary interactions. The MC truth matched photons are shown in the third plot of Fig. 4.26, where on average multiplicity of 1.6 photons are found per event, and only roughly 32% of events have two photons. In nearly 50% of events only one or no MC truth matched photons can be found. This dramatically reduced the MC truth matched efficiency of reconstructed $\pi^0$ candidates. As discussed in Sec. 4.2.3, it is necessary to apply a photon pre-selection with a minimal energy threshold of 40 MeV to achieve the best significance. After applying the energy threshold cut, the mean multiplicity goes down to 6.5, as shown in the middle plot of Fig. 4.26.

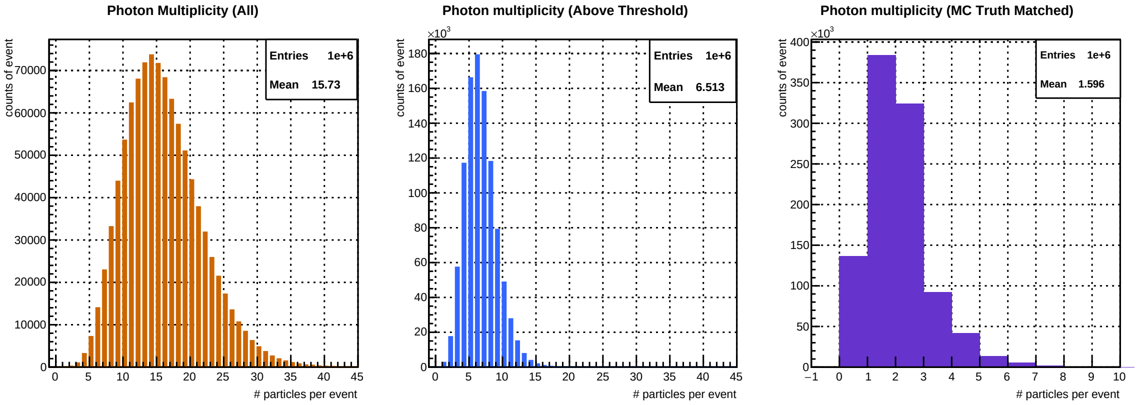

**Figure 4.26:** Photon multiplicity distributions in the decay $\pi^0 \to \gamma\gamma$ in tag mode A. Left: multiplicity distribution of raw photons without any cuts. Middle: multiplicity of photons above 40 MeV. Right: multiplicity distribution of MC truth matched photons in raw photons.

The detailed selection cuts applied in the $\pi^0$ reconstruction procedure are listed below:

- Photon energy threshold: $E_\gamma \geq 40$ MeV,
- Mass window of raw $\pi^0$ candidates: $M = (0.135 \pm 0.025)$ GeV/$c^2$,
- Probability of the mass constraint fit on $(\gamma, \gamma)$: prob > 1%.

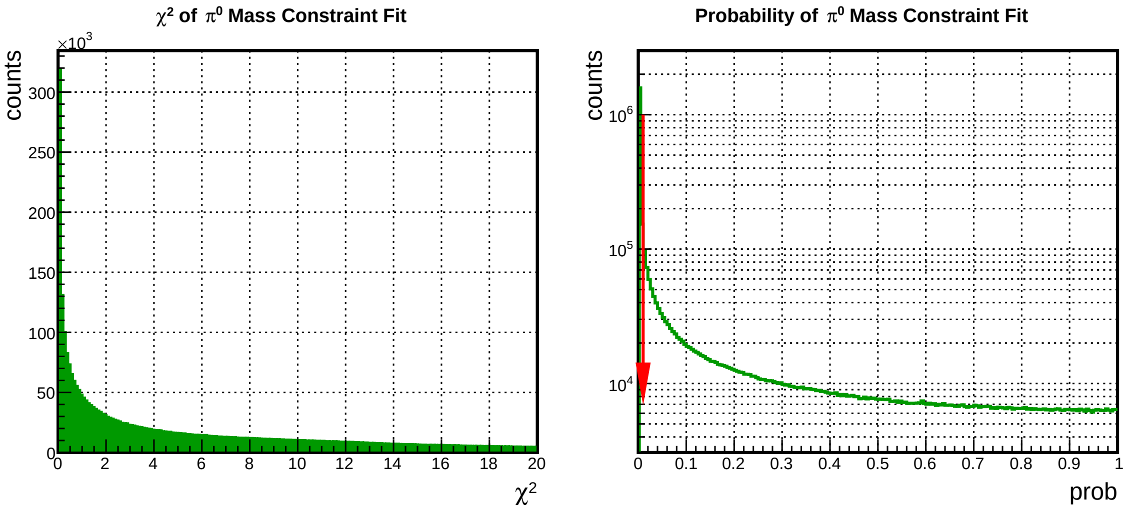

**Figure 4.27:** The $\chi^2$ (left) and probability (right) distributions of $\pi^0$ mass constraint fit in tag mode A. Candidates with probability lower than 1% (indicated by red arrow) are rejected.

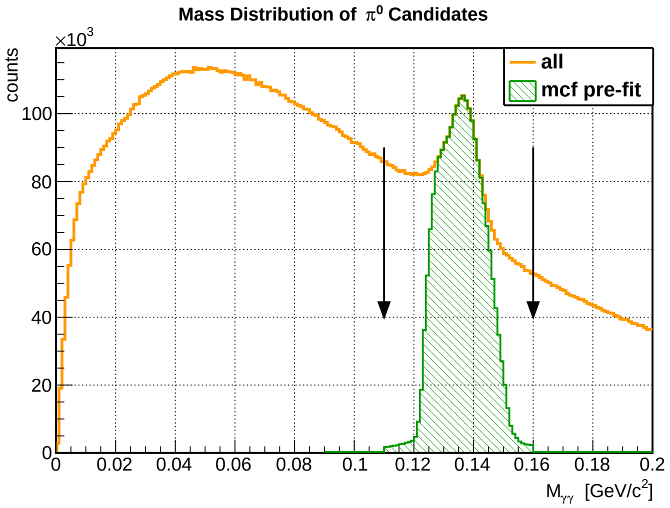

**Figure 4.28:** The two-photon invariant mass distribution for tag mode A. The distribution of all combined $(\gamma, \gamma)$ candidates is indicated by the orange line; the black arrows indicate the mass window centered at the PDG mass of the $\pi^0$ meson. The green filled histogram shows the pre-fit distribution of candidates after being accepted by the mass constraint fit.

After pre-selecting the photons, the $\pi^0$ candidates are established by combining two photons in each event. Then, the invariant mass of the two-photon system is constrained to the $\pi^0$ mass. Fig. 4.27 shows the $\chi^2$ and probability distributions of the mass constraint fit on the $\pi^0$ candidates. The candidates with low probability, i.e. prob $<$ 1%, are rejected in this fit. In Fig. 4.28, the orange line shows the mass distribution of all the $\pi^0$ candidates, and the mass window of $M = (0.135 \pm 0.025)$ GeV/$c^2$ is indicated by the black arrows. After applying the probability cut, the mass distribution of the selected candidates is shown by the green filled

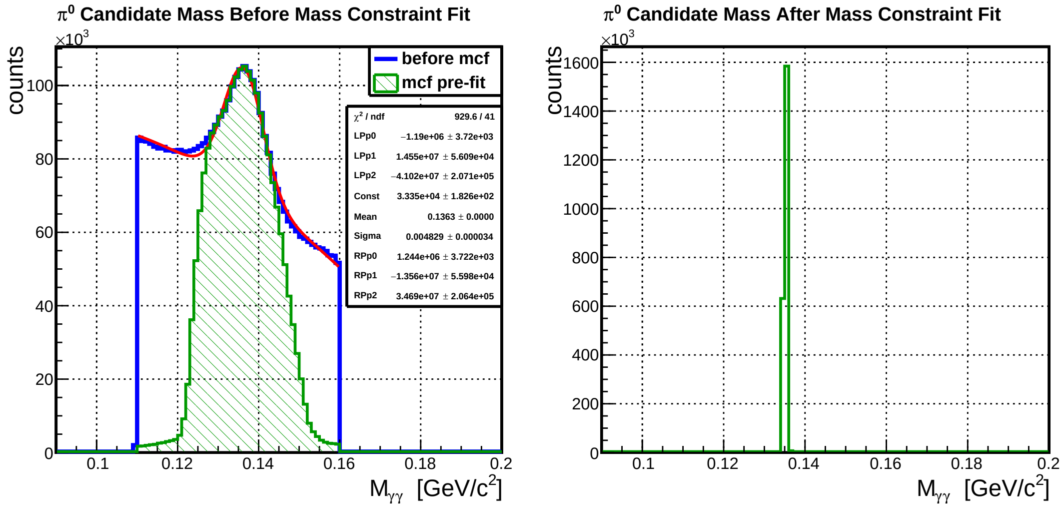

**Figure 4.29:** The two-photon invariant mass distribution of reconstructed $\pi^0$ candidates in tag mode A. Left: the distribution inside of the mass window and before the mass constraint fit; the red line is a polynomial+Gaussian fit to determine the resolution. Right: the mass distribution of the fitted candidates.

histogram (pre-fit). To extract the resolution, the mass distribution before the mass constraint fit was fit by a polynomial+Gaussian function. Fig. 4.29 shows that the resolution is $\sim$4.8 MeV/$c^2$, and after the mass constraint fit the $\pi^0$ mass distribution goes to a peak at $M = 0.135\,\text{GeV}/c^2$, as expected. In this step, it is allowed to reconstruct more than one $\pi^0$ candidate per event if they survive the probability cut, because all the $\pi^0$ candidates will be re-examined in further steps of the $\eta \to \pi^+\pi^-\pi^0$ reconstruction by the $\eta$ invariant mass constraint.

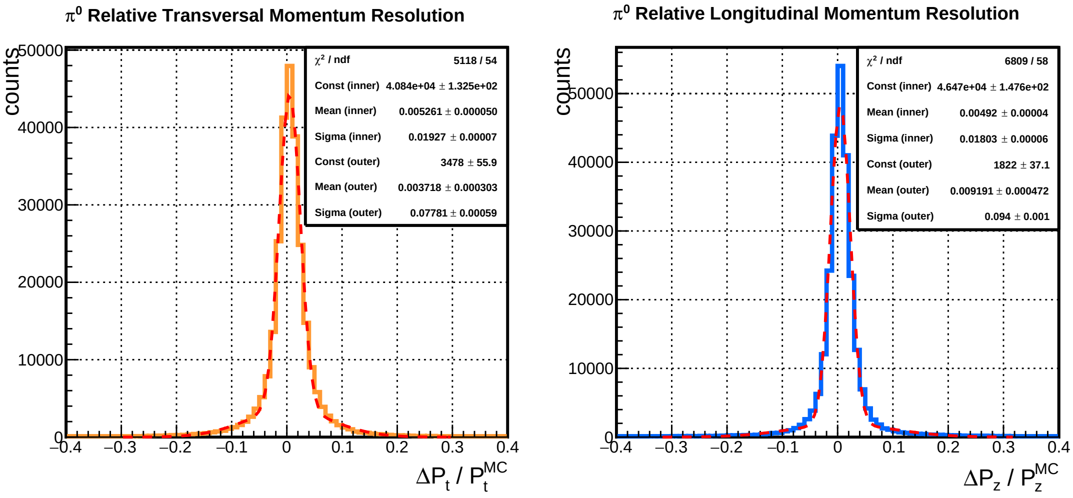

**Figure 4.30:** The relative resolution of the reconstructed $\pi^0$ transversal momentum (left, orange) and longitudinal momentum (right, blue) in tag mode A. The red dashed line shows a double-Gaussian function fit to determine the resolution.

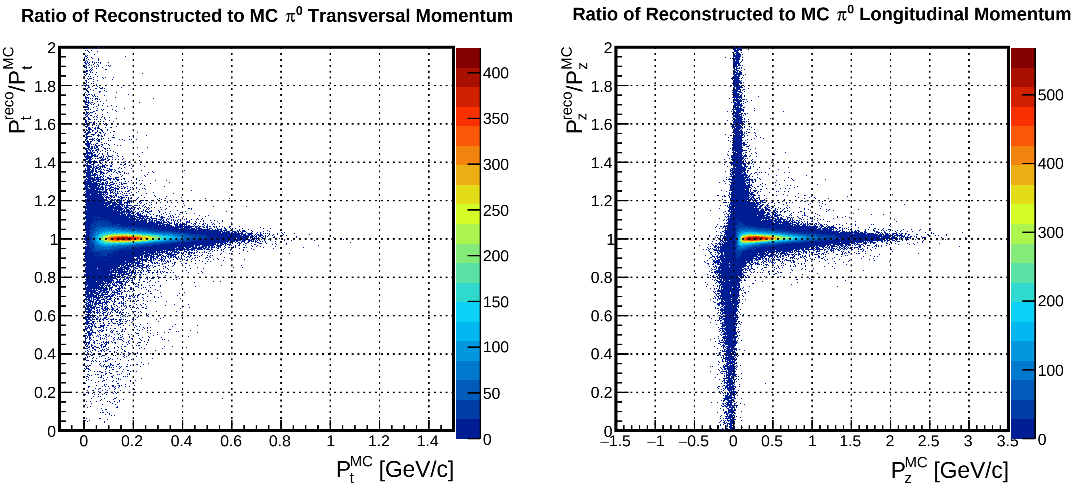

**Figure 4.31:** Ratio of the reconstructed to MC momentum of the $\pi^0$ in tag mode A. Left: the ratio as a function of the transversal momentum. Right: the ratio as a function of the longitudinal momentum.

The relative momentum resolution of the reconstructed $\pi^0$ candidates is shown in Fig. 4.30, where the relative momentum components resolution is defined as $(P^{\text{reco}} - P^{\text{MC}})/P^{\text{MC}}$. For both the transversal and longitudinal momentum a double-Gaussian fit was used to determine the resolution. It is found that $\Delta P_t/P_t^{\text{MC}} = 1.9\%$ and $\Delta P_z/P_z^{\text{MC}} = 1.8\%$. The ratio of momenta between the reconstructed candidates and the MC truth $P^{\text{reco}}/P^{\text{MC}}$ are plotted in Fig. 4.31 as a function of the MC true momenta $P^{\text{MC}}$. On both transversal and longitudinal coordinates, the ratios are peaked at around one, as expected. However, the longitudinal projection is lower than it should be if the $\pi^0$ flies backward, i.e. $P_z^{\text{MC}} < 0$.

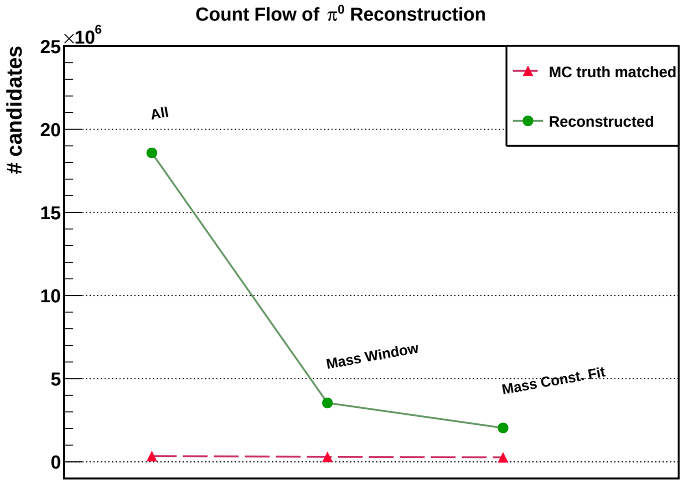

**Figure 4.32:** Count flow of the $\pi^0$ reconstruction in tag mode A. The data points follow the order of the reconstruction procedure from left to right. Green: the number of reconstructed candidates. Red: the number of MC truth matched candidates.

Fig. 4.32 shows the count flow of the $\pi^0$ reconstruction for the one million event data set. A very large number of $\pi^0$ candidates, up to more than $20 \times 10^6$, is found in the two-photon combination. This is 20 times the total number of simulated events and results from the high multiplicity of photons, i.e. 6.5 photons reconstructed on average per event above the energy threshold of 40 MeV. After the mass window selection, the count rate of candidates is dramatically reduced. About $2.2 \times 10^6$ $\pi^0$ candidates passed the mass constraint fit. However, only $2.7 \times 10^5$ counts of MC truth matched candidates remain. This leads to a large discrepancy between the count rate of reconstructed and MC truth matched $\pi^0$ candidates. Another reason for this discrepancy is all the reconstructed $\pi^0$ candidates fulfilling the probability cut in the mass constraint fit were kept for the next step of the $\eta$ reconstruction, in contrast to only the best candidate was selected per event in the $D_s^-$ reconstruciton. This MC truth matched efficiency 27.4% basically matches the rate of events having two MC photons, which is 32% as mentioned at the beginning of this section. However, it is not satisfied with roughly 10% of the reconstructed $\pi^0$ being matched with MC truth. Further improvements to the $\pi^0$ reconstruction are needed. To understand the efficiency loss of the MC truth matched photons would be a good starting point. Table 4.5 summarizes the $\pi^0$ reconstruction results.

**Table 4.5:** Summary of the reconstruction results for the $\pi^0$ meson in tag mode A.

| MCT eff. | $\sigma_{\text{mass}}$ | $\sigma_P/P$ | |
|---|---|---|---|
| | [MeV/$c^2$] | $P_t$ | $P_z$ |
| 27.4% | 4.8 | 1.9% | 1.8% |

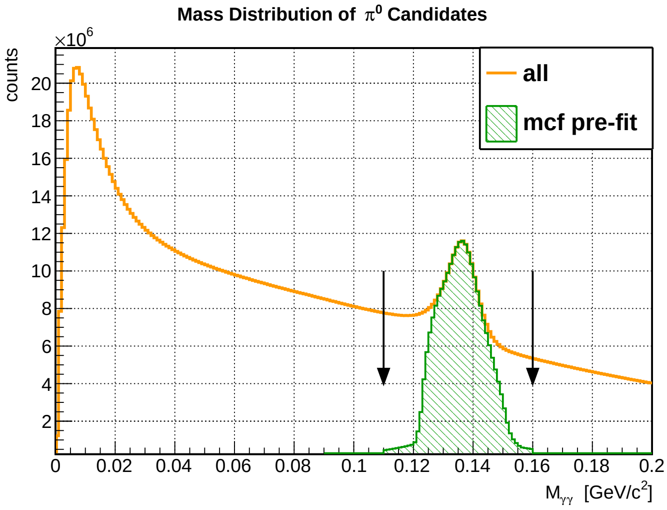

**Figure 4.33:** The invariant mass distribution of the two-photon system in the DPM events in tag mode A. Orange: the mass distribution of all combined $(\gamma, \gamma)$ candidates. The black arrows denote the mass window centered at the PDG mass of the $\pi^0$ meson. Green filled histogram: the pre-fit invariant mass distribution after being accepted by the mass constraint fit.

**Background Events** With the data set of 100 million background events simulated by the DPM generator at $p_{\bar{p}} = 8\,\text{GeV}$, the $\pi^0$ candidates were reconstructed in the same way as the signal events. The photon energy threshold was set to 40 MeV as well. The mass distribution of the $\pi^0$ candidates is shown in Fig. 4.33. Comparing the distributions of signal events (see Fig. 4.28), the first peak of the orange line is higher, and the $\pi^0$ signal is wider. The combinatorial background is also high and remains after the mass constraint fit.

### 4.4.3 Reconstruction of $\eta \to \pi^+\pi^-\pi^0$

The reconstruction of $\eta$ meson candidates was basically done in two steps: determine the vertex, and then constrain the mass of candidates, as illustrated in Fig. 4.14. In the following section, the details on reconstructing the $\eta$ meson candidates are presented.

Since the neutral particle $\pi^0$ has no tracks in the detector, the decay vertex of the $\eta$ meson is determined by the intersection of its charged daughters $\pi^+$, $\pi^-$. The method to determine the vertex is to combine the $\pi^+$ and $\pi^-$, and then apply a vertex fit on the combination, as it is done for the $D_s^-$. However, in the case of $\eta$ the obtained vertex resolution from this method was not satisfying. It might be due to the combinatorial background containing $\pi^-$ from $D_s^-$ decay, and if it is close to the $\pi^+$ then the vertex constraints of the two tracks are wrongly taken into the fit. Therefore, it is necessary to use the track information of an additional charged particle close to the $\eta$ decay vertex to discriminate the influence of $\pi^-$ from $D_s^-$. The $e^+$ in the decay of $D_s^+ \to \eta e^+ \nu_e$ was considered (see Fig. 4.34). The full width of the $\eta$ is $\Gamma = (1.30 \pm 0.07)\,\text{keV}$ [9], which corresponds to a decay length $c\tau = (0.152 \pm 0.008)\,\text{nm}$. Since the decay length of the $\eta$ is very short compared to the spatial resolution of the detector, which is on the order of $100\,\mu\text{m}$, it is reasonable to assume that the $(\pi^+, \pi^-)$ and $e^+$ come from the "same" vertex, and use the track information of the three to determine the decay vertex of the $\eta$ meson.

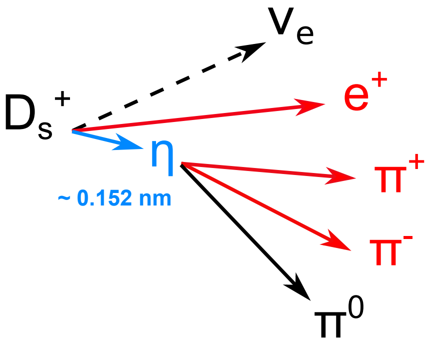

**Figure 4.34:** Illustration of $D_s^+ \to \eta e^+ \nu_e$ decay. The $\eta$ meson (in blue) has a very short decay length, therefore $\pi^+$, $\pi^-$ and $e^+$ (in red) can be assumed to come from the same vertex.

The two techniques were studied and compared with a data sample simulated at $p_{\bar{p}} = 8\,\text{GeV}$. As shown in Fig. 4.35, with the additional track information from the $e^+$ the resolution of the reconstructed $\eta$ vertex (green line) was improved by nearly a factor of two compared to that obtained from only the $(\pi^+\pi^-)$ [161] (orange line).

Since the positrons are involved in the $\eta$ reconstruction, the acceptance of the positron influences the $\eta$ reconstruction efficiency. Fig. 4.36 shows the multiplicity distribution of the $e^+$.

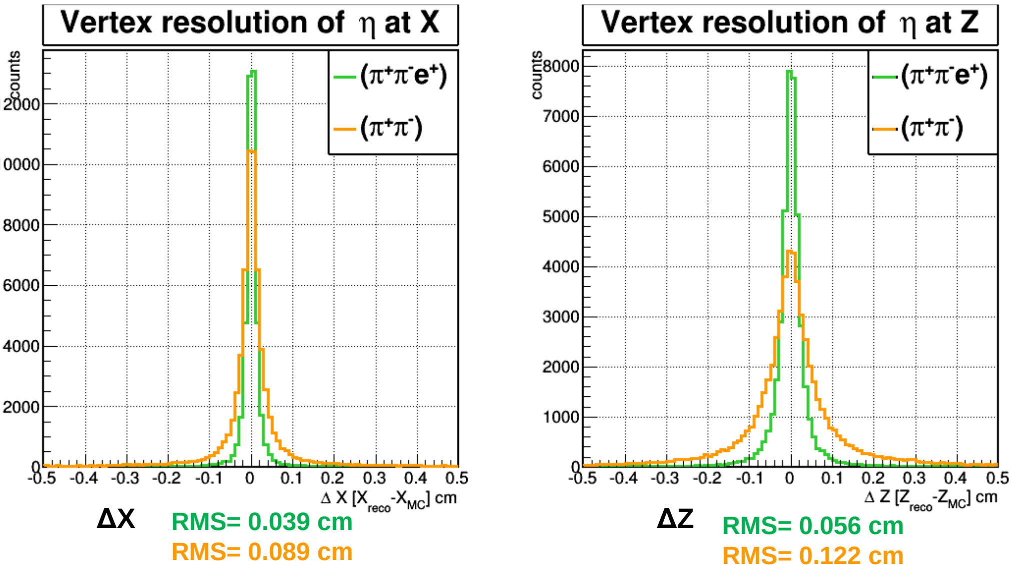

**Figure 4.35:** Vertex resolutions of the reconstructed η with two different techniques after the vertex fit. Left: the X-coordinate resolution. Right: the Z-coordinate resolution. Orange: the result obtained by combining ($\pi^+$, $\pi^-$). Green: that of the ($\pi^+$, $\pi^-$, $e^+$) combination. The Root Mean Square (RMS) of the distribution is shown below the figures for both techniques.

The mean value indicates that on average one $e^+$ is detected in each event, however in nearly 18% of events no $e^+$ can be found.

The detailed selection cuts applied in the η reconstruction procedure are listed below:

- Mass window of raw η candidates: $M = (0.548 \pm 0.025)\ \mathrm{GeV}/c^2$,

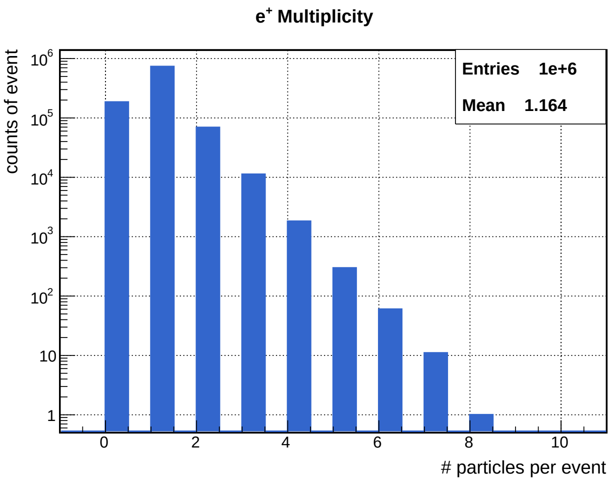

**Figure 4.36:** Multiplicity distribution of $e^+$ in the decay $D_s^+ \to \eta e^+ \nu_e$ in tag mode A.

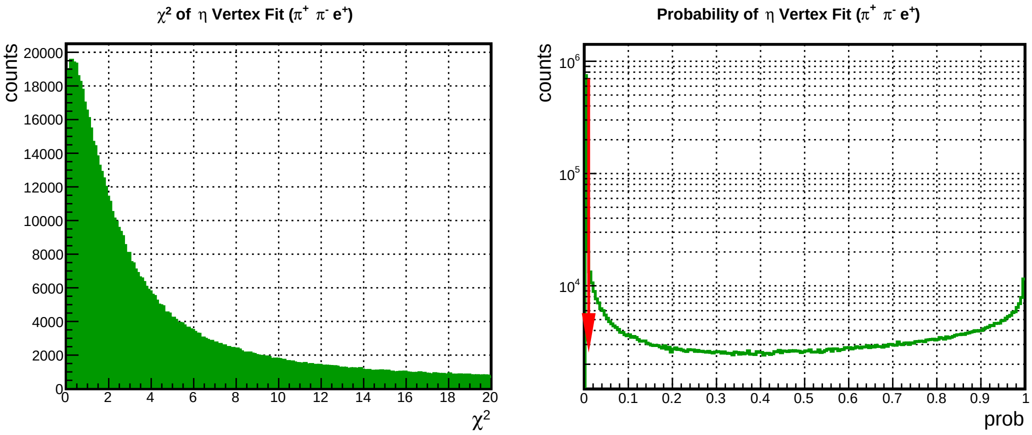

**Figure 4.37:** The $\chi^2$ (left) and probability (right) distributions of the ($e^+$, $\pi^+$, $\pi^-$) vertex fit in tag mode A. Candidates with lower than 1% (red arrow) were rejected.

- Probability of the vertex fit on ($e^+$, $\pi^+$, $\pi^-$): prob > 1%,
- In the mass constraint fit on ($\pi^+$, $\pi^-$, $\pi^0$) the candidate with the smallest $\chi^2$ value for each event was selected.

Fig. 4.37 shows the $\chi^2$ and probability distributions of the vertex fit on the combination of ($e^+$, $\pi^+$, $\pi^-$). One can notice that the probability distribution tilts upward as it approaches one, which has also been seen for the $D_s^-$ vertex fit (in Fig. 4.16). A cut on the probability was applied to suppress the combinatorial background.

After the vertex fit, the selected pair of $\pi^+$ and $\pi^-$ were combined with the reconstructed $\pi^0$ to establish the $\eta$ candidate in each event. The high combinatorial background in the $\pi^0$ spectrum effects the $\eta$ mass distribution. The invariant mass of the combination ($\pi^+$, $\pi^-$,

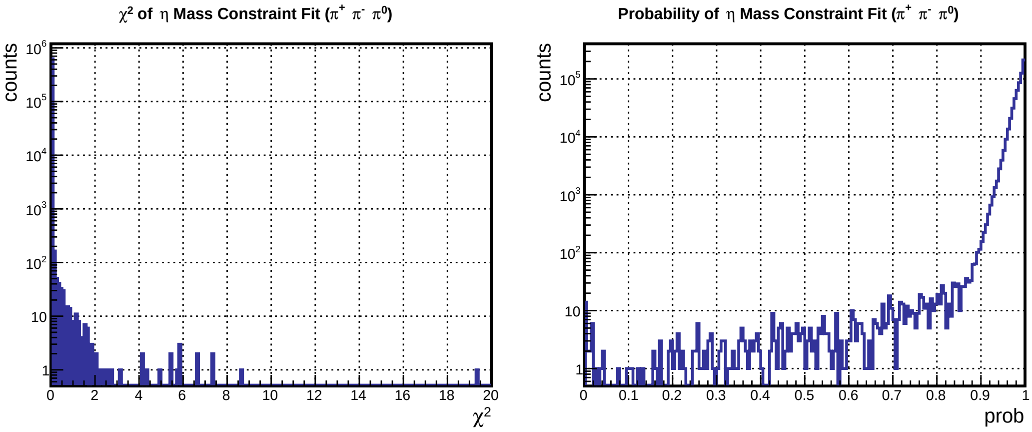

**Figure 4.38:** The $\chi^2$ (left) and probability (right) distributions of the $\eta$ mass constraint fit on ($\pi^+$ $\pi^-$ $\pi^0$) in tag mode A.

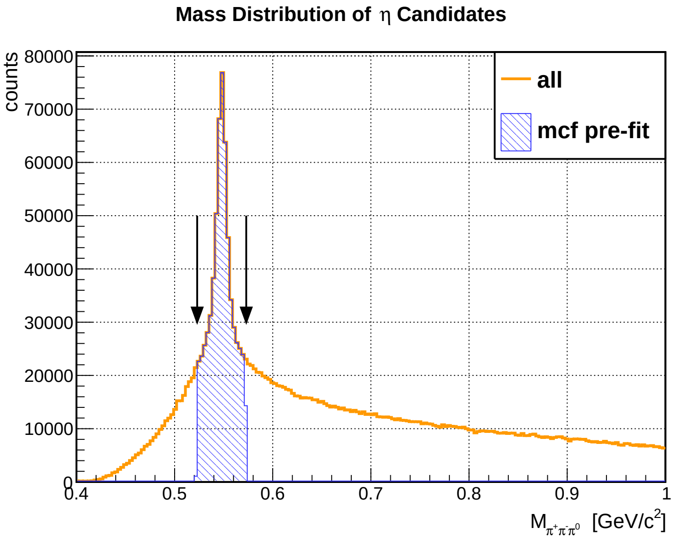

**Figure 4.39:** The invariant mass distribution of the η candidates in tag mode A. Orange line: the distributions of all candidates. The black arrows indicate the mass window centered at the PDG mass of the η meson. Blue field: the mass distribution of the pre-fit candidates.

$\pi^0$) was constrained to be the mass of η meson. Fig. 4.38 shows the distributions of $\chi^2$ and probability for the mass constraint fit. It is found that most $\chi^2$ values are extremely small, and the probabilities are skewed close to one. This problem is only seen for the η reconstruction,

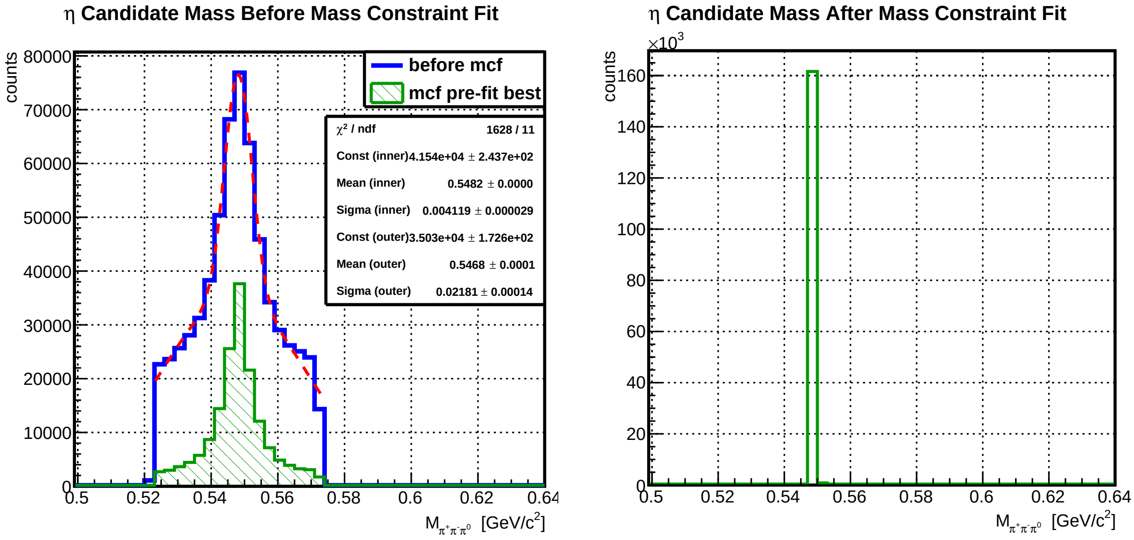

**Figure 4.40:** Mass distributions of the reconstructed η candidates in tag mode A. Left: the blue line shows the distribution before the mass constraint fit inside of the mass window, and a double-Gaussian fit to this is shown by the red dashed line; the green filled histogram indicates the pre-fit mass of the "best" η candidate. Right: the fitted mass distribution of the reconstructed η.

which includes both charged and neutral candidates in the decay tree. The reason is under investigation. It could be caused by too small elements of the covariance matrix or inappropriate smearing parameters of a sub-detector etc..

Due to the problem in the probability distribution in the $\eta$ mass constraint fit, no feasible cut can be applied on this fit as for other particles. The candidate was selected with the smallest $\chi^2$ in the mass constraint fit of the three-pion system as the "best" $\eta$ in each event. The $\eta$ mass distribution is shown in Fig. 4.39, where all the entries in the mass window are plotted as pre-fit data since no cut was applied in the fit.

The mass resolution was extracted by fitting the distribution to a double-Gaussian function (see Fig. 4.40). The sigma value of the inner Gaussian, which indicates the $\eta$ mass resolution, is 4.1 MeV/$c^2$. After the selection of $\chi^2$, the $\eta$ mass distribution is close to a delta function peaked at the PDG mass of the $\eta$ meson, as expected. For every selected $\eta$ candidate, the $\pi^+$ and $\pi^-$ daughters were used to find the "best" $e^+$ in the vertex fitted candidates ($e^+$, $\pi^+$, $\pi^-$). This ensures the correct multiplicity and correspondence of the reconstructed $\eta$ and $e^+$ for calculating the missing mass of the whole system below (see Sec. 4.4.4).

The $\eta$ vertex location distribution and resolutions are shown in Fig. 4.41. The vertex distributions in the X and Y projections are similar, and the Z coordinate is obviously boosted forward, as seen for the $D_s^-$ vertex distribution. The vertex resolutions were determined via a double-Gaussian fit as shown by the red dashed line. In the X and Y projections the resolutions are

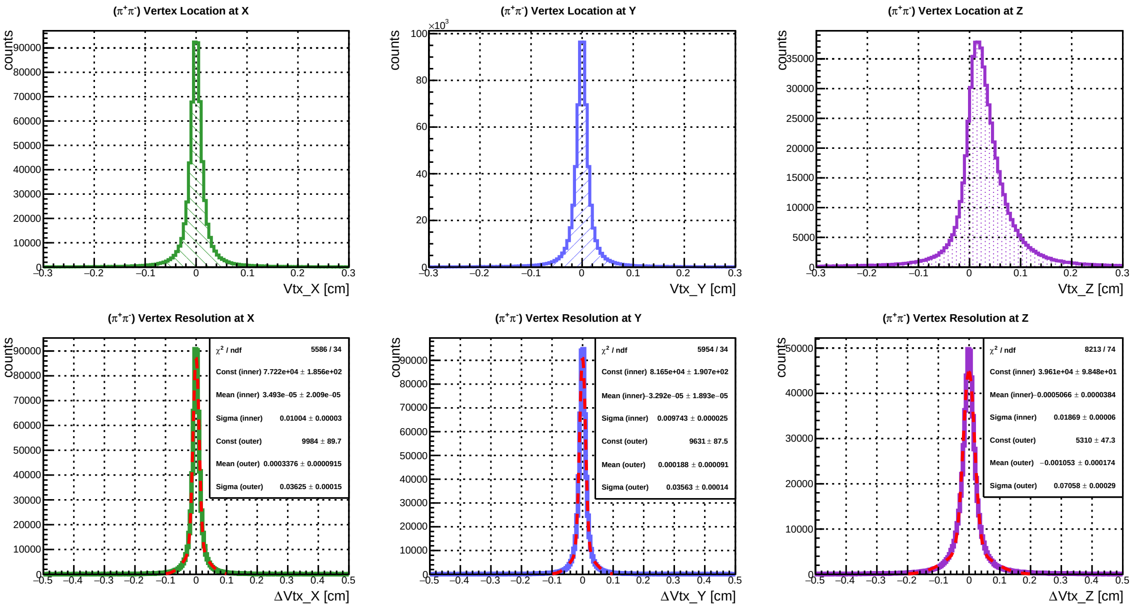

**Figure 4.41:** The vertex location distribution and resolutions of the reconstructed $\eta$ in tag mode A. The histograms in the upper frame show the reconstructed vertex distributions in the X, Y, Z projections. The lower three histograms show the vertex resolutions $\Delta\text{Vtx} = \text{Vtx}_{\text{MC}} - \text{Vtx}_{\text{reco}}$, where the red dashed lines present a fit to a double-Gaussian function. The sigma value of the inner Gaussian indicates the resolution.

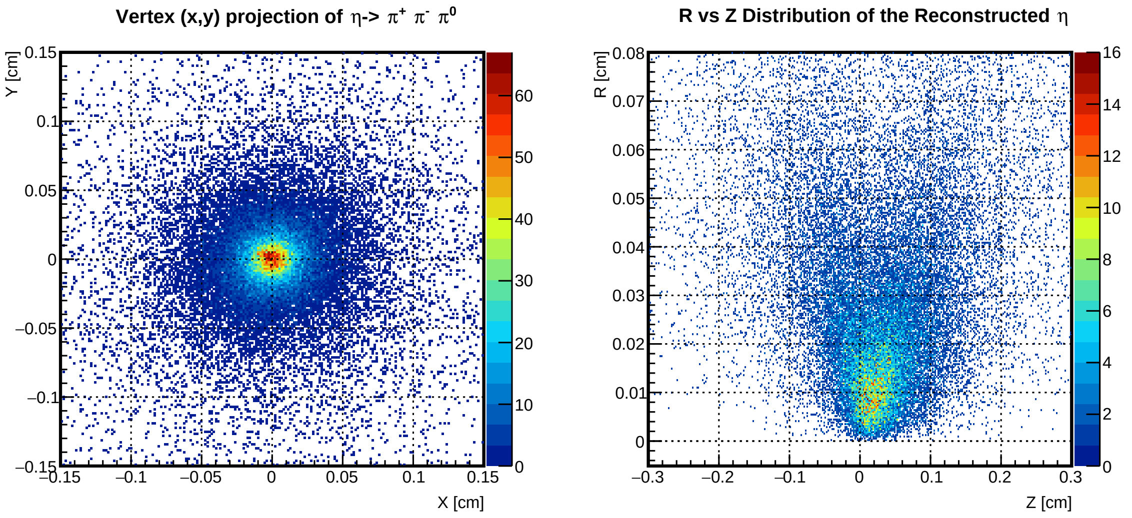

**Figure 4.42:** Decay vertex distributions of the reconstructed η candidates in tag mode A. Left: the vertex projection on the X-Y plane. Right: the radius R versus Z distribution, where $R = \sqrt{X^2 + Y^2}$.

around 100 μm, and in Z it is about 187 μm. In Fig. 4.42, the left frame shows the decay points of the reconstructed η in the X and Y projections, where the peak is symmetric around the point (0, 0). The right frame shows the η decay vertex in the R-Z projection, where $R = \sqrt{X^2 + Y^2}$. The distribution is shift to positive Z values due to the finite lifetime of the $D_s^-$ meson.

Fig. 4.43 shows the relative momentum resolution $(P^{\mathrm{reco}} - P^{\mathrm{MC}})/P^{\mathrm{MC}}$ of the reconstructed η candidates. A double-Gaussian fit indicates the resolutions to be $\Delta P_t/P_t^{\mathrm{MC}} = 1.6\%$ and

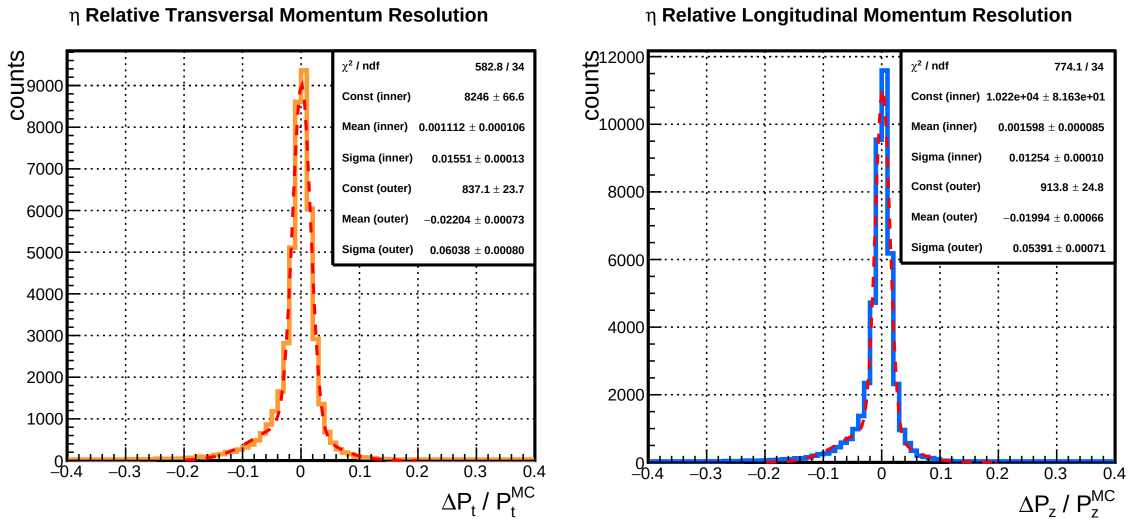

**Figure 4.43:** The relative resolutions of the reconstructed η transversal (left) and longitudinal (right) momentum in the tag mode A. The red lines present the double-Gaussian fits, and the sigma value of the inner Gaussians indicate the resolutions.

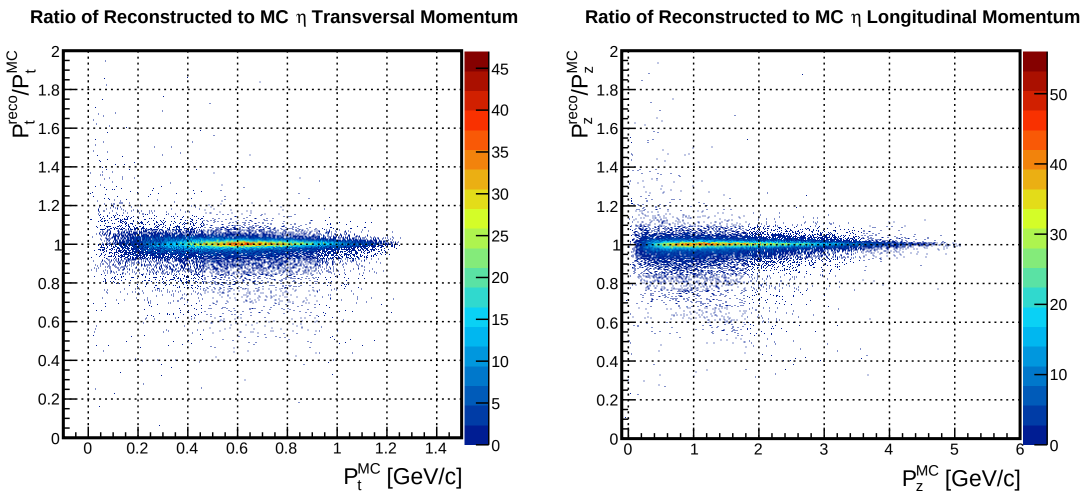

**Figure 4.44:** Ratio of the reconstructed to MC momenta of the η in tag mode A. Left is the ratio as a function of the transversal momentum, and right is as a function of the longitudinal momentum.

$\Delta P_z / P_z^{\text{MC}} = 1.3\%$. The ratios of momenta between the reconstructed candidates and MC truth are shown in Fig. 4.44. The ratios are peaked at $P^{\text{reco}}/P^{\text{MC}} = 1$, as expected.

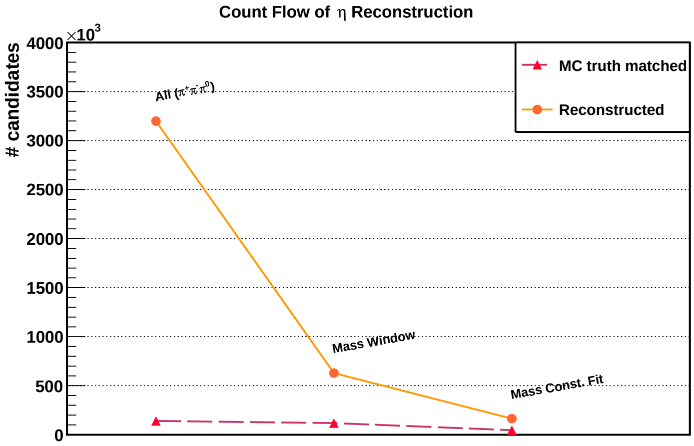

**Figure 4.45:** Count flow of the reconstructed η candidates in the decay $\eta \rightarrow \pi^+\pi^-\pi^0$ in tag mode A. The data points follow the order of the reconstruction procedure from left to right. Orange: the number of reconstructed candidates. Red: count flow for the MC truth matched candidates.

The count flow in the η reconstruction process is shown in Fig. 4.45 , where every step is labeled except the vertex fit because there is no MC truth for the virtual combination of ($e^+$, $\pi^+$, $\pi^-$). The number of MC truth matched candidates is only a few percent of the total, due to the low MC truth match efficiency but high combinatorial background of the reconstructed $\pi^0$ (see Fig. 4.32). The problem in reconstructing $\pi^0$ candidates passed into the η reconstruction at the beginning stage. After selecting candidates within the mass window, and the mass constraint fit, a considerable fraction of the combinatorial background was rejected and the number of reconstructed η mesons was getting close to that of the MC truth matched. Table 4.6

**Table 4.6:** Summary of the reconstruction results for the $\eta$ meson in tag mode A.

| Reco eff. | MCT eff. | $\sigma_{\text{mass}}$ | $\sigma_{\text{vtx}}$ [μm] | | | $\sigma_P/P$ | |
|---|---|---|---|---|---|---|---|
| | | [MeV/$c^2$] | $X$ | $Y$ | $Z$ | $P_t$ | $P_z$ |
| 16.4% | 4.6% | 4.1 | 100 | 97 | 187 | 1.6% | 1.3% |

summarizes the reconstruction results of the $\eta$ candidates in the present analysis.

**Background Events** The $\eta$ meson was reconstructed by the same strategy applied in the signal events using the same data set of $10^8$ background events used for the $D_s^-$ and $\pi^0$ analysis. The mass distribution of the reconstructed $\eta$ candidates is shown in Fig. 4.46. Only a tiny bump can be seen near the PDG mass of the $\eta$. The combinatorial background is very high.

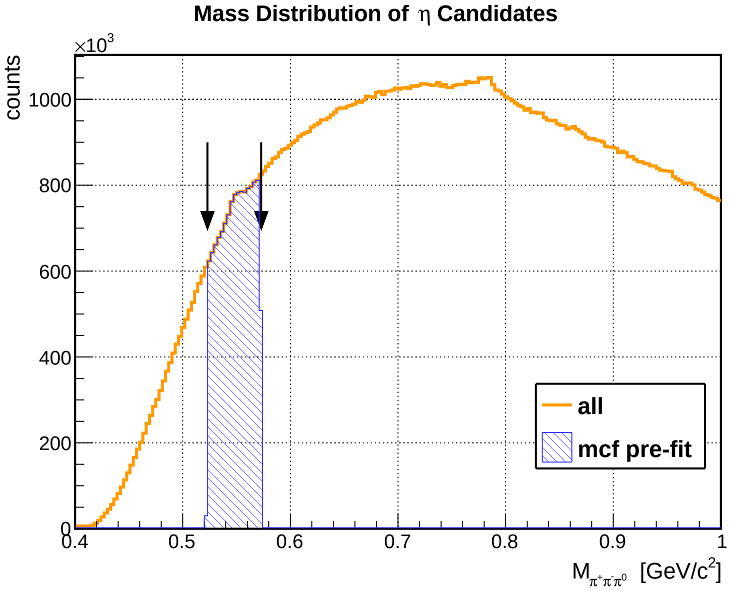

**Figure 4.46:** The $(\pi^+, \pi^-, \pi^0)$ invariant mass distribution of the reconstructed $\eta$ candidates in DPM events in tag mode A. Orange: the mass distributions of all $\eta$ candidates. The black arrows denote the mass window centered at the PDG mass of the $\eta$ meson. The blue field indicates the pre-fit mass distribution after the mass window cut.

In order to get more information to discriminate background events, the distance between the $D_s^-$ and $D_s^+$ (see Fig. 4.47) was calculated using the reconstructed $D_s^-$ vertex and the decay position of the $D_s^+$ (determined by the $\eta$—$e^+$ "vertex") as $\Delta\vec{V} = \overrightarrow{V_{D_s^+}} - \overrightarrow{V_{D_s^-}}$. The position difference $\Delta R$ versus $\Delta Z$ and the $\Delta Z$ distribution are shown in Fig. 4.48, where $\Delta R = \sqrt{\Delta V_X^2 + \Delta V_Y^2} = \sqrt{(X_{D_s^+} - X_{D_s^-})^2 + (Y_{D_s^+} - Y_{D_s^-})^2}$ and $\Delta Z = \Delta V_Z = Z_{D_s^+} - Z_{D_s^-}$.

The distance distribution between the reconstructed $D_s^-$ and $D_s^+$ candidate's vertices in the

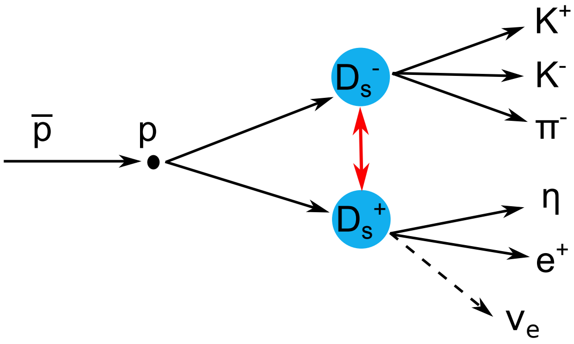

**Figure 4.47:** Illustration of the distance between the $D_s^+$ and the $D_s^-$ in tag mode A.

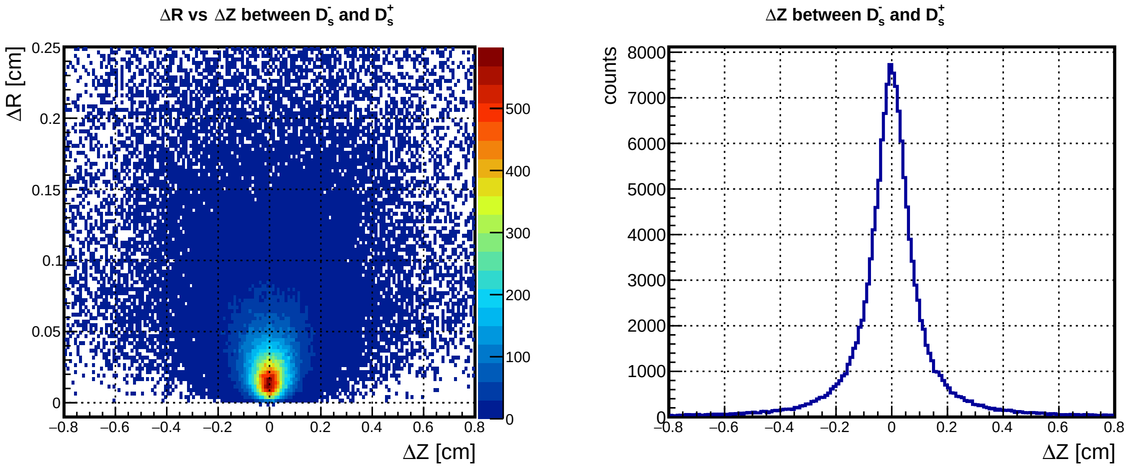

**Figure 4.48:** Distance distribution between the $D_s^+$ and the $D_s^-$ decay vertices in signal events in tag mode A. Left: distance distribution between the $D_s^+$ and the $D_s^-$ decay vertices shown with $\Delta R - \Delta Z$ correlation, where $\Delta R = \sqrt{(X_{D_s^+} - X_{D_s^-})^2 + (Y_{D_s^+} - Y_{D_s^-})^2}$ and $\Delta Z = Z_{D_s^+} - Z_{D_s^-}$. Right: projection of the left distribution onto the $\Delta Z$ axis.

DPM events is shown in Fig. 4.49. A pseudo significance defined as significance $= N_{\text{signal}}/\sqrt{N_{\text{DPM}}}$ is used to estimate the background suppression, where the $N_{\text{signal}}$ and $N_{\text{DPM}}$ represent the count number of the signal and background events, respectively. Since the relative scale factor between the number of signal and background events generated is not taken into account in this step, it is called the *pseudo significance*. Fig. 4.50 shows the pseudo significance distribution as a function of the half width of the cut applied to $\Delta Z$, for example, a cut of 0.6 cm means that candidates with $|\Delta Z| \leq 0.6$ cm are selected to calculate the significance. From this distribution, one can find that the cut of $|\Delta Z| \leq 0.1$ cm produces the highest significance. The missing scale factor mentioned above will not change this optimal cut value. Since only one event of $(e^+\nu_e)$ was reconstructed after all fits in the background data set of 100 million DPM events (will be shown later in Sec. 4.4.4), the statistics is not sufficient to study the performance of the background suppression in detail for the semileptonic form factor measurement. We leave this issue for future study.

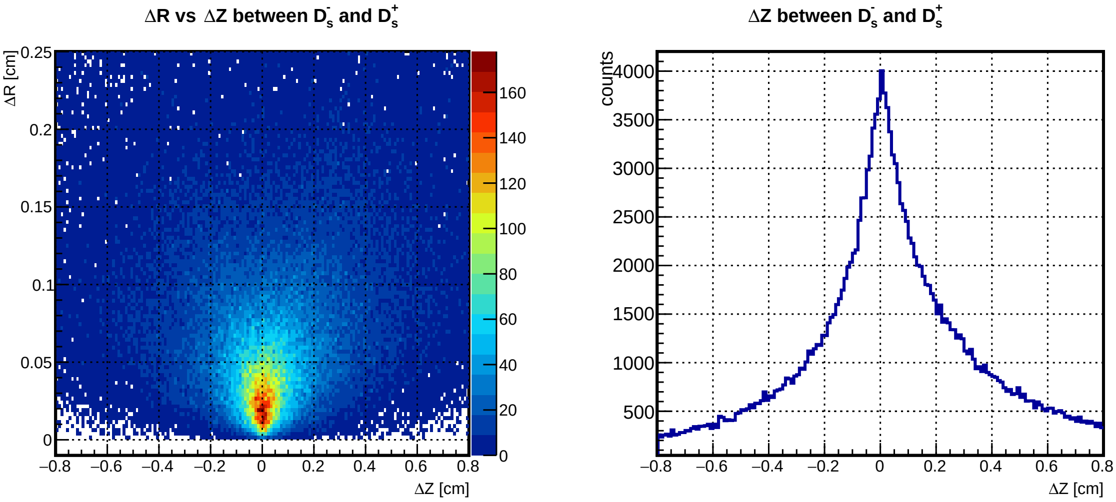

**Figure 4.49:** Distribution of Fig. 4.48 for the DPM event data set.

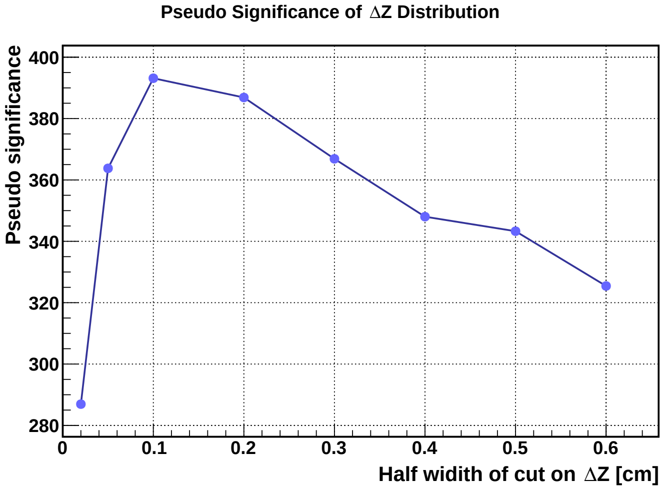

**Figure 4.50:** Pseudo significance of the $\Delta Z$ distribution as a function of the maximum half width in tag mode A.

### 4.4.4 Reconstruction of Positron-Neutrino System

After reconstructing the intermediate particles, i.e. $D_s^-$ (in Sec. 4.4.1) and $\eta$ (in Sec. 4.4.3), and selecting the positron from the $\eta$, a four-momentum conservation can be entered to calculate the mass squared of the undetected neutrino $M^2(\nu_e)$ and the four-momentum transfer squared $q^2$ in the semileptonic decay $D_s^+ \to \eta e^+ \nu_e$ as

$$M^2(\nu_e) = \left(E_{\bar{p}p} - E_{D_s^-} - E_\eta - E_{e^+}\right)^2 - \left|\mathbf{p}_{\bar{p}p} - \mathbf{p}_{D_s^-} - \mathbf{p}_\eta - \mathbf{p}_{e^+}\right|^2, \tag{4.3}$$

$$q^2 \equiv M^2(\nu_e e^+) = \left(E_{\bar{p}p} - E_{D_s^-} - E_\eta\right)^2 - \left|\mathbf{p}_{\bar{p}p} - \mathbf{p}_{D_s^-} - \mathbf{p}_\eta\right|^2, \tag{4.4}$$

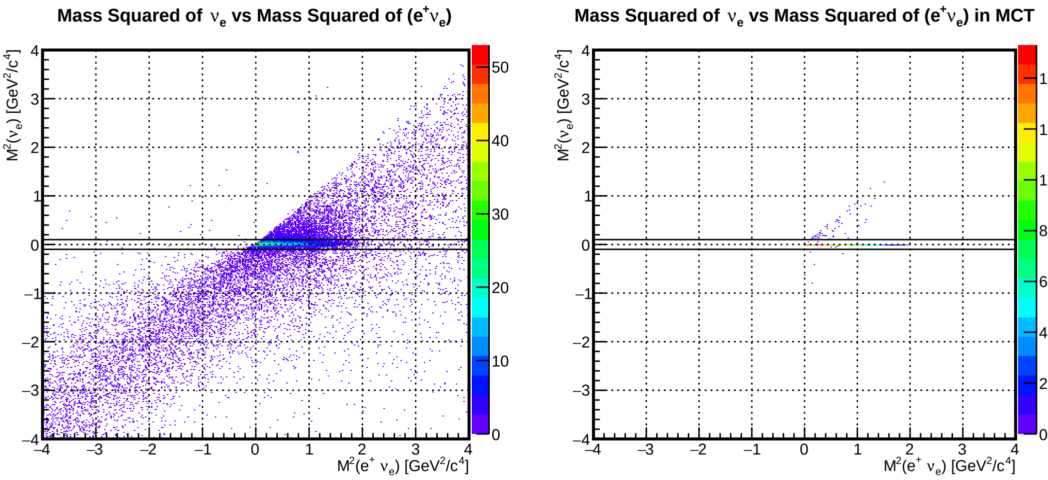

**Figure 4.51:** Distribution of the mass squared of the $\nu_e$ candidates (Eq. 4.3) versus the invariant mass squared of the (e$^+\nu_e$) system (Eq. 4.4). Left: the result obtained from the reconstructed particles. Right: that of the MC truth matched particles. The black solid lines indicates the selection window for the $\nu_e$: $|M^2(\nu_e)| \leq 0.1$ GeV$^2/c^4$.

where $E_{\bar{p}p}(\mathbf{p}_{\bar{p}p})$ is the energy (three-momentum) of the initial anti-proton beam and proton target system, and the same definitions for other particles. It is important to ensure that the multiplicity of the reconstructed D$_s^-$, η and e$^+$ is exactly one for this calculation of every event in the data set. This ensures the correctness of the kinematics correlation between these particles, and allows to study the event-wise precision via calculating the above equations with the MC truth matched D$_s^-$, η and e$^+$ candidates.

Fig. 4.51 shows the correlation between the $\nu_e$ mass squared and the invariant mass squared of the lepton-neutrino system. The right figure is obtained from calculating Eq. 4.3 and Eq. 4.4 with the reconstructed D$_s^-$, η and e$^+$. For every event, the MC truth matched D$_s^-$, η and e$^+$ were used to get the result in the left figure, where a few entries seen outside the $|M^2(\nu_e)|$ window. And they dominate in $M^2(\nu_e) > 0$. This is due to the limited resolution of low momentum particles, e.g. D$_s^-$, η and e$^+$, which spoils the kinematics for calculating $M^2(\nu_e)$ in Eq. 4.3. The so called MC truth matched $\nu_e$ is different with the MC true $\nu_e$ in concept. Comparing the two figures, one can identify a window to suppress the combinatorial background in the reconstructed data. The window of $|M^2(\nu_e)| \leq 0.1$ GeV$^2/c^4$ was chosen, since ∼ 99.13% of the MC truth matched $\nu_e$ events were found in this region.

The mass-squared distributions of the reconstructed $\nu_e$ and the lepton-neutrino system are shown in Fig. 4.52. It is found that the mass squared distribution of $\nu_e$ is peaked close to zero due to the extremely small mass of the $\nu_e$, as shown in the left frame. The window selects $\nu_e$ candidates in the peak (yellow), and suppresses the major combinatorial background in the (e$^+\nu_e$) system, as shown in the right frame. One notices that a small fraction of the $M^2(\nu_e e^+)$ spectrum is in the negative region, which is due to the limited detector resolution for the low momentum particles. In this case, a selection of $M^2(\nu_e e^+) > 0$ is applied to reject the unphysical events.

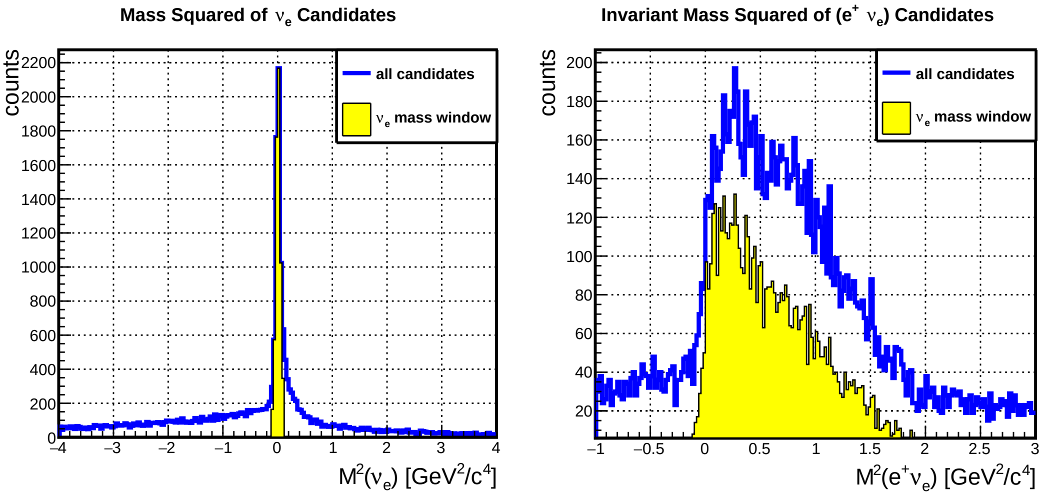

**Figure 4.52:** Left: mass squared distribution of $\nu_e$ candidates. Right: invariant mass squared distribution of the lepton-neutrino system. In both figures, the blue line shows the distributions of all candidates; the yellow solid histogram indicates the distribution after applying a cut of $|M^2(\nu_e)| \leq 0.1$ GeV$^2/c^4$.

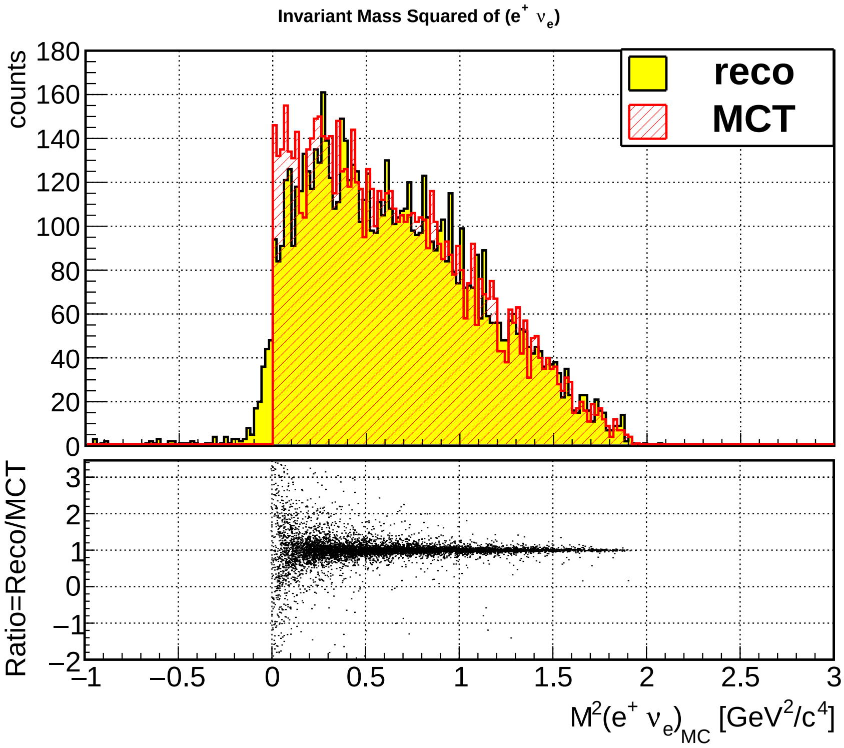

**Figure 4.53:** The event-wise precision of the reconstructed $M^2(\nu_e e^+)$. Yellow: the reconstructed result with a cut on $|M^2(\nu_e)| \leq 0.1$ GeV$^2/c^4$. Red: the $M^2(\nu_e e^+)$ distribution calculated with the MC truth matched particles. Black dots: the event-wise ratio of the $M^2(\nu_e e^+)$ values between the reconstructed and MC truth matched data.

The physical range of the $q^2$ distribution is $0 \leq q^2 \leq (M_{D_s} - M_\eta)^2$. As shown in the Dalitz plot (see Fig. 4.5), the physical range of $M^2(\nu_e e^+)$ is $0 \leq M^2(\nu_e e^+) \leq 2.02\ \mathrm{GeV}^2/c^4$. This Dalitz plot is the pure MC truth simulated with the ISGW2 [156] decay model (see Sec. 4.1.2) without accounting for the finite detector resolution. The reconstructed $M^2(\nu_e e^+)$ distribution is shown as the yellow area in the right frame of Fig. 4.52, and is consistent with that of the Dalitz plot projection (lower frame in Fig. 4.5).

The event-wise precision of the reconstructed $M^2(\nu_e e^+)$ value was studied. Fig. 4.53 shows the reconstructed $M^2(e^+ \nu_e)$ distribution with a comparison of the event-wise MC truth matched data. It is shown that a good agreement with the MC data in the large momentum transfer region $M^2(\nu_e e^+) > 0.2\ \mathrm{GeV}^2/c^4$ can be achieved in the reconstruction.

Fig. 4.54 shows the count flow of reconstructing the $\nu_e e^+$ system for one million events. After all selections, the reconstruction efficiency is 0.6% in tag mode A, which is consistent with the product of the MC truth matched efficiencies of the reconstructed $D_s^-$ (13.8%) and $\eta$ (4.6%). In order to improve the statistics for measuring the form factor, another tag mode for the $D_s^-$ meson, i.e. $D_s^- \to \pi^+\pi^-\pi^-$, has been considered. The reconstruction result with this tag mode is presented in Sec. 4.5.

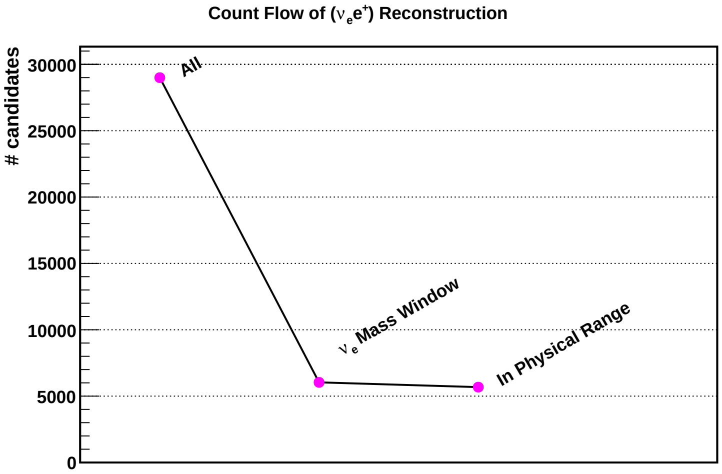

**Figure 4.54:** Count flow of reconstructing $(\nu_e e^+)$ in tag mode A. The data points follow the order of the reconstruction procedure from left to right. The mass window cut is $|M^2_{\nu_e}| \leq 0.1\ \mathrm{GeV}^2/c^4$, and the physical range cut is $0 \leq M^2(\nu_e e^+) \leq 2.02\ \mathrm{GeV}^2/c^4$.

**Background Events** 100 million events of $\bar{p}p \to$ everything contains about 50 events of $\bar{p}p \to D_s^+ D_s^-$, assuming the cross section is 20 nb [94]. Consider that the branching ratio of $D_s^+ \to \eta e^+ \nu_e$ is 2.67%, there are around two $\nu_e$ events generated. On the side of reconstruction, only one candidate of $\nu_e$ and the $(\nu_e e^+)$ system was found after all selections (as shown in Fig. 4.55). The statistics are not sufficient to quantify the background suppression. For further investigation, more computing resources will be needed to get sufficient statistics. The present ratio of the signal to background rate is $S/B \approx 1/80$.

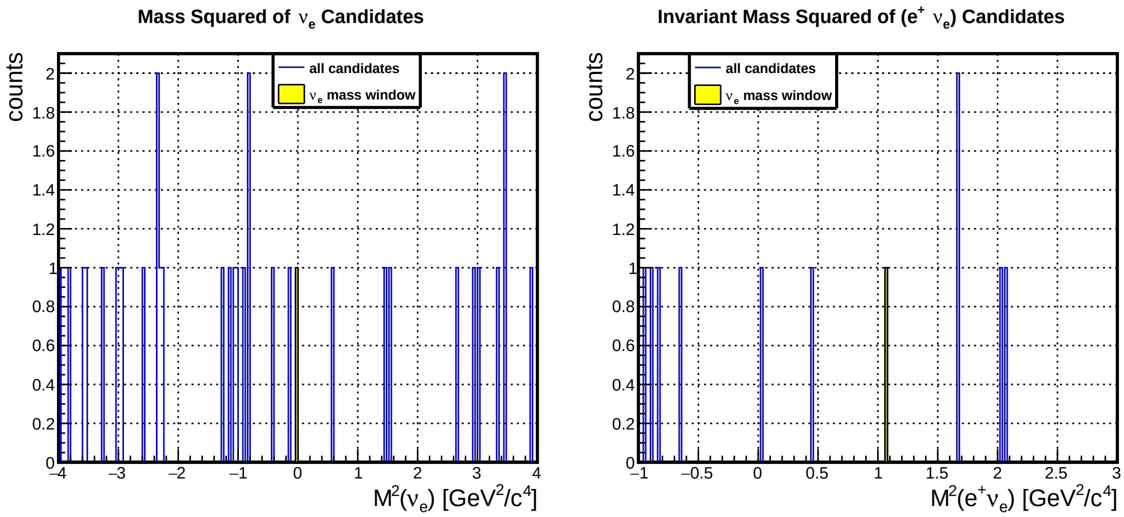

**Figure 4.55:** The mass squared distributions of the reconstructed $(\nu_e e^+)$ in DPM events in tag mode A. That of the signal events shown in Fig. 4.52. Left: mass squared of $\nu_e$ candidates. Right: invariant mass squared of the lepton-neutrino system. In both figures, the blue line shows the distributions of all candidates; the yellow area indicates the distribution with the $|M^2(\nu_e)| \leq 0.1$ GeV$^2/c^4$ selection.

## 4.5 Simulation with the $D_s^- \to \pi^+\pi^-\pi^-$ Tag

In order to increase the usable statistics of the $e^+\nu_e$ system, the decay channel $D_s^- \to \pi^+\pi^-\pi^-$ was considered as a second tag mode for the $D_s^-$ meson. This decay channel was chosen because its branching ratio is relatively high and there is no neutral daughter particle in its decay products. Since the MC truth match efficiency of neutral particles is not currently satisfactory, the decays with only charged daughters are preferred at present, despite a higher combinatorial background due to the high multiplicity of pions in this mode.

One million signal events of the decay tree (see Fig. 4.4 in Sec. 4.1.2) were simulated with the tag mode B: $D_s^- \to \pi^+\pi^-\pi^-$. The simulation settings are listed in Table 4.3. In the following, the detailed reconstruction results of an anti-proton beam of 8 GeV/$c$ are presented. Figures for $p_{\bar{p}} = 7.3, 7.7$ GeV/$c$ are shown in Appendix A and B.

### 4.5.1 Reconstruction of $D_s^- \to \pi^+\pi^-\pi^-$

The reconstruction strategy is basically the same for both tag modes (as shown in Fig. 4.14). The $D_s^-$ candidates were formed by combining three charged pions in each event. In tag mode A one $D_s^-$ candidate only combines with one other $\pi^-$ in the event. In contrast, the combinatorial background is higher in tag mode B, because the multiplicity of charged pions is higher: two $\pi^+$ and three $\pi^-$ are generated in every MC true event. It means one signal $D_s^-$ will have 11 combinatorial candidates. The situation becomes even more tough when additional charged pions are generated in secondary interactions. The multiplicity distribution of $D_s^-$ daughter particles is shown in Fig. 4.56. It is found that on average approximately two $\pi^+$ and three $\pi^-$ are reconstructed per event, and $\sim$ 13.6% of events have at least one secondary $\pi^+$ and $\sim$ 11.5% have at least one secondary $\pi^-$.

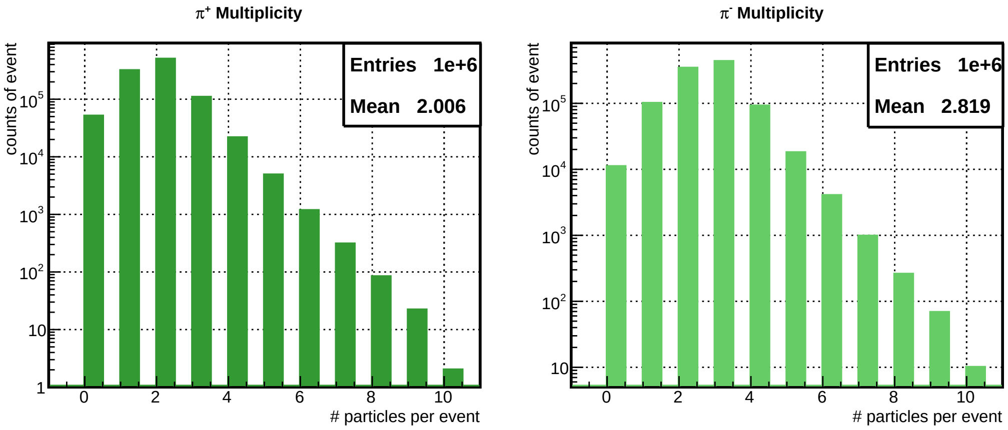

**Figure 4.56:** Multiplicity of reconstructed $\pi^+$ (left) and $\pi^-$ (right) in the complete decay tree with tag mode B.

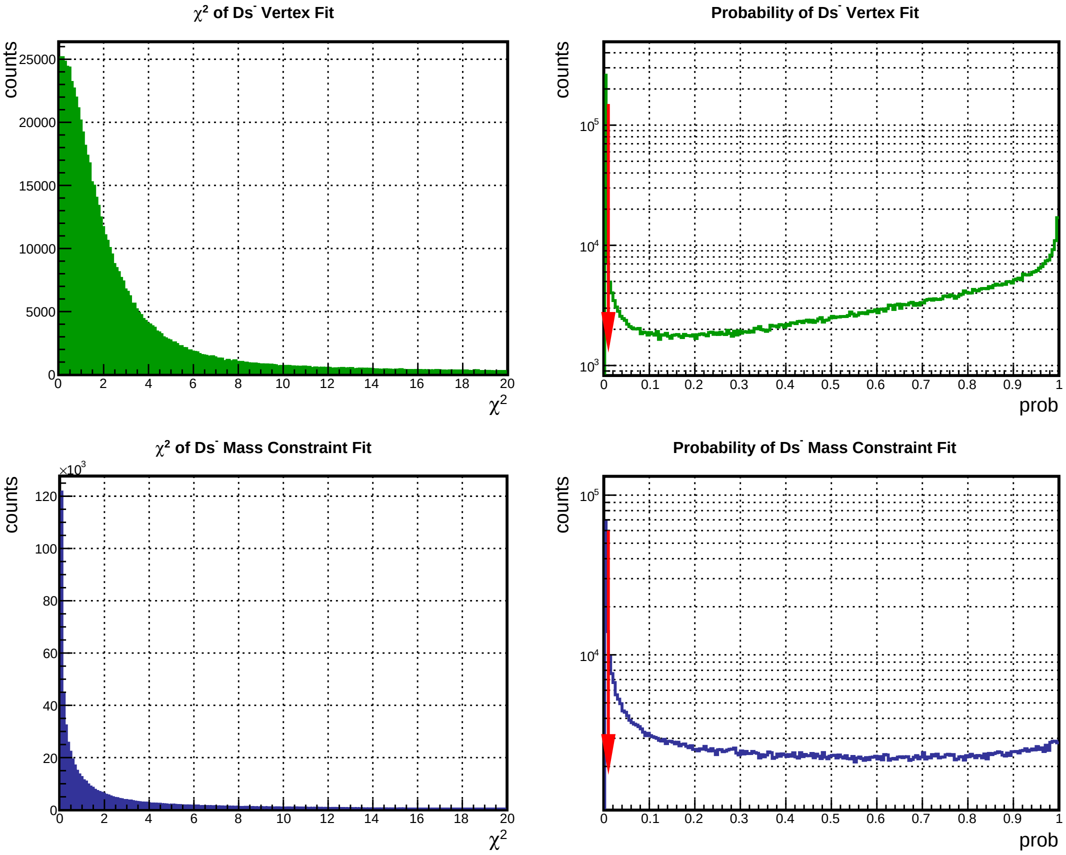

**Figure 4.57:** The $\chi^2$ (left column) and probability (right column; log scale) distributions of the $D_s^-$ vertex fit (top row) and mass constraint fit (bottom row). In both fits the candidates with probabilities lower than 1% are rejected, as indicated by the red arrows.

In order to reject the high combinatorial background and discriminate low momentum secondary pions, a mass window of $M = (1.968 \pm 0.08)$ GeV/$c^2$ was applied on the mass distribution of the ($\pi^+$, $\pi^-$, $\pi^-$) combination before the kinematic fit. Fig. 4.57 shows the $\chi^2$ and probability distributions of the $D_s^-$ vertex fit and mass constraint fit. The problem of the probability distribution in the vertex fit seen in tag mode A (see Fig. 4.16) appears again here. In both fits, the candidates of higher probabilities, i.e. prob $> 1\%$, were selected. The selection criteria are listed below.

- Mass window of raw $D_s^-$ candidates: $M = (1.968 \pm 0.08)$ GeV/$c^2$,
- Probability of the vertex fit: prob $> 1\%$,
- Probability of the mass constraint fit: prob $> 1\%$,
- After requiring prob $> 1\%$ in the mass constraint fit, the candidate with the smallest $\chi^2$ value for each event was selected.

Fig. 4.58 shows the invariant mass distributions of the $D_s^-$ candidates. The orange line indicates the distribution of all candidates without any fits. Comparing the $D_s^-$ mass distribution in tag mode A (see Fig. 4.17), the combinatorial background is higher, especially in the lower mass region. Low momentum secondary pions and charged pions from the $\eta$ meson decay dominate the background. As shown by the green line, after the mass window cut and vertex fit part of the background is rejected, but a broad distribution still remains under the mass peak.

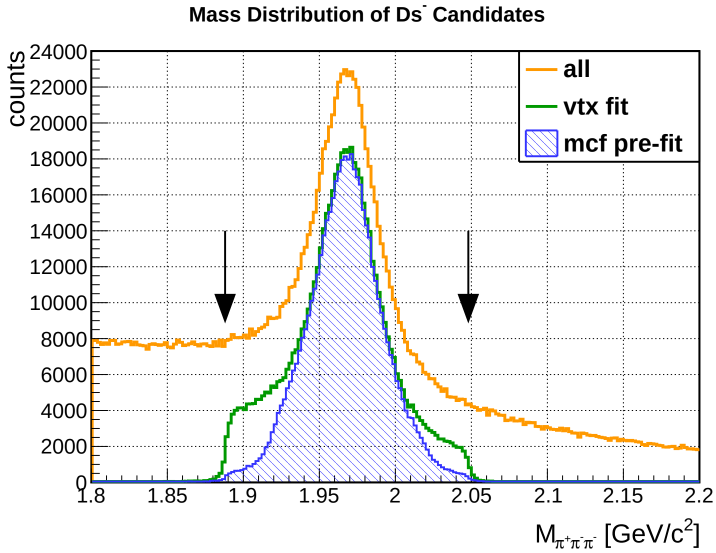

**Figure 4.58:** The mass distribution of the reconstructed $D_s^-$ candidates in tag mode B. The ($\pi^+$, $\pi^-$, $\pi^-$) invariant mass distribution of all combinations is shown by the orange line; the distribution after the vertex fit is shown in green, and the striped blue area presents the pre-fit values after further selection based on the probability of the mass constraint fit. The black arrows indicate the mass window of 160 MeV/$c^2$ centered at the PDG mass value of the $D_s^-$ meson.

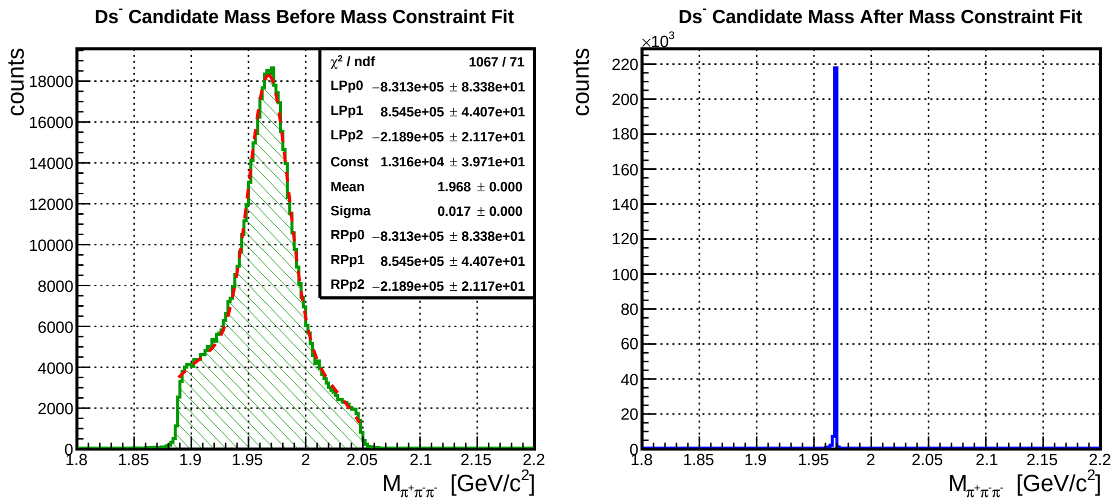

**Figure 4.59:** The mass resolution of the $D_s^-$ candidates in tag mode B. The mass distribution of the reconstructed $D_s^-$ candidates before the mass constraint fit (left) is fitted with a polynomial-Gaussian function to determine the resolution. The mass distribution after the mass constraint fit approaches a delta function (right).

This is expected to improve when the problem appearing in the vertex fit probability distribution is solved. The pre-fit mass value (blue) after the probability cut of the mass constraint fit is similar to a Gaussian distribution but with wide tails. Comparing the green line and the blue region, one can note that some of the combinatorial background candidates in the asymmetric shoulder were rejected by the mass constraint fit, indicating that the remaining background also peaks under the $D_s^-$ peak. With the mass distribution after the vertex fit, a polynomial-Gaussian function fit was applied to determine the reconstructed mass resolution, as shown in the left plot of Fig. 4.59. The mass resolution is $17.0\,\mathrm{MeV}/c^2$, which is about $4\,\mathrm{MeV}/c^2$ worse than obtained in tag mode A. The $D_s^-$ candidates mass distribution after the mass constraint fit is shown on the right. It approaches a delta function, as expected.

In every event with more than one $D_s^-$ candidate, the best fitted candidate with the smallest $\chi^2$ for the mass constraint fit was selected. In tag mode B, approximately 23.4% $D_s^-$ were reconstructed, and 20.3% were MC truth matched.

The $D_s^-$ vertex locations and resolutions are shown in Fig. 4.60, where the vertex resolutions are determined via a double-Gaussian fit. The sigma of the inner Gaussian is taken as the resolution. In the X and Y coordinates the resolutions are ~50 μm, and in the Z direction it is ~87 μm. Compared to the values in tag mode A, the vertex resolutions in tag mode B are about 10 μm better for the X-Y coordinates and 40 μm for Z. This is because the pions have higher momentum in tag mode B. In Fig. 4.61, the left frame shows the X and Y projections of the $D_s^-$ vertex distribution. Here the peak is symmetric and centered at zero. The right frame shows the $D_s^-$ decay vertex R-Z correlation.

Fig. 4.62 shows the momentum distribution of the reconstructed $D_s^-$ candidates, and the relative resolutions $(P^{\mathrm{reco}} - P^{\mathrm{MC}})/P^{\mathrm{MC}}$. The longitudinal momentum distribution shows a more

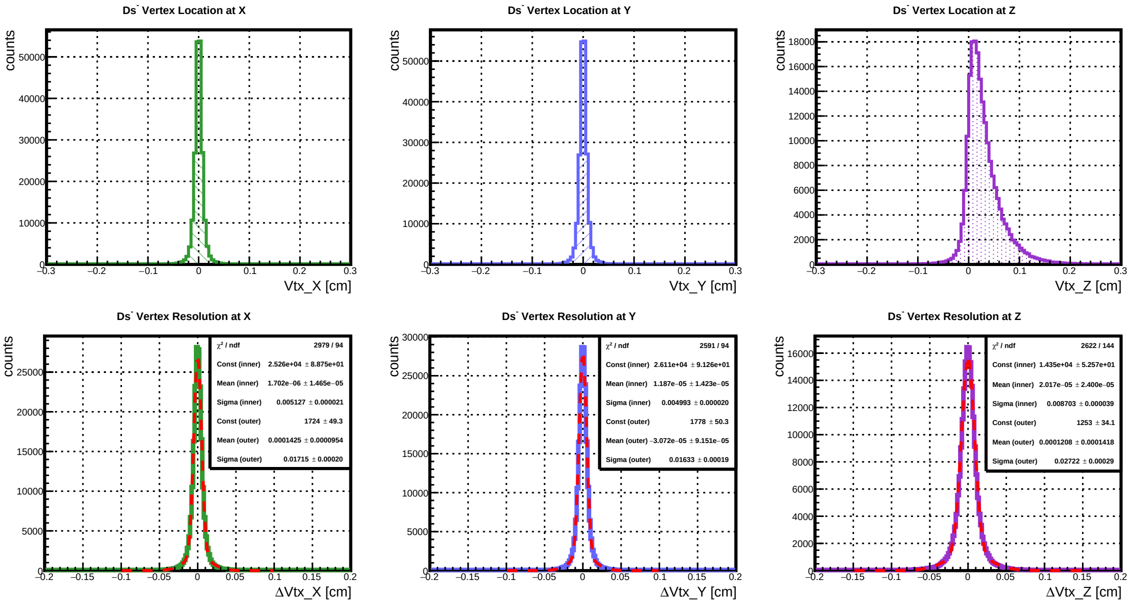

**Figure 4.60:** Vertex location distribution and resolutions of reconstructed $D_s^-$ candidates in tag mode B. The upper frame indicates the reconstructed vertex distribution for the $D_s^-$ decay, and the lower line indicates the vertex resolution in the X, Y, Z projections.

obvious efficiency loss comparing to that in tag mode A (see Fig. 4.21). A double-Gaussian fit indicates the resolutions to be $\Delta P_t/P_t^{\mathrm{MC}} = 2.2\%$ and $\Delta P_z/P_z^{\mathrm{MC}} = 0.7\%$. They are the same as the values obtained in tag mode A. The ratio of the reconstructed candidates' momenta to the MC truth value as a function of the corresponding momentum is shown in Fig. 4.63. In both transversal and longitudinal projections the ratios are peaked at $P^{\mathrm{reco}}/P^{\mathrm{MC}} = 1$, as expected.

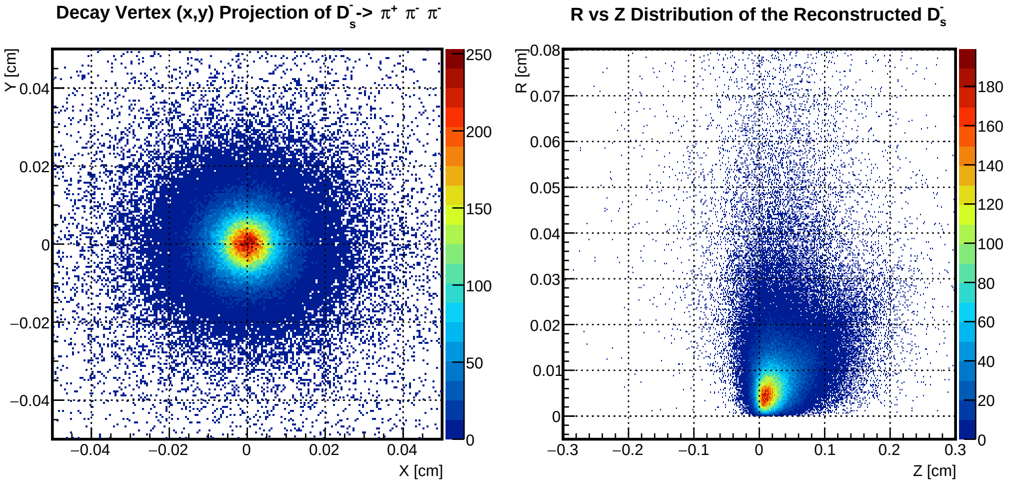

**Figure 4.61:** Decay vertex distribution of the decay $D_s^- \to \pi^+\pi^-\pi^-$. Left: the vertex projection on the X-Y plane. Right: the X-Y radius R versus Z distribution, where $R = \sqrt{X^2 + Y^2}$.

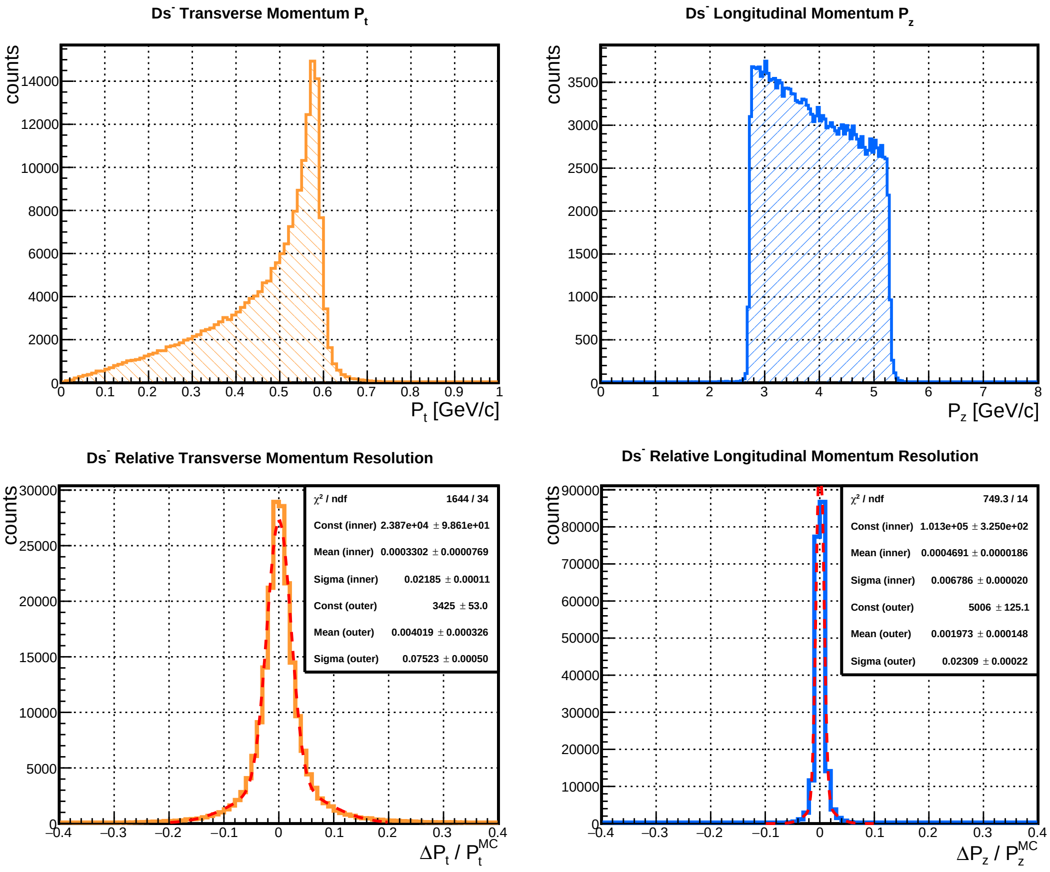

**Figure 4.62:** The reconstructed $D_s^-$ momentum distributions (upper row) in the decay of $D_s^- \rightarrow \pi^+\pi^-\pi^-$. Transversal (orange) and longitudinal (blue) momentum are shown. In the relative resolutions (lower row), the red dashed line presents a double-Gaussian fit.

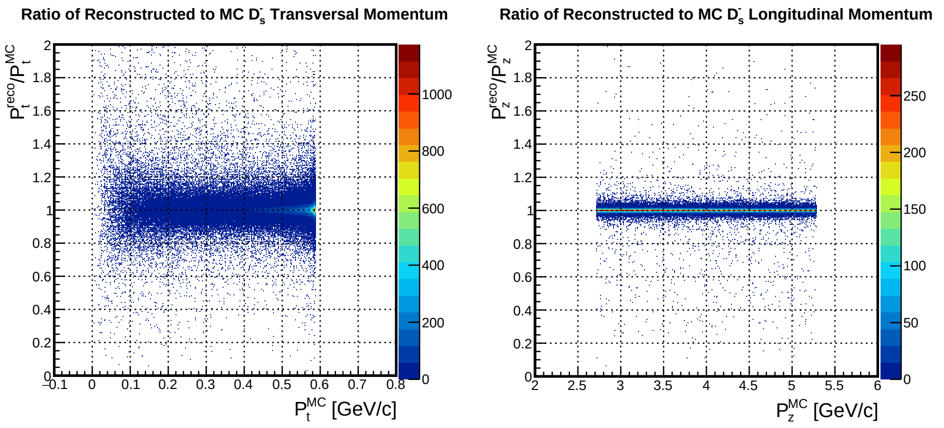

**Figure 4.63:** Ratio of the reconstructed to MC momenta of the $D_s^-$ for tag mode B. Left is the ratio as a function of the transversal momentum, and right is the ratio as a function of the longitudinal momentum.

**Table 4.7:** Summary of the reconstruction results of the $D_s^-$ for the decay $D_s^- \to \pi^+\pi^-\pi^-$.

| Reco eff. | MCT eff. | $\sigma_{\mathrm{mass}}$ | $\sigma_{\mathrm{vtx}}$ [μm] | | | $\sigma_P/P$ | |
|---|---|---|---|---|---|---|---|
| | | [MeV/$c^2$] | $X$ | $Y$ | $Z$ | $P_t$ | $P_z$ |
| 23.4% | 20.3% | 17.0 | 51 | 50 | 87 | 2.2% | 0.7% |

The count flow in the $D_s^-$ reconstruction process is shown in Fig. 4.64. The number of reconstructed raw $D_s^-$ candidates (labeled as "All") is around ten times higher than the number found in tag mode A. This high combinatorial background is however effectively rejected after the reconstruction chain, as shown by the counts of reconstructed $D_s^-$ approaching to that of the MC truth matched after fits. The reconstruction efficiency and resolutions of the $D_s^-$ are summarized in Table 4.7.

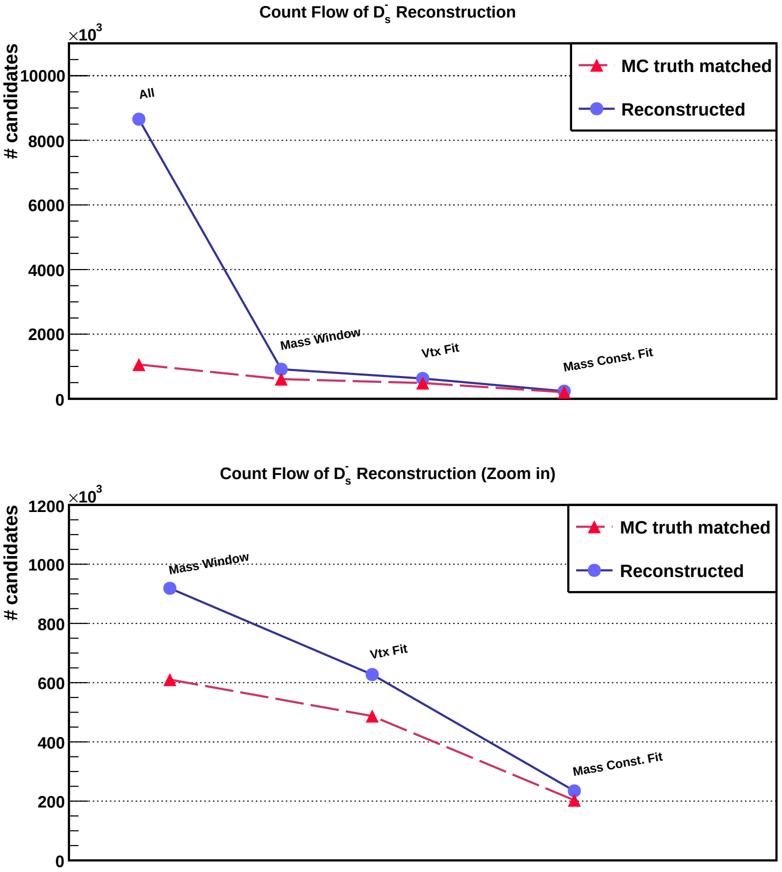

**Figure 4.64:** Count flow of the $D_s^-$ reconstruction for the decay of $D_s^- \to \pi^+\pi^-\pi^-$. The data points follow the order of reconstruction procedure from left to right. Blue: the number of reconstructed candidates. Red: the number of the MC truth matched candidates. The lower plot is a zoom-in view of the upper plot, excluding the number of counts of all candidates.

**Background Events** 100 million background events were simulated with the DPM generator using a $\bar{p}$ beam of 8 GeV/$c$, in order to estimate the background contribution. Except the beam momentum, all other settings are the same as in Table 4.3. The background reconstruction was performed following the same strategy and selection criteria as for signal events. Comparing the mass distribution in Fig. 4.65 and Fig. 4.49, the background of tag mode B is ∼ 100 times more than in tag mode A.

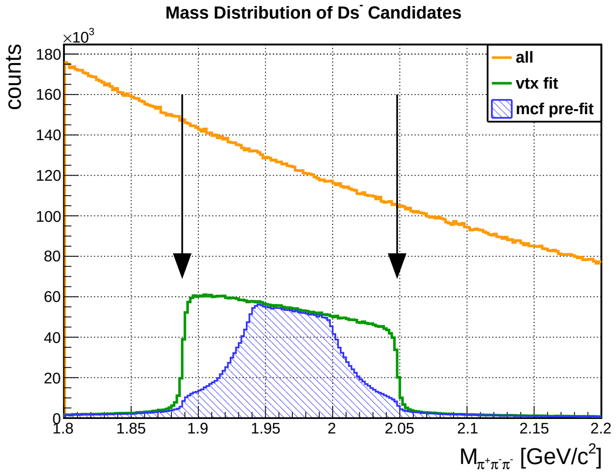

**Figure 4.65:** The mass distribution of the reconstructed $D_s^-$ candidates in the background study of tag mode B. Orange: the invariant mass distributions of all candidates. Green: the distribution after the vertex fit. Blue: the pre-fit mass distribution after a cut on the probability from the mass constraint fit. The black arrows indicate the mass window.

### 4.5.2 Reconstruction of $\pi^0 \to \gamma\gamma$

The reconstruction of the $\pi^0$ decay has been studied for tag mode B. The photon multiplicity distributions are shown in Fig. 4.66. The photon energy threshold was set to 40 MeV, as for

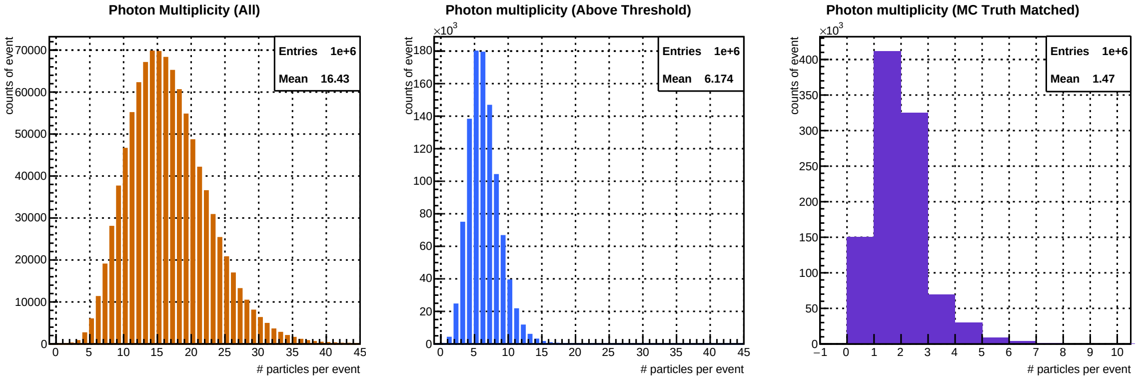

**Figure 4.66:** Photon multiplicity distributions for tag mode B. Left: multiplicity of raw photons without any cuts. Middle: multiplicity distribution for photons above 40 MeV. Right: multiplicity distribution of MC truth matched photons.

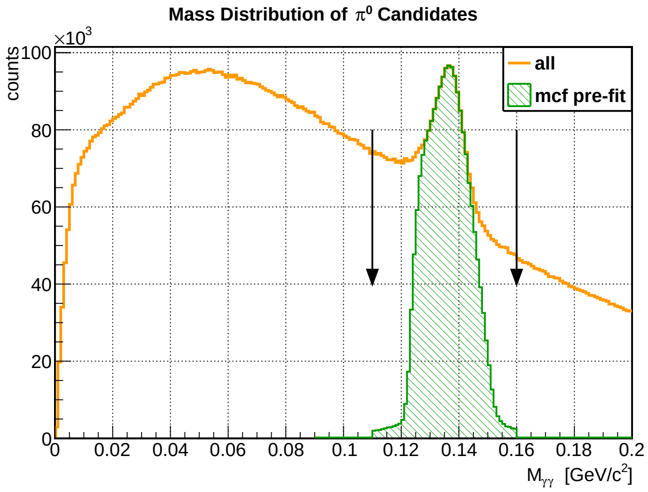

**Figure 4.67:** The two-photon invariant mass distributions with tag mode B. The distributions of all ($\gamma$, $\gamma$) pairs is indicated by the orange line; the black arrows indicate the mass window width centered at the PDG mass of $\pi^0$. The green filled histogram presents the pre-fit distribution after the mass constraint fit.

tag mode A. The mean values indicated the average multiplicity: ~ 16 photons per event without threshold cut; ~ 6 photons per event found after cut; ~ 1.5 photons per event are MC truth matched. These numbers are consistent with what has been seen in tag mode A. That is expected since varying the $D_s^-$ tagging mode does not change the total number of charged tracks and neutral particles in the final products, and therefore makes no significant influence on the photon reconstruction result.

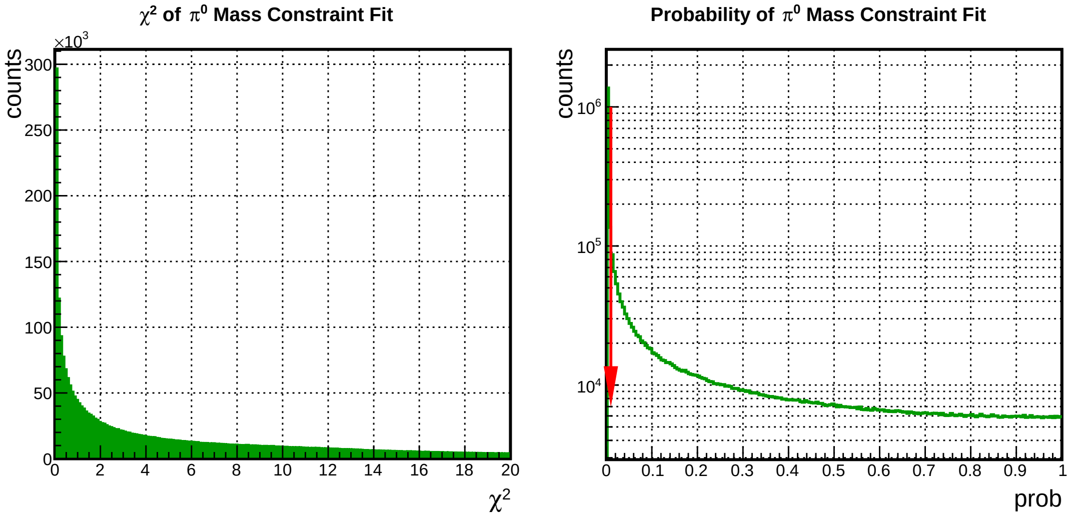

**Figure 4.68:** The $\chi^2$ (left) and probability (right; in log scale) distributions of $\pi^0$ mass constraint fit in tag mode B. The candidates with probability lower than 1% (red arrow) were rejected.

The $\pi^0$ candidates were formed by combining two photons and applied a mass constraint fit. Fig. 4.67 shows the two-photon invariant mass distribution, which is quite similar to the distribution in tag mode A. The mass window was set to $M = (0.135 \pm 0.025)$ GeV/$c^2$. Fig. 4.68 shows the $\chi^2$ and probability distributions of the $\pi^0$ mass constraint fit.

The mass resolution of the $\pi^0$ candidates was obtained by a polynomial-Gaussian fit to the distribution before the mass constraint fit. Fig. 4.69 shows the resolution is $\sim 4.9\,\mathrm{MeV}/c^2$, and after the mass constraint fit the $\pi^0$ mass goes to a peak at $M = 0.135$ GeV/$c^2$, as expected.

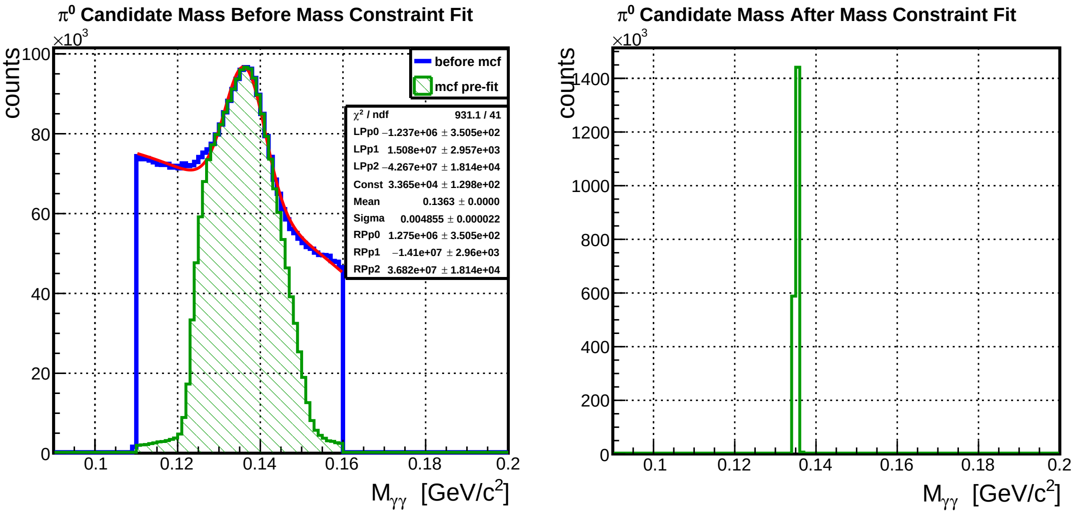

**Figure 4.69:** The mass distribution of reconstructed $\pi^0$ candidates in tag mode B. Left: the distribution inside of the mass window and before the mass constraint fit; red line is a polynomial+Gaussian fit to extract the resolution. Right: the mass distribution of the fitted candidates.

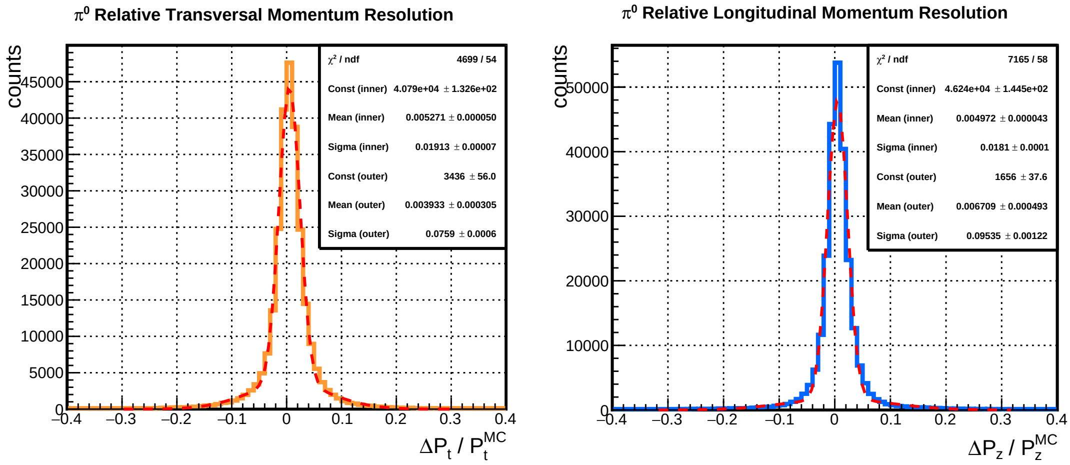

**Figure 4.70:** The relative resolutions of reconstructed $\pi^0$ transversal momentum (left, orange) and longitudinal momentum (right, blue) in tag mode B. The red dashed line shows a double-Gaussian function fit, and the sigma of the inner Gaussian is taken as the resolution.

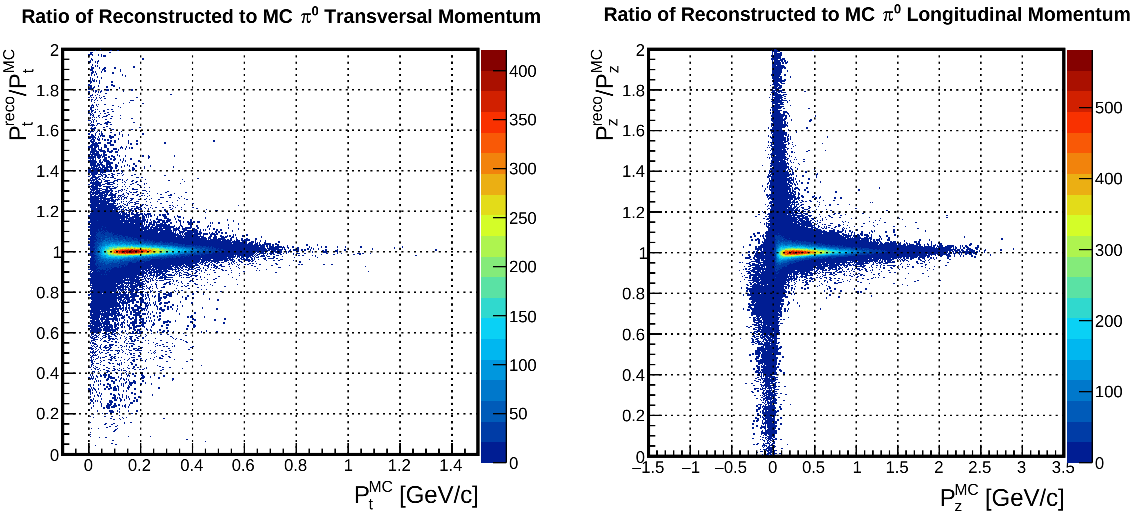

**Figure 4.71:** Ratio of the reconstructed to the MC true momenta of the $\pi^0$ in tag mode B. Left is the ratio as a function of the transversal momentum. Right is the ratio as a function of the longitudinal momentum.

Fig. 4.70 shows the relative resolutions of momentum of the reconstructed $\pi^0$ candidates, i.e. $(P^{\text{reco}} - P^{\text{MC}})/P^{\text{MC}}$. In both transversal and longitudinal momentum components a double-Gaussian fit was used to determine the resolution. They are found to be $\Delta P_t/P_t^{\text{MC}} = 1.9\%$ and $\Delta P_z/P_z^{\text{MC}} = 1.8\%$. The ratios of momenta between the reconstructed candidates and MC truth $P^{\text{reco}}/P^{\text{MC}}$ are plotted as a function of the MC true momenta $P^{\text{MC}}$ in Fig. 4.71. The distributions are similar to the results shown for tag mode A.

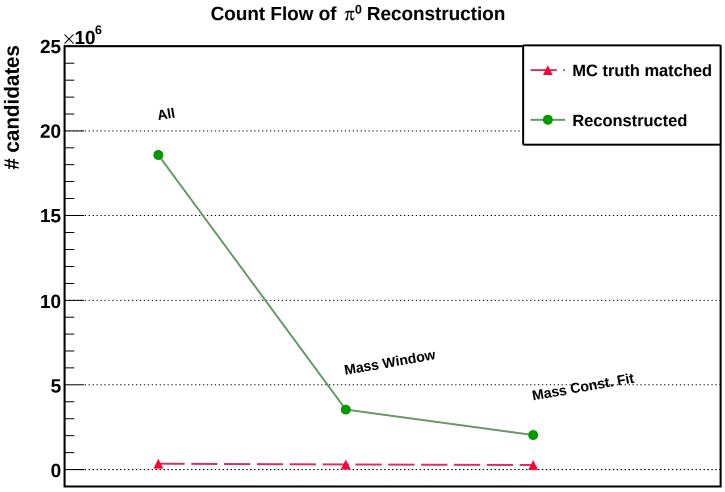

**Figure 4.72:** Count flow of the $\pi^0$ reconstruction in tag mode B. The data points follow the order of the reconstruction procedure from left to right. Green: the number of reconstructed candidates. Red: the number of the MC truth matched candidates.

The count flow of the $\pi^0$ reconstruction for one million events is shown in Fig. 4.72. As seen in tag mode A, the large number of $\pi^0$ candidates, up to more than $20 \times 10^6$, are also found in the two-photon combination in tag mode B. The MC truth matched efficiency drops from 34.5% to 26.9% after all cuts. On average two $\pi^0$ candidates were reconstructed in each event, and all of them were kept in this step. Later in calculating the $\eta$ invariant mass, all selected $\pi^0$ candidates will be taken into account without bias. Since the multiplicity of the reconstructed $\pi^0$ is $\sim 2$ and the MC truth matched count is low, the gap between the two data points after the mass constraint fit is obviously larger than the result of the $D_s$ reconstruction. Table 4.5 lists the $\pi^0$ reconstruction results.

**Table 4.8:** Summary of the reconstruction results for the $\pi^0$ in tag mode B.

| MCT Efficiency | $\sigma_{\text{mass}}$ | $\sigma_P/P$ | |
|---|---|---|---|
| | [MeV/$c^2$] | $P_t$ | $P_z$ |
| 26.9% | 4.9 | 1.9% | 1.8% |

**Background Events** In the 100 million DPM events data set, the $\pi^0$ were reconstructed in the same way as it in the signal events. The energy threshold of photons was set to 40 MeV. The mass distribution of the $\pi^0$ candidates is shown in Fig. 4.73, which is consistent with the distribution obtained in tag mode A (see Fig. 4.33). Comparing the DPM events with the signal (in Fig. 4.67), a higher peak in the low mass region is seen. The $\pi^0$ mass peak was selected by a probability cut of prob $> 1\%$ in the mass constraint fit on those candidates within the mass window.

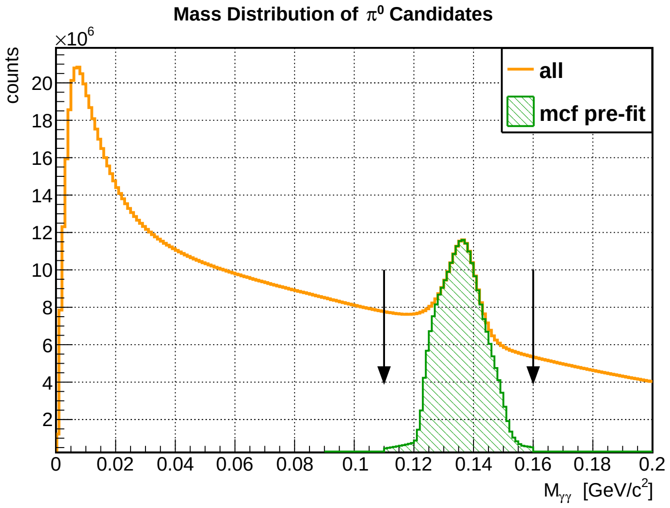

**Figure 4.73:** The two-photon invariant mass distributions for DPM events in tag mode B. Orange: the mass distribution of all combined $(\gamma, \gamma)$ candidates. The black arrows denote the mass window centered at the PDG mass of the $\pi^0$ meson. Green: distribution of the pre-fit candidates after selecting on the probability of the mass constraint fit.

### 4.5.3 Reconstruction of $\eta \to \pi^+\pi^-\pi^0$

The reconstruction of $\eta \to \pi^+\pi^-\pi^0$ started by determining the decay vertex. As explained in Sec. 4.4.3, the positron from the $D_s^+$ decay was included into a vertex fit with the $\pi^+$ and $\pi^-$. The mean $e^+$ multiplicity (see Fig. 4.74) is ∼ 1.15 counts per event, which is very close to the value ∼ 1.16 found in tag mode A. About 19% of events have no $e^+$ found in the charged tracks. Therefore, the $e^+$ acceptance will reduce the $\eta$ reconstruction efficiency by a factor of about one fifth, in both tag mode A and B.

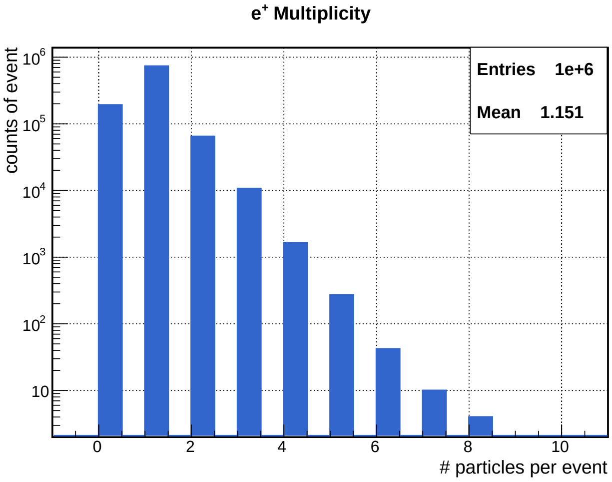

**Figure 4.74:** Multiplicity distribution of reconstructed $e^+$ in the decay $D_s^+ \to \eta e^+ \nu_e$ in tag mode B.

Fig. 4.75 shows the $\chi^2$ and probability distributions of the $\eta$ vertex fit for the ($e^+$, $\pi^+$, $\pi^-$) combination in tag mode B. The problem of the probability distribution showing a rise toward

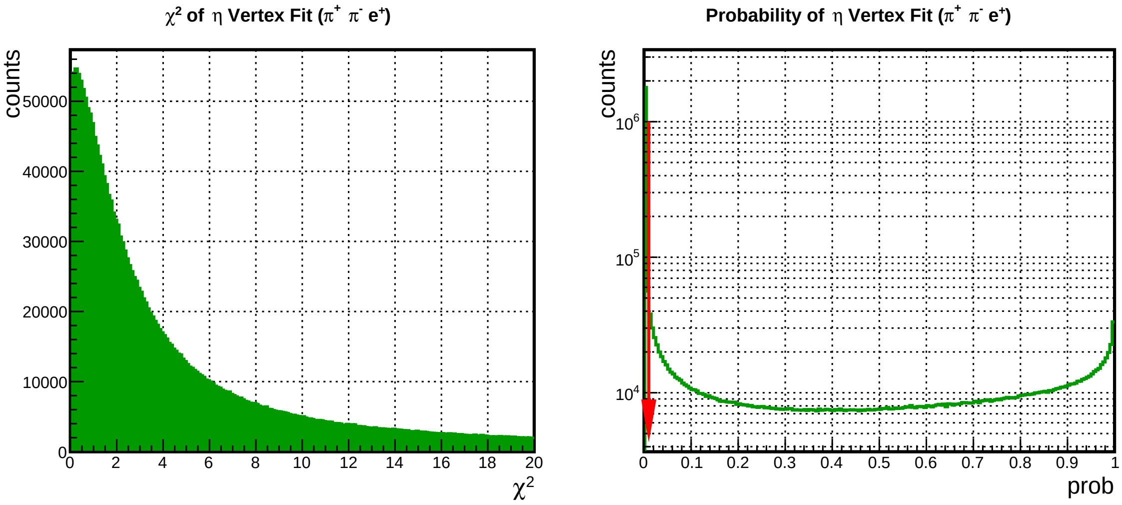

**Figure 4.75:** The $\chi^2$ (left) and probability (right) distributions of the $\eta$ vertex fit on ($e^+$, $\pi^+$, $\pi^-$) in tag mode B. The candidate was rejected if the probability was lower than 1% (red arrow).

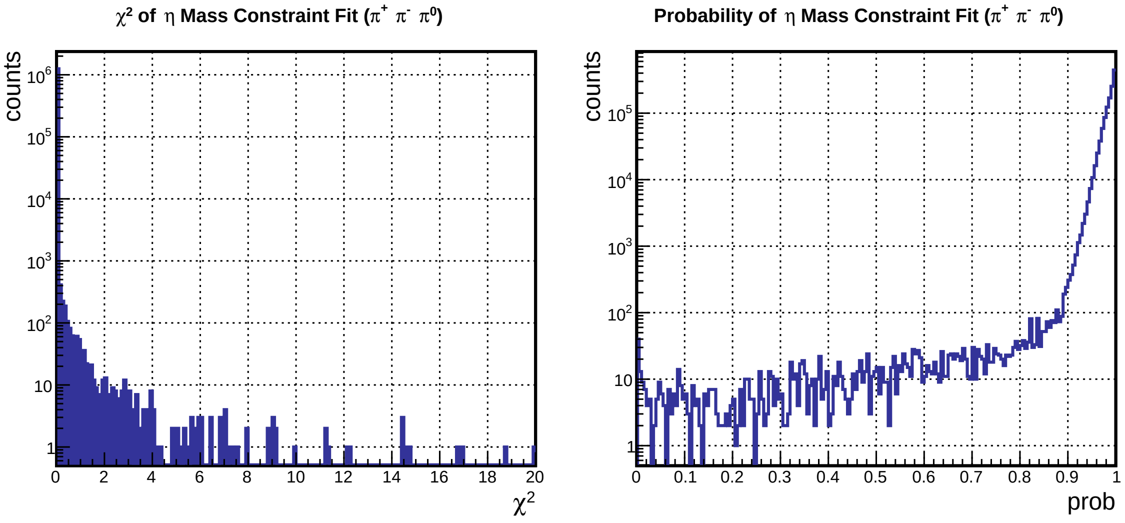

**Figure 4.76:** The $\chi^2$ (left) and probability (right) distributions of the $\eta$ mass constraint fit on ($\pi^+$ $\pi^-$ $\pi^0$) in tag mode B.

prob = 1 has also been seen in the $D_s^-$ vertex fit. A probability cut of prob < 1% was applied to reject the combinatorial background.

The selected $\pi^+\pi^-$ pair in the vertex fit was combined with the reconstructed $\pi^0$ from the previous step to generate the $\eta$ candidate. In the mass constraint fit, the invariant mass of the combination ($\pi^+$, $\pi^-$, $\pi^0$) was constrained to be the PDG mass of the $\eta$ meson. Fig. 4.76 shows

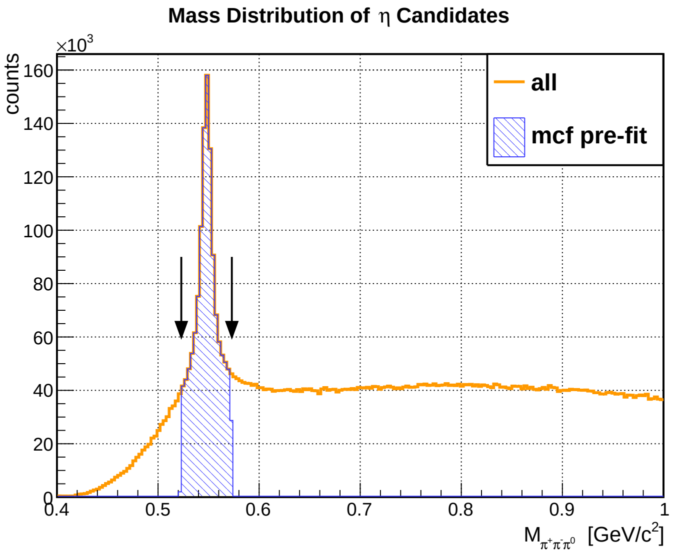

**Figure 4.77:** The invariant mass distribution of the $\eta$ candidates in tag mode B. Orange line: the distributions of all candidates. The black arrows denote the mass window width centered at the PDG mass of the $\eta$. The mass distribution of the pre-fit candidates is marked in blue.

the distributions of $\chi^2$ and probability from the mass constraint fit. As found in the result of the $\eta$ mass fit with tag mode A, the $\chi^2$ values are too small, and the probabilities are skewed close to one. The cause of this is still under investigation. Due to this problem, no probability cut was applied in this fit, and instead by selecting the candidate in a given event with the smallest $\chi^2$.

In the mass constraint fit the $\eta$ candidate with the smallest $\chi^2$ in each event was selected as the "best" $\eta$. The mass distribution of $\eta$ candidates is shown in Fig. 4.77. The blue region marks those candidates that were used for the mass constraint fit. In Fig. 4.78, one can notice that the gap between the blue and the green histograms is larger than in tag mode A (see Fig. 4.40). Actually, the number of the reconstructed $\eta$ in both tag modes is similar. The larger gap is due to a higher combinatorial background caused by a three times higher multiplicity of pions in tag mode B. The mass resolution was extracted by fitting the distribution by a double-Gaussian function (red dashed line). The $\eta$ mass resolution is determined to be 4.0 MeV/$c^2$ from the sigma value of the inner Gaussian. After the selection based on $\chi^2$, the $\eta$ mass distribution is close to a delta function peaked at the PDG mass of the $\eta$ meson, as expected.

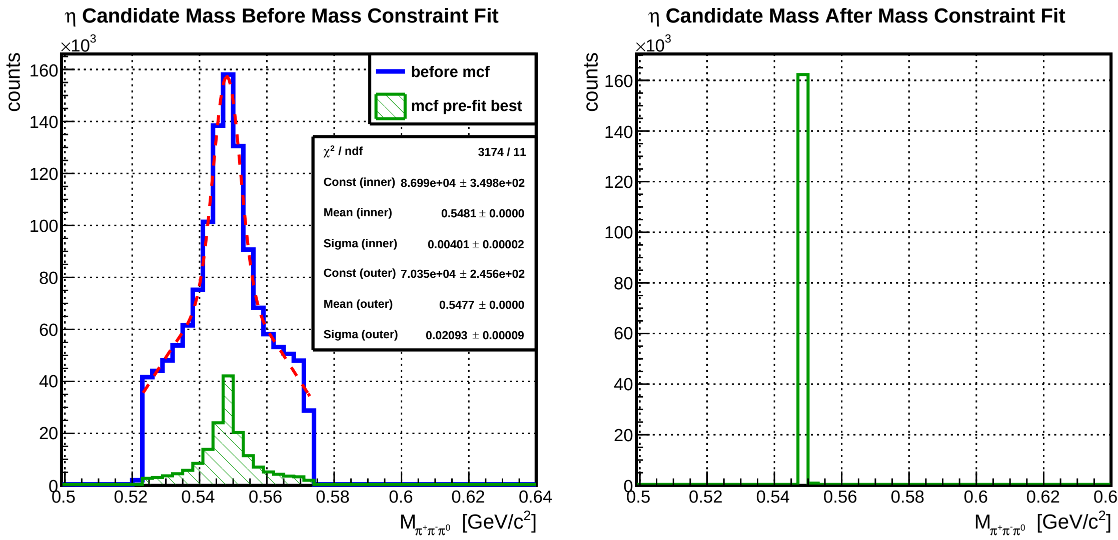

**Figure 4.78:** Mass distribution of the reconstructed $\eta$ candidates in tag mode B. Left: the blue line shows the distribution before the mass constraint fit inside of the mass window, and a double-Gaussian fit to this is shown by the red dashed line; the green histogram indicates the pre-fit mass of the "best" $\eta$ candidate. Right: the fitted mass distribution of the reconstructed $\eta$.

The $\eta$ vertex location and resolution are shown in Fig. 4.79. The vertex resolutions were determined via a double-Gaussian fit as shown by the red dashed line. The resolutions are $\sigma_X = 90\ \mu\text{m}$, $\sigma_Y = 86\ \mu\text{m}$ and $\sigma_Z = 170\ \mu\text{m}$. The vertex resolutions on all projections are about 10 μm better than in tag mode A.

Fig. 4.80 shows the decay vertex distributions of the reconstructed $\eta$ candidates in tag mode B. The left frame combining the vertex locations in X and Y projections shows the decay points of the reconstructed $\eta$ normal to the beam axis, where the peak is symmetric around the point of (0, 0). The right frame shows the $\eta$ decay vertex R-Z correlation. There is no obvious differences found between the distributions in tag mode A and B.

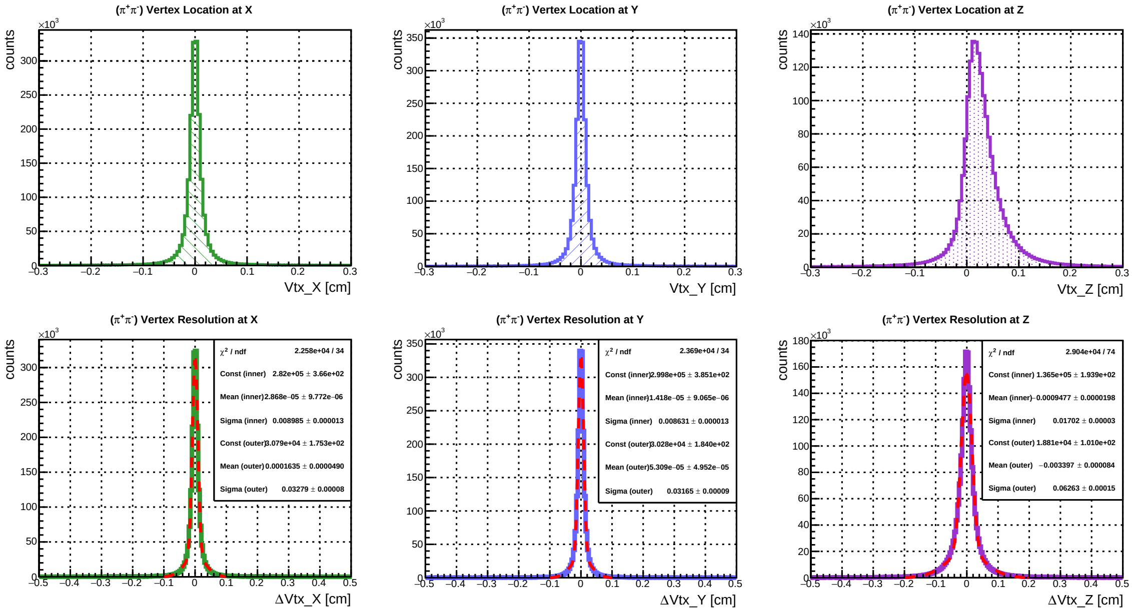

**Figure 4.79:** The vertex location and resolutions of the reconstructed η in tag mode B. The histograms in the upper frame are the reconstructed vertex distributions in the X, Y, Z projections. The lower histograms show the vertex resolution distributions $\Delta\mathrm{Vtx} = \mathrm{Vtx}_{\mathrm{MC}} - \mathrm{Vtx}_{\mathrm{reco}}$, where the red dashed lines present a fit to a double-Gaussian function. The sigma value of the inner Gaussian indicates the resolution.

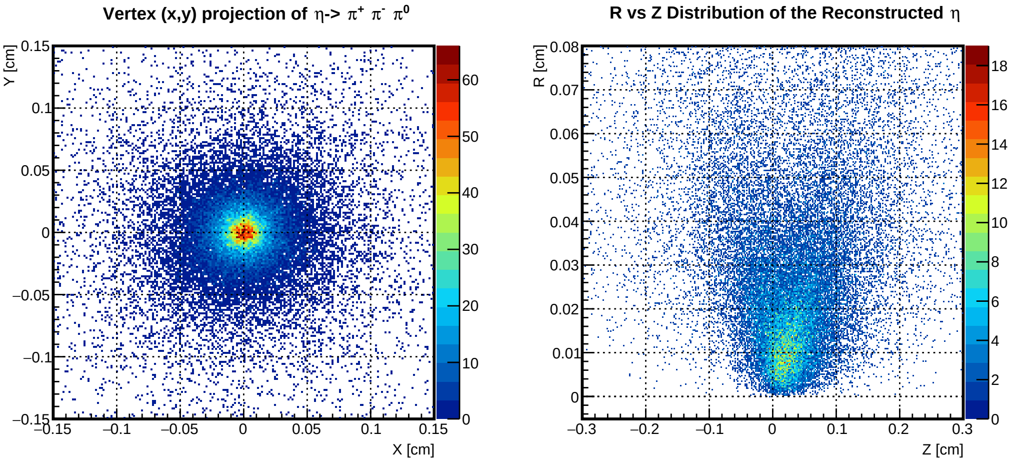

**Figure 4.80:** Decay vertex distributions of the reconstructed η candidates in tag mode B. Left: the vertex projection on the X-Y plane. Right: the X-Y radius R versus Z distribution, where $R = \sqrt{X^2 + Y^2}$.

The relative momentum resolution $(P^{\mathrm{reco}} - P^{\mathrm{MC}})/P^{\mathrm{MC}}$ of the reconstructed η candidates is shown in Fig. 4.81. A double-Gaussian fit indicates the resolutions to be $\Delta P_t/P_t^{\mathrm{MC}} = 1.6\%$ and $\Delta P_z/P_z^{\mathrm{MC}} = 1.2\%$, which are about the same as obtained in tag mode A. The ratios of momenta between the reconstructed candidates and the MC truth are shown in Fig. 4.82. The ratios peak at $\Delta P^{\mathrm{reco}}/P^{\mathrm{MC}} = 1$, as expected.

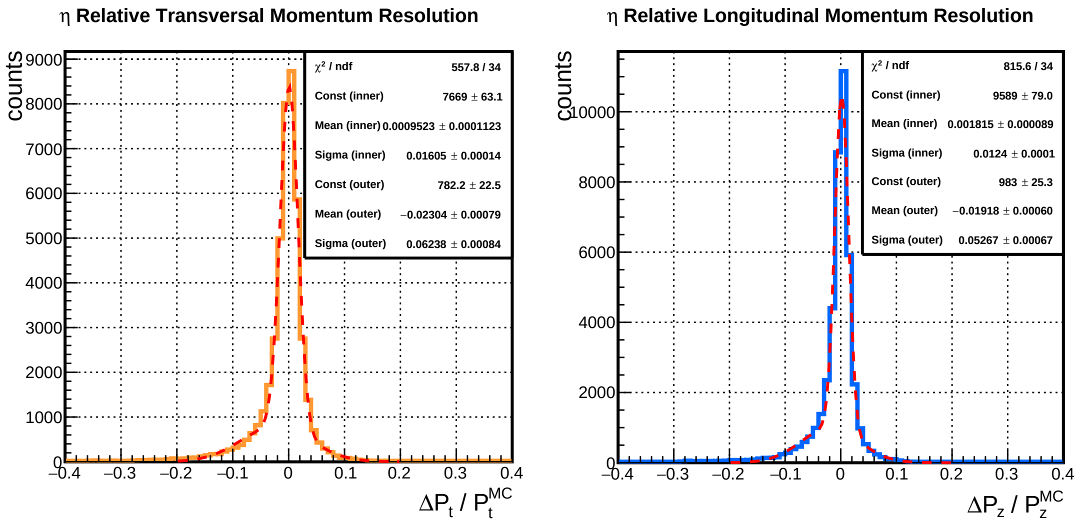

**Figure 4.81:** The relative resolutions of the reconstructed η transversal (left) and longitudinal (right) momentum in tag mode B. The red lines present double-Gaussian fits, and the sigma value of the inner Gaussian indicates the resolution.

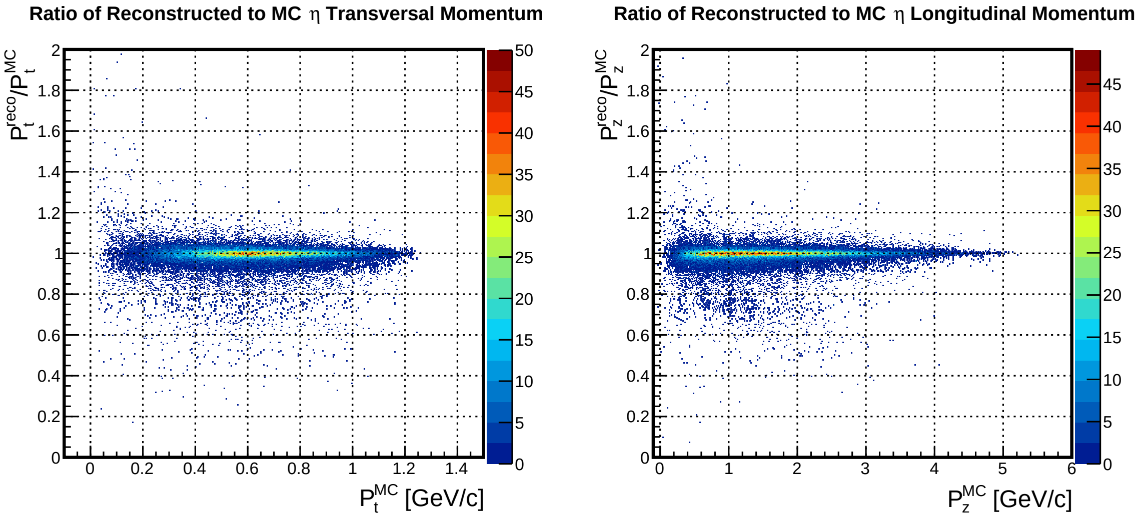

**Figure 4.82:** Ratio of the reconstructed to MC momenta of the η in tag mode B. Left is the ratio as a function of the transversal momentum, and the right is as a function of the longitudinal momentum.

As a summary, Table 4.9 lists the reconstruction results for the η candidates in the present analysis. Fig. 4.83 shows the count flow in the η reconstruction process with tag mode B. The results obtained in tag mode B are basically the same as in tag mode A for the reconstruction of the η meson. The MC truth matched efficiency is 4.4%, which means only about one fourth of the reconstructed η candidates are matched with MC truth. The cause for the low MC truth efficiency is under investigation.

**Table 4.9:** Summary of the reconstruction results for the η in tag mode B.

| Reco eff. | MCT eff. | $\sigma_{\text{mass}}$ | $\sigma_{\text{vtx}}$ [µm] | | | $\sigma_P/P$ | |
|---|---|---|---|---|---|---|---|
| | | [MeV/$c^2$] | $X$ | $Y$ | $Z$ | $P_t$ | $P_z$ |
| 16.5% | 4.4% | 4.0 | 90 | 86 | 170 | 1.6% | 1.2% |

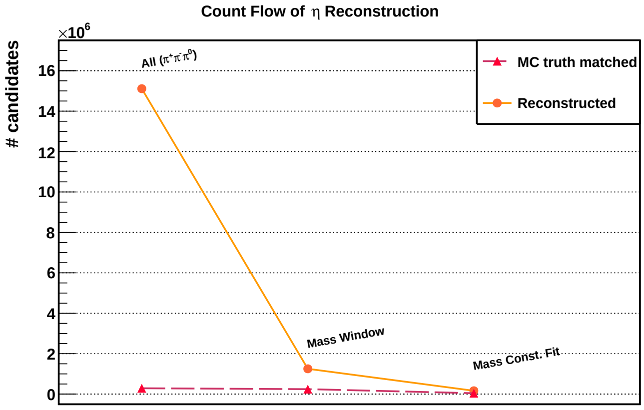

**Figure 4.83:** Count flow of reconstructing η in the decay $\eta \to \pi^+\pi^-\pi^0$ in tag mode B. The data points follow the order of reconstruction procedure from left to right. Orange: the number of reconstructed candidates. Red: that of the MC truth matched candidates.

**Background Events** 100 million DPM events were generated, and the η candidates were reconstructed by the same strategy as for the signal events. The mass distribution of the

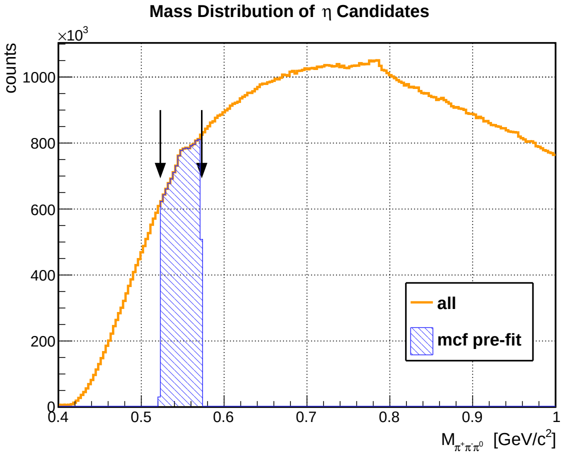

**Figure 4.84:** The invariant mass distributions of the reconstructed η candidates in DPM events in tag mode B. Orange: the mass distributions of all η candidates. The black arrows indicate the mass window centered at the PDG mass of the η meson. The pre-fit candidates after the mass window cut are shown by the blue histogram.

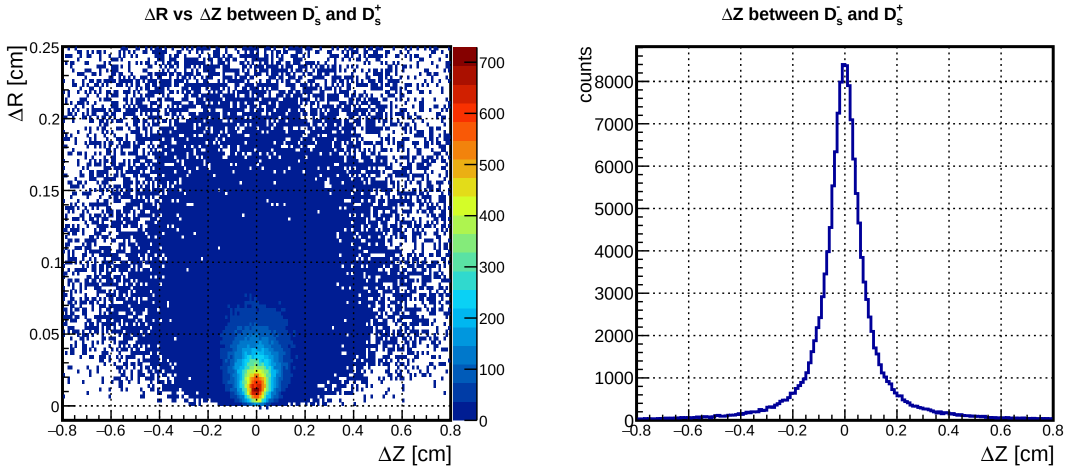

**Figure 4.85:** Distribution of the distance between the $D_s^+$ and the $D_s^-$ decay vertices in tag mode B. Left: distance between the $D_s^+$ and the $D_s^-$ decay vertices shown with $\Delta R - \Delta Z$ correlation, where $\Delta R = \sqrt{(X_{D_s^+} - X_{D_s^-})^2 + (Y_{D_s^+} - Y_{D_s^-})^2}$ and $\Delta Z = Z_{D_s^+} - Z_{D_s^-}$. Right: the projection of the left distribution onto the $\Delta Z$ axis.

reconstructed $\eta$ candidates is shown in Fig. 4.84. As seen in the distribution of tag mode A, the combinatorial background is very high. There are two tiny bumps, the one between the black arrows is from the $\eta$ candidates. The other one is located around 782 MeV/$c^2$, and comes from the $\omega$ meson candidates.

As in tag mode A, the distance between the $D_s^-$ and $D_s^+$ vertices was obtained from the distance between the reconstructed $D_s^-$ vertex and the $\eta - e^+$ position, since the $D_s^+$ was not directly reconstructed. The position difference $\Delta R$ versus $\Delta Z$ and the $\Delta Z$ distribution are obtained for both the signal events and DPM events, as show in Fig. 4.85 and Fig. 4.86, respectively.

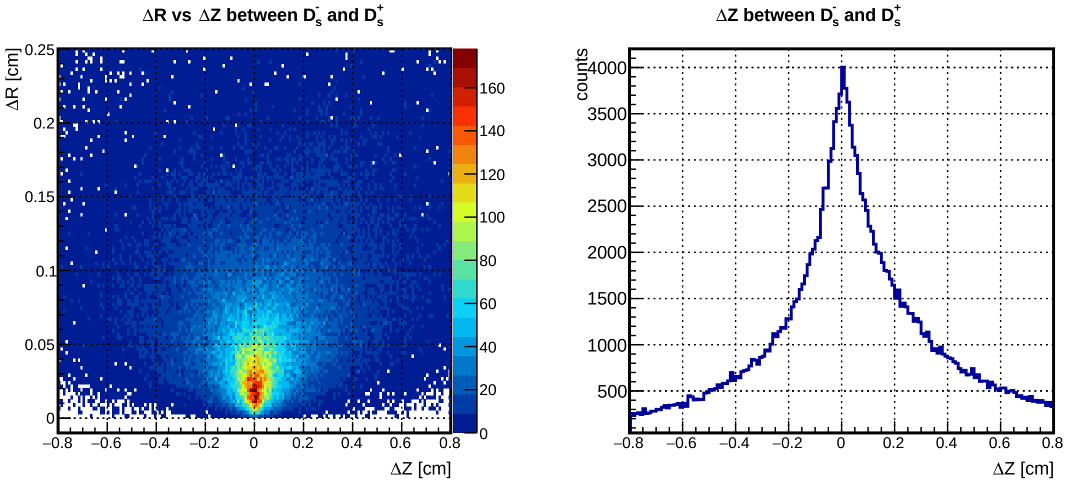

**Figure 4.86:** Distribution of Fig. 4.85 for the DPM event data set.

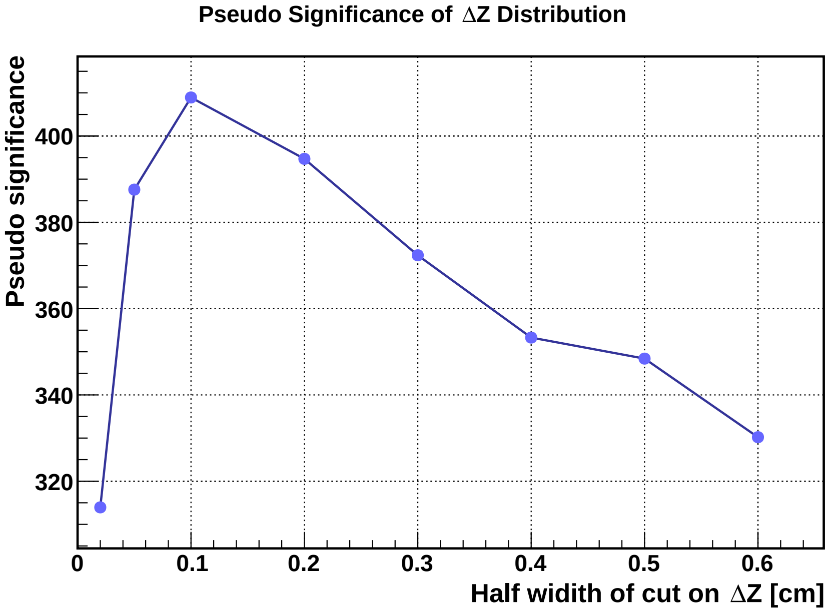

**Figure 4.87:** Pseudo significance of the $\Delta Z$ distribution as a function of half width of various cut windows in tag mode B.

The pseudo significance of the $\Delta Z$, significance $= N_{\text{signal}}/\sqrt{N_{\text{DPM}}}$, is plotted as a function of the half width of the cut applied to $\Delta Z$ (see Fig. 4.87). It is shown that the cut of $|\Delta Z| \leq 0.1$ cm brings the highest significance. This optimal cut value is the same with the result found in tag mode A, which has been presented in Sec. 4.4.3.

### 4.5.4 Reconstruction of Positron-Neutrino System

As introduced in Sec. 4.4.4, the four-momentum transfer squared $q^2$ in the semileptonic decay $D_s^+ \to \eta e^+ \nu_e$ can be calculated via four-momentum conservation from the initial $\bar{p}p$ system to the final measured system.

The correlation between the $\nu_e$ mass squared and the invariant mass squared of the lepton-neutrino system is shown in Fig. 4.88. The right histogram is obtained from Eq. 4.3 and Eq. 4.4 with the reconstructed $D_s^-$, $\eta$ and $e^+$ candidates. For every event, the MC truth matched $D_s^-$, $\eta$ and $e^+$ were used to get the result in the left histogram. The black lines indicate the window to reject the combinatorial background in the reconstructed data.

Fig. 4.89 shows the mass squared distributions of the reconstructed $\nu_e$ and the lepton-neutrino system in tag mode B. As expected, the mass squared distribution of the $\nu_e$ is peaked at around zero (left plot). The window selects the $\nu_e$ candidates in the peak (yellow), and suppresses most of the combinatorial background in the $(e^+\nu_e)$ system (right plot). The statistics of tag mode A is $\sim 40\%$ lower in tag mode B. This is for two reasons. One is that the acceptance of pions is about 10% higher than for kaons, which has been seen in the reconstruction of $D_s^-$. The other is the remaining combinatorial background in the vertex reconstruction of $D_s^- \to \pi^+\pi^-\pi^-$.

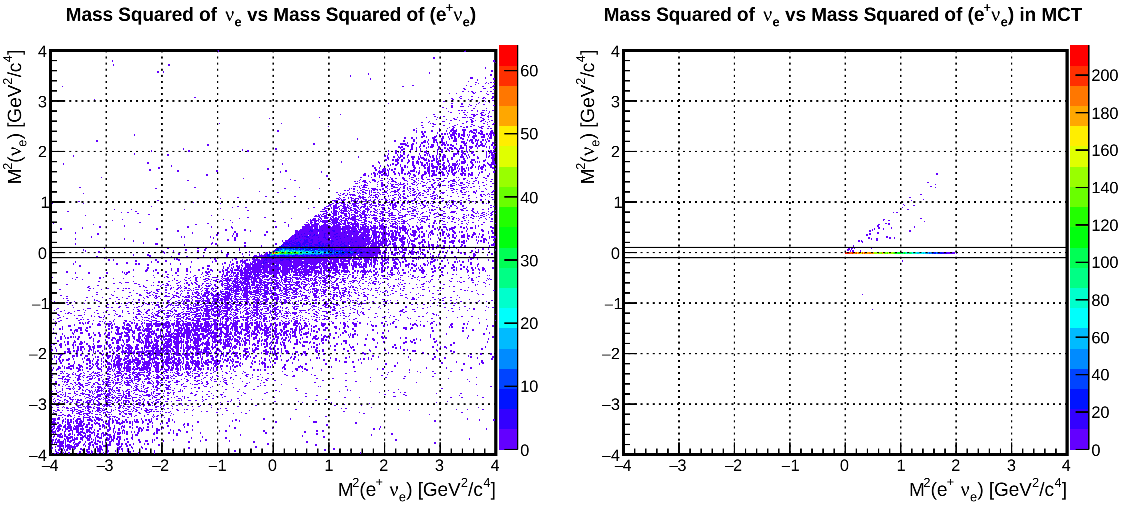

**Figure 4.88:** Mass squared of the $\nu_e$ candidates (Eq. 4.3) versus the invariant mass squared of the lepton-neutrino system (Eq. 4.4) in tag mode B. Left: the result obtained from all reconstructed particles. Right: that of the MC truth matched particles. The black lines indicate the cut window of the $\nu_e$ mass squared: $|M^2(\nu_e)| \leq 0.1$ GeV$^2/c^4$.

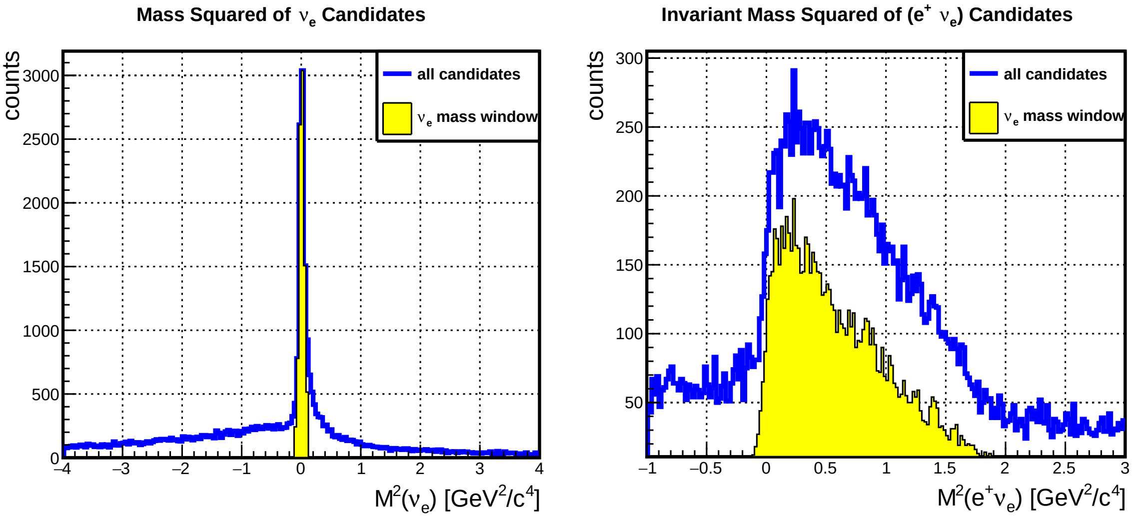

**Figure 4.89:** Reconstruction of the $(e^+\nu_e)$ system in tag mode B. Left: mass squared of $\nu_e$ candidates. Right: invariant mass squared of the lepton-neutrino system. In both figures, the blue line shows the distributions of all candidates; the yellow area indicates the distribution with a cut of $\left|M(\nu_e)\right|^2 \leq 0.1$ GeV$^2/c^4$.

In addition, the event-wise precision of the reconstructed $M^2(\nu_e e^+)$ was studied. Fig. 4.90 shows the reconstructed $M^2(e^+\nu_e)$ distribution with a comparison of the event-wise MC truth matched data. A good agreement with the MC data is achieved in the large momentum transfer region $M^2(\nu_e e^+) > 0.2$ GeV$^2/c^4$ in the reconstruction. This is consistent with the result in tag mode A.

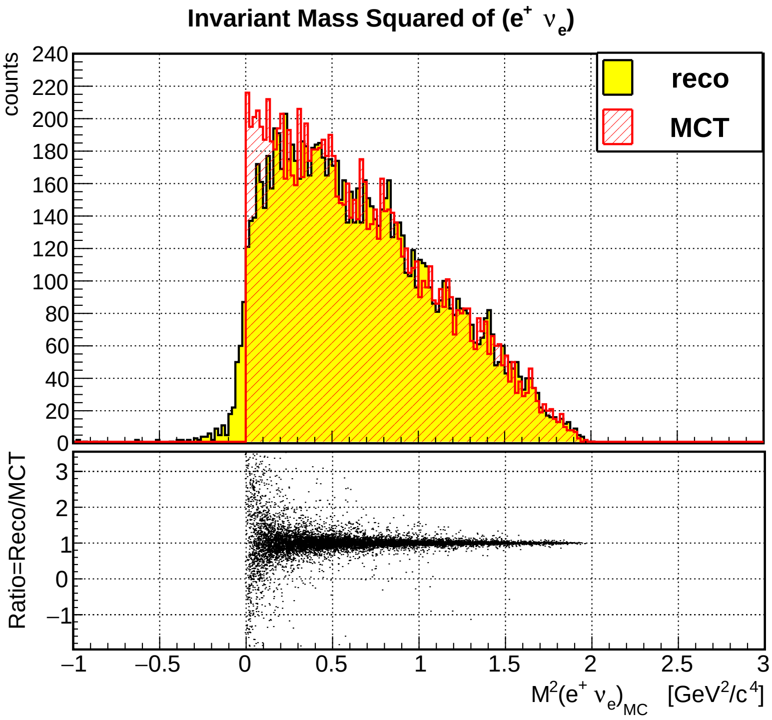

**Figure 4.90:** The event-wise precision of the reconstructed $M^2(\nu_e e^+)$ in tag mode B. Yellow area: the reconstructed result with a cut on $\left|M(\nu_e)\right|^2 \leq 0.1$ GeV$^2/c^4$. Red histogram: the $M^2(\nu_e e^+)$ calculated with the MC truth matched particles. Black dots: the ratio of the two data sets above.

Fig. 4.91 shows the count flow in the $e^+\nu_e$ system reconstruction process. After all selections, the reconstruction efficiency is 0.9% in tag mode B, which is basically consistent with the product of the MC truth matched efficiencies of the reconstructed $D_s^-$ (20.3%) and $\eta$ (4.4%).

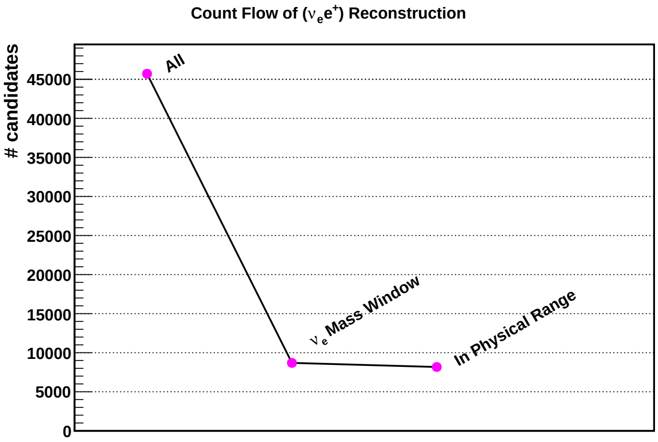

**Figure 4.91:** Count flow of reconstructing $(\nu_e e^+)$ in tag mode B. The data points follow the order of reconstruction procedure from left to right. The mass window cut is $|M^2(\nu_e)| \leq 0.1$ GeV$^2/c^4$, and the physical range cut is $0 \leq M^2(\nu_e e^+) \leq 2.02$ GeV$^2/c^4$.

**Background Events** In the $10^8$ events of $\bar{p}p \to$ everything, about 80 events of $\bar{p}p \to D_s^+D_s^-$ were constructed in tag mode B, as shown in Fig. 4.92. In tag mode A, one reconstructed event was found. Considering the reconstruction efficiency is 0.9%, the present ratio of the signal to background rates is found to be $S/B \approx 1/4400$.

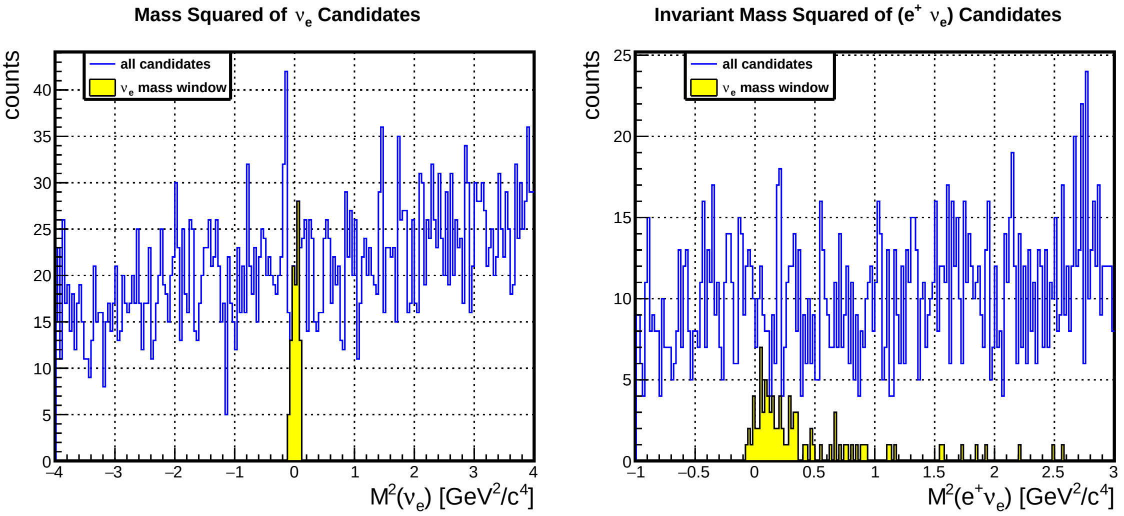

**Figure 4.92:** The mass squared distributions of the reconstructed $(\nu_e e^+)$ in DPM events in tag mode B. That of the signal events shown in Fig. 4.89. Left: mass squared of $\nu_e$ candidates. Right: invariant mass squared of lepton-neutrino system. In both figures, the blue line shows the distributions of all candidates; the yellow area indicates the distribution with a cut of $|M^2(\nu_e)| \leq 0.1$ GeV$^2/c^4$.

**Bremsstrahlung Correction** The effect of the bremsstrahlung correction on the $e^+$ was studied in tag mode B, with an independent data set of one million events with $P_{\text{beam}} = 8$ GeV$/c$. The method of Bremsstrahlung correction implemented in PandaRoot is introduced in Ref. [162]. It searches for clusters in the EMC generated by the Bremsstrahlung photons associated with each track and adds the total energy to the track's energy. The association criteria includes an energy selection $E_{\text{bumps}}/E_{\text{track}} > 1\%$ and limitations on the opening angle between the EMC bump and the $e^+$ track. Fig. 4.93 shows the ratio of the reconstructed divided by the MC true $e^+$ momentum, with and without the Bremsstrahlung correction. The distribution with the Bremsstrahlung correction has a narrower and slightly higher peak. It is found that the Bremsstrahlung correction generally improves the precision in reconstructing the $e^+$ momentum except for the addition of a small bump located at $P^{\text{reco}}/P^{\text{MC}} \approx 1.43$.

Fig. 4.94 compares the mass squared distributions of the reconstructed $(e^+\nu_e)$ with the corrected $e^+$ and without, after applying the cuts of $|M^2(\nu_e)| \leq 0.1$ GeV$^2/c^4$ and $0 \leq M^2(e^+\nu_e) \leq 2.02$ GeV$^2/c^4$. It is found that the $M^2(\nu_e)$ distribution (left) obtained with Bremsstrahlung correction has a lower peak in the signal region, leading to a lower number of counts found in the $M^2(e^+\nu_e)$ distribution (right). In addition, the ratio between the reconstructed and MC generated $M^2(e^+\nu_e)$ is studied with and without the Bremsstrahlung correction, as shown in Fig. 4.95. The ratio reflects the reconstruction efficiency of the $M^2(e^+\nu_e)$. In both distributions, the efficiency is relatively stable in the physical range of $M^2(e^+\nu_e)$. The improvement on the measurement precision from the Bremsstrahlung correction is not obvious. Consistent with the

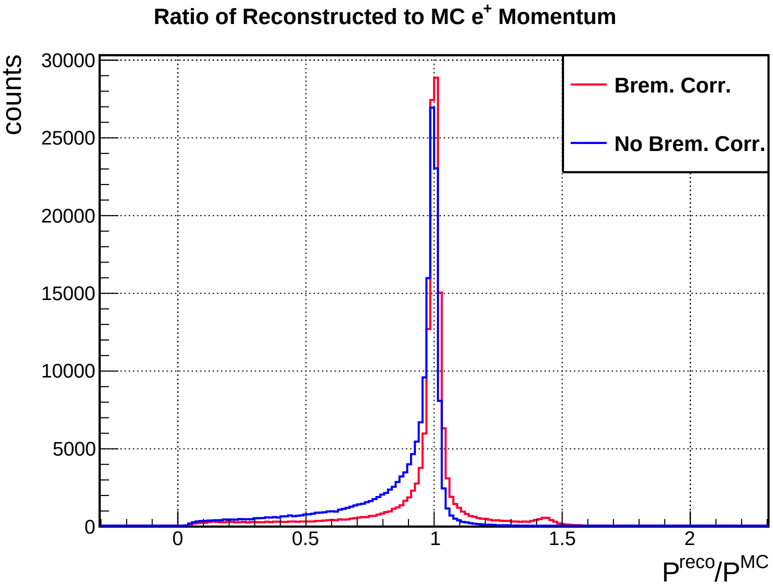

**Figure 4.93:** Ratio between the reconstructed to the MC truth matched e$^+$ momentum in tag mode B with and without Bremsstrahlung corrections. The blue line shows the distributions without the Bremsstrahlung corrections on the e$^+$; the red line indicates the distribution using the Bremsstrahlung corrections.

result of Fig. 4.94, the efficiency drops from about 0.9% (without the correction) to 0.7% (with the correction).

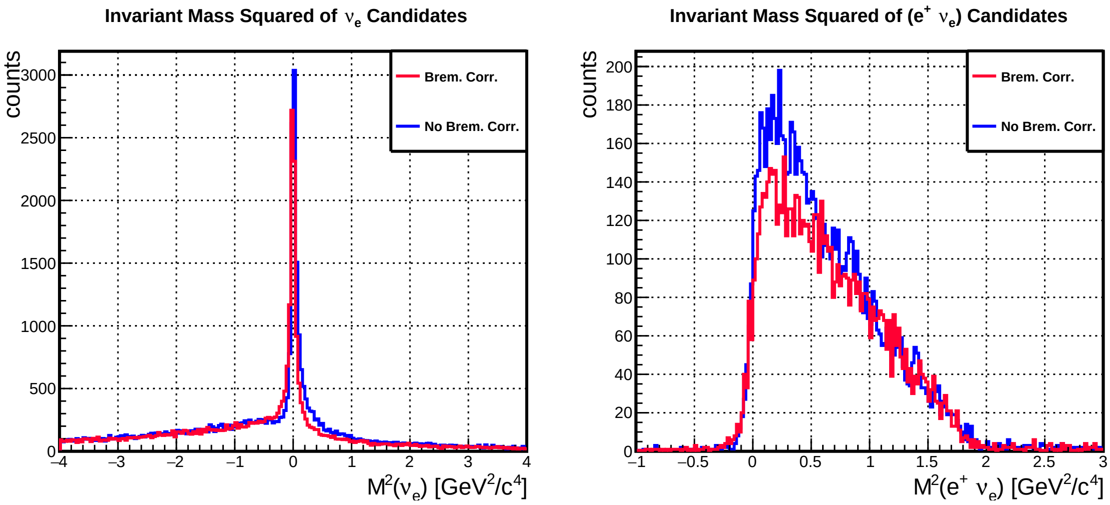

**Figure 4.94:** The mass squared distributions of the reconstructed $(e^+\nu_e)$ in tag mode B. Left: mass squared of $\nu_e$ candidates. Right: invariant mass squared of lepton-neutrino system with $|M^2(\nu_e)| \leq 0.1$ GeV$^2/c^4$ and $0 \leq M^2(e^+\nu_e) \leq 2.02$ GeV$^2/c^4$. In both figures, the blue line denotes the distributions without the Bremsstrahlung corrections on the e$^+$; the red line indicates the distribution using the Bremsstrahlung corrections.

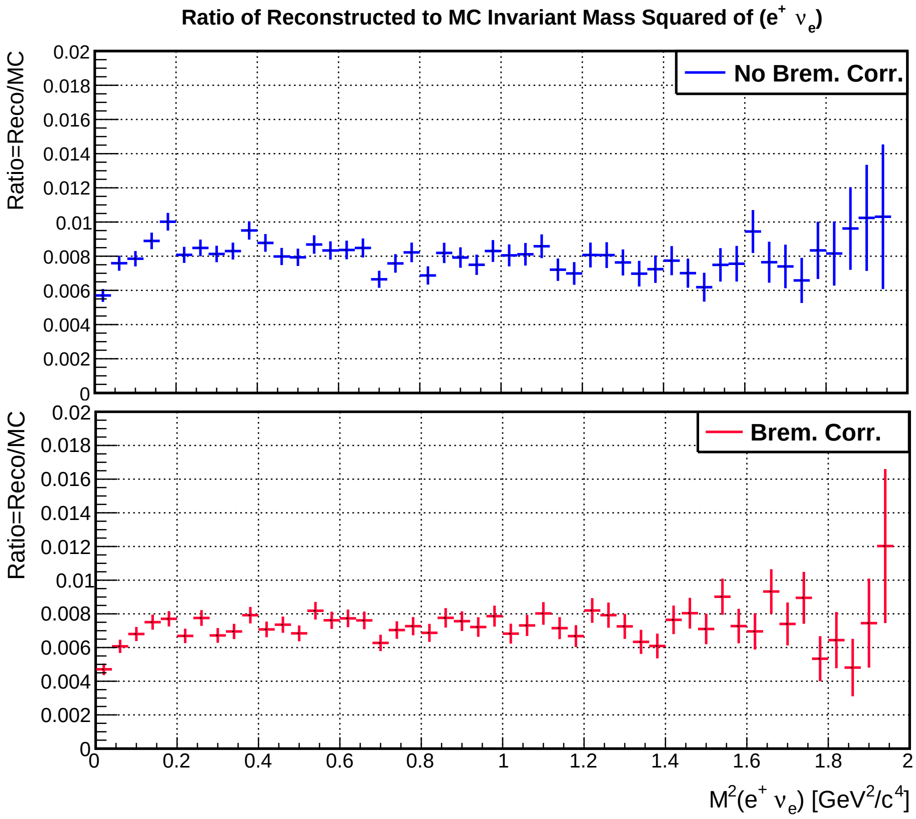

**Figure 4.95:** Ratio between the reconstructed to the MC generated $M^2(e^+\nu_e)$ distributions in tag mode B. The blue line shows the distributions without the Bremsstrahlung corrections on the $e^+$; the red line indicates the distribution using the Bremsstrahlung corrections.

The tool of Bremsstrahlung correction was developed and tested in the decay chain $\bar{p}p \rightarrow \pi^0 J/\psi$, $J/\psi \rightarrow e^+e^-$, which is a relative clean decay tree with much higher $e^+/e^-$ momentum. This study shows that the Bremsstrahlung correction can improve the precision of the reconstructed $e^+$ momentum when correct photons are correlated, but it is not sufficient to find the correct photon and therefore does not help in this case of reconstructing the $(e^+\nu_e)$ system due to the complex situation in this decay chain.

## 4.6 Efficiency and Resolution

With the present software, the decay chain has been reconstructed with two tag modes. Table 4.10 summarizes the reconstruction results with an anti-proton beam of 8 GeV/$c$.

The $D_s^-$ in tag mode B has almost eight percentage points higher reconstruction efficiency and a better vertex resolution. The momentum resolutions are the same in both tag modes. The $\eta$ reconstruction is influenced by the pion multiplicity in tag mode B, where the combinatorial background is higher than that in tag mode A. In both tag modes, the efficiencies and resolutions of the reconstructed $\pi^0$ are very similar, since the photon reconstruction is the same: both modes have six charged tracks in the decay chain.

The reconstruction efficiency of the neutrino-lepton system is consistent with the production of the MC truth match efficiencies of $D_s^-$ and $\eta$. Due to a higher acceptance of pions than kaons and the higher combinatorial background in tag mode B, the $e^+\nu_e$ efficiency is higher than for tag mode A.

In the following, the useful event rate for measuring the $D_s$ semileptonic decay form factor is estimated with the present reconstruction results (see Sec. 4.6.1). As mentioned in Sec. 4.1.1, the cross section of $\bar{p}p \to D_s^+D_s^-$ is still unclear. The simulation study at two other beam momentum settings has been carried out and the momentum dependent reconstruction efficiency of $D_s^-$ is presented in Sec. 4.6.2.

**Table 4.10:** Efficiency and resolution of the reconstructed intermediate particles in the decay chain with tag mode A: $D_s^- \to K^+K^-\pi^-$ and B: $D_s^- \to \pi^+\pi^-\pi^-$. Reconstruction efficiency (Reco. Eff.) and MC truth efficiency (MCT Eff.) are listed, and followed by mass resolution $\sigma_{\text{mass}}$, vertex resolution $\sigma_{\text{vtx}}$ and relative momentum resolution $\sigma_P/P$. Reco. Eff. is accounted for only the best candidate selected in each event. Since the multiplicity of the reconstructed $\pi^0$ is $\sim 2$, its reconstruction efficiency is not listed for comparison.

| Tag Mode | Particle | Reco. Eff. | MCT Eff. | $\sigma_{\text{mass}}$ | $\sigma_{\text{vtx}}$ [μm] | | | $\sigma_P/P$ | |
|---|---|---|---|---|---|---|---|---|---|
| | | | | [MeV/$c^2$] | $X$ | $Y$ | $Z$ | $P_t$ | $P_z$ |
| A | $D_s^-$ | 15.1% | 13.8% | 13.1 | 62 | 61 | 130 | 2.2% | 0.7% |
| | $\pi^0$ | - | 27.4% | 4.8 | | | | 1.9% | 1.8% |
| | $\eta$ | 16.4% | 4.6% | 4.1 | 100 | 97 | 187 | 1.6% | 1.3% |
| | $(e^+\nu_e)$ | 0.6% | | | | | | | |
| B | $D_s^-$ | 23.4% | 20.3% | 17.0 | 51 | 50 | 87 | 2.2% | 0.7% |
| | $\pi^0$ | - | 26.9% | 4.9 | | | | 1.9% | 1.8% |
| | $\eta$ | 16.5% | 4.4% | 4.0 | 90 | 86 | 170 | 1.6% | 1.2% |
| | $(e^+\nu_e)$ | 0.9% | | | | | | | |

### 4.6.1 Event Rate Estimate

The theoretical calculations bring a wide range of estimates on the cross section of charm production in proton-antiproton interaction, as discussed in Sec. 4.1.1. Here, we assume the cross section to produce a $D_s$ pair at $\overline{\text{P}}$ANDA is 20 nb for a beam momentum of 8 GeV/$c$, according to the predictions of Ref. [94]. The event rate $R$ is given by

$$R = L \times t \times \sigma \times (\epsilon_A \times BR_A + \epsilon_B \times BR_B), \tag{4.5}$$

where $L$ presents the luminosity, $t$ is the operating time, $\sigma$ is the cross section of $\bar{p}p \to D_s^+ D_s^-$, $\epsilon$ is the efficiency to measure the $(e^+ \nu_e)$ system, and the $BR$ stands for the branching ratio product of all channels in the decay chain (see Table 4.1). The subscripts $A(B)$ indicate the tag mode. These values are:

$$\begin{aligned}
L &= 2 \times 10^{32}\,\text{cm}^{-2}\text{s}^{-1} \qquad \text{(High Luminosity Mode)},\\
t &= 3 \times 10^{6}\,\text{s} \approx 35\ \text{days},\\
\sigma &= 20\,\text{nb},\\
\epsilon_A &= 0.6\%,\\
\epsilon_B &= 0.9\%,\\
BR_A &= 2.67\% \times 5.39\% \times 39.4\% \times 98.8\% \approx 5.60 \times 10^{-4},\\
BR_B &= 2.67\% \times 1.09\% \times 39.4\% \times 98.8\% \approx 1.13 \times 10^{-4}.
\end{aligned}$$

Therefore, the production rate is estimated to be approximately 52 events in 35 days with the high luminosity mode. 40 events are from tag mode A, and 12 events are from tag mode B. Notice that this channel has only been measured by CLEO in 2009 with a statistics of 82 events [82] (see Table 2.1). $\overline{\text{P}}$ANDA is expected to achieve this yield in about two months of operation. Precise measurement of the decay form factor however requires higher statistics, e.g. $\sim 500$ events, which means long-term data taking will be needed.

### 4.6.2 Beam Momentum Dependence

Since the charm production cross section in $\bar{p}p$ annihilation is unknown (see Sec. 4.1.1), it is necessary to study the beam momentum dependence of the $D_s$ meson reconstruction efficiency. Fig. 4.96 shows the three various beam momenta, along with the estimated cross section for $\bar{p}p \to D_s^+ D_s^-$. The consideration of choosing the beam momenta is to cover the energy range close to the threshold (7.3 GeV/$c$ and 7.7 GeV/$c$), and a higher momentum 8 GeV/$c$. Table 4.11 lists the beam momenta and the corresponding center-of-mass energies of the $p\bar{p}$ system.

For each $\bar{p}$ beam momentum one million signal events of the complete decay chain in tag mode A, i.e. $D_s^- \to K^+ K^- \pi^-$, have been simulated according to the settings in Table 4.3. The reconstruction strategy applied in this study is the same as in Sec. 4.4.1.

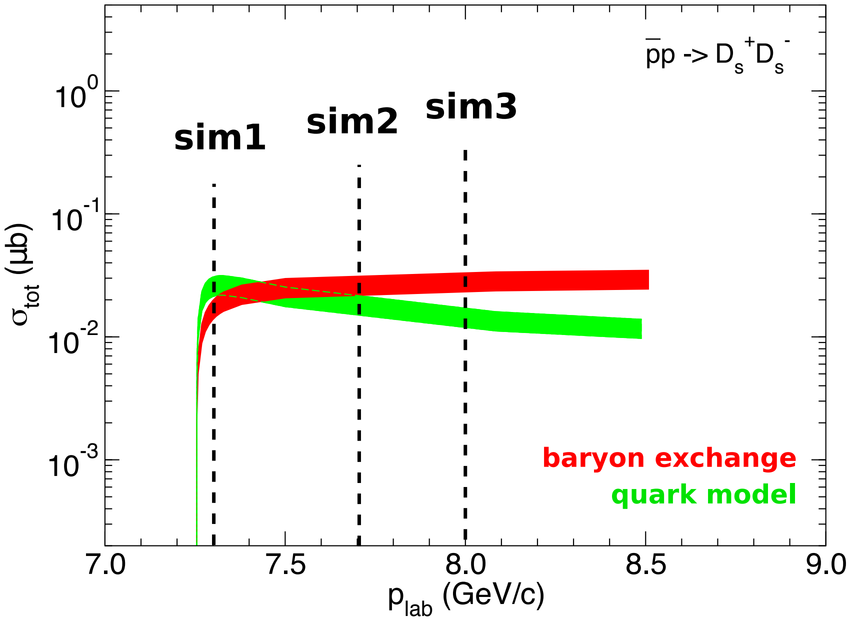

**Figure 4.96:** Simulated $\bar{p}$ beam momenta shown on the predicted cross section. The theoretical predictions of the $\bar{p}p \to D_s^+ D_s^-$ cross section are from Ref. [94], where the red band shows the result based on a baryon exchange model, and the green is from a quark model calculation. Details of the simulated $\bar{p}$ beam momenta are listed in Table. 4.11. Figure adapted from [94].

**Table 4.11:** Simulated $\bar{p}$ beam momenta and the corresponding center-of-mass energy $\sqrt{s}$ of the $p\bar{p}$ system. The threshold of $\bar{p}p \to D_s^+ D_s^-$ is listed for comparison.

| | $\sqrt{s}$ [GeV] | $P_{\text{beam}}$ [GeV/$c$] |
|---|---|---|
| threshold | 3.936 | 7.257 |
| simulation 1 | 3.946 | 7.3 |
| simulation 2 | 4.039 | 7.7 |
| simulation 3 | 4.108 | 8.0 |

From the $D_s^-$ reconstruction at three different beam momenta (see Fig. 4.97), it is seen that the count flows are very close in both reconstructed and MC truth matched candidates. The data set of "sim3" (shown in red) is slightly higher than the other two in all reconstruction steps. Fig. 4.98 shows the final reconstruction efficiency of $D_s^-$ as a function of beam momentum.

The momentum distributions of the reconstructed $D_s^-$ candidates for the different beam momenta are shown in Fig. 4.99. From the longitudinal momentum distribution, it is found that the efficiency loss in the high momentum range is more obvious for the low beam momentum.

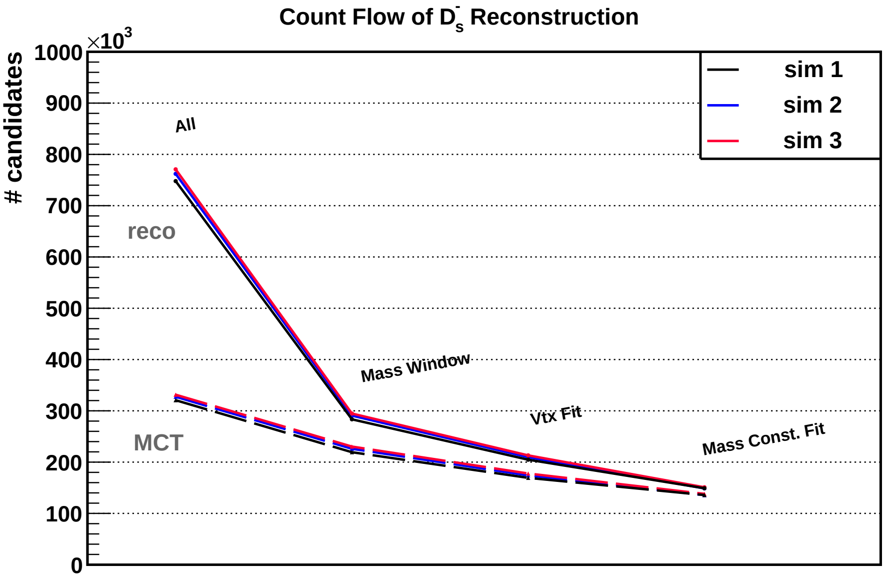

**Figure 4.97:** Count flow of $D_s^-$ reconstruction in tag mode A for three different beam momenta. The data points follow the order of the reconstruction procedure from left to right. Red, blue and black lines presents the data of the three simulations listed in Table 4.11, respectively. The solid line indicates the number of the reconstructed $D_s^-$ candidates. The dashed line presents the number of the MC truth matched $D_s^-$ candidates. A data set of one million events was used for each beam momentum.

This is consistent with the result shown in Fig. 4.98 that the $D_s^-$ reconstruction efficiency is the highest for $P_{\text{beam}} = 8$ GeV/$c$. Based on this study, $P_{beam} = 8\,\text{GeV}/c$ is recommended for the future data taking in the measurement of $D_s$ semileptonic decay form factor.

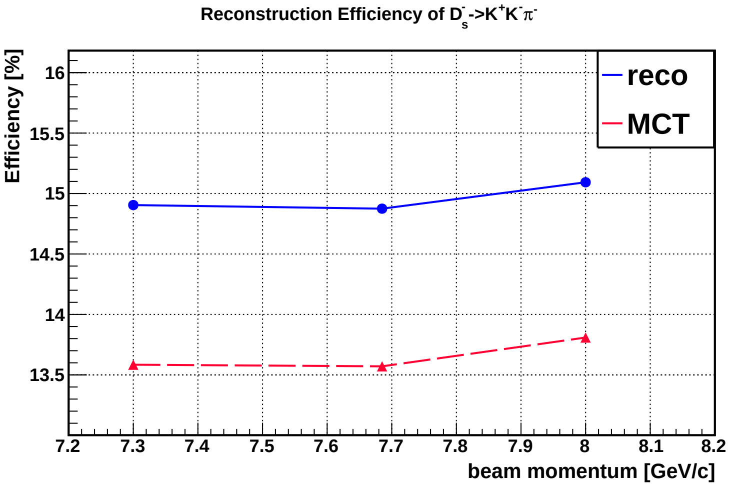

**Figure 4.98:** Reconstruction efficiency of the $D_s^-$ meson in tag mode A as a function of the beam momenta. Blue: the efficiency of the reconstructed $D_s^-$ candidates. Red: the efficiency of the MC truth matched $D_s^-$ candidates after all fits and cuts.

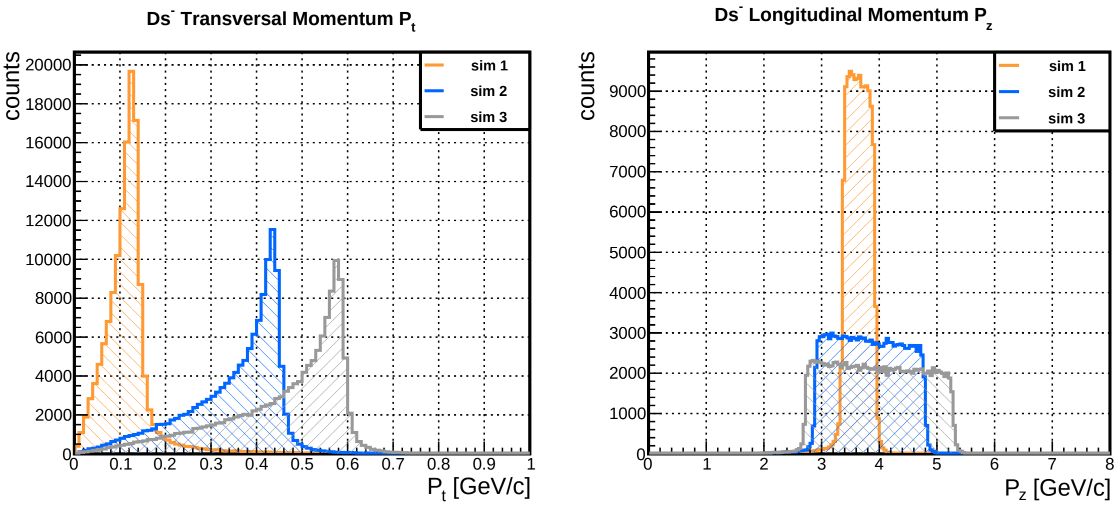

**Figure 4.99:** The reconstructed $D_s^-$ momentum distributions in the decay of $D_s^- \to K^+K^-\pi^-$ with three different beam momenta. Transversal (left) and longitudinal (right) momentum are shown. Orange: simulation of 7.3 GeV/$c$. Blue: simulation of 7.7 GeV/$c$. Gray: simulation of 8 GeV/$c$.

## 4.7 Conclusion

With the present software, the full decay chain has been reconstructed with two tag modes. A signal data set of one million events for each tag mode and a DPM data set of 100 million events have been simulated and analyzed.

For reconstructing the neutral particles in the decay chain, the EMC correlation parameters and the photon energy threshold have been systematically studied. It is found that the highest significance can be achieved when the neutral correlation parameter is 100 cm$^2$, and the photon energy threshold is 40 MeV. Due to the new strategy of reconstructing the $\eta$ vertex, the vertex resolution has been improved by a factor of two. In both tag modes, the reconstruction efficiency and resolutions of the reconstructed $D_s$, $\eta$ and $\pi^0$ are presented. The results are reasonably good except that the MC truth matched efficiencies of the neutral particles are very low in both tag modes. Due to a higher acceptance of pions than kaons, and a higher multiplicity of pions in decay chain, the combinatorial background is obviously higher in tag mode B than that in tag mode A. A problem of the mass constraint fit is found in the $\eta$ reconstruction, where the $\chi^2$ values are too small, and the probabilities are skewed close to one. The probability distribution of the vertex fit showing a rise toward prob = 1 has also been seen for both $D_s^-$ and $\eta$. The cause of this is still under investigation. It is shown that a cut on the distance between $D_s^-$ and $D_s^+$, i.e. $|\Delta Z| \leq 0.1$ cm, might help to suppress the background events.

The kinematics of the neutrino have been reconstructed based on four-momentum conservation. The $M^2(\nu_e e^+)$ resolution is reasonably good in the large momentum transfer region $M^2(\nu_e e^+) > 0.2\ \mathrm{GeV}^2/c^4$. The count rate of useful events to measure the decay form factor is estimated to be about 52 events in 35 days with the high luminosity mode. In the DPM background events, one reconstructed event in tag mode A, and 80 in tag mode B are found. Since the statistics is not sufficient to study the performance of background suppression in detail, we leave this issue for future study. With the present results, the ratio of the signal to background rates is found to be $S/B \approx 1/80$ for tag mode A, and $S/B \approx 1/4400$ for tag mode B.

Three different beam momenta have been simulated to study the momentum dependence of the $D_s$ meson reconstruction efficiency. The beam momentum of 8 GeV/$c$ is found to produce the highest reconstruction efficiency, and the cross section is not expected to vary much in this kinematic region.

# In-Beam Tests of The Micro-Vertex-Detector Pixel Readout ASIC

# 5

To study the $D_s$ semileptonic decay form factor it is essential to select those events out of the huge background with high efficiency and purity. At a $\bar{p}$ momentum of 8 GeV/$c$, the cross section ratio between $\bar{p}p \rightarrow$ everything and $\bar{p}p \rightarrow D_s^+ D_s^-$ is expected to be about $2 \times 10^6 : 1$. One way to discriminate the signal is to measure the displaced vertex from the $D_s$ decay with a decay length of $c\tau = 150\,\mu m$. For this purpose high quality tracking and a precise reconstruction of the decay vertices are essential. As the most central sub-detector of $\overline{\text{P}}$ANDA, the MVD plays an important role in the whole tracking system. The tracking resolution of the MVD is expected to be better than one hundred micrometers. In addition to the spatial precision requirement for the MVD, another aspect is the high data rate. The rate capability and tracking performance of the recent ASIC prototype for the readout of the MVD was tested in a proton beam. This chapter mainly presents the analysis of the test-beam data.

## 5.1 Basics on the ToPix ASIC

The readout ASIC for the hybrid pixel detector, ToPix, is under development at the Istituto Nazionale de Fisica Nuleare (INFN) Torino. It is a custom development in 0.13 µm Complementary Metal Oxide Semiconductor (CMOS) [163]. It will measure the charged hit 2D position, the arrival time and provide information about the deposited charge.

As introduced in Sec. 3.3.2, semiconductor pixel detectors will be used in those parts of the MVD that are close to the interaction point and at forward angles to handle the high particle flux in a high radiation environment. For high granularity, a pixel size of $100 \times 100\ \mu m^2$ is chosen. Each full size chip will have 12,760 pixels arranged in 55 double-columns with 116 pixels per column [124].

The analogue electronics in each pixel cell provides for signal amplification and charge measurement. The schematics of the analogue part is illustrated by Fig. 5.1. When a charged particle hits a sensor (labeled in green), a current signal will be created, and passed to a Charge

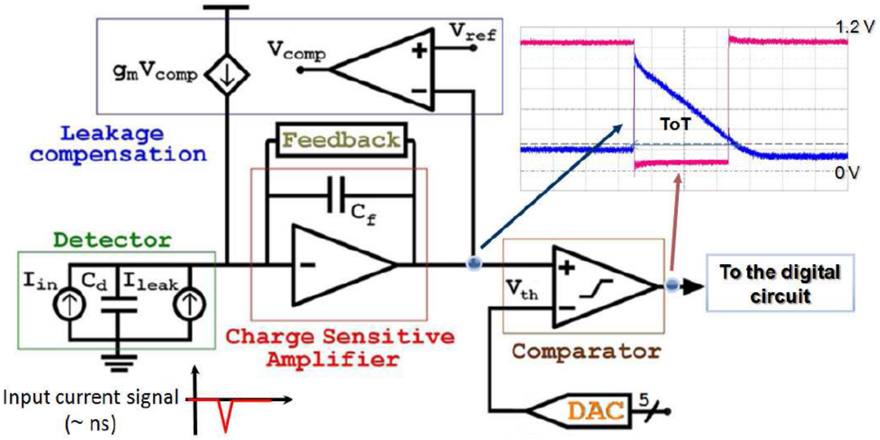

**Figure 5.1:** Analogue readout chain of the ToPix ASIC. Figure cited from Ref. [164].

Sensitive Amplifier (CSA) circuit (in red), where the signal pulse is integrated via accumulating the electrons on the feedback capacitance $C_f$. A constant current is provided to discharge $C_f$, since the leakage current caused by free charge carriers leads to a baseline shift of the measuring signal, a leakage compensation is applied to the CSA with a given reference voltage. In the comparator circuit (in brown), the signal will be compared with a defined threshold voltage $V_{th}$. If the output of the CSA (blue line) is higher than $V_{th}$, the comparator changes the logical state (from `1` to `0`, shown in pink).

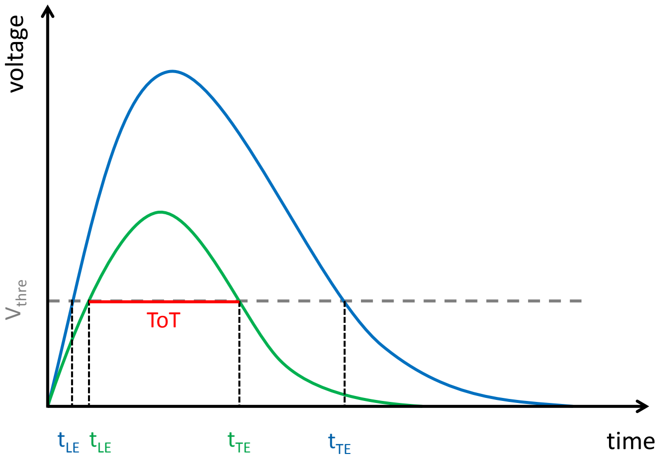

**Figure 5.2:** Schematic diagram of time-over-threshold (ToT).

The time duration of the logical state being `0` is called the Time-over-Threshold (ToT). As illustrated in Fig. 5.2, two signals after the CSA (green and blue) are depicted, where $t_{LE}$ is the time at the rising edge (leading edge) of the signal, and $t_{TE}$ is the time at the falling edge (trailing edge). The gap between $t_{LE}$ and $t_{TE}$ is the ToT, as indicated by the red line for the green signal. The ToT is proportional to the deposited charge in the sensor. Larger ToT values correspond to larger amounts of charge, i.e. the deposited charge of the blue signal is greater than that of the green one in this example. The threshold voltage can be uniform for all pixels, and also can be adjusted pixel-wise. A low threshold ensures a small effect of *time walk* (variation of $t_{LE}$ for different signal amplitudes), which is important for precise time measurements. On the other hand, the threshold has to be sufficiently high to reject noise fluctuations for a low fake hit rate.

The output of the comparator is passed to the digital readout chain. A global time information (time stamp) is generated according to the internal clock provided by the Chip Control Unit (CCU), and distributed to each pixel cell. The time stamps for the leading edge and trailing edge can be processed and stored as 12-bit (= 0d4095) digitized signals. In addition, a configuration register for each pixel allows to save the pixel configuration and adjust its voltage threshold. The pixels of a double-column are read out by a group of signals, which are set in the Column Readout Control Unit (CRCU). When both of the leading edge and trailing edge time stamp have been loaded in the corresponding pixel register, the pixel sends a busy signal to the column controller via a fast-OR chain. Then the column controller allows the pixel to write its address and time stamp data on the readout bus. The readout priority of pixels is fixed and is given by the busy fast-OR chain. The active pixel with the highest row number is read out first. The freeze signal is set by the overflow of the 12-bit time stamp counter. It basically prevents upcoming events to enter in the readout sequence in order to avoid conflicts on the data bus. It is asserted at the beginning of each time stamp counter cycle and de-asserted when the 3 Most Significant Bit (MSB)s of the time stamp becomes equals to the 3 MSBs of the chip configuration register to avoid mixing data of different frames [165]. It is also asserted during any column readout phase to avoid bus conflicts. The readout buses for each double-column are connected to a 32-entries deep First In First Out (FIFO) storage. All the FIFOs on one chip are read out by the CCU via a 320 Mb/s serial link based on the Scalable Low Voltage Signal (SLVS) standard.

The main designed specifications of the final version of ToPix are listed in Table 5.1.

**Table 5.1:** List of the ToPix main specifications [163].

| | |
|---|---|
| Pixel size | $100\,\mu\text{m} \times 100\,\mu\text{m}$ |
| Chip active area | $11.4\,\text{mm} \times 11.6\,\text{mm}$ |
| d$E$/d$x$ measurement | ToT, 12-bit dynamic range |
| Max input charge | 50 fC |
| Preamplifier noise | $< 32$ aC (200 $e^-$) |
| Input clock frequency | 160 MHz |
| Time resolution | 6.25 ns (r.m.s 1.8 ns) |
| Power consumption | $< 800\,\text{mW/cm}^2$ |
| Max hit rate | $6.1 \times 10^6/\text{cm}^2$ |
| Total ionizing dose | $< 100$ kGy |

## 5.2 Prototype ToPix4 ASIC

The fourth version of the ToPix prototype (ToPix4) [163] is a reduced size prototype with 640 pixels on a 3 mm × 6 mm die. Fig. 5.3 shows the layout scheme of ToPix4. The pixels are arranged on the left part of the ASIC in a 20 × 32 cells matrix. There are four double-columns. The two long double-columns located in the center consist of 2 × 128 pixel cells. They are folded and four times longer than the short double-columns located at the top and bottom, which consist of 2 × 32 pixel cells. The digital interface is placed on the right part of the die.

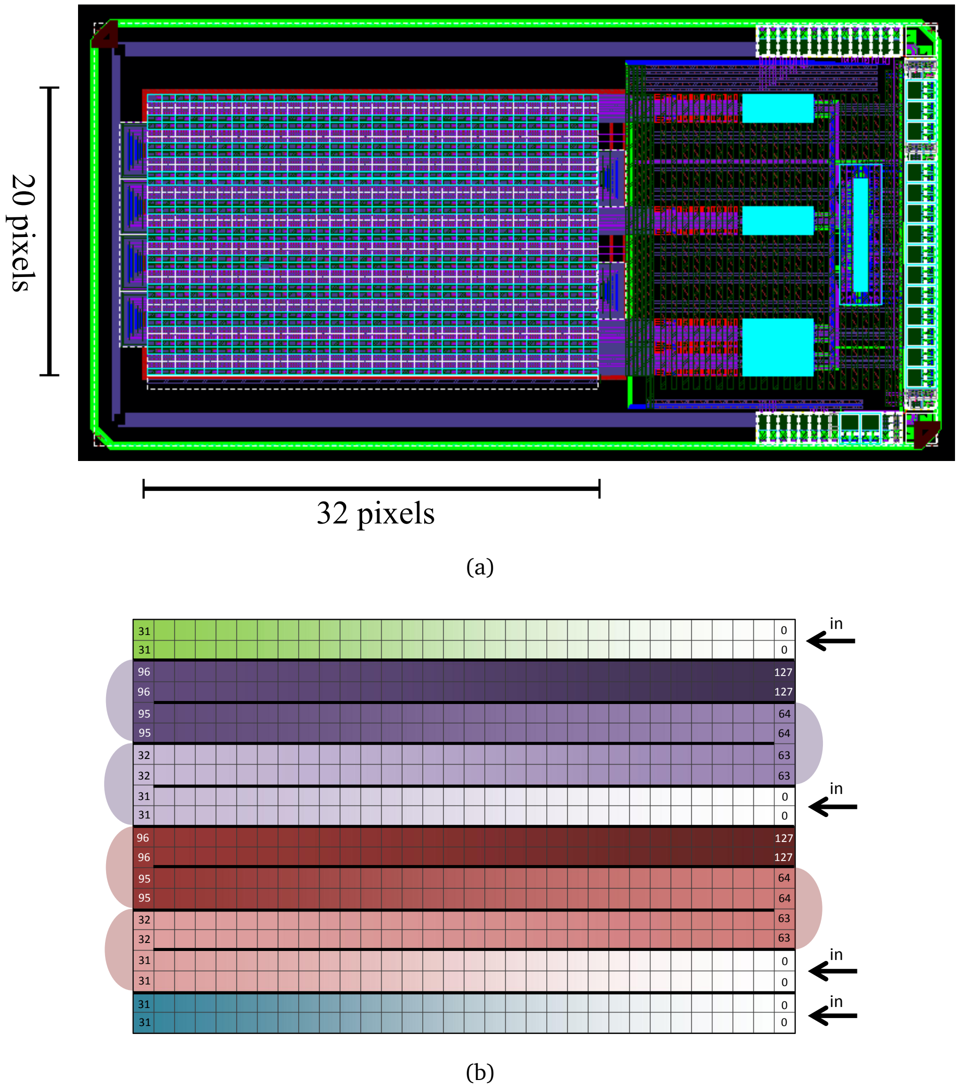

**Figure 5.3:** Layout of the ToPix4 prototype. (a) The pixels of a 20 × 32 cells matrix is located on the left part. The right part is the digital interface. Figure adapted from Ref. [163]. (b) Pixel address numbering scheme of the ToPix4. Four double-columns are shown in green and blue (short columns), purple and red (long columns). The color gradient from white to dark indicates the number increasing direction in each double-column. A connection to the digital interface is located at the "0" pixels for every double-column.

In the final version of the MVD, the basic sensitive elements will be a readout module. This module consists of a large scale sensor with variable size and 2-6 ToPix ASICs to readout the sensor. At the edges where two front-ends meet the size of the sensor pixels is enlarged to bridge the gap between the two ASICs.

Since the chip contains both analog and digital parts, the charge signal from the sensor is amplified and measured by the analog part and then digitized, as introduced in Sec. 5.1. The data structure of ToPix4 output includes the frame header, the data packages, and the frame trailer. Each of them contains 40 bits. As shown in Table 5.3 each packet has an individual bit definition. The frame header and the frame trailer packets are sent at the beginning and at the end of each frame, respectively. In between several data packages can be sent. The main content of one data package is the time stamp information of the leading edge and trailing edge, and the pixel address. The pixel address contains the pixel number (shown in Fig. 5.3(b)), the label indicating which column, and the left/right side label due to the double-column structure. In addition, an Error Correction Code (ECC) and Cyclic Redundancy Check (CRC) are used to detect and correct data corruption during transmission.

**Table 5.2:** Bit definition of ToPix4 output data. In total 40 bits are used for each packet.

| Frame Header | | Data Package | | Frame Trailer | |
|---|---|---|---|---|---|
| # bits | content | # bits | content | # bits | content |
| 2 | header (0b01) | 2 | header (0b11) | 2 | header (0b10) |
| 12 | chip address | 14 | pixel address | 16 | # events |
| 8 | frame counter | 12 | leading edge | 16 | frame CRC |
| 12 | not used | 12 | trailing edge | 6 | ECC |
| 6 | ECC | | | | |

## 5.3 Jülich Digital Readout System

In order to test the readout front-end ASIC of the MVD, the Jülich Digital Readout System (JDRS) [166] was developed. The readout system is based on a FPGA firmware and is easily adoptable to test different versions of ToPix prototypes. It has been used, e.g. in the ToPix3 in-beam test [167].

Fig. 5.4 illustrates the major components of the JDRS. The software framework, which is written in C++, enables the data communication and accessing the functionality of the firmware and chips. Therefore, the prototype ToPix4 ASIC can be controlled by the users with a GUI on PC. The central hardware component is the FPGA-based digital Readout Board. It is configured with a firmware which implements the desired functionality and configures the interfaces. The Readout Board is used to transport the commands and process data in subtask modules. The Test Board is the interface between the ToPix4 and the readout system JDRS (see Fig. 5.5). It

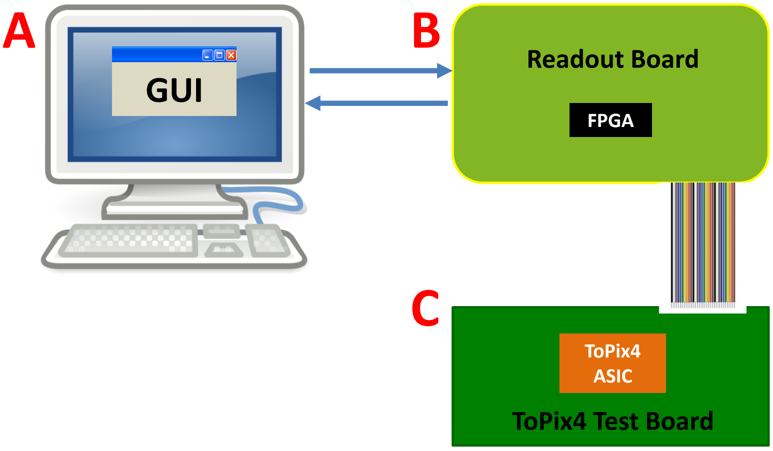

**Figure 5.4:** Schematic drawing of the JDRS. A: MVD readout framework software with GUI running on a PC. B: Readout Board, based on FPGA and connected to the ASIC test board. C: Test Board, where the ToPix4 ASIC is implemented for testing.

supplies the required voltages to ToPix4 and converts the signals between the ToPix4 (in SLVS format) and the JDRS (in Low Voltage Differential Signal (LVDS) format).

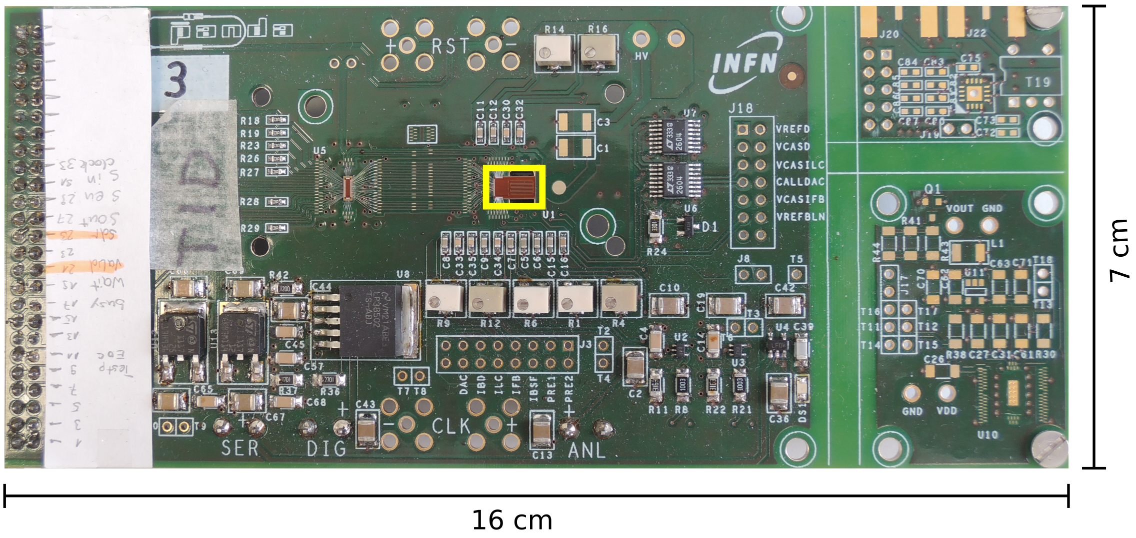

**Figure 5.5:** Photograph of the Test Board with an equipped ToPix4 ASIC. The ToPix4 is in the center, highlighted in yellow.

## 5.4 Experimental Setup

An in-beam test of the ToPix4 front-end ASIC was performed in October 2014 at the Forschungszentrum Jülich (FZJ) in order to study the tracking performance with four planes and to develop the data analysis framework. Details of this experiment are presented in the following section.

### 5.4.1 Beam Conditions

A proton beam with 2.95 GeV/$c$ was provided by COSY. This momentum ensures that the protons are Minimum Ionizing Particles (MIP). COSY is a cooler synchrotron located in FZJ and a storage ring for (polarised) protons and deuterons in the momentum range between 0.3 GeV/$c$ to 3.7 GeV/$c$. It contains two cooling systems to reduce the phase space volume of the beam [168]. The beam particles are produced by the Jülich Light Ion Cyclotron (JULIC) and transported to COSY. This accelerator complex has been used to perform hadron physics

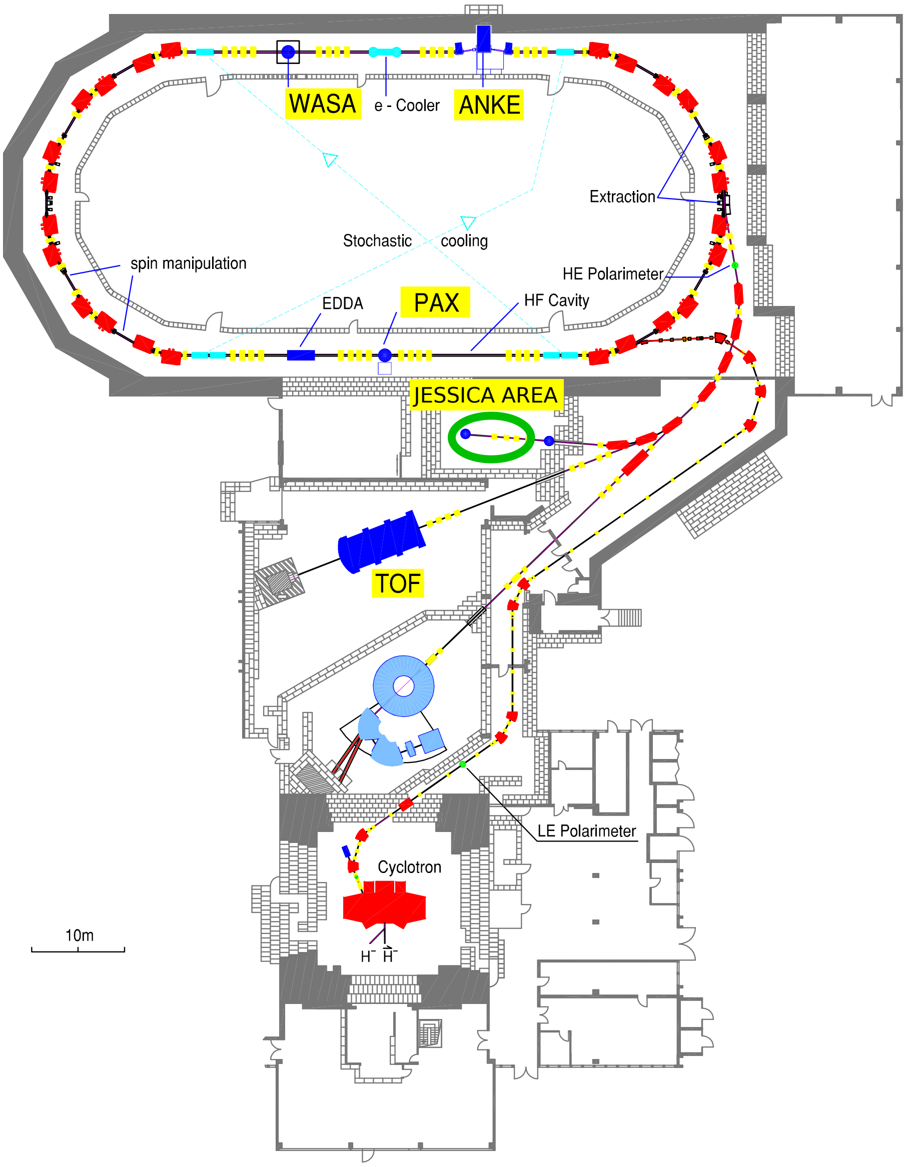

**Figure 5.6:** Layout of the COSY cooler synchrotron. The experiments which have been recently performed at COSY are highlighted in yellow. The ToPix4 test area is indicated in green. Figure adapted from Ref. [168, 169].

experiments, e.g. WASA and TOF, with either internal circulating beam or extracted beam. The ToPix4 test was carried out with an external beam at the former Jessica area, as shown in Fig. 5.6.

The beam intensity can be verified via an external Micropulse (MP) trigger. When the MP is disabled, all protons from JULIC will be injected into COSY and passed to the test setup. The MP can be varied between 0 and 1, or switched off. Lower MP values lead to a lower beam intensity. The highest intensity is reached when the MP is switched off. Various settings of the MP allow the performances of ToPix4 to be studied under different beam intensities, as data files listed in Table. 5.3.

### 5.4.2 Test System

In the beam test, four ToPix4 front-end ASICs were set up, as shown in Fig. 5.7. The four ASICs were placed in the beam line with a 6 cm gap between each. Before and after the test beam crossed the ASICs, a layer of silicon strip detectors was equipped for detecting protons, and a scintillator paddle was installed as a trigger for the strip readout. Every ASIC was connected to an individual readout system. One of the four ToPix4 ASICs has a double sized sensor row at its edges. All of them were operated without threshold tuning. The internal clock frequency of ToPix4 was varied from 50 MHz to 100 MHz, 125 MHz, 150 MHz and 160 MHz. Because of readout problems for frequencies above 50 MHz only the measurement at 50 MHz is presented here.

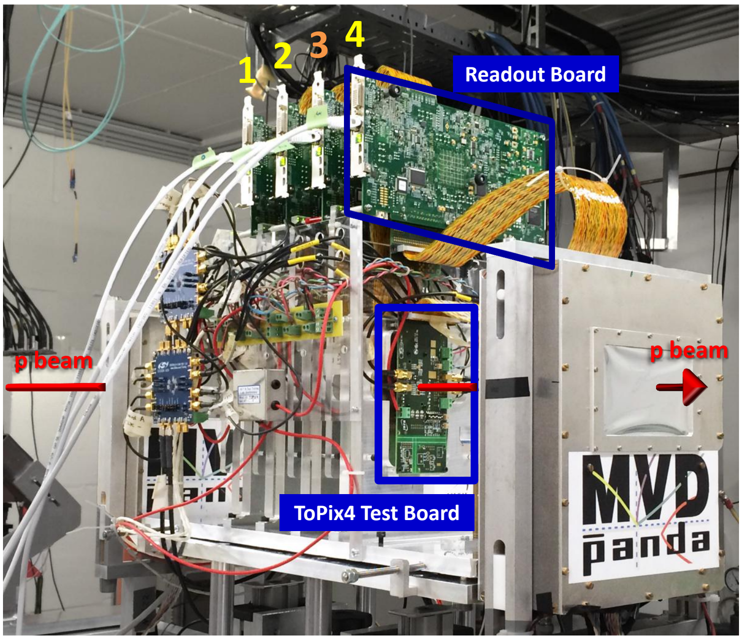

**Figure 5.7:** Experimental setup of four ToPix4 prototypes in the test beam extracted from COSY. The distance between them is 6 cm. ToPix4 No.3 has double sized sensors in the first and the last row. Photo taken from [170].

## 5.5 Test-Beam Data Analysis

**Analysis Workflow** The analysis workflow contains several steps, which are shown in Fig. 5.8. The output data of each front-end chip is stored in separate binary files, and encoded in Gray code. The first step is to convert the raw data to Root files, which are accessible by the PandaRoot framework. The procedure of decoding is basically to access the information packets as defined in Table 5.3. If a complete set of header-data-trailer is found, the check on ECC and CRC is applied before storing the data. For the incomplete set, i.e. header or/and trailer is missing, the data is not stored. The raw data is converted by PndMvdReadInTBDataTask to be PndSdsDigiTopix4, which stores the information on the number of the front-end, pixel address, time stamp, leading/trailing edge and so on.

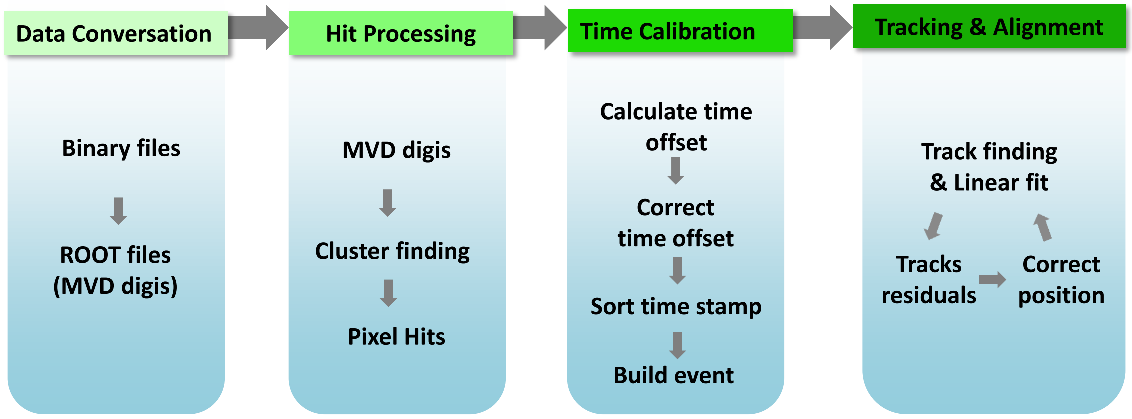

**Figure 5.8:** Workflow of the data analysis.

The Digis are sorted by time stamp for each front-end. The clustering algorithm searches for direct neighbours for each Digi. All neighbouring Digis in a small time window are associated to a cluster. According to the shape of the clusters, 3D space points are constructed as ToPix4Hits by PndMvdToPix4ClusterTask, where the information stored in PndSdsDigiTopix4 is passed to ToPix4Hits.

In the ideal case, all the clocks of the readout front-ends are synchronous and starting at the same time. However, due to a wrong reset signal, the clock are synchronous but the start time is randomly different for all four ASICs. Therefore, a time calibration is needed before event building. The idea is to find a time offset via calculating the hit-wise time differences between one reference front-end to the others, and shift the time stamp of all pixels according to the time offset. If the time offset is a global value during the whole run time, the time shift can be done commonly to all pixels, otherwise it needs to be treated in different time periods, adapting to the variation of the time offset.

Time sorting is applied on the time calibrated ToPix4Hits of all four font-ends. A time gap between hits is used to associate the clusters from the four front-ends to an event. The acceptable time gap for consecutive hits to be considered being from the same event is $\leq 50\,\mathrm{ns}$.

The last procedure is tracking and alignment. For each event, a track finder searches for possible straight lines through the four front-ends with the ToPix4Hits. The track fitting is based on a linear fitting algorithm. Afterwards, the residuals of the reconstructed tracks are calculated. A simple alignment procedure can be done by shifting the front-ends positions in the $X-Y$ plane (perpendicular to the beam direction) according to the mean value of the calculated residuals, and performing the tracking again with the updated `ToPix4Hits`. The results of each step are shown in this section.

**Data Files** In the beam test, various data sets were obtained. The analysed data files are listed in Table 5.3 with information on the Micropulse (MP), trigger rate of the scintillator detectors and the number of particle spills (extraction time and beam pauses). The trigger rate is taken as a relative measure of the beam intensity. The relationship between MP and trigger rate is not strictly linear as shown in Fig. 5.9, where the trigger rate is plotted as a function of MP.

**Table 5.3:** List of the analysed data files at an operating frequency of 50 MHz. The values of the trigger rate are approximate.

| MP | Trigger Rate [$\times 10^3$ 1/s] | # Spill | File Name |
|---|---|---|---|
| Disabled | 290 | 10 | 2014-10-26-22-30-15 |
| | | 1 | 2014-10-26-22-39-36 |
| 0.8 | 175 | 1 | 2014-10-26-23-05-20 |
| 0.6 | 105 | 1 | 2014-10-26-23-25-15 |
| 0.4 | 52 | 1 | 2014-10-26-23-46-09 |
| 0.2 | 15 | 1 | 2014-10-27-00-06-02 |
| | | 9 | 2014-10-26-23-50-34 |
| 0.02 | 0.94 | 11 | 2014-10-27-00-11-29 |
| | | 1 | 2014-10-27-00-20-16 |

Fig. 5.10 shows the number of hits as a function of the time stamp (MP disabled) for one spill of the proton beam and ten spills, respectively. In this case, one spill is about 17 s long and contains approximately $2.8 \times 10^6$ hits.

There is a known problem in the readout that dummy events with wrong pixel addresses are produced when a hit is found in a "busy critical" area [171]. In addition, if only high priority pixels are hit, fake events can be generated due to the busy signal from the column is sampled twice for one event since the transition of busy signal is not fast enough to prevent a second sampling. Therefore, the data set taken with 50 MHz clock frequency was chosen to study the tracking performance.

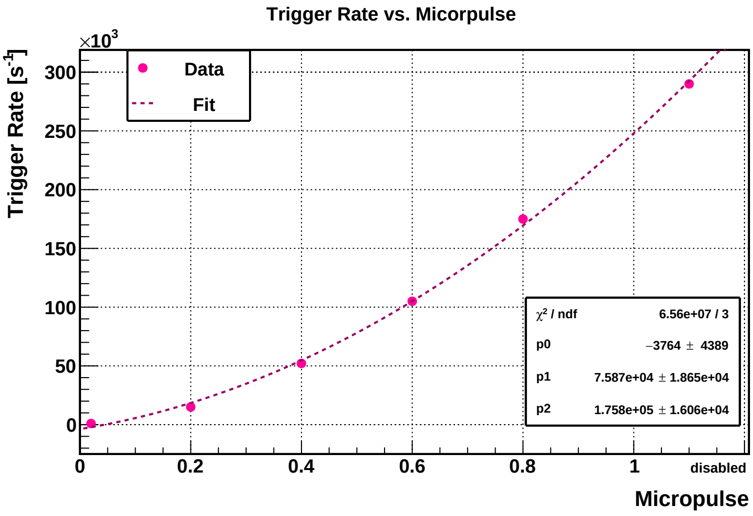

**Figure 5.9:** Trigger rate versus MP distribution. The dashed line represents a polynomial fit to the data.

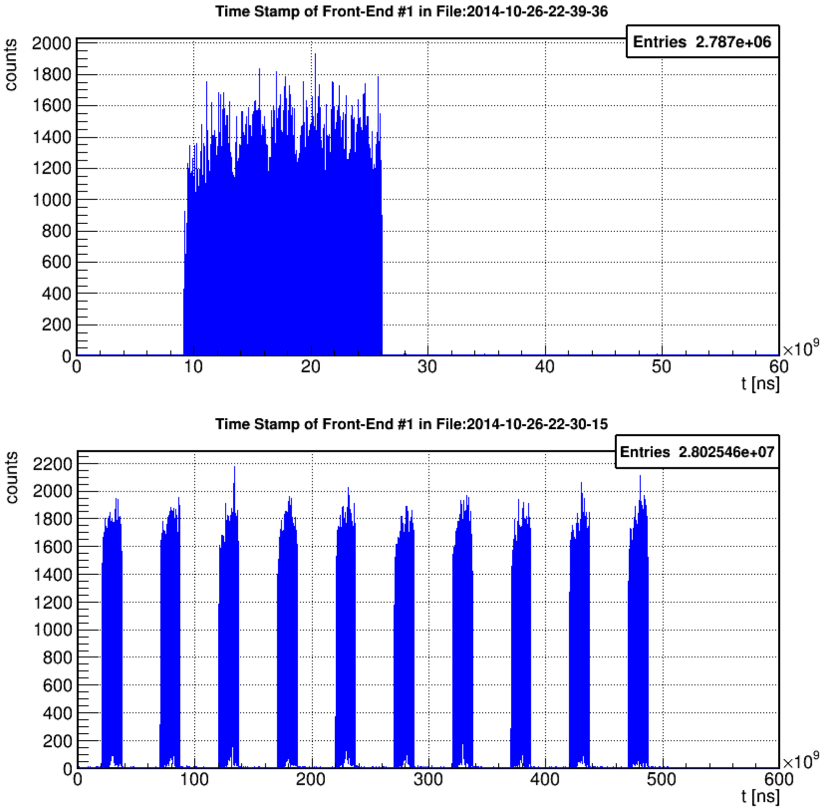

**Figure 5.10:** Number of hits as a function of the time stamp on the first front-end: one spill (upper frame) and ten spills (lower frame). The individual spills are clearly visible.

### 5.5.1 Measurement of Time-over-Threshold

As introduced in Sec. 5.1, the deposited energy of a charged track in the pixel sensor can be measured via the ToT method. This section summarizes the results on the ToT measurements.

The leading edge and trailing edge distributions are shown in Fig. 5.11 and Fig. 5.12, respectively, where each histogram contains one proton spill each for six different beam intensities for one front-end ASIC. One would expect a flat distribution as it can be seen for the lowest intensity, but a continuous drop of the count rate appears if the leading or trailing edge is in the range of 2050-2070. After that drop the count rate increases again. The region of the efficiency drop matches exactly the point when the freeze stop signal is set to zero and the data readout starts. Therefore, it is assumed that the efficiency loss is caused by the readout.

In order to estimate the efficiency loss, it is assumed that for low time stamps, where the count rate is highest, all hits are measured. Therefore, the average count rate of the first 200 bins in the leading/trailing edge distributions for front-end #1 (upper right figure in Fig. 5.11 and 5.12) were used to evaluate the efficiency loss. The difference between the average rate minus the count rate in each bin was used to calculated the bin-wise efficiency loss.

For both the leading edge and the trailing edge, the efficiency loss is shown in Fig. 5.13 as a function of the trigger rate. It is found that the efficiency loss of the leading and trailing edges behave similarly. As the trigger rate increases, the efficiency loss rises, up to 27.7% for the trailing edge and 26.1% for the leading edge. Furthermore, the mean values of the count rates in the first 200 bins of the leading and trailing edge distributions are plotted as a function of

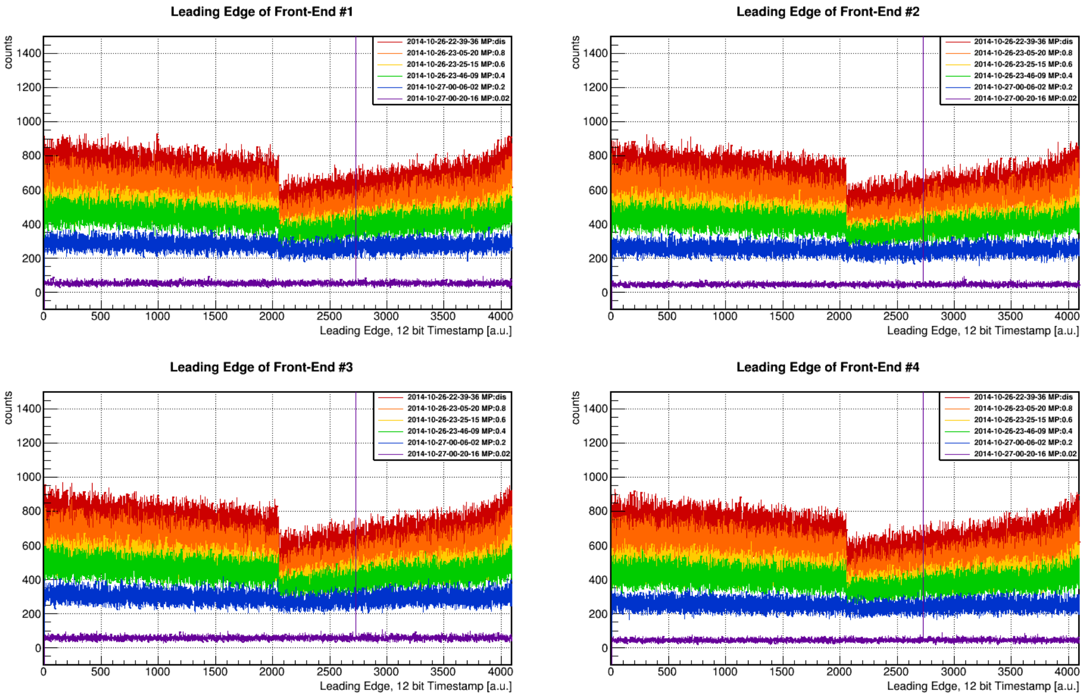

**Figure 5.11:** Leading edge distribution for six different beam intensities.

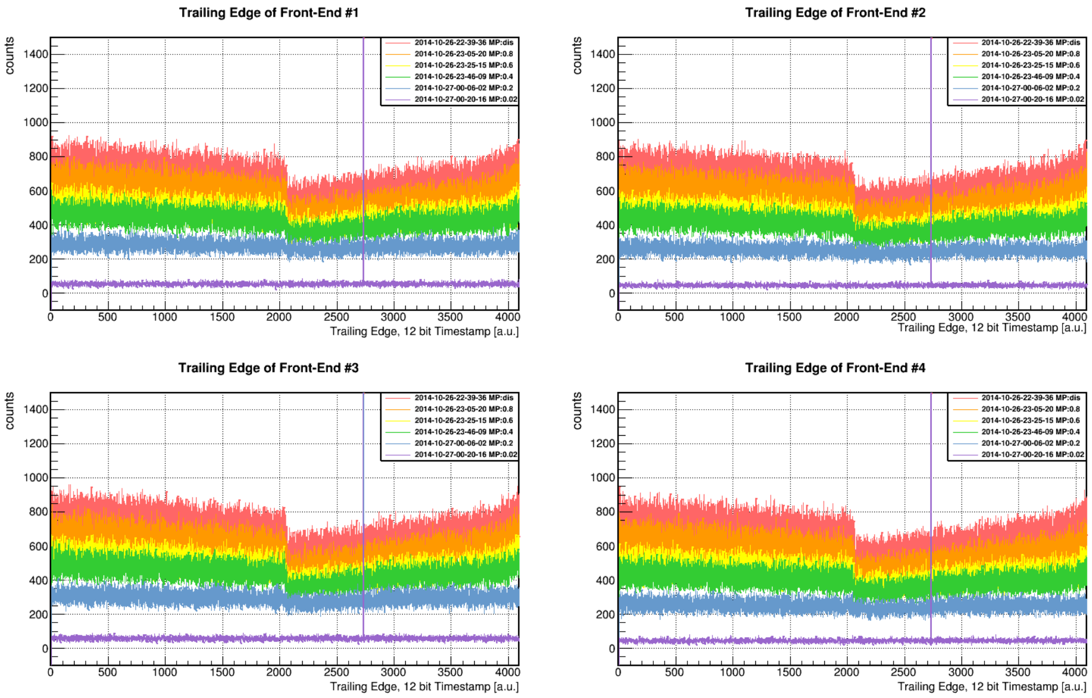

**Figure 5.12:** Trailing edge distribution for six different beam intensities.

the trigger rate in Fig. 5.14. The distribution is not linear, which implies that in addition to the difference between the first 200 bins of the time stamp to the other bins, a general efficiency loss happens as the trigger rate increases, not only at the drops caused by the freeze mechanism. The reason why the behaviour is different for the leading edge and the trailing edge is not clear.

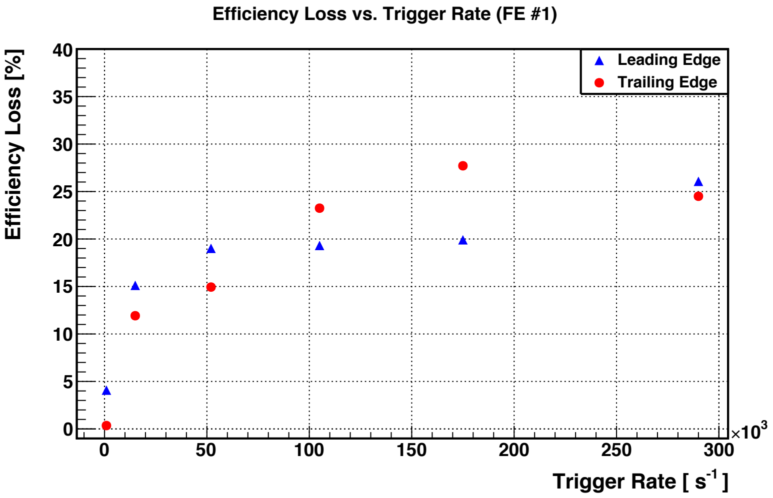

**Figure 5.13:** Efficiency loss as a function of the trigger rate. The blue triangles show the leading edge data; the purple dots indicate the trailing edge data. This result was obtained from front-end #1.

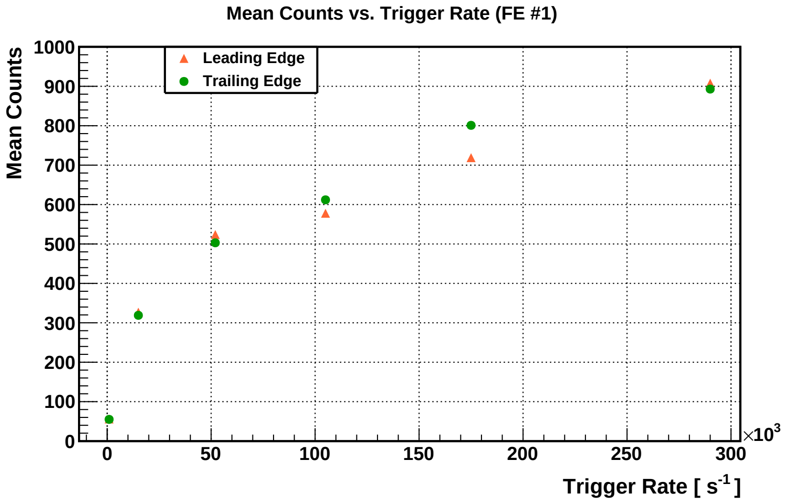

**Figure 5.14:** Mean number of counts as a function of the trigger rate. The orange triangles show the leading edge data; green dots indicate the trailing edge data. The mean values are taken by averaging the first 200 bins of Fig. 5.11 (leading edge) and Fig. 5.12 (trailing edge) for front-end #1.

This question can only be answered by detailed simulations of the ASIC, which go beyond the scope of this thesis.

In addition, a sharp spike at 2730 (less obvious but also exists at 2729 and 2731) can be seen in the figures of all beam intensities for both leading edge and trailing edge. It is due to a readout problem, where dummy hits are produced with the leading or trailing edge's

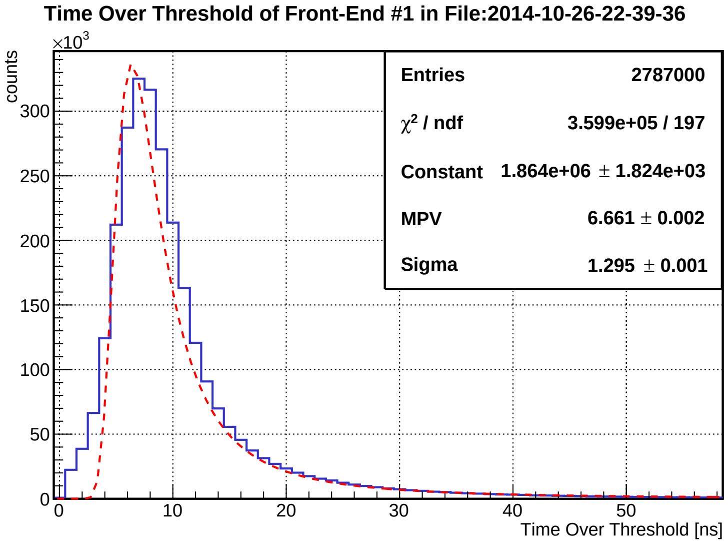

**Figure 5.15:** Time-over-threshold distribution (blue solid line). A Landau function is fit to the data (red dashed line). The fit parameters are listed. [File: 2014-10-26-22-39-36]

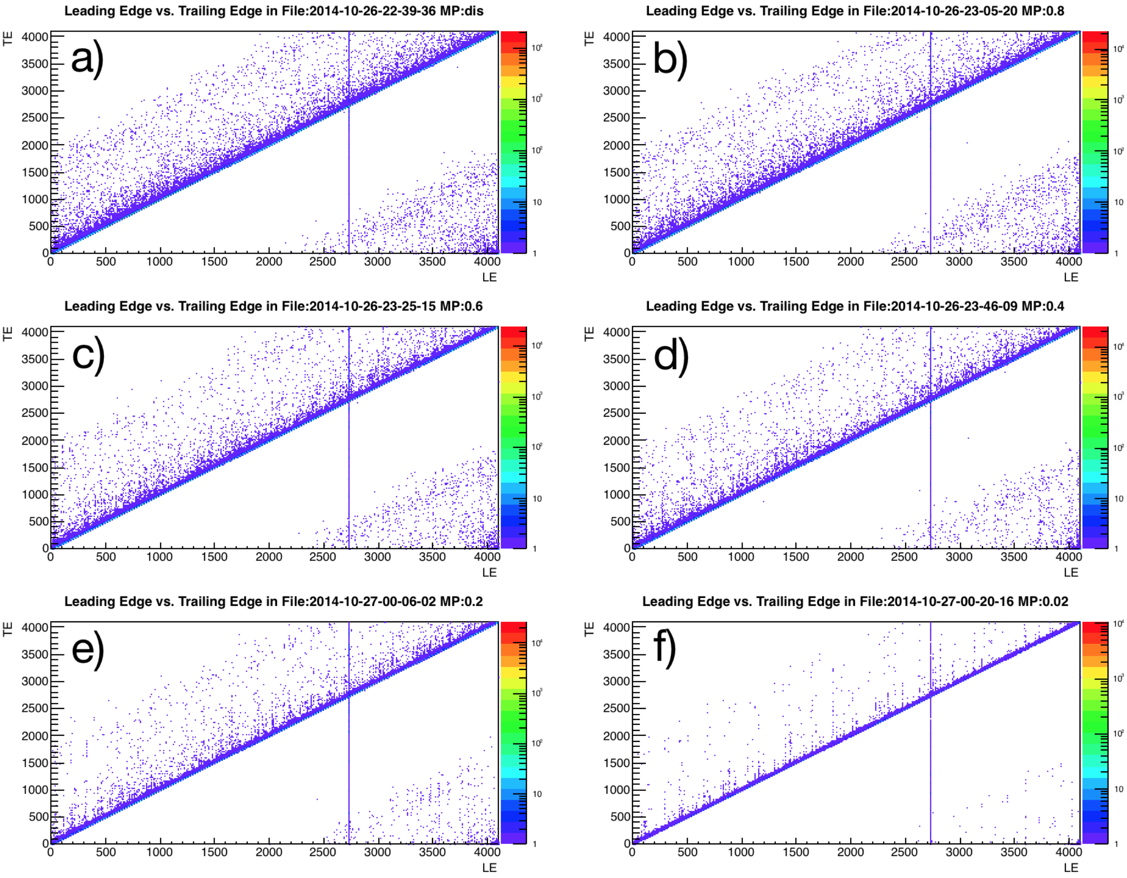

**Figure 5.16:** Trailing edge vs. leading edge for six different beam intensities. The beam intensity reduces from frame a) to frame f).

corresponding Gray code digits are all set to 1. This behaviour has been seen in the ToPix3 [167], and stays in ToPix4. These dummy events are excluded in the data set during the hit processing step.

The difference between the trailing edge and the leading edge (ToT) is proportional to the deposited charge. The ToT distribution is approximated by a Landau function, as shown in Fig. 5.15. For the ToPix4 front-end, a MIP in the 100 µm silicon epitaxial sensor produces an ionizing charge of approximately 1.3 fC.

Fig. 5.16 shows the distribution of the trailing edge versus the leading edge. Since the leading edge and trailing edge are correlated by a Landau distributed ToT, it is expected to see an intense diagonal line coming from the peak of the Landau function, and a loose band along the line from the trailing edge side due to the long tail of the ToT distribution. With increasing beam intensity, the pattern of the distribution becomes more obvious. On each figure, there is a segment of counts on the bottom right area. It is the overflow from the top part of the diagonal distribution. The vertical line on the leading edge is due to the same dummy events as in Fig. 5.11.

### 5.5.2 Clusterization

As illustrated in Fig. 5.8, cluster finding is one step of the hit processing. Clusterization is important to reconstruct signal and rejecting the Digis caused by dispersed noise. The clusterization step was done by PndMvdToPix4ClusterTask to search for neighbouring Digis and group them to form ToPix4Hits in 3D space.

Fig. 5.17 shows the Digi multiplicity distribution after clusterization, where roughly 95% of clusters are constructed as a single Digi. For the 5% of clusters containing more than one Digi, the 3D positions of ToPix4Hits are defined at the energy weighted geometric center. Clusters containing two Digis bring a better spatial resolution in reconstructing the ToPix4Hits compared to clusters with only one Digi.

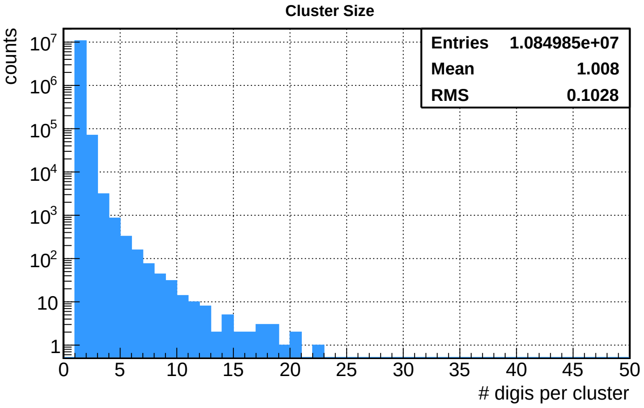

**Figure 5.17:** Cluster size distribution. [File: 2014-10-26-22-39-36]

### 5.5.3 Hit Map

Fig. 5.18 shows the hit map of the four front-ends. The ToPix4Hits are plotted in a 20 × 32 pixel matrix. The beam spot can be clearly seen. As mentioned in Sec. 5.4.2, the third front-end is equipped with double size sensor pixels at the top and bottom edges, therefore the number of hit counts in these areas is approximately two times higher than that on other front-ends. In all plots, there is a blank patten jumping every two pixels at Col=2 (short double-column). The reason for this is still under investigation.

The hit map for the highest beam intensity is shown in Fig. 5.19. Regions of high statistics is found for the pixels of all front-ends. The reason for this behaviour is the readout scheme of ToPix, which gives higher readout priorities to the pixels with higher index numbers. Due to the folding structure of the double-columns (see Fig. 5.3(b)) one gets the pattern measured. This effect becomes more obvious as the trigger rate increases, because the efficiency loss is larger for higher beam intensities. Thus, the end regions of both the long and the short columns have more hits, and the double-column structure can been seen.

In addition, it can clearly be seen that the beam spot is not precisely at the same position in each of the four front-ends. This is due to the limited mounting precision and the beam

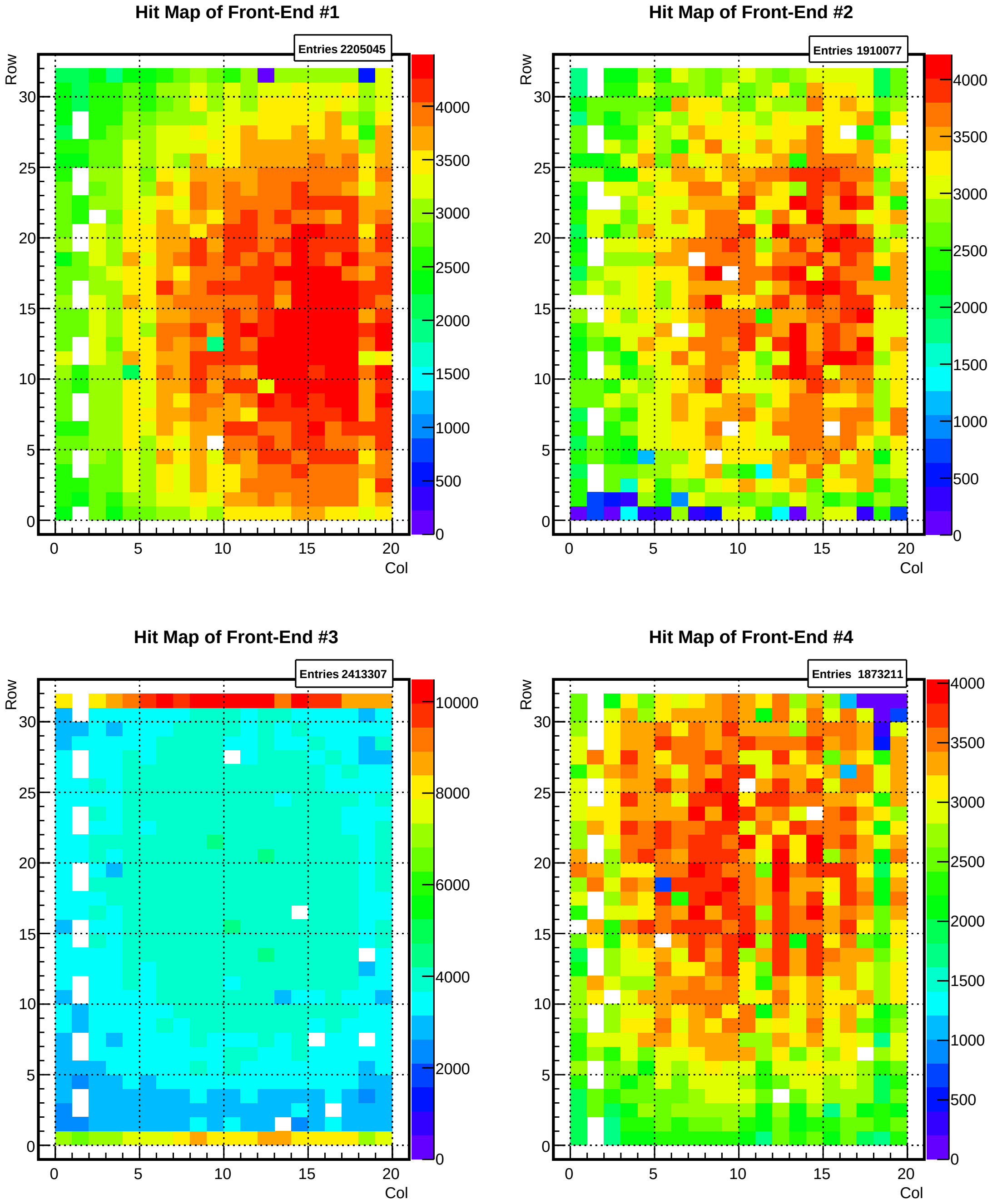

**Figure 5.18:** Hit map of the four front-ends, excluding the dummy hits. Front-end #3 has double sized sensor pads in the first and the last row, therefore the hit map in that region shows a different distribution than the others. [File: 2014-10-27-00-11-29]

direction being not strictly along the nominal direction. For adjusting the mounting position, an alignment on the front-ends is necessary to study the tracking performance (see Sec. 5.5.6).

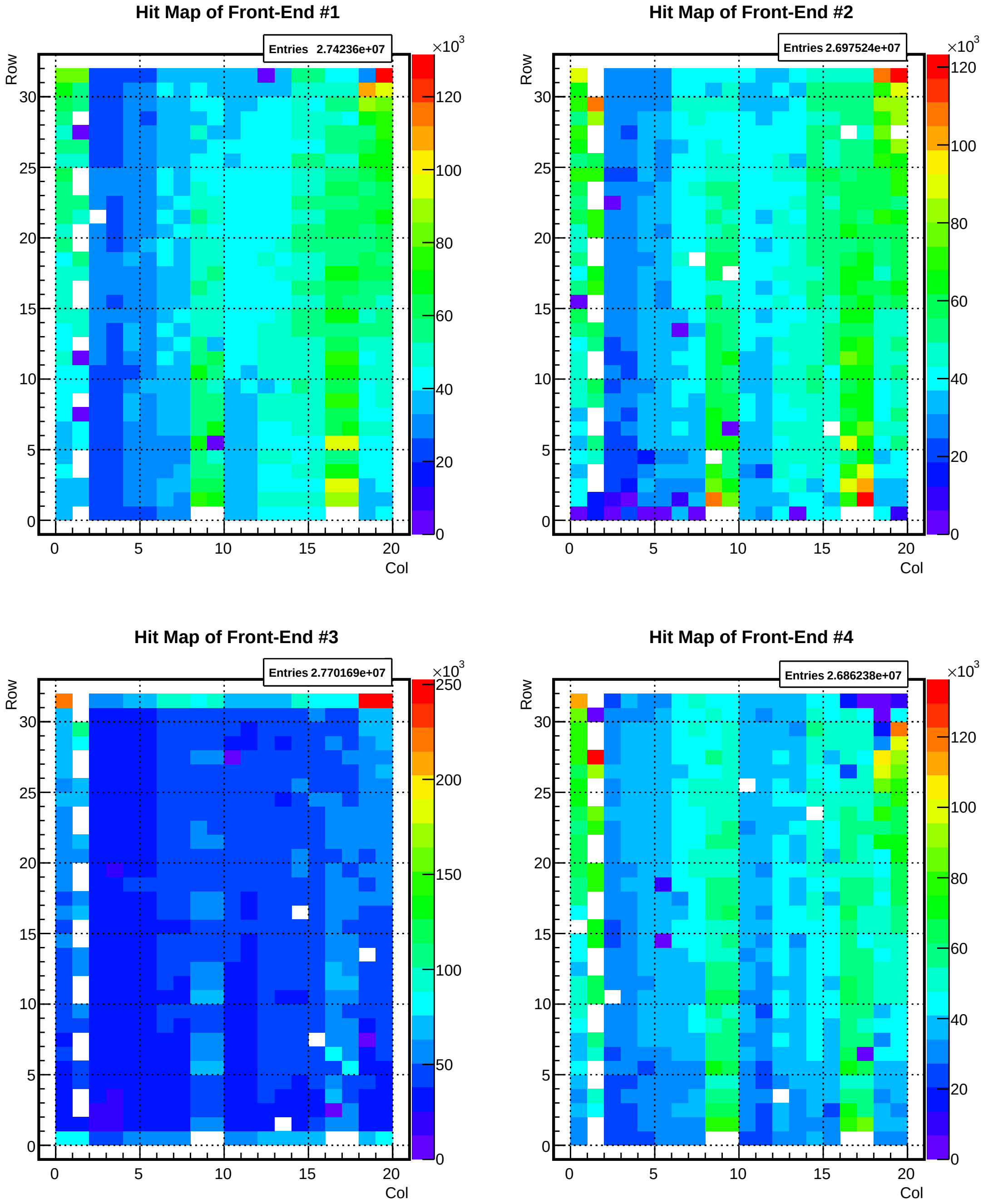

**Figure 5.19:** Hit map of the four front-ends with high beam intensity. [File: 2014-10-26-22-30-15]

### 5.5.4 Time Calibration and Event Building

The time information is essential for the event building. Before event building, the time calibration and time sorting are performed on the ToPix4Hits. In order to get the time offset information, the hit-wise time differences between the first front-end to other three front-ends

($T_1 - T_i$, i=2, 3, 4) were calculated. After looping over all the hits, a spike in the distribution is expected for the correct combination. The run times for one spill (shown in Fig. 5.10) were divided into five bins: $[5 \times 10^9, 10 \times 10^9]$ ns, $(10 \times 10^9, 15 \times 10^9]$ ns, $(15 \times 10^9, 20 \times 10^9]$ ns, $(20 \times 10^9, 25 \times 10^9]$ ns, $(25 \times 10^9, 30 \times 10^9]$ ns. Each bin contains 5 s of data. It is found that the time offsets in each bin are exactly the same, i.e. the time offset is a global value during the whole run time (as shown in Fig. 5.20). This is mandatory for a global correction on time, and allows to shift the time information of all ToPix4Hits with a common offset in each front-end.

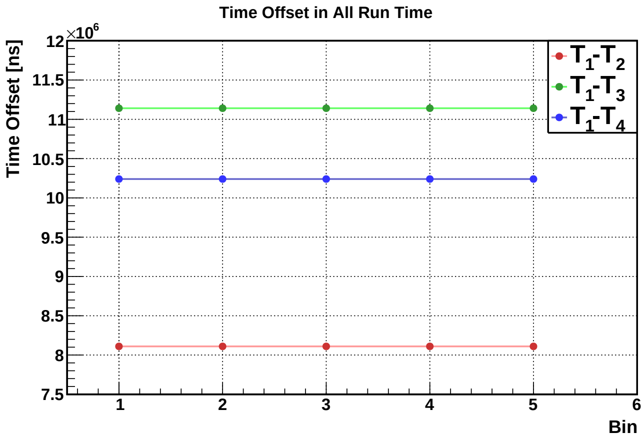

**Figure 5.20:** Time offset differences during the full run time for all four front-ends. Each $T_1 - T_i (i = 2, 3, 4)$ contains five data points, which are obtained in the five time bins. [File: 2014-10-26-22-39-36]

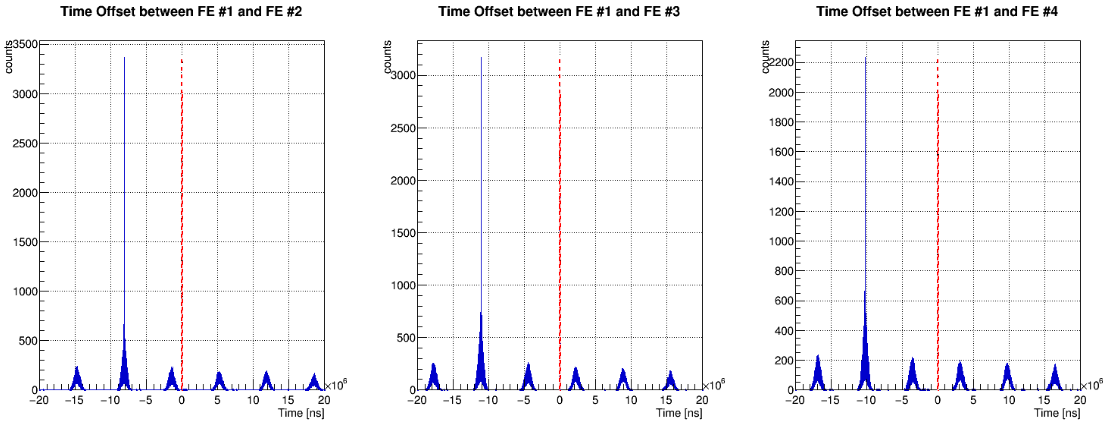

**Figure 5.21:** Time difference spectra between front-end #1 and the others before the time correction. The red line indicates the position of offset time = 0. [File: 2014-10-26-22-39-36]

Fig. 5.21 shows the time difference spectra between the first front-end to other three front-ends, where the red line stands for the expected value $\Delta T = 0$. The distance gap between the red line and the spike in the count rate is taken as the time offset. The time differences are $T_1 - T_2 = 8.1$ ms, $T_1 - T_3 = 11.1$ ms and $T_1 - T_4 = 10.2$ ms, with a precision dominated by the 20 ns resolution of ToPix from the 50 MHz clock speed and smeared by the time walk effect. According to these offset parameters, the global time stamp of the other three front-ends were

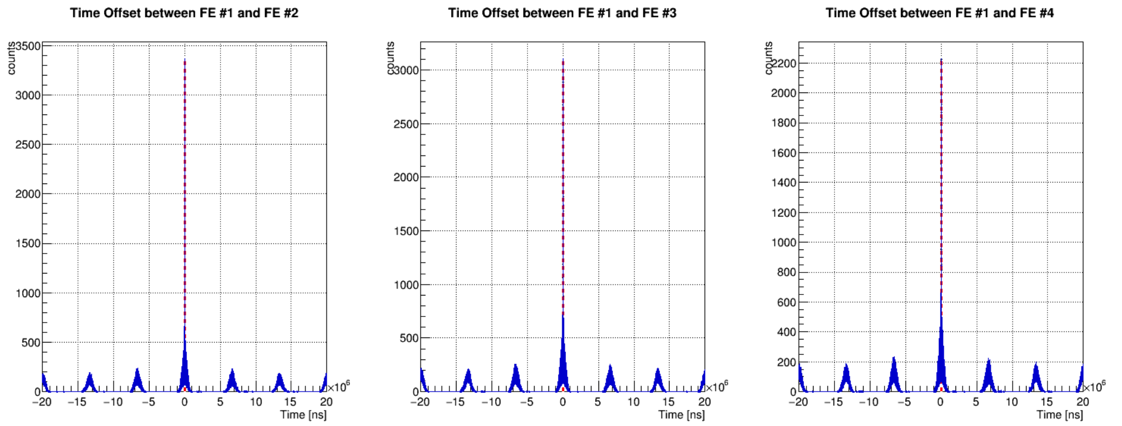

**Figure 5.22:** See Fig. 5.21 after correction. [File: 2014-10-26-22-39-36]

shifted by PndTSCorrectorTask. After correction, the time differences are $T_1 - T_i = 0$ as shown in Fig. 5.22. The time sorting was applied after time calibration with PndMapSorterTask.

A time gap of $\leq 50\,\text{ns}$ between two hits was applied to assemble the pixel hits of the four front-ends into one event. Fig. 5.23 shows the multiplicity of pixel hits per event. Most of the events contain less than 6 hits. On average 2.3 hits are found per event. For tracking at least three hits distributed over at least three planes are needed.

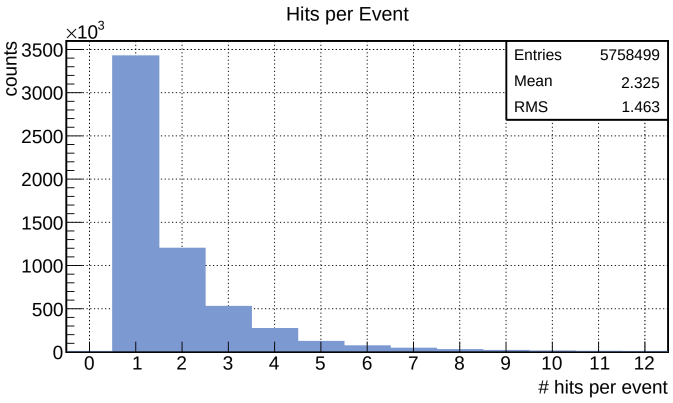

**Figure 5.23:** Multiplicity distribution of the number of hits per event. [File: 2014-10-26-22-39-36]

## 5.5.5 Tracking

For each event, a track finder searches for a straight line of ToPix4Hits throughout the four front-ends with the PndStraightLineTrackFinderTask. It calculates a straight line between the first front-end and the second front-end, and then searches for hits close to the extrapolation of this line in the following front-ends. Immediately after the track finding task, PndLmdLinFitTask is applied to perform a straight line fit.

Fig. 5.24 shows the reduced $\chi^2$ ($\chi^2$/NDF) distribution of the linear fit. Tracks with good

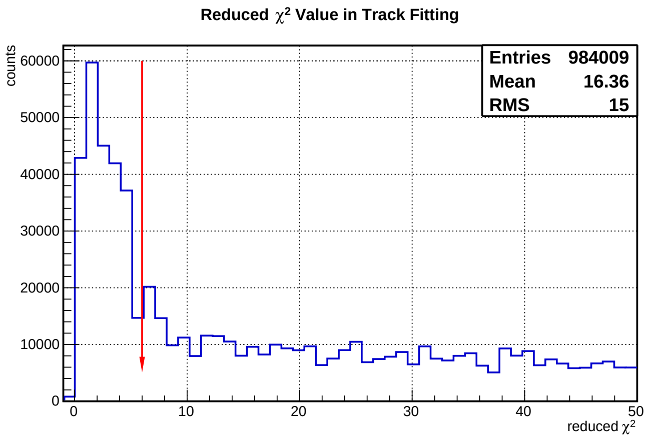

**Figure 5.24:** Reduced $\chi^2$ distribution from the track fitting. The red arrow denotes the maximum reduced $\chi^2$ allowed for selected tracks. [File: 2014-10-26-22-39-36]

tracking quality were selected by having $\chi^2/\text{NDF} < 6$. One example of a fitted track is shown in Fig. 5.25, where the residuals on four front-ends between the measured and the fitted position are relatively small.

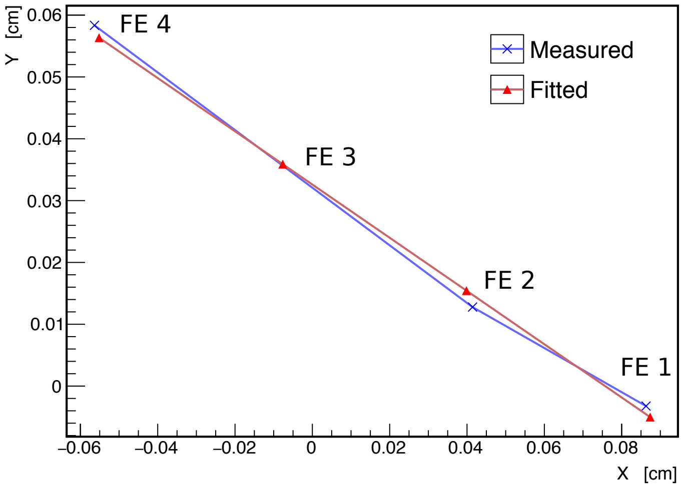

**Figure 5.25:** X-Y projection of a 3D linear track fit to the four front-ends. [File: 2014-10-26-22-39-36]

### 5.5.6 Alignment

The mounting of the sensors can only be done with a certain precision, therefore differences in the real position and the assumed position reduce the track reconstruction performance. The goal of the alignment is to determine the real position of the detectors. Otherwise, one will assume that the sub-detectors are in the nominal positions, and cannot correctly estimate the parameters of track. This problem is illustrated by Fig. 5.26. What happens in reality is shown

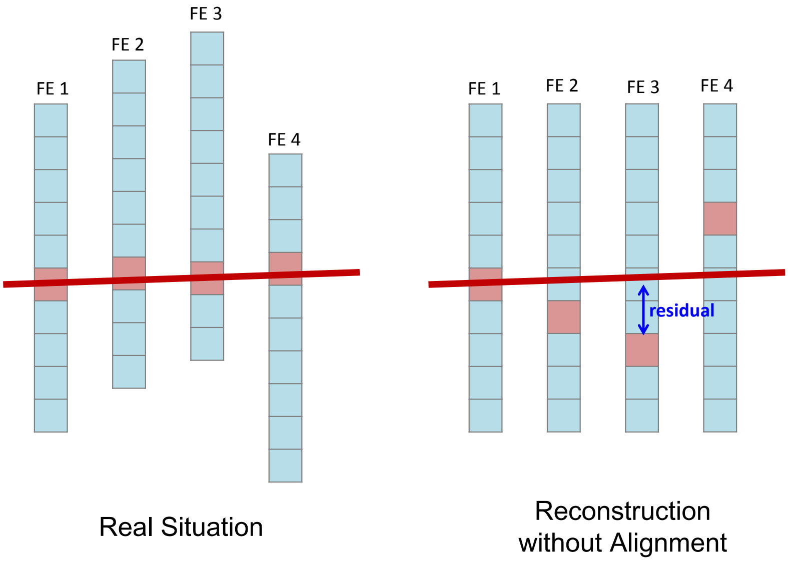

**Figure 5.26:** Schematic diagram of misalignment. The red straight line is a track passing through the four front-ends, which creates one hit (light red) on each front-end. Left: measured hits in the real situation. Right: tracking with the misaligned front-ends. The average distance between a hit and the fitted track is defined as the residual (blue).

by the left figure. Without performing the alignment procedure (right figure), the non-aligned hits leads to a systematically worse track reconstruction. If the misalignments are very large, tracks can be lost. Therefore, alignment is mandatory for tracking detectors.

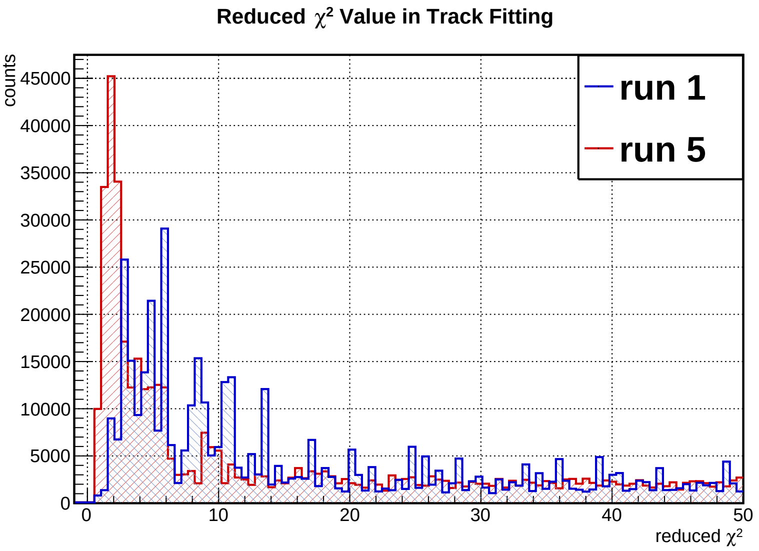

**Figure 5.27:** Reduced $\chi^2$ value in track fitting after alignment. The result of the first iteration run (blue) and the last run (red) are compared. [File: 2014-10-26-22-39-36]

**Table 5.4:** Mean residuals all for four front-ends (FE) after a $\chi^2$/NDF < 6 cut was applied. $\Delta X$ and $\Delta Y$ are the mean values of the residuals on the X and Y coordinates, respectively. **Iteration** indicates the number of alignment iteration; 0 means without alignment. The residuals are in units of μm.

| Mean | **Iteration** | FE #1 | FE #2 | FE #3 | FE #4 |
|---|---|---|---|---|---|
| $\Delta X$ | **0** | 8.9 | -34 | 55 | -26 |
| | **1** | 1.5 | -9.7 | 18 | -12 |
| | **2** | 0.77 | -4.3 | 8.1 | -5.3 |
| | **3** | -0.22 | -0.62 | 2.3 | -2.4 |
| | **4** | -0.21 | -0.0042 | 0.75 | -1.0 |
| | **5** | -0.065 | -0.00026 | 0.26 | -0.35 |
| $\Delta Y$ | **0** | 32 | -43 | -2.0 | 59 |
| | **1** | 8.2 | -9.8 | -3.5 | 18 |
| | **2** | 2.0 | -1.7 | -2.6 | 5.7 |
| | **3** | 0.63 | -0.37 | -1.1 | 1.8 |
| | **4** | 0.27 | -0.17 | -0.44 | 0.52 |
| | **5** | 0.12 | -0.048 | -0.22 | 0.066 |

Minimizing the residuals is one method of alignment. In the procedure, the residuals of the reconstructed tracks were calculated for all front-ends. Then, the mean value of the calculated residuals was used to correct the front-ends' positions in the $X$ and $Y$ coordinates. Afterwards the tracking was performed again with the updated ToPix4Hits, and a $\chi^2$/NDF cut was applied. This step can be repeated several times, until the residuals fulfill a convergence criterion.

Fig. 5.28 and Fig. 5.29 show the X and Y residuals, respectively for the four front-ends obtained in the first alignment run. After five alignment runs, the reduced $\chi^2$ distribution is shown in Fig. 5.27 with a comparison of the one obtained in the first run. And the residuals after alignment are shown in Fig. 5.30 and Fig. 5.31. The mean residuals decrease after every iteration. A few orders of magnitude improvement was achieved for both X and Y directions. Table 5.4 summarizes the mean residuals for the four front-ends obtained in five iterations of the alignment.

The Full Width at Half Maximum (FWHM) of the residual distributions are calculated and listed in Table 5.5. In general, the FWHM values improve with more iterations, but some fluctuations can be seen. In the best case, the initial FWHM is improved by nearly 60%.

For the X coordinate of front-end #2 and the Y coordinate of front-end #4, the alignment does not improve the FWHM. In addition, one can notice a big jump of FWHM appearing during the iterations of the two front-ends: FWHM_$\Delta X_1 = 2$ in front-end #2 and for FWHM_$\Delta X_1 = 8$

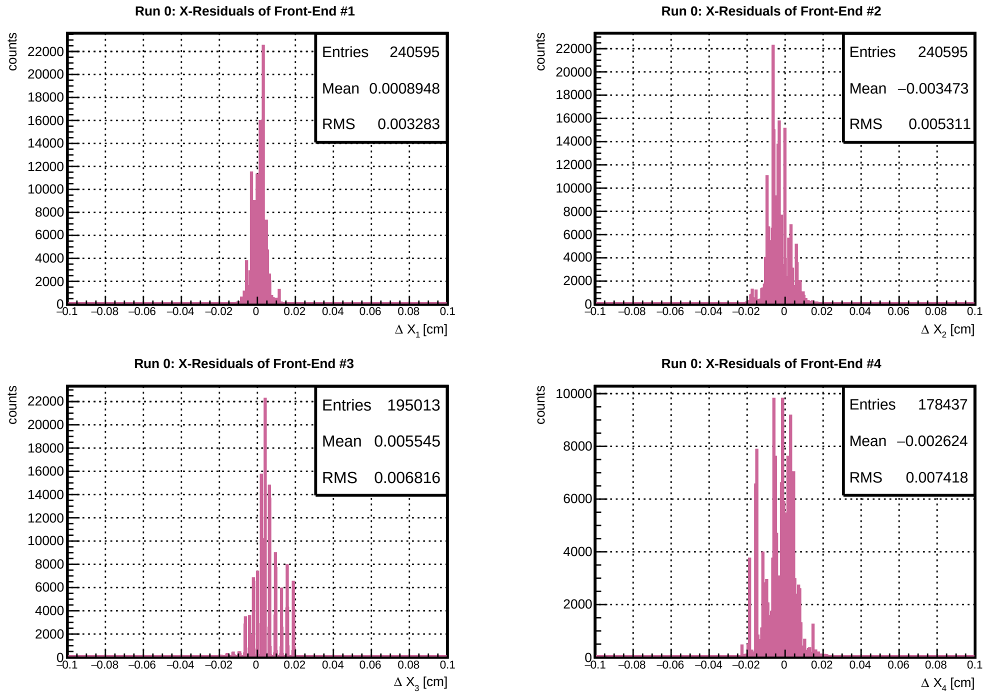

**Figure 5.28:** Residuals of tracking on X after the first alignment run. [File: 2014-10-26-22-39-36]

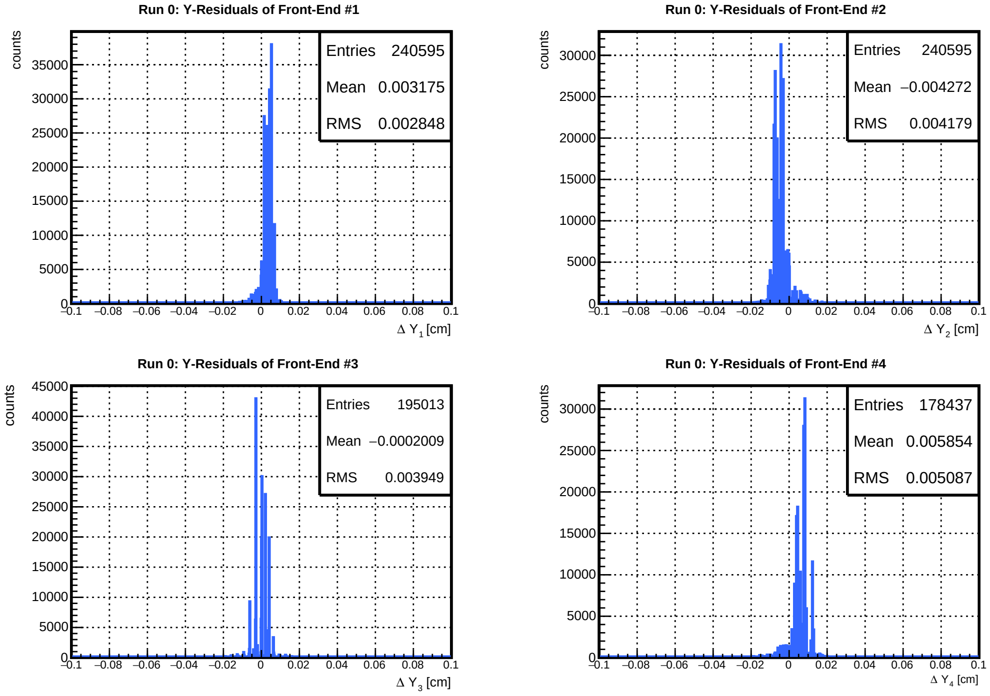

**Figure 5.29:** Residuals of tracking on Y after the first alignment run. [File: 2014-10-26-22-39-36]

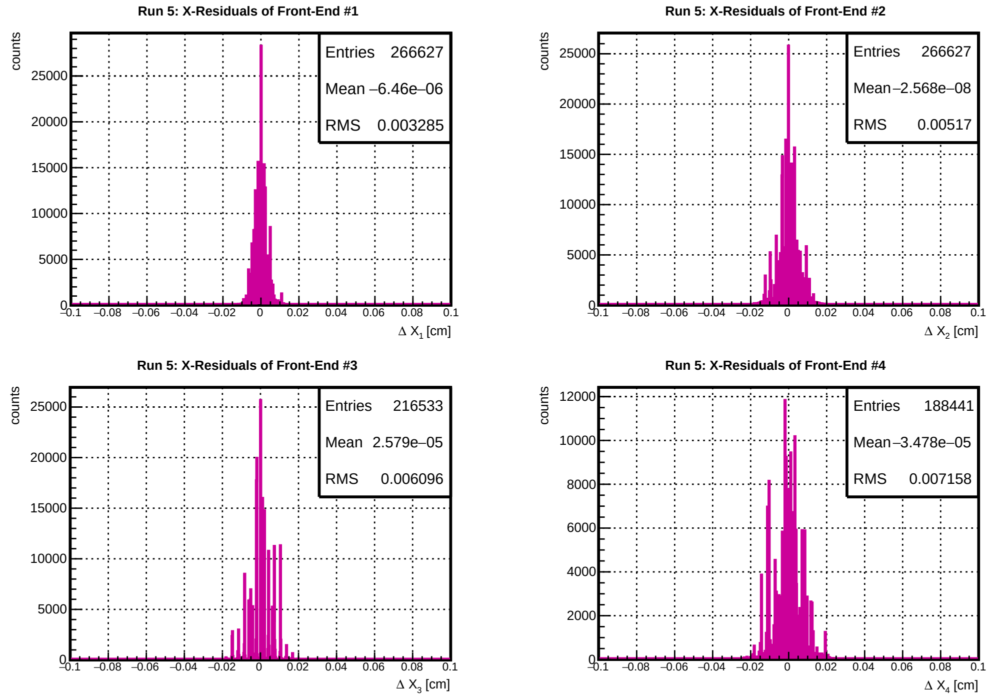

**Figure 5.30:** Residuals of tracking on X after five alignment runs. [File: 2014-10-26-22-39-36]

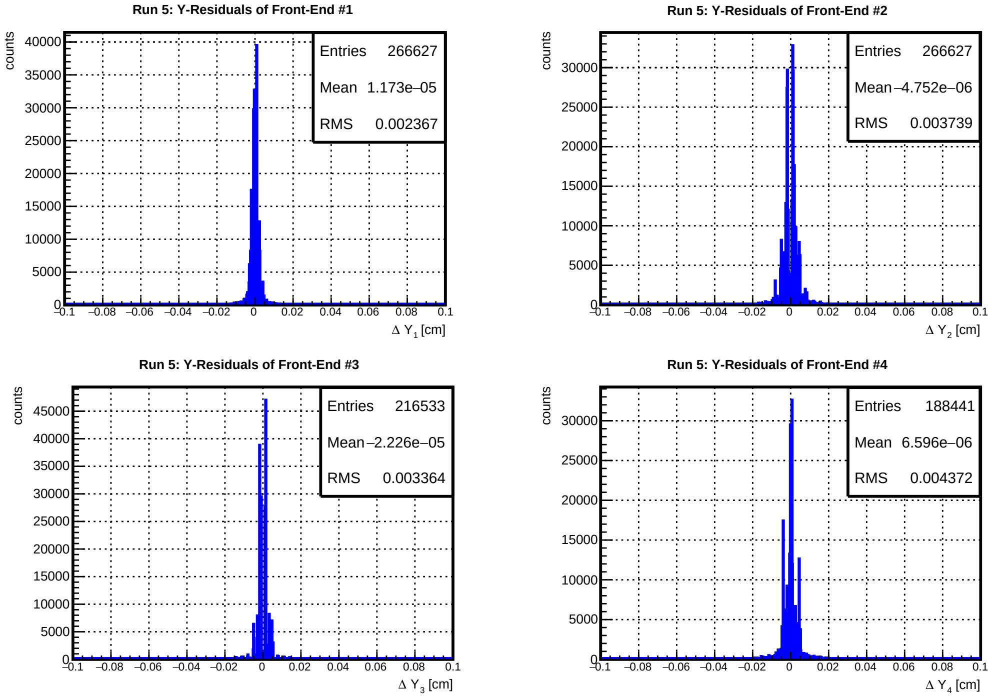

**Figure 5.31:** Residuals of tracking on Y after five alignment runs. [File: 2014-10-26-22-39-36]

in front-end #4. It implies that only a few bins are above the half maximum of the residual distribution. This is a problem of the alignment and a possible cause for making no improvements in the two cases. It could be because the present alignment method of shifting the front-end in the X-Y plane is not able to deal with the case of tilting. Therefore, implementing a more powerful alignment tool is needed.

**Table 5.5:** FWHM (Full Width at Half Maximum) of residuals of reconstructed tracks for four front-ends (FE) after a $\chi^2$/NDF < 6 cut in the track fit. **Iteration** indicates the number of the alignment runs; 0 means without alignment. The FWHMs of the residuals are in units of µm.

| | **iteration** | FE #1 | FE #2 | FE #3 | FE #4 |
|---|---|---|---|---|---|
| FWHM_$\Delta X$ | **0** | 62 | 62 | 44 | 200 |
| | **1** | 64 | 2 | 48 | 194 |
| | **2** | 36 | 64 | 42 | 196 |
| | **3** | 32 | 64 | 42 | 194 |
| | **4** | 32 | 62 | 20 | 142 |
| | **5** | 32 | 64 | 42 | 144 |
| FWHM_$\Delta Y$ | **0** | 38 | 48 | 50 | 44 |
| | **1** | 26 | 34 | 42 | 8 |
| | **2** | 18 | 32 | 34 | 46 |
| | **3** | 32 | 38 | 32 | 46 |
| | **4** | 16 | 38 | 32 | 46 |
| | **5** | 16 | 38 | 32 | 46 |

**Table 5.6:** Number of reconstructed tracks after a $\chi^2$/NDF < 6 cut in track fit for four front-ends (FE) in alignment iteration. **Iteration** indicates the number of alignment runs; 0 means without alignment.

| **iteration** | FE #1 | FE #2 | FE #3 | FE #4 |
|---|---|---|---|---|
| **0** | 240595 | 240595 | 195013 | 178437 |
| **1** | 264336 | 264336 | 214582 | 187901 |
| **2** | 266233 | 266233 | 216294 | 188353 |
| **3** | 266811 | 266811 | 216858 | 188347 |
| **4** | 266658 | 266658 | 216565 | 188434 |
| **5** | 266627 | 266627 | 216533 | 188441 |

As mentioned above, reasonable alignment can also improve the tracking efficiency. Table 5.6 shows the number of reconstructed tracks after a $\chi^2/\mathrm{NDF} < 6$ cut in track fit. The number of tracks is found to increase after each iteration of the alignment. For every front-end, roughly 10% more tracks are found due to the alignment.

## 5.6 Conclusion

The ToPix4 prototype ASIC of the MVD hybrid pixel detector has been tested with a proton beam at COSY in FZJ. In the measurement, four ToPix4 front-ends were aligned along the beam and connected with an individual readout system. The data set with a clock frequency of 50 MHz and various beam intensities has been studied.

The time stamp of each front-end has been investigated. For the leading edge and trailing edge distribution, the expected behaviour has been seen for different rates of particles. A problem of the busy signal propagation seen in the ToPix3 remain in the ToPix4. Efficiency loss at freeze stop is another problem found in both versions. The ToT distribution matches well with a Landau function.

The tracking performance has been studied with the four front-ends, in a complete workflow including data conversion, hit processing, time calibration, tracking and alignment. For the alignment, the residual minimization method was employed. After correcting the position of the front-ends, the mean residuals are improved by three to five orders of magnitude. The FWHM of the residuals also shows a general improvement. In addition, the tracking efficiency was increased by roughly 10% for all front-ends due to alignment. From these results, one can see that the residual minimization method can be used to improve the alignment. Nevertheless, the residual correction is currently only able to operate in the X-Y plane and does not take any rotations into account. The next step would be to test how much the alignment can be further improved by using a more powerful algorithm like the Millepede-2 approach [172].

# Summary and Outlook 6

In this thesis, the performance of $\overline{\text{P}}$ANDA to measure the semileptonic decay form factor of $D_s^+ \to \eta e^+ \nu_e$ has been studied via Monte Carlo simulations, and the in-beam test data of the recent ASIC prototype for the readout of the MVD has been analyzed. This chapter summarizes that work and presents a outlook for future investigations.

## 6.1 Simulation of $D_s$ Semileptonic Decay

A brief review on the recent research of the $D_s$ semileptonic decay has been presented from both experimental and theoretical point of view. The main purpose of the work in this thesis is to estimate the production rate of useful signal events and the available precision in measuring the $D_s$ semileptonic decay form factor. An additional objective is the continuous development of the analysis tools of PandaRoot, necessary for the in-depth study of the detector's performance.

The simulated decay chain includes $\bar{p}p \to D_s^+ D_s^-$, $D_s^+ \to \eta e^+ \nu_e$, $\eta \to \pi^0 \pi^+ \pi^-$, $\pi^0 \to \gamma\gamma$, and the decays of the tagged $D_s^-$ in mode A: $D_s^- \to K^+ K^- \pi^-$ and mode B: $D_s^- \to \pi^+ \pi^- \pi^-$. With the present software, a signal data set of one million events for each tag mode and a background data set of 100 million events have been simulated and analyzed. For reconstructing the neutral particles in the decay chain, the EMC correlation parameters and the selection of the photon energy threshold have been systematically studied. It is found that the highest significance can be achieved when the neutral correlation parameter is 100 cm$^2$, and the photon energy threshold is 40 MeV. Due to the new strategy of reconstructing the $\eta$ vertex, the vertex resolution has been improved by a factor of two. The results on the reconstruction efficiency and resolutions of the reconstructed $D_s$, $\eta$ and $\pi^0$ are reasonably good, except that the MC truth matched efficiency of the neutral particles is very low in both tag modes. Due to a higher acceptance of pions compared to kaons and a higher combinatorial background, the efficiency of $(e^+ \nu_e)$ is higher in tag mode B than in tag mode A.

The kinematics of the unmeasured neutrino have been reconstructed with a complete simulation model of the detector and reconstruction tools. Comparing with the result of my pre-study [173], the reconstruction resolutions have been improved due to improvements of software in particular on the kinematic fitter, e.g. the $\eta$ vertex resolution has been improved from 318 μm to 100 μm on the X direction. The count rate of useful events is estimated to be 52 events in 35 days with the high luminosity mode available in the MSV 5 stage of the FAIR project. In the simulated background sample, one falsely reconstructed ($e^+\nu_e$) event with tag mode A, and 80 with tag mode B were found. Those numbers need to be scaled by a factor 25,000 to be compared to the expected signal rate in 35 days. The background contamination in tag mode B is relatively high. With the present results, the ratio of the signal to background rates is found to be $S/B \approx 1/80$ for tag mode A, and $S/B \approx 1/4400$ for tag mode B. Since the statistics is not sufficient to study the performance of background suppression in detail, we leave this issue for future study.

Three different beam momenta have been simulated to study the momentum dependence of the $D_s$ meson reconstruction efficiency. The beam momentum of 8 GeV/$c$ is found to have the best reconstruction efficiency of 15.1%. The reconstruction efficiencies at 7.3 GeV/$c$ and 7.7 GeV/$c$ are both about 14.9%.

**Outlook** The present efficiency to reconstruct ($e^+\nu_e$) is not sufficient to determine the decay form factor with high precision in a feasible time. Future studies should include a modification of the present software to improve the efficiency, and take more tag modes into account. Furthermore, the charge conjugate system, i.e. $D_s^- \to \eta e^- \nu_e$ and tagging $D_s^+$, needs to be studied. On the first issue, there are a few aspects for possible developments. The MC truth matched efficiency of the reconstructed neutral particles is not satisfying, which is the main reason leading to a low reconstruction efficiency of the positron-neutrino system. Therefore, it is worth to study the neutral reconstruction systematically, including developing a track momentum dependent EMC correlation algorithm, and improve the covariance matrix of the neutral candidates and also all the utilized fitters in the reconstruction process. Meanwhile, the PandaRoot framework is under development. New analysis tools are expected to bring better results, e.g. the global tree fitter [174], which allows to constrain the decay vertices, momenta and masses of the intermediate particles in the decay system at once, and is available for decays with unmeasured particle, such as the neutrino.

In order to expand the $D_s^-$ tag mode, possible candidates for decay channels are listed below with the corresponding branching ratio (*BR*) [9]:

- $D_s^- \to K^+K^-\pi^-\pi^0$, $BR = (6.3 \pm 0.6)\%$;
- $D_s^- \to K_S^0K^+\pi^-\pi^-$, $BR = (1.67 \pm 0.10)\%$;
- $D_s^- \to K_S^0K^-$, $BR = (1.50 \pm 0.05)\%$;
- $D_s^- \to \eta\pi^-$, $BR = (1.70 \pm 0.09)\%$;
- $D_s^- \to \eta\rho^-$, $BR = (8.9 \pm 0.8)\%$.

Besides using the $D_s^-$ tag, it is also reasonable to consider additional decay modes of the $\eta$ meson to increase the statistics, e.g. $\eta \to \gamma\gamma$ ($BR = (39.41 \pm 0.20)\%$) [9]. This will be feasible when the neutral particle reconstruction efficiency improves.

In addition, a more detailed study of the background suppression is needed, in particular for tag mode B of the $D_s^-$. This will require a larger data set of DPM events, for instance $10^{10}$ events.

On the other hand, the simulation of the $D_s$ semileptonic decay $D_s^+ \to \eta e^+ \nu_e$ can be extended to the decay with $\eta'$. The exclusive $D_s$ decays to final states containing $\eta$ and $\eta'$ represent nearly 30% of the total decay rate of the $D_s$ meson. Therefore, $D_s$ could be a suitable system to gather information on important aspects of the $\eta$-$\eta'$ phenomenology (see Sec. 2.4). Due to the low branching ratio of $D_s^+ \to \eta' e^+ \nu_e$, which is nearly one order of magnitude lower than the decay to $\eta$, it will challenge the performance of the detector and the analysis tools.

## 6.2 ToPix4 In-Beam Tests Data Analysis

The ToPix4 prototype ASIC of the MVD hybrid pixel detector has been tested with a proton beam at COSY in FZJ. In the measurement, four ToPix4 front-ends were aligned along the beam and connected with individual readout systems. The data set with a clock frequency of 50 MHz and various beam intensity settings has been studied. The time stamp of each front-end has been investigated. For the leading edge and trailing edge distributions, the expected behaviour has been seen for different particle rates. The ToT distribution matches well with a Landau function. A problem of the busy signal propagation seen in ToPix3 remains in the ToPix4. An efficiency loss at freeze stop is another problem found in both versions. These problem are under investigation and are expected to be fixed in the next version of the ToPix.

With the four front-ends in the test system, the tracking performance has been studied in a complete workflow, including data conversion, hit processing, time calibration, tracking and alignment. For the alignment, the residual minimization method was employed. After correcting the position of the front-ends, the mean residuals have been improved by three to five orders of magnitude compared to the initial state. The FWHM of the residuals also shows a general improvement. In addition, the tracking efficiency was increased by roughly 10% for all front-ends as a result of the alignment.

**Outlook** The residual minimization method utilized in the alignment is only able to correct shifts in the X-Y plane and does not take any rotations into account. In addition, the alignment (global) parameters are not involved in the local track fitting. Detector alignment based on track fits is one of the least squares fit problems, where the interest is only in optimal values of the global parameters, the alignment parameters. The next step will employ a more powerful alignment algorithm using e.g. Millepede-2 [172]. It solves the linear least squares problem with a simultaneous fit of all global and local parameters, irrespective of the number of local parameters, keeping all correlations in the solution. This method is able to correct the position of all sensor planes in X, Y, Z and also compensates rotations in all three axis. In addition, the full-size version of ToPix is expected to be available in the next in-beam test.

# Reconstruction Result with $p_{\bar{p}} = 7.3\,\mathrm{GeV}/c$

# A

The simulation with beam momentum at 7.3 GeV/$c$ for tag mode A has been studied. Except the beam momentum, all other settings are the same as in Table 4.3, and the reconstruction strategy is also the same as in Sec. 4.4.1. Table A.1 summarizes the results of $\mathrm{D}_s^-$ reconstruction.

**Table A.1:** Summary of the $\mathrm{D}_s^-$ reconstruction results for the decay $\mathrm{D}_s^- \to \mathrm{K}^+\mathrm{K}^-\pi^-$ at $P_{\mathrm{beam}} = 7.3$ GeV/$c$.

| Reco eff. | MCT eff. | $\sigma_{mass}$ | $\sigma_{vtx}$ [µm] | | | $\sigma_P/P$ | |
|---|---|---|---|---|---|---|---|
| | | [MeV/$c^2$] | $X$ | $Y$ | $Z$ | $P_t$ | $P_z$ |
| 14.9% | 13.8% | 13.6 | 61 | 60 | 121 | 21.3% | 0.7% |

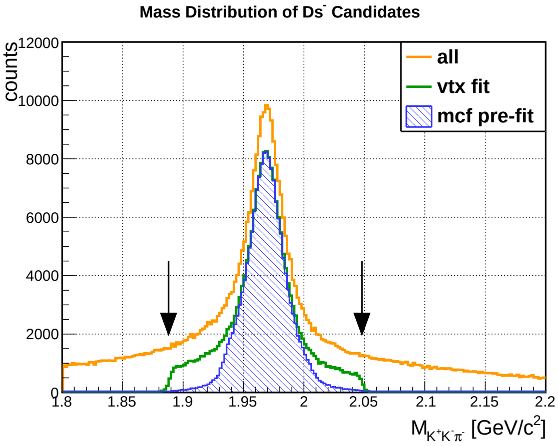

**Figure A.1:** The mass distribution of the reconstructed $\mathrm{D}_s^-$ candidates in tag mode A. The invariant mass distribution for all combinations of ($\mathrm{K}^+$, $\mathrm{K}^-$, $\pi^-$) is shown by the orange line; the distribution after the vertex fit is in green, and the blue area presents that of the pre-fit candidates after the mass constraint fit. The black arrows indicate the mass window of $M = (1.968 \pm 0.08)$ GeV/$c^2$.

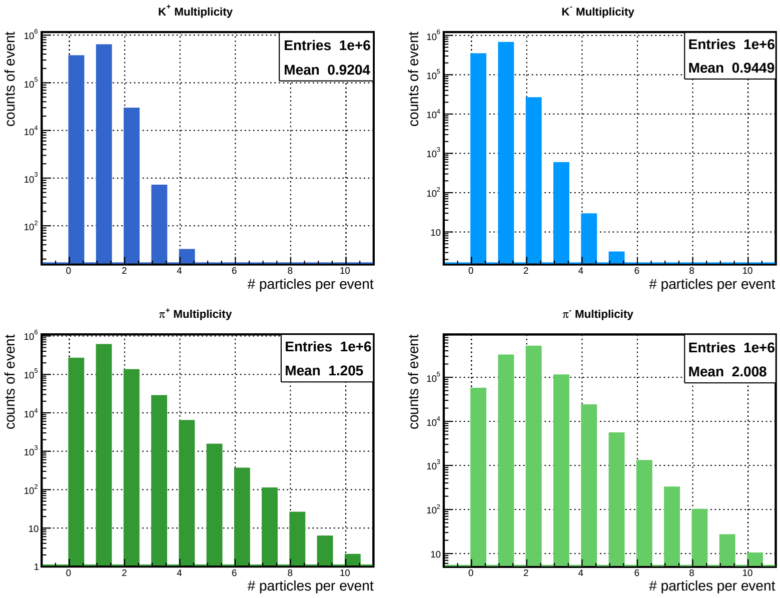

**Figure A.2:** Multiplicity distribution of $K^{\pm}$ (upper row) and $\pi^{\pm}$ (lower row) in the complete decay tree with the $D_s^- \rightarrow K^+K^-\pi^-$ tagging mode. The Y-axis has a logarithmic scale.

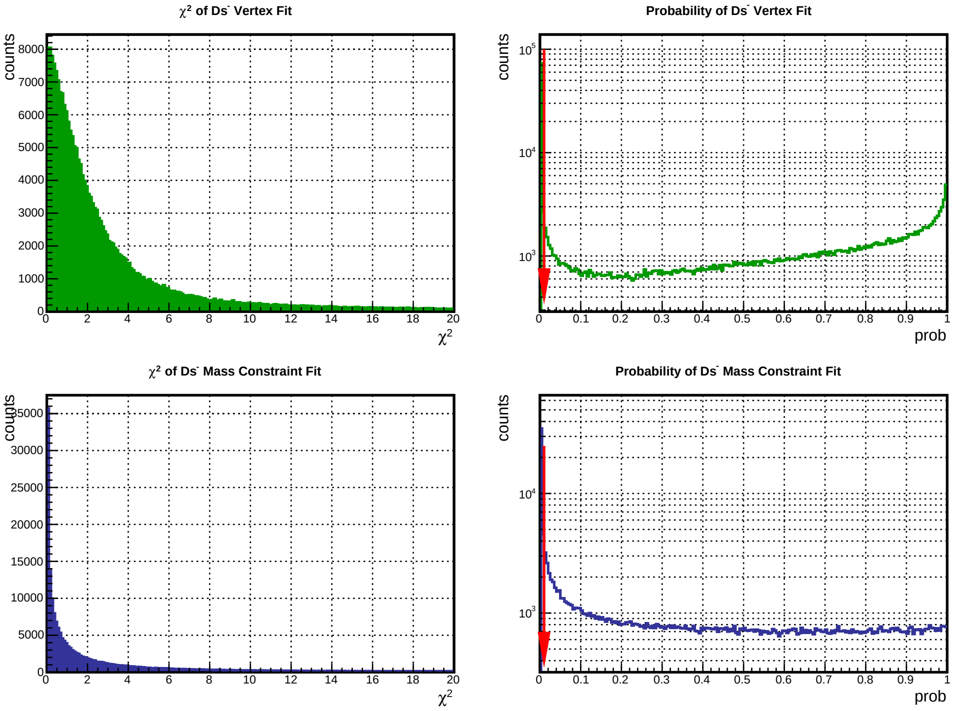

**Figure A.3:** The $\chi^2$ (left column) and probability (right column) distributions of the $D_s^-$ vertex fit (upper row), and mass constraint fit (bottom row). In both cases the rejected candidates with probabilities lower than 1% are indicated by the red arrows.

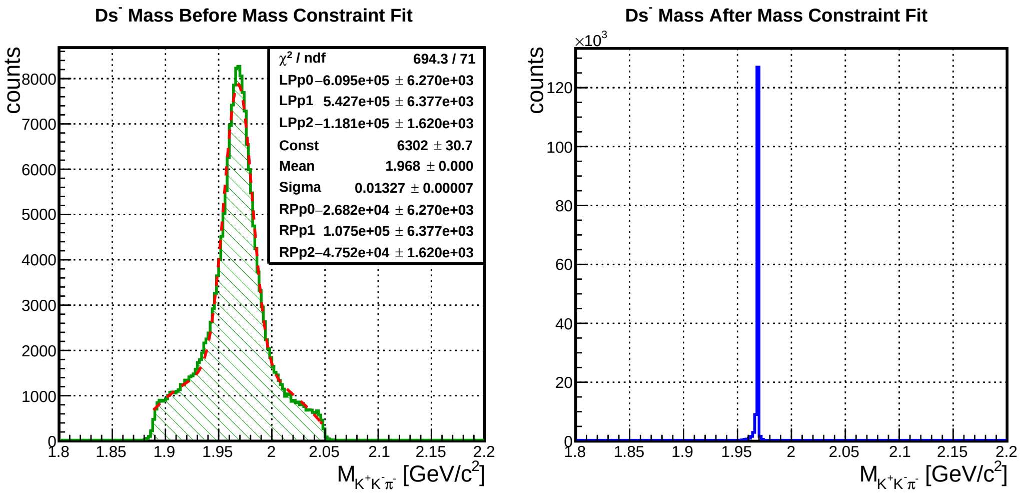

**Figure A.4:** The invariant mass distribution of the reconstructed $D_s^-$ candidates before the mass constraint fit (left) has been fit with a polynomial-Gaussian function to determine the resolution ($\sigma = 13.1\,\mathrm{MeV}/c^2$). The mass distribution after the mass constraint fit approaches a delta function (right).

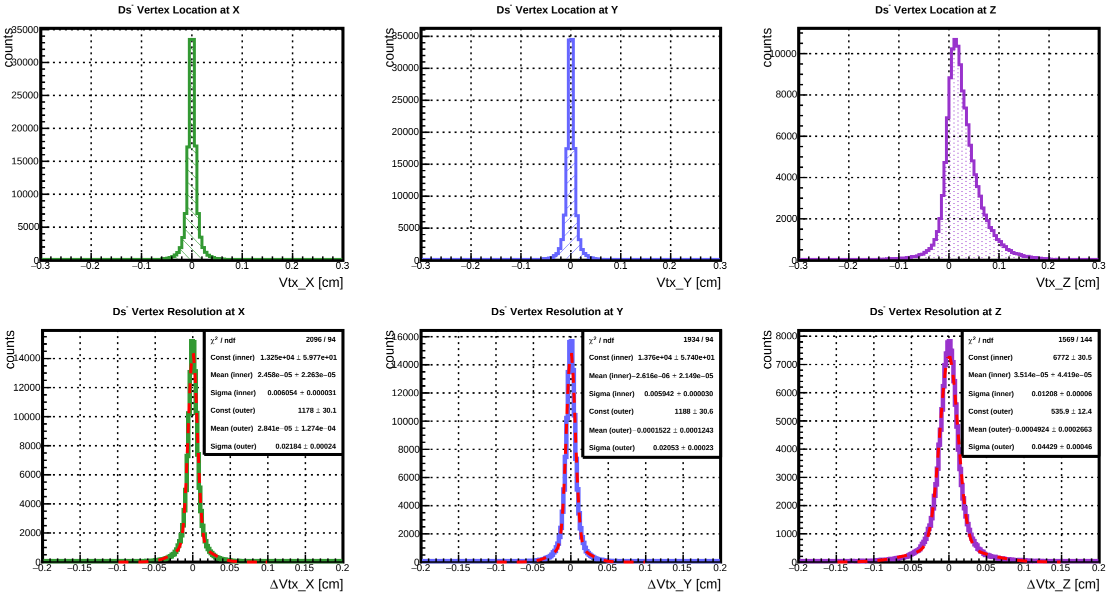

**Figure A.5:** The vertex locations and resolutions of the reconstructed $D_s^-$ in $D_s^- \to K^+K^-\pi^-$. The upper three histograms show the reconstructed vertex distributions in the X, Y, Z projections, and the lower three show the vertex resolutions $\Delta\mathrm{Vtx} = \mathrm{Vtx}_{\mathrm{MC}} - \mathrm{Vtx}_{\mathrm{reco}}$, where the red dashed line presents a fit using a double-Gaussian function.

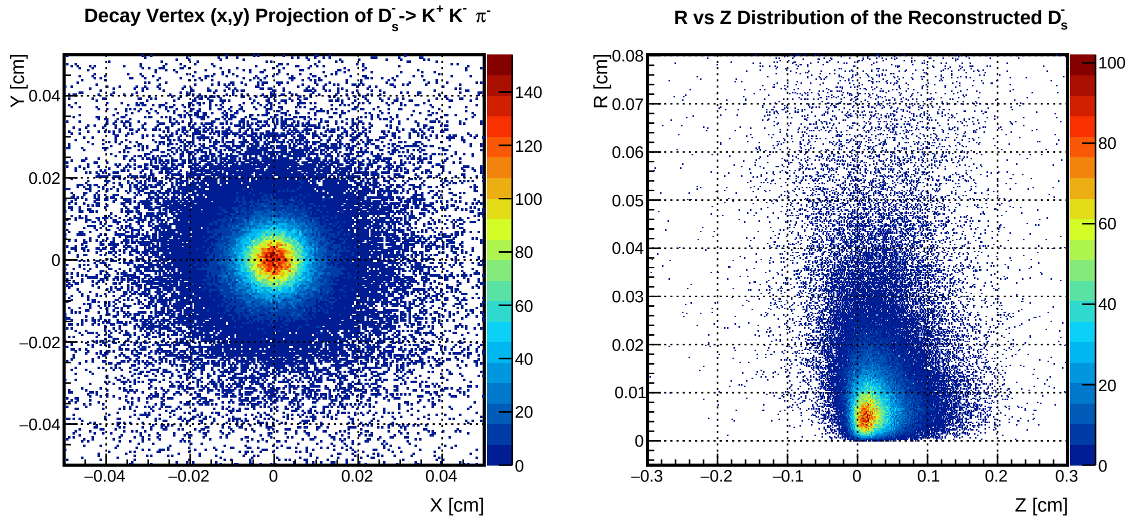

**Figure A.6:** Decay vertex distributions of the decay $\mathrm{D_s^-} \rightarrow \mathrm{K^+K^-\pi^-}$. Left: projection of the vertex distribution on the X-Y plane. Right: the X-Y radius R versus Z position distribution, where $R = \sqrt{X^2+Y^2}$.

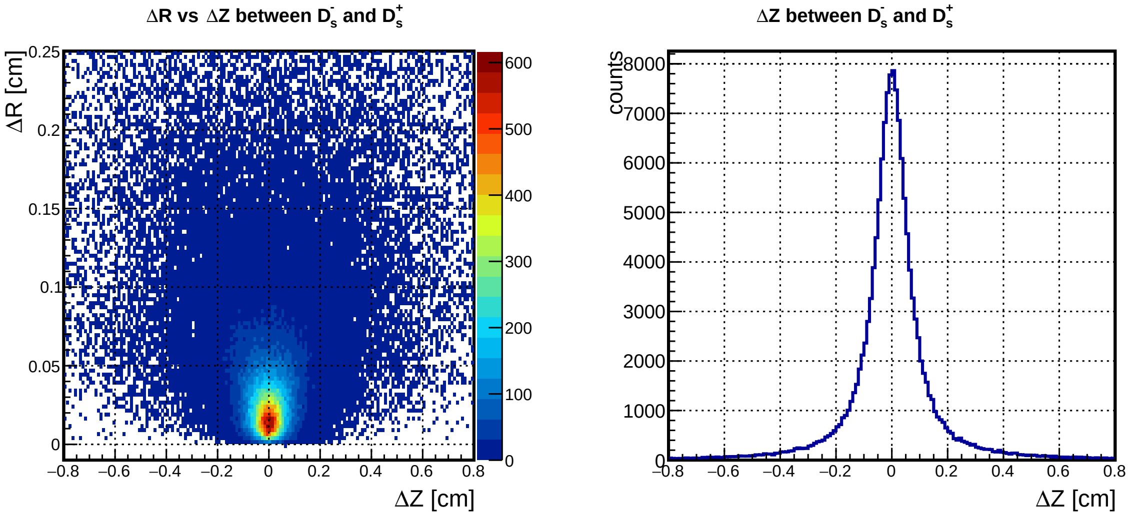

**Figure A.7:** Left: distance between the $\mathrm{D_s^+}$ and the $\mathrm{D_s^-}$ decay vertices shown with $\Delta R - \Delta Z$ correlation in tag mode A, where $\Delta R = \sqrt{(X_{\mathrm{D_s^+}} - X_{\mathrm{D_s^-}})^2 + (Y_{\mathrm{D_s^+}} - Y_{\mathrm{D_s^-}})^2}$ and $\Delta Z = Z_{\mathrm{D_s^+}} - Z_{\mathrm{D_s^-}}$. Right: the projection of the left histogram onto the $\Delta Z = \Delta V_Z$ axis.

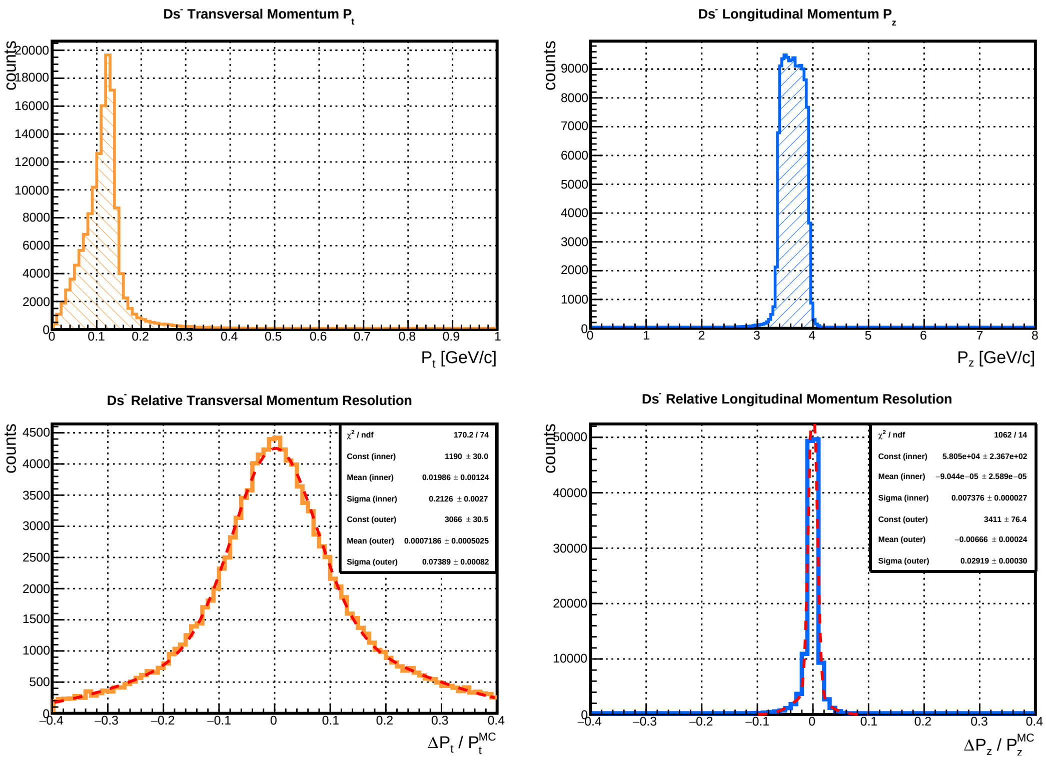

**Figure A.8:** The reconstructed $D_s^-$ momentum distributions in the decay of $D_s^- \rightarrow K^+K^-\pi^-$. Transversal (orange) and longitudinal (blue) momentum distributions are shown. The relative resolutions are shown in the lower frame: the red dashed lines present double-Gaussian fits.

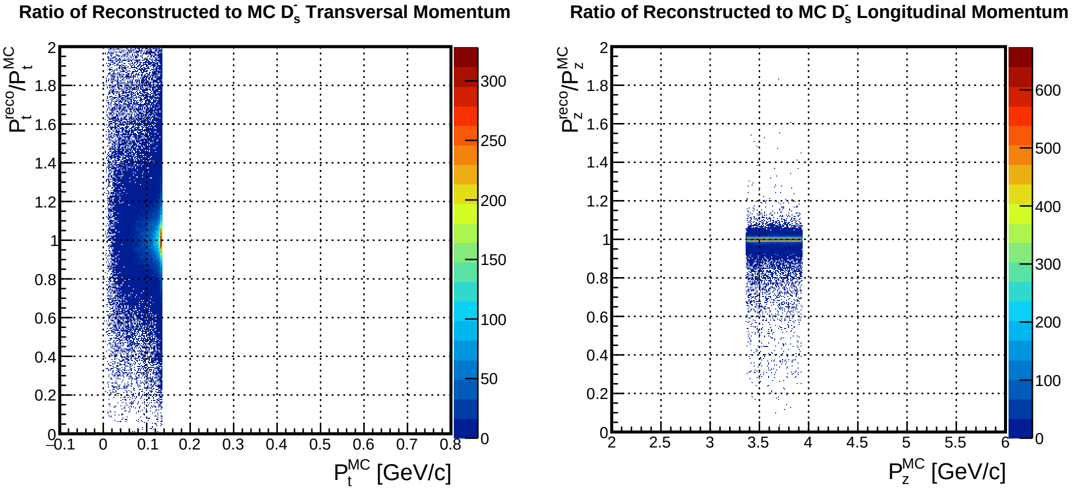

**Figure A.9:** Ratio of the reconstructed and MC momenta of the $D_s^-$ in tag mode A. Left is the ratio as a function of the transversal momentum, and right is the ratio as a function of the longitudinal momentum.

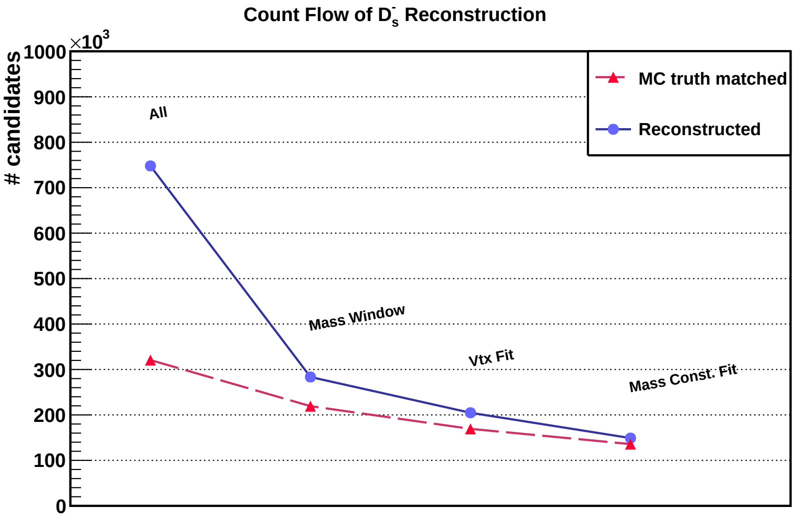

**Figure A.10:** Count flow of $D_s^-$ reconstruction in the decay $D_s^- \rightarrow K^+K^-\pi^-$. The data points follow the order of the reconstruction procedure from left to right. Blue: the number of reconstructed candidates. Red: the number of MC truth matched candidates.

# B

# Reconstruction Result with $p_{\bar{\mathrm{p}}} = 7.7\,\mathrm{GeV}/c$

This section shows the reconstruction results at $P_{\mathrm{beam}} = 7.7$ GeV/$c$ for tag mode A. The results of $\mathrm{D}_s^-$ reconstruction are listed in Table B.1. The histograms show the details for the reconstructed $\mathrm{D}_s^-$ candidates.

**Table B.1:** Summary of the $\mathrm{D}_s^-$ reconstruction results for the decay $\mathrm{D}_s^- \rightarrow \mathrm{K}^+\mathrm{K}^-\pi^-$ at $P_{\mathrm{beam}} = 7.7$ GeV/$c$.

| Reco eff. | MCT eff. | $\sigma_{mass}$ | $\sigma_{vtx}$ [µm] | | | $\sigma_P/P$ | |
|---|---|---|---|---|---|---|---|
| | | [MeV/$c^2$] | $X$ | $Y$ | $Z$ | $P_t$ | $P_z$ |
| 14.9% | 13.6% | 13.3 | 62 | 60 | 126 | 2.7% | 0.7% |

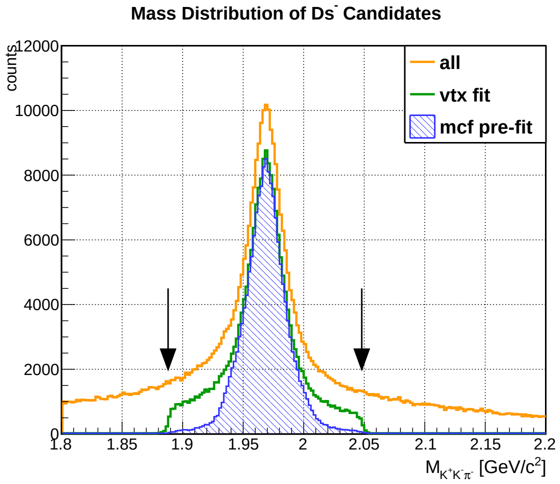

**Figure B.1:** The mass distribution of the reconstructed $\mathrm{D}_s^-$ candidates in tag mode A. The invariant mass distribution for all combinations of ($\mathrm{K}^+$, $\mathrm{K}^-$, $\pi^-$) is shown by the orange line; the distribution after the vertex fit is in green, and the blue area presents that of the pre-fit candidates, after the mass constraint fit. The black arrows indicate the mass window of $M = (1.968 \pm 0.08)$ GeV/$c^2$.

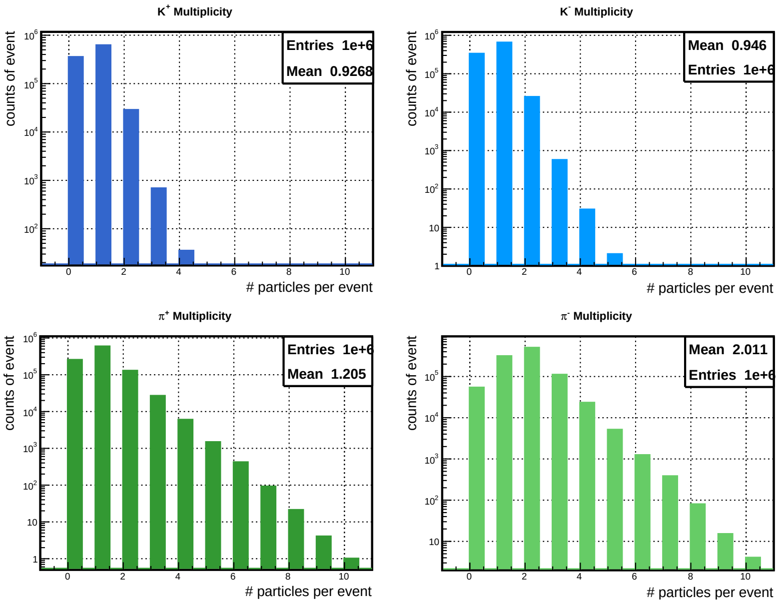

**Figure B.2:** Multiplicity distribution of $\mathrm{K}^{\pm}$ (upper row) and $\pi^{\pm}$ (lower row) in the complete decay tree with the $\mathrm{D}_s^- \to \mathrm{K}^+\mathrm{K}^-\pi^-$ tagging mode. The Y-axis has a logarithmic scale.

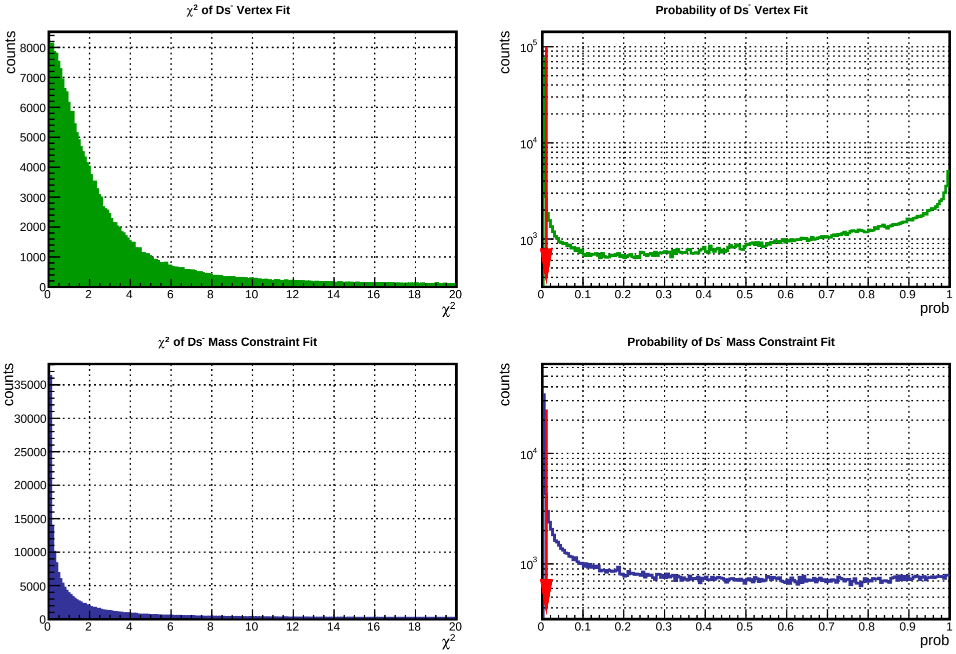

**Figure B.3:** The $\chi^2$ (left column) and probability (right column) distributions of the $\mathrm{D}_s^-$ vertex fit (upper row), and mass constraint fit (bottom row). In both cases the rejected candidates with probabilities lower than 1% are indicated by the red arrows.

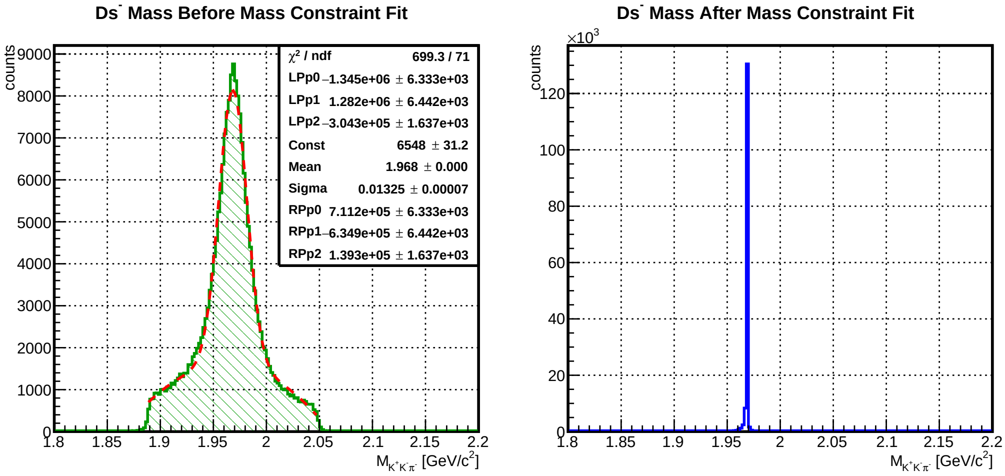

**Figure B.4:** The invariant mass distribution of the reconstructed $D_s^-$ candidates before the mass constraint fit (left) has been fit with a polynomial-Gaussian function to determine the resolution ($\sigma = 13.1\,\mathrm{MeV}/c^2$). The mass distribution after the mass constraint fit approaches a delta function (right).

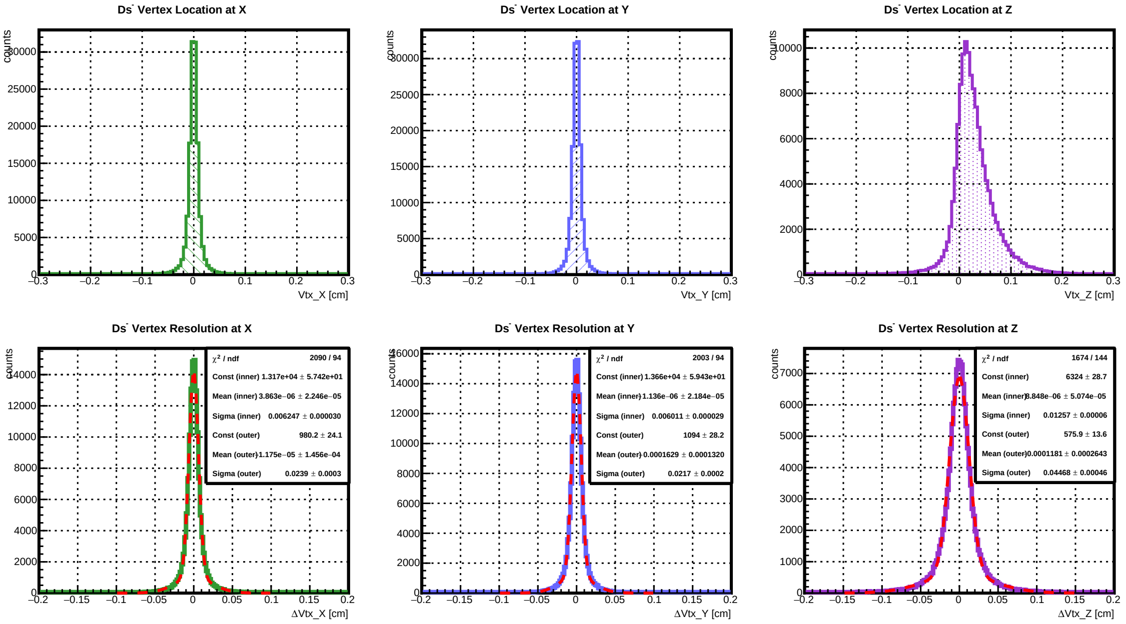

**Figure B.5:** The vertex locations and resolutions of the reconstructed $D_s^-$ in $D_s^- \to K^+K^-\pi^-$. The upper three histograms show the reconstructed vertex distributions in the X, Y, Z projections, and the lower three show the vertex resolutions $\Delta\mathrm{Vtx} = \mathrm{Vtx}_{\mathrm{MC}} - \mathrm{Vtx}_{\mathrm{reco}}$, where the red dashed line presents a fit using a double-Gaussian function.

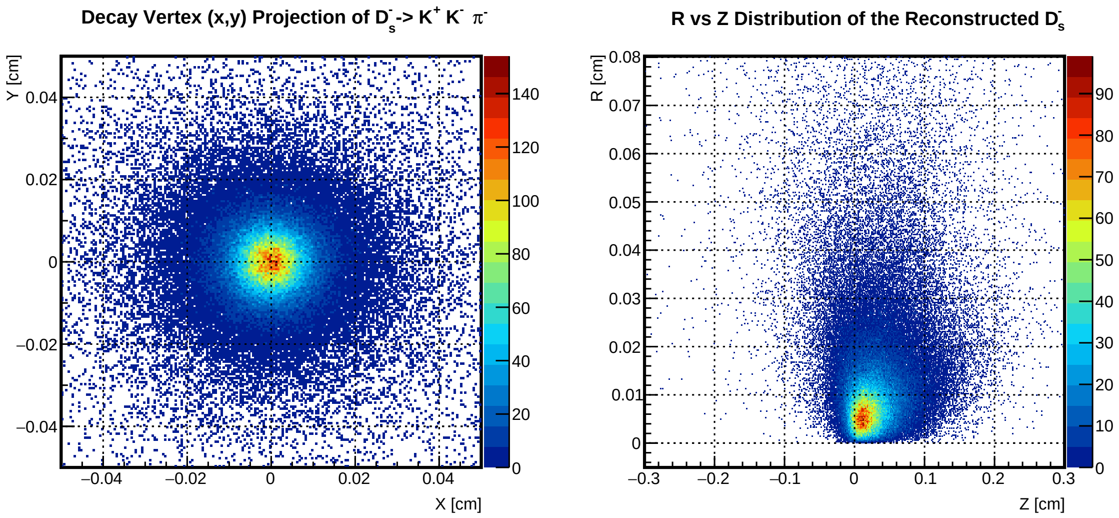

**Figure B.6:** Decay vertex distributions of the decay $\mathrm{D_s^-} \rightarrow \mathrm{K^+K^-\pi^-}$. Left: projection of the vertex distribution on the X-Y plane. Right: the X-Y radius R versus Z position distribution, where $R = \sqrt{X^2+Y^2}$.

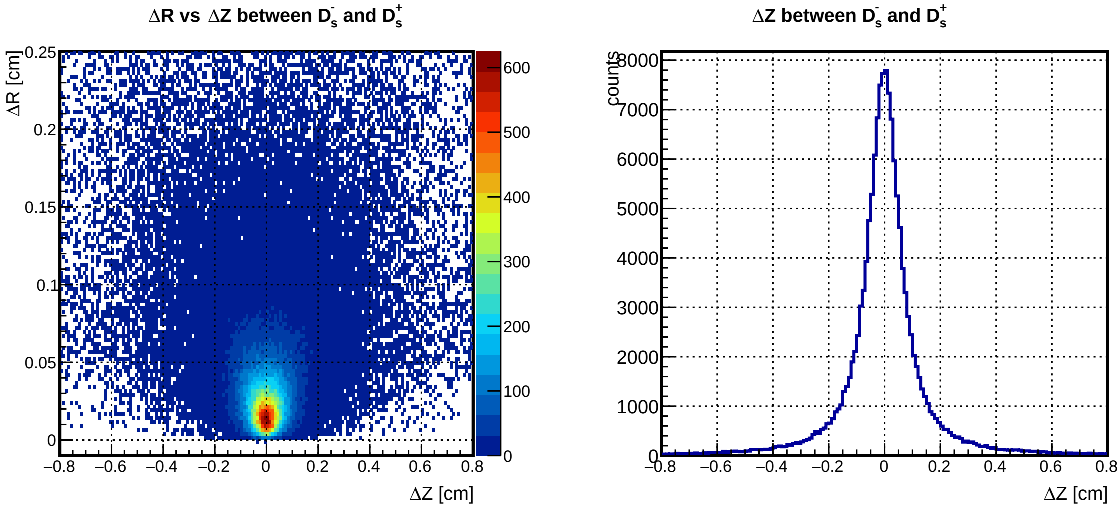

**Figure B.7:** Left: distance between the $\mathrm{D_s^+}$ and the $\mathrm{D_s^-}$ decay vertices shown with $\Delta R - \Delta Z$ correlation in tag mode A, where $\Delta R = \sqrt{(X_{\mathrm{D_s^+}} - X_{\mathrm{D_s^-}})^2 + (Y_{\mathrm{D_s^+}} - Y_{\mathrm{D_s^-}})^2}$ and $\Delta Z = Z_{\mathrm{D_s^+}} - Z_{\mathrm{D_s^-}}$. Right: the projection of the left histogram onto the $\Delta Z = \Delta V_Z$ axis.

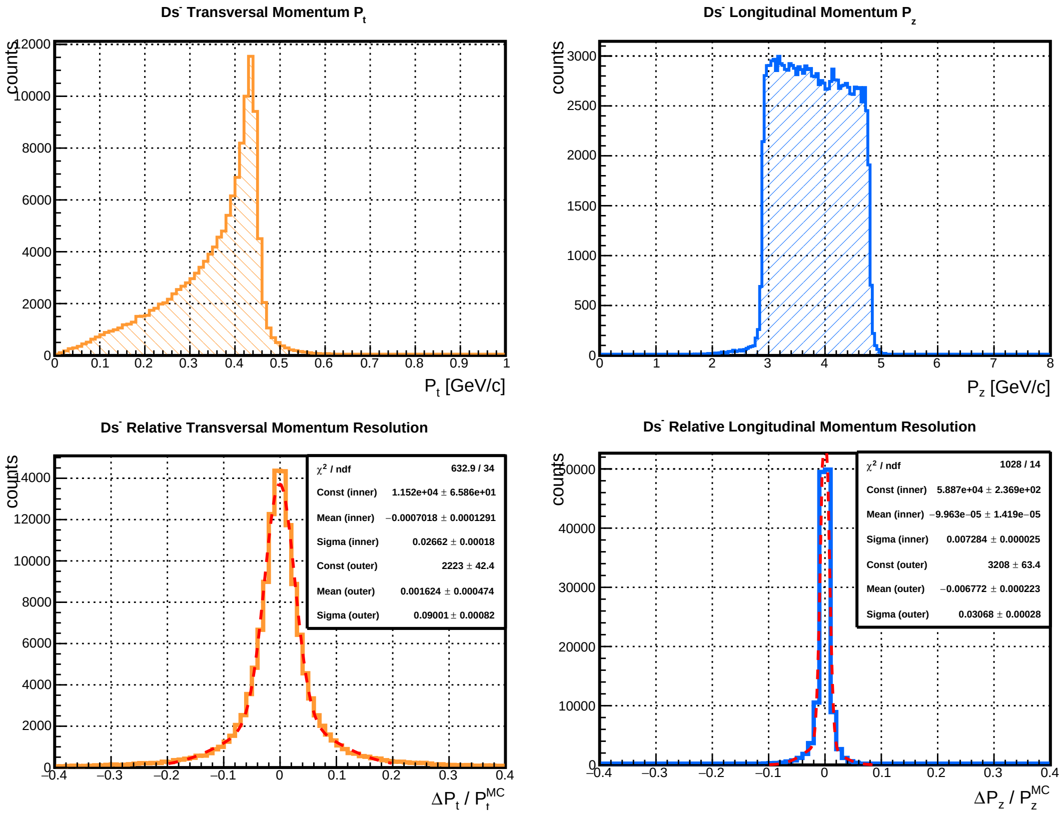

**Figure B.8:** The reconstructed $D_s^-$ momentum distributions in the decay of $D_s^- \to K^+K^-\pi^-$. Transversal (orange) and longitudinal (blue) momentum distributions are shown. The relative resolutions are shown in the lower frame: the red dashed lines present double-Gaussian fits.

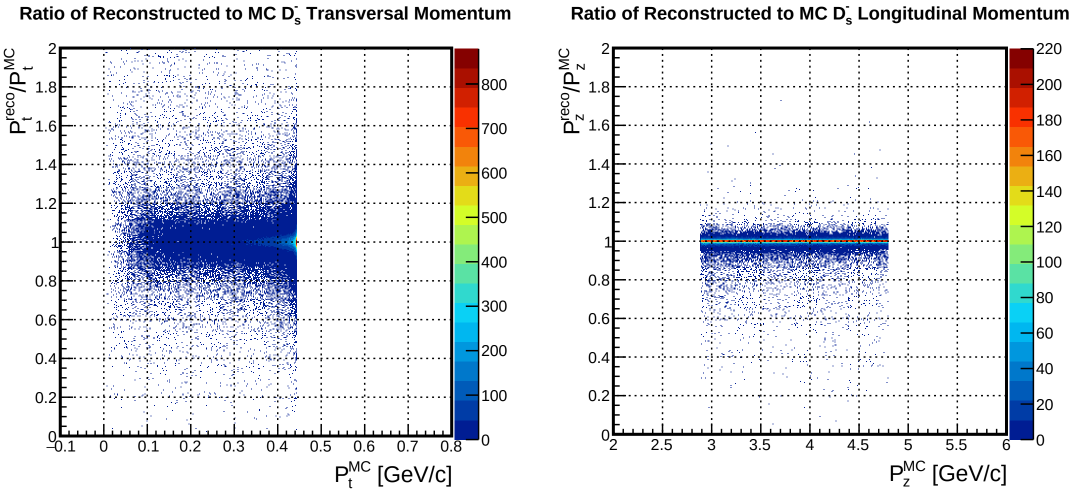

**Figure B.9:** Ratio of the reconstructed and MC momenta of the $D_s^-$ in tag mode A. Left is the ratio as a function of the transversal momentum, and right is the ratio as a function of the longitudinal momentum.

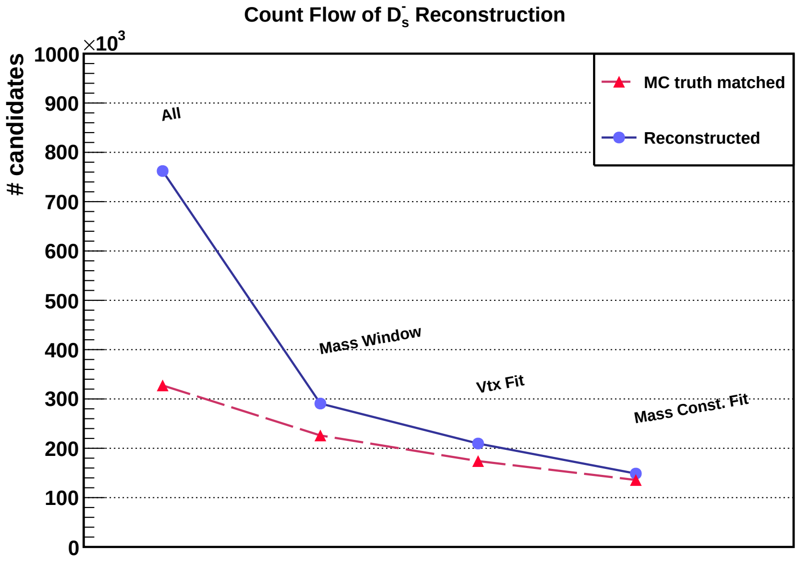

**Figure B.10:** Count flow of $D_s^-$ reconstruction in the decay $D_s^- \to K^+K^-\pi^-$. The data points follow the order of the reconstruction procedure from left to right. Blue: the number of reconstructed candidates. Red: the number of MC truth matched candidates.

# Bibliography

[1] Yorikiyo Nagashima. *Elementary Particle Physics: Foundations of the Standard Model*. Wiley-VCH, 2010. `doi:10.1002/9783527630097`.

[2] T. Rothman and S. Boughn. Can gravitons be detected? *Found. Phys.*, 36:1801–1825, 2006. `arXiv:gr-qc/0601043`, `doi:10.1007/s10701-006-9081-9`.

[3] B. P. Abbott *et al.* Observation of Gravitational Waves from a Binary Black Hole Merger. *Phys. Rev. Lett.*, 116(6):061102, 2016. `arXiv:1602.03837`, `doi:10.1103/PhysRevLett.116.061102`.

[4] Arthur I. Miller. *Early Quantum Electrodynamics: A Source Book*. Cambridge University Press, 1995.

[5] Michael E. Peskin and Dan V. Schroeder. *An Introduction To Quantum Field Theory*. Westview Press, 1995.

[6] A. Salam and J. C. Ward. Electromagnetic and weak interactions. *Physics Letters*, 13(2):168 – 171, 1964. `doi:http://dx.doi.org/10.1016/0031-9163(64)90711-5`.

[7] H. Nastase. Introduction to Supergravity. 2011. `arXiv:1112.3502`.

[8] Michael B. Green, John H. Schwarz, and Edward Witten. *Superstring Theory. Volume 1 Introduction*. Cambridge University Press, 2012.

[9] K. A. Olive *et al.* Review of Particle Physics. *Chin. Phys.*, C38:090001, 2014. `doi:10.1088/1674-1137/38/9/090001`.

[10] Wikipedia: The Standard Model of Elementary Particles. 2014. `http://en.wikipedia.org/wiki/Standard_Model` Accessed: 2014.11.16.

[11] M. Gell-Mann. A schematic model of baryons and mesons. *Physics Letters*, 8(3):214–215, 1964. `doi:http://dx.doi.org/10.1016/S0031-9163(64)92001-3`.

[12] G. Zweig. An SU(3) model for strong interaction symmetry and its breaking. Version 1. 1964.

[13] David Griffiths. *Introduction to Elementary Particles*. Wiley-VCH, 2nd edition, 2008.

[14] Vernon D. Barger and Roger J. N. Phillips. *Collider Physics*. Westview Press, 1996.

[15] S. M. Bilenky. Neutrinoless double beta-decay. *Phys. Part. Nucl.*, 41:690–715, 2010. `arXiv:1001.1946`, `doi:10.1134/S1063779610050035`.

[16] C. E. Aalseth *et al.* The IGEX $^{76}$Ge neutrinoless double beta decay experiment: Prospects for next generation experiments. *Phys. Rev.*, D65:092007, 2002. `arXiv:hep-ex/0202026`, `doi:10.1103/PhysRevD.65.092007`.

[17] R. Arnold *et al.* Limits on different Majoron decay modes of $^{100}$Mo and $^{82}$Se for neutrinoless double beta decays in the NEMO-3 experiment. *Nucl. Phys.*, A765:483–494, 2006. `arXiv:hep-ex/0601021`, `doi:10.1016/j.nuclphysa.2005.11.015`.

[18] Z. Maki, M. Nakagawa, and S. Sakata. Remarks on the Unified Model of Elementary Particles. *Progress of Theoretical Physics*, 28:870–880, 1962. `doi:10.1143/PTP.28.870`.

[19] B. Pontecorvo. Neutrino Experiments and the Problem of Conservation of Leptonic Charge. *Soviet Journal of Experimental and Theoretical Physics*, 26:984, 1968.

[20] S. Stone. New physics from favour. *PoS*, ICHEP2012:033, 2013. `arXiv:1212.6374`.

[21] The Nobel Prize in Physics 2015. *Nobelprize.org.*, Nobel Media AB 2014. Web. 17. `http://www.nobelprize.org/nobel_prizes/physics/laureates/2015/` Accessed: 2016.04.04.

[22] PANDA Home Page. `http://www-panda.gsi.de/` Accessed: 2015.02.09.

[23] F. Englert and R. Brout. Broken symmetry and the mass of gauge vector mesons. *Phys. Rev. Lett.*, 13:321–323, 1964. URL: `http://link.aps.org/doi/10.1103/PhysRevLett.13.321`, `doi:10.1103/PhysRevLett.13.321`.

[24] P. W. Higgs. Broken symmetries and the masses of gauge bosons. *Phys. Rev. Lett.*, 13:508–509, 1964. URL: `http://link.aps.org/doi/10.1103/PhysRevLett.13.508`, `doi:10.1103/PhysRevLett.13.508`.

[25] G. Aad *et al.* Observation of a new particle in the search for the Standard Model Higgs boson with the ATLAS detector at the LHC. *Phys. Lett.*, B716:1–29, 2012. `arXiv:1207.7214`, `doi:10.1016/j.physletb.2012.08.020`.

[26] S. Chatrchyan *et al.* Observation of a new boson at a mass of 125 GeV with the CMS experiment at the LHC. *Phys. Lett.*, B716:30–61, 2012. `arXiv:1207.7235`, `doi:10.1016/j.physletb.2012.08.021`.

[27] J. Beringer *et al.* Review of particle physics. *Phys. Rev.*, D86:010001, 2012. `doi:10.1103/PhysRevD.86.010001`.

[28] P. Teixeira-Dias. Higgs boson searches at LEP. *J. Phys. Conf. Ser.*, 110:042030, 2008. `arXiv:0804.4146`, `doi:10.1088/1742-6596/110/4/042030`.

[29] V. Ahrens *et al.* Updated Predictions for Higgs Production at the Tevatron and the LHC. *Phys. Lett.*, B698:271–274, 2011. arXiv:hep-ph/1008.3162. `arXiv:1008.3162`, `doi:10.1016/j.physletb.2010.12.072`.

[30] S. Aoki *et al.* Review of lattice results concerning low-energy particle physics. *Eur. Phys. J.*, C74:2890, 2014. `arXiv:1310.8555`, `doi:10.1140/epjc/s10052-014-2890-7`.

[31] D. Besson *et al.* Improved measurements of $D$ meson semileptonic decays to $\pi$ and $K$ mesons. *Phys. Rev.*, D80:032005, 2009. `arXiv:0906.2983`, `doi:10.1103/PhysRevD.80.032005`.

[32] L. Widhalm *et al.* Measurement of $D^0 \to \pi l \nu (K l \nu)$ Form Factors and Absolute Branching Fractions. *Phys. Rev. Lett.*, 97:061804, 2006. `doi:10.1103/PhysRevLett.97.061804`.

[33] B. Aubert *et al.* Measurement of the hadronic form factor in $D^0 \to K^- e^+ \nu_e$ decays. *Phys. Rev.*, D76:052005, 2007. `arXiv:0704.0020`, `doi:10.1103/PhysRevD.76.052005`.

[34] E. Rutherford. Bakerian Lecture. Nuclear Constitution of Atoms. *Proceedings of the Royal Society of London*, A97(686):374–400, 1920. `doi:10.1098/rspa.1920.0040`.

[35] Walter Greiner and Berndt Mueller. *Quantum Mechanics: Symmetries*. Springer, 2nd edition, 2001.

[36] A. Bramon, R. Escribano, and M. D. Scadron. The $\eta$-$\eta\prime$ mixing angle revisited. *Eur. Phys. J.*, C7:271–278, 1999. `arXiv:hep-ph/9711229`, `doi:10.1007/s100529801009`.

[37] T. N. Pham. $\eta$-$\eta\prime$ mixing. *Phys. Rev.*, D92(5):054021, 2015. `arXiv:1504.05414`, `doi:10.1103/PhysRevD.92.054021`.

[38] K. Abe *et al.* Search for proton decay via $p \to \nu K^+$ using 260 kiloton·year data of Super-Kamiokande. *Phys. Rev.*, D90(7):072005, 2014. `arXiv:1408.1195`, `doi:10.1103/PhysRevD.90.072005`.

[39] R. Aaij *et al.* Observation of $J/\psi$ Resonances Consistent with Pentaquark States in $\Lambda_b^0 \to J/\psi K^- p$ Decays. *Phys. Rev. Lett.*, 115:072001, 2015. `arXiv:1507.03414`, `doi:10.1103/PhysRevLett.115.072001`.

[40] P. Adlarson *et al.* Abashian-Booth-Crowe Effect in Basic Double-Pionic Fusion: A New Resonance? *Phys. Rev. Lett.*, 106:242302, 2011. `arXiv:1104.0123`, `doi:10.1103/PhysRevLett.106.242302`.

[41] M. Bashkanov, S. J. Brodsky, and H. Clement. Novel Six-Quark Hidden-Color Dibaryon States in QCD. *Phys. Lett.*, B727:438–442, 2013. `arXiv:1308.6404`, `doi:10.1016/j.physletb.2013.10.059`.

[42] P. Adlarson *et al.* Evidence for a New Resonance from Polarized Neutron-Proton Scattering. *Phys. Rev. Lett.*, 112(20):202301, 2014. `arXiv:1402.6844`, `doi:10.1103/PhysRevLett.112.202301`.

[43] S. Okubo. Note on unitary symmetry in strong interactions. *Progress of Theoretical Physics*, 27(5):949–966, 1962. URL: `http://ptp.oxfordjournals.org/content/27/5/949.abstract`, `doi:10.1143/PTP.27.949`.

[44] M. Gell-Mann. *THE EIGHTFOLD WAY: A THEORY OF STRONG INTERACTION SYMMETRY*. 1961. `doi:10.2172/4008239`.

[45] Ian J. R. Aitchison. Supersymmetry and the MSSM: An Elementary introduction. 2005. `arXiv:hep-ph/0505105`.

[46] M. N. Rosenbluth. High Energy Elastic Scattering of Electrons on Protons. *Phys. Rev.*, 79:615–619, 1950. `doi:10.1103/PhysRev.79.615`.

[47] Bogdan Povh *et al. Particles and Nuclei: An Introduction to the Physical Concepts*. Springer-Verlag Berlin Heidelberg, 6th edition, 2008.

[48] K. K. Seth. Timelike form-factors. In *Workshop on Exclusive Reactions at High Momentum Transfer Newport News, Virginia, May 21-24, 2007*, 2007. `arXiv:0712.0356`.

[49] W. Erni *et al.* Physics Performance Report for PANDA: Strong Interaction Studies with Antiprotons. 2009. `arXiv:0903.3905`.

[50] A. Zichichi *et al.* Proton anti-proton annihilation into electrons, muons and vector bosons. *Nuovo Cim.*, 24:170–180, 1962. `doi:10.1007/BF02785769`.

[51] E. A. Kuraev, A. Dbeyssi, and E. Tomasi-Gustafsson. A model for space and time-like proton (neutron) form factors. *Physics Letters B*, 712(3):240 – 244, 2012. `doi:10.1016/j.physletb.2012.04.073`.

[52] B. Aubert *et al.* A Study of $e^+e^- \to p\bar{p}$ using initial state radiation with BABAR. *Phys. Rev.*, D73:012005, 2006. `arXiv:hep-ex/0512023`, `doi:10.1103/PhysRevD.73.012005`.

[53] A. Antonelli *et al.* The first measurement of the neutron electromagnetic form-factors in the timelike region. *Nucl. Phys.*, B517:3–35, 1998. `doi:10.1016/S0550-3213(98)00083-2`.

[54] D. Bisello *et al.* A Measurement of $e^+e^- \to \bar{p}p$ for (1975$\leq \sqrt{s} \leq$2250) MeV. *Nucl. Phys.*, B224:379, 1983. `doi:10.1016/0550-3213(83)90381-4`.

[55] D. Bisello *et al.* Baryon pairs production in $e^+e^-$ annihilation at $\sqrt{s} = 2.4$ GeV. *Z. Phys.*, C48:23–28, 1990. `doi:10.1007/BF01565602`.

[56] B. Delcourt *et al.* Study of the Reaction $e^+e^- \to p\bar{p}$ in the Total Energy Range 1925-2180 MeV. *Phys. Lett.*, B86:395, 1979. `doi:10.1016/0370-2693(79)90864-5`.

[57] M. Ablikim *et al.* Measurement of the cross section for $e^+e^- \to p\bar{p}$ at center-of-mass energies from 2.0 GeV to 3.07 GeV. *Phys. Lett.*, B630:14–20, 2005. `arXiv:hep-ex/0506059`, `doi:10.1016/j.physletb.2005.09.044`.

[58] T. K. Pedlar *et al.* Precision measurements of the timelike electromagnetic form-factors of pion, kaon, and proton. *Phys. Rev. Lett.*, 95:261803, 2005. `arXiv:hep-ex/0510005`, `doi:10.1103/PhysRevLett.95.261803`.

[59] G. Bardin *et al.* Determination of the electric and magnetic form-factors of the proton in the timelike region. *Nucl. Phys.*, B411:3–32, 1994. `doi:10.1016/0550-3213(94)90052-3`.

[60] M. Ambrogiani *et al.* Measurements of the magnetic form-factor of the proton in the timelike region at large momentum transfer. *Phys. Rev.*, D60:032002, 1999. `doi:10.1103/PhysRevD.60.032002`.

[61] M. Andreotti *et al.* Measurements of the magnetic form-factor of the proton for timelike momentum transfers. *Phys. Lett.*, B559:20–25, 2003. `doi:10.1016/S0370-2693(03)00300-9`.

[62] T. A. Armstrong *et al.* Measurement of the proton electromagnetic form-factors in the timelike region at 8.9 to 13.0 GeV$^2$. *Phys. Rev. Lett.*, 70:1212–1215, 1993. `doi:10.1103/PhysRevLett.70.1212`.

[63] E. P. Solodov. Measurements of the photon-meson transition form factors at babar. 2011. Talk in the XIV International Conference on Hadron Spectroscopy. URL: `http://www.slac.stanford.edu/econf/C110613/slides/45-slides.pdf`.

[64] R. Escribano, P. Masjuan, and P. Sanchez-Puertas. The $\eta$ transition form factor from space- and time-like experimental data. *Eur. Phys. J.*, C75(9):414, 2015. `arXiv:1504.07742`, `doi:10.1140/epjc/s10052-015-3642-z`.

[65] H. J. Behrend *et al.* A Measurement of the $\pi^0$, $\eta$ and $\eta'$ electromagnetic form-factors. *Z. Phys.*, C49:401–410, 1991. `doi:10.1007/BF01549692`.

[66] J. Gronberg *et al.* Measurements of the meson - photon transition form-factors of light pseudoscalar mesons at large momentum transfer. *Phys. Rev.*, D57:33–54, 1998. `arXiv:hep-ex/9707031`, `doi:10.1103/PhysRevD.57.33`.

[67] P. del Amo Sanchez *et al.* Measurement of the $\gamma\gamma^* \to \eta$ and $\gamma\gamma* \to \eta'$ transition form factors. *Phys. Rev.*, D84:052001, 2011. `arXiv:1101.1142`, `doi:10.1103/PhysRevD.84.052001`.

[68] R. Arnaldi *et al.* Study of the electromagnetic transition form-factors in $\eta \to \mu^+\mu^-\gamma$ and $\omega \to \mu^+\mu^-\pi^0$ decays with NA60. *Phys. Lett.*, B677:260–266, 2009. `arXiv:0902.2547`, `doi:10.1016/j.physletb.2009.05.029`.

[69] H. Berghauser *et al.* Determination of the eta-transition form factor in the $\gamma p \to p\eta \to p\gamma e^+e^-$ reaction. *Phys. Lett.*, B701:562–567, 2011. `doi:10.1016/j.physletb.2011.06.069`.

[70] P. Aguar-Bartolome *et al.* New determination of the $\eta$ transition form factor in the Dalitz decay $\eta \to e^+e^-\gamma$ with the Crystal Ball/TAPS detectors at the Mainz Microtron. *Phys. Rev.*, C89(4):044608, 2014. `arXiv:1309.5648`, `doi:10.1103/PhysRevC.89.044608`.

[71] D. M. Asner *et al.* Physics at BES-III. *Int. J. Mod. Phys.*, A24:S1–794, 2009. `arXiv:0809.1869`.

[72] I. Kanamori. Lattice calculations of $D_s$ to eta and eta' decay form factors. 2013. `arXiv:hep-lat/1302.6087`.

[73] D. Becirevic and A. B. Kaidalov. Comment on the heavy → light form-factors. *Phys. Lett.*, B478:417–423, 2000. `arXiv:hep-ph/9904490`, `doi:10.1016/S0370-2693(00)00290-2`.

[74] D. Scora and N. Isgur. Semileptonic Meson Decays in the Quark Model: An Update. *Phys. Rev.*, D52:2783–2812, 1995. `arXiv:hep-ph/9503486`, `doi:10.1103/PhysRevD.52.2783`.

[75] P. Ball and R. Zwicky. New results on $B \to \pi, K, \eta$ decay formfactors from light-cone sum rules. *Phys. Rev.*, D71:014015, 2005. `arXiv:hep-ph/0406232`, `doi:10.1103/PhysRevD.71.014015`.

[76] M. A. Shifman *et al.* QCD and Resonance Physics. Theoretical Foundations. *Nucl. Phys.*, B147:385–447, 1979. `doi:10.1016/0550-3213(79)90022-1`.

[77] P. Colangelo and F. De Fazio. $D_s$ decays to $\eta$ and $\eta\prime$ final states: a phenomenological analysis. *Phys. Lett.*, B520:78–86, 2001. `arXiv:hep-ph/0107137`, `doi:10.1016/S0370-2693(01)01112-1`.

[78] N. Offen, F. A. Porkert, and A. Schäfer. Light-cone sum rules for the $D_{(s)} \to \eta^{(\prime)} l \nu_l$ form factor. *Phys. Rev.*, D88(3):034023, 2013. `arXiv:1307.2797`, `doi:10.1103/PhysRevD.88.034023`.

[79] K. Azizi, R. Khosravi, and F. Falahati. Exclusive $D_s \to (\eta, \eta\prime) l \nu$ decays in light-cone QCD. *J. Phys. G*, 38(9):095001, 2011. `doi:10.1088/0954-3899/38/9/095001`.

[80] G. C. Donald *et al.* $V_{cs}$ from $D_s \to \phi \ell \nu$ semileptonic decay and full lattice QCD. *Phys. Rev.*, D90:074506, 2014. `arXiv:1311.6669`, `doi:10.1103/PhysRevD.90.074506`.

[81] G. S. Bali *et al.* $D_s \to \eta, \eta'$ semileptonic decay form factors with disconnected quark loop contributions. *Phys. Rev.*, D91(1):014503, 2015. `arXiv:1406.5449`, `doi:10.1103/PhysRevD.91.014503`.

[82] J. Yelton *et al.* Absolute Branching Fraction Measurements for Exclusive $D_s$ Semileptonic Decays. *Phys. Rev.*, D80:052007, 2009. `arXiv:0903.0601`, `doi:10.1103/PhysRevD.80.052007`.

[83] K. Kodama *et al.* A Study of the semimuonic decays of the $D_{(s)}$. *Phys. Lett.*, B309:483–491, 1993. `doi:10.1016/0370-2693(93)90965-K`.

[84] R. E. Mitchell *et al.* Observation of $D^+ \to \eta e^+ \nu_e$. *Phys. Rev. Lett.*, 102:081801, 2009. `arXiv:0802.4222`, `doi:10.1103/PhysRevLett.102.081801`.

[85] J. Yelton *et al.* Studies of $D^+ \to \eta^{'}, \eta, \phi e^+ \nu_e$. *Phys. Rev.*, D84:032001, 2011. `arXiv:1011.1195`, `doi:10.1103/PhysRevD.84.032001`.

[86] J. M. Link *et al.* New measurements of the $D_s^+ \to \phi \mu^+ \nu$ form-factor ratios. *Phys. Lett.*, B586:183–190, 2004. `arXiv:hep-ex/0401001`, `doi:10.1016/j.physletb.2004.02.015`.

[87] E. M. Aitala *et al.* Measurement of the form-factor ratios for $D_s^+ \to \phi$lepton $+\nu$ lepton. *Phys. Lett.*, B450:294–300, 1999. `arXiv:hep-ex/9812013`, `doi:10.1016/S0370-2693(99)00141-0`.

[88] P. L. Frabetti *et al.* Measurement of the form-factors for the decay $D_s^+ \to \phi \mu^+ \nu$. *Phys. Lett.*, B328:187–192, 1994. `doi:10.1016/0370-2693(94)90449-9`.

[89] K. M. Ecklund *et al.* Study of the semileptonic decay $D_s^+ \to f_0(980) e^+ \nu_e$ and implications for $B_s^0 \to J/\psi f_0$. *Phys. Rev.*, D80:052009, 2009. `arXiv:0907.3201`, `doi:10.1103/PhysRevD.80.052009`.

[90] B. Aubert *et al.* Study of the decay $D_s^+ \to K^+ K^- e^+ \nu_e$. *Phys. Rev.*, D78:051101, 2008. `arXiv:0807.1599`, `doi:10.1103/PhysRevD.78.051101`.

[91] P. Avery *et al.* Measurement of the ratios of form-factors in the decay $D_s^+ \to \phi e^+ \nu_e$. *Phys. Lett.*, B337:405–410, 1994. `doi:10.1016/0370-2693(94)90994-6`.

[92] L. Martin *et al.* Search for the decay $D_s^+ \to \omega e^+ \nu$. *Phys. Rev.*, D84:012005, 2011. `arXiv:1105.2720`, `doi:10.1103/PhysRevD.84.012005`.

[93] D. Cronin-Hennessy *et al.* Measurement of Charm Production Cross Sections in $e^+e^-$ Annihilation at Energies between 3.97 and 4.26 GeV. *Phys. Rev.*, D80:072001, 2009. `arXiv:0801.3418`, `doi:10.1103/PhysRevD.80.072001`.

[94] J. Haidenbauer and G. Krein. Production of charmed pseudoscalar mesons in antiproton-proton annihilation. *Phys. Rev.*, D89(11):114003, 2014. `arXiv:1404.4174`, `doi:10.1103/PhysRevD.89.114003`.

[95] Facility for Antiproton and Ion Research. `http://www.fair-center.de/` Accessed: 2015.02.09.

[96] A. Dolinskii *et al.* Antiproton complex at the FAIR project. *Nucl. Instrum. Meth.*, A629:16–24, 2011. `doi:10.1016/j.nima.2010.11.037`.

[97] P. Sievers *et al.* Concept for the Antiproton Production Target at FAIR. *Conf. Proc.*, C1205201:2570–2572, 2012.

[98] A. Lehrach *et al.* Beam dynamics of the High-Energy Storage Ring (HESR) for FAIR. *Int. J. Mod. Phys.*, E18:420–429, 2009. `doi:10.1142/S021830130901246X`.

[99] H. Stockhorst *et al.* Cooling Scenario for the HESR Complex. *AIP Conf. Proc.*, 821:190–195, 2006. [,190(2006)]. `doi:10.1063/1.2190110`.

[100] B. Sharkov. Measurements of the photon-meson transition form factors at babar. 2014. In the International Conference on Science and Technology for FAIR in Europe. URL: `https://indico.gsi.de/getFile.py/access?contribId=23&sessionId=0&resId=0&materialId=slides&confId=2443`.

[101] Andreas Herten. *GPU-based Online Track Reconstruction for PANDA and Application to the Analysis of $D \to K\pi\pi$*. PhD thesis, Ruhr-Universität Bochum, 2015. `http://hdl.handle.net/2128/9276`.

[102] W. Erni *et al.* Technical Design Report for the PANDA: Strong Interaction Studies with Antiprotons. 2011. `https://panda.gsi.de/oldwww/archive/public/panda_tpr.pdf`.

[103] L. Cao, Y. Yang, and H. Chen. Charmonium states in QCD-inspired quark potential model using Gaussian expansion method. *Few Body Syst.*, 53:327–342, 2012. `arXiv:1206.3008`, `doi:10.1007/s00601-012-0478-z`.

[104] L. Liu *et al.* Excited and exotic charmonium spectroscopy from lattice QCD. *PoS*, LATTICE2012:138, 2012.

[105] M. Yu. Barabanov, A.S. Vodopyanov, and S.L. Olsen. New research of charmonium over $D\bar{D}$ threshold using the antiproton beam with momentum ranging from 1 to 15 GeV/c. *Phys. Atom. Nucl.*, 77:126–130, 2014. `doi:10.1134/S1063778814010049`.

[106] F. E. Close and E. S. Swanson. Dynamics and decay of heavy-light hadrons. *Phys. Rev.*, D72:094004, 2005. `arXiv:hep-ph/0505206`, `doi:10.1103/PhysRevD.72.094004`.

[107] E. Prencipe. Perspectives of open charm physics at PANDA. *EPJ Web Conf.*, 95:04052, 2015. `arXiv:1410.5680`, `doi:10.1051/epjconf/20159504052`.

[108] G. Moir *et al.* Excited spectroscopy of mesons containing charm quarks from lattice QCD. *PoS*, LATTICE2013:242, 2014. `arXiv:1312.1361`.

[109] Colin J. Morningstar and Mike J. Peardon. Efficient glueball simulations on anisotropic lattices. *Phys. Rev.*, D56:4043–4061, 1997. `arXiv:hep-lat/9704011`, `doi:10.1103/PhysRevD.56.4043`.

[110] C. J. Morningstar and M. J. Peardon. The Glueball spectrum from an anisotropic lattice study. *Phys. Rev.*, D60:034509, 1999. `arXiv:hep-lat/9901004`, `doi:10.1103/PhysRevD.60.034509`.

[111] A. Abele *et al.* Exotic $\eta\pi$ state in $\bar{p}d$ annihilation at rest into $\pi - \pi^0\eta$ pspectator. *Phys. Lett.*, B423:175–184, 1998. `doi:10.1016/S0370-2693(98)00123-3`.

[112] J. Reinnarth. Evidence for an exotic partial wave in $\pi\eta'$. *Nucl. Phys.*, A692:268–274, 2001. `doi:10.1016/S0375-9474(01)01186-1`.

[113] C. Amsler and F. E. Close. Evidence for a a scalar glueball. *Phys. Lett.*, B353:385–390, 1995. `arXiv:hep-ph/9505219`, `doi:10.1016/0370-2693(95)00579-A`.

[114] W. M. Yao *et al.* Review of Particle Physics. *J. Phys.*, G33:1–1232, 2006. `doi:10.1088/0954-3899/33/1/001`.

[115] T. Melde, W. Plessas, and B. Sengl. Quark-Model Identification of Baryon Ground and Resonant States. *Phys. Rev.*, D77:114002, 2008. `arXiv:0806.1454`, `doi:10.1103/PhysRevD.77.114002`.

[116] B. Alessandro *et al.* A New measurement of J/psi suppression in Pb-Pb collisions at 158 GeV per nucleon. *Eur. Phys. J.*, C39:335–345, 2005. `arXiv:hep-ex/0412036`, `doi:10.1140/epjc/s2004-02107-9`.

[117] A. B. Larionov *et al.* Charmonium production in antiproton-nucleus reactions at low energies. *Phys. Rev.*, C87(5):054608, 2013. `arXiv:1303.0236`, `doi:10.1103/PhysRevC.87.054608`.

[118] B. P. Singh *et al.* Experimental access to Transition Distribution Amplitudes with the PANDA experiment at FAIR. *Eur. Phys. J.*, A51(8):107, 2015. `arXiv:1409.0865`, `doi:10.1140/epja/i2015-15107-y`.

[119] J. P. Ralston and D. E. Soper. Production of Dimuons from High-Energy Polarized Proton Proton Collisions. *Nucl. Phys.*, B152:109, 1979. `doi:10.1016/0550-3213(79)90082-8`.

[120] N. Kaiser and W. Weise. Chiral SU(3) dynamics and Lambda-hyperons in the nuclear medium. *Phys. Rev.*, C71:015203, 2005. `arXiv:nucl-th/0410062`, `doi:10.1103/PhysRevC.71.015203`.

[121] S. C. Pieper. Quantum Monte Carlo calculations of light nuclei. *Riv. Nuovo Cim.*, 31:709–740, 2008. `arXiv:0711.1500`, `doi:10.1393/ncr/i2009-10039-1`.

[122] J. Pochodzalla. Future hypernuclear physics at MAMI-C and PANDA-GSI. *Nucl. Phys.*, A754:430–442, 2005. `doi:10.1016/j.nuclphysa.2005.01.027`.

[123] W. Erni *et al.* Technical design report for the PANDA (AntiProton Annihilations at Darmstadt) Straw Tube Tracker. *Eur. Phys. J.*, A49:25, 2013. `arXiv:1205.5441`, `doi:10.1140/epja/i2013-13025-8`.

[124] W. Erni *et al.* Technical Design Report for the PANDA Micro Vertex Detector. 2012. `arXiv:1207.6581`.

[125] W. Erni *et al.* Technical Design Report for the PANDA Muon System. 2012. `http://www.fair-center.eu/fileadmin/fair/publications_exp/Muon_TDR.pdf`.

[126] B. Singh *et al.* Technical Design Report for PANDA Electromagnetic Calorimeter (EMC). 2008. `arXiv:0810.1216`.

[127] J. E. Augustin *et al.* Discovery of a Narrow Resonance in $e^+e^-$ Annihilation. *Phys. Rev. Lett.*, 33:1406–1408, 1974. [Adv. Exp. Phys.5,141(1976)]. `doi:10.1103/PhysRevLett.33.1406`.

[128] M. Andreotti *et al.* Measurement of the resonance parameters of the $\chi_1(1^3P_1)$ and $\chi_2(1^3P_2)$ states of charmonium formed in $p\bar{p}$ annihilations. *Nucl. Phys.*, B717:34–47, 2005. `arXiv:hep-ex/0503022`, `doi:10.1016/j.nuclphysb.2005.03.042`.

[129] W. Erni *et al.* Technical Design Report for the PANDA Solenoid and Dipole Spectrometer Magnets. 2009. `arXiv:0907.0169`.

[130] Q. Hu *et al.* A recoil detector for the measurement of antiproton-proton elastic scattering at angles close to 90°. *Eur. Phys. J.*, A50(10):156, 2014. arXiv:1409.8595, doi:10.1140/epja/i2014-14156-0.

[131] I. Konorov *et al.* SODA: Time distribution system for the PANDA experiment. In *Nuclear Science Symposium Conference Record (NSS/MIC), 2009 IEEE*, pages 1863–1865, 2009. doi:10.1109/NSSMIC.2009.5402172.

[132] S. Spataro. Event reconstruction in the PandaRoot framework. *J. Phys. Conf. Ser.*, 396:022048, 2012. doi:10.1088/1742-6596/396/2/022048.

[133] I. Antcheva *et al.* ROOT: A C++ framework for petabyte data storage, statistical analysis and visualization. *Comput. Phys. Commun.*, 182:1384–1385, 2011. doi:10.1016/j.cpc.2011.02.008.

[134] R. Brun and F. Rademakers. ROOT: An object oriented data analysis framework. *Nucl. Instrum. Meth.*, A389:81–86, 1997. doi:10.1016/S0168-9002(97)00048-X.

[135] S. Agostinelli *et al.* GEANT4: A Simulation toolkit. *Nucl. Instrum. Meth.*, A506:250–303, 2003. doi:10.1016/S0168-9002(03)01368-8.

[136] J. Allison *et al.* Geant4 Developments and Applications. *Nuclear Science, IEEE Transactions on*, 53(1):270–278, 2006. doi:10.1109/TNS.2006.869826.

[137] M. Al-Turany *et al.* The FairRoot framework. *J. Phys. Conf. Ser.*, 396:022001, 2012. doi:10.1088/1742-6596/396/2/022001.

[138] Ralf Kliemt. *Simulations with the Panda Micro-Vertex-Detector*. PhD thesis, Universität Bonn, 2012. URL: http://hss.ulb.uni-bonn.de/2013/3303/3303.htm.

[139] Anders Ryd *et al.* EvtGen: A Monte Carlo Generator for B-Physics. 2005. URL: http://robbep.web.cern.ch/robbep/EvtGen/GuideEvtGen.pdf.

[140] EvtGen Development Team. http://evtgen.warwick.ac.uk/ Accessed: 2015.12.04.

[141] A. Capella *et al.* Dual parton model. *Phys. Rept.*, 236:225–329, 1994. doi:10.1016/0370-1573(94)90064-7.

[142] C. Hoppner, S. Neubert, B. Ketzer, and S. Paul. A Novel Generic Framework for Track Fitting in Complex Detector Systems. *Nucl. Instrum. Meth.*, A620:518–525, 2010. arXiv:0911.1008, doi:10.1016/j.nima.2010.03.136.

[143] A. Fontana *et al.* Use of GEANE for tracking in virtual Monte Carlo. *J. Phys. Conf. Ser.*, 119:032018, 2008. doi:10.1088/1742-6596/119/3/032018.

[144] J. Rauch and T. Schlüter. GENFIT — a Generic Track-Fitting Toolkit. *J. Phys. Conf. Ser.*, 608(1):012042, 2015. arXiv:1410.3698, doi:10.1088/1742-6596/608/1/012042.

[145] R. Novotny *et al.* Electromagnetic calorimetry with $PbWO_4$ in the energy regime below 1 GeV. *Nuclear Science, IEEE Transactions on*, 47(4):1499–1502, 2000. doi:10.1109/23.873004.

[146] W. Erni *et al.* Technical Design Report for the PANDA Forward Spectrometer Calorimeter. in preparation.

[147] Rho: A framework for particle physics analysis. https://code.google.com/archive/p/rhoframework/ Accessed: 2015.12.09.

[148] J. Haidenbauer *et al.* Reaction $p\ \ p \to \Lambda\Lambda$ in the meson-exchange picture. *Phys. Rev.*, C45:931–946, 1992. doi:10.1103/PhysRevC.45.931.

[149] A. T. Goritschnig, B. Pire, and W. Schweiger. Production of heavy meson pairs in $p\bar{p}$ collisions within a double handbag approach. *J. Phys. Conf. Ser.*, 503:012012, 2014. arXiv:1311.1607, doi:10.1088/1742-6596/503/1/012012.

[150] A. Khodjamirian *et al.* How much charm can PANDA produce? *Eur. Phys. J.*, A48:31, 2012. arXiv:1111.3798, doi:10.1140/epja/i2012-12031-8.

[151] J. Haidenbauer, K. Holinde, and J. Speth. A meson-exchange model for the antihyperon-hyperon production. *Nucl. Phys.*, A562:317–351, 1993. doi:10.1016/0375-9474(93)90202-9.

[152] P. D. Barnes *et al.* Measurement of the reactions $\bar{p}p \to \bar{\Sigma}^+\Sigma^+$ and $\bar{p}p \to \bar{\Sigma}^-\Sigma^-$ close to threshold. *Phys. Lett.*, B402:227–236, 1997. doi:10.1016/S0370-2693(97)00420-6.

[153] A. I. Titov and B. Kämpfer. Exclusive charm production in $\bar{p}p$ collisions at $\sqrt{s} \lesssim 15$ GeV. *Phys. Rev.*, C78:025201, 2008. arXiv:0807.1822, doi:10.1103/PhysRevC.78.025201.

[154] B. Kerbikov and D. Kharzeev. $NN$ annihilation at the open charm threshold. *Phys. Rev.*, D51:6103–6106, 1995. arXiv:hep-ph/9408378, doi:10.1103/PhysRevD.51.6103.

[155] P. Kroll, B. Quadder, and W. Schweiger. Exclusive production of heavy flavours in proton-antiproton annihilation. *Nucl. Phys.*, B316:373–390, 1989. doi:10.1016/0550-3213(89)90036-9.

[156] N. Isgur *et al.* Semileptonic $B$ and $D$ decays in the quark model. *Phys. Rev.*, D39:799–818, 1989. doi:10.1103/PhysRevD.39.799.

[157] R. E. Mitchell *et al.* Dalitz plot analysis of $D_s^+ \to K^+K^-\pi^+$. *Phys. Rev.*, D79:072008, 2009. arXiv:0903.1301, doi:10.1103/PhysRevD.79.072008.

[158] P. del Amo Sanchez *et al.* Dalitz plot analysis of $D_s^+ \to K^+K^-\pi^+$. *Phys. Rev.*, D83:052001, 2011. arXiv:1011.4190, doi:10.1103/PhysRevD.83.052001.

[159] B. Aubert *et al.* Dalitz Plot Analysis of $D_s^+ \to \pi^+\pi^-\pi^+$. *Phys. Rev.*, D79:032003, 2009. arXiv:0808.0971, doi:10.1103/PhysRevD.79.032003.

[160] F. Ambrosino *et al.* Determination of $\eta \rightarrow \pi^+ \pi^- \pi^0$ Dalitz plot slopes and asymmetries with the KLOE detector. *JHEP*, 05:006, 2008. `arXiv:hep-ex/0801.2642`, `doi:10.1088/1126-6708/2008/05/006`.

[161] L. Cao and J. Ritman. Simulated Measurement of the $D_s$ Meson Semileptonic Decay Form Factor with the $\bar{\text{P}}$ANDA Detector. 2014. To be published on Nucl. Phys. B Proc. Supp.

[162] E. Atomssa *et al.* A new method for correcting electron momentum reconstruction in the panda detector for the bremsstrahlung effect. *PANDA Technical Note*, (TN-STT-2015-001), 2015.

[163] G. Mazza *et al.* The ToPiX v4 prototype for the triggerless readout of the PANDA silicon pixel detector. *JINST*, 10(01):C01042, 2015. `doi:10.1088/1748-0221/10/01/C01042`.

[164] Thanushan Kugathasan. *Low-Power High Dynamic Range Front-End Electronics for the Hybrid Pixel Detectors of the PANDA MVD*. PhD thesis, Universiti Turino, 2011. URL: `http://dottorato.ph.unito.it/Studenti/Tesi/XXIII/kugathasan.pdf`.

[165] Gianni Mazza. Private commnunication. 2016.

[166] S. Esch *et al.* Development of a readout system for the bar PANDA Micro Vertex Detector. *JINST*, 8:C01043, 2013. `doi:10.1088/1748-0221/8/01/C01043`.

[167] Simone Esch. *Evaluation of the PANDA Silicon Pixel Front-End Electronics and Investigation of the* $\Lambda\bar{\Lambda}$ *Final State*. PhD thesis, Ruhr-Universität Bochum, 2014. URL: `http://www-brs.ub.ruhr-uni-bochum.de/netahtml/HSS/Diss/EschSimone/diss.pdf`.

[168] R. Maier. Cooler synchrotron COSY: Performance and perspectives. *Nucl. Instrum. Meth.*, A390:1–8, 1997. `doi:10.1016/S0168-9002(97)00324-0`.

[169] IKP 2013 Annual Report. 2013. `http://www.fz-juelich.de/ikp/EN/Service/Download/Downloads/jahresbericht_2013.html.`

[170] IKP 2014 Annual Report. 2014. `http://www.fz-juelich.de/ikp/EN/Service/Download/Downloads/jahresbericht_2014.html?nn=498262`.

[171] Gianni Mazza. ToPiX v4 User's Guide. 2014.

[172] Millepede: Linear least squares fits with a large number of parameters. `http://www.desy.de/~blobel/mptalks.html` Accessed: 11-06-2016.

[173] L. Cao and J. Ritman. Simulations on the measurement of the $D_s$ meson semileptonic form factor with the PANDA detector. *J. Phys.: Conf. Ser.*, 503(1):12024–12028, 2014. `doi:10.1088/1742-6596/503/1/012024`.

[174] Ralf Kliemt. Global tree fitter. 2016. Talk in the LVI PANDA Collaboration Meeting.

# Acronyms

**P̄ANDA** Antiproton Annihilation at Darmstadt

**APPA** Atomic, Plasma Physics and Applications
**ASIC** Application-Specific Integrated Circuit

**CBM** Compressed Baryonic Matter
**CCU** Chip Control Unit
**CKM** Cabibbo-Kobayashi-Maskawa matrix
**CMOS** Complementary Metal Oxide Semiconductor
**COSY** Cooler Synchrotron
**CRC** Cyclic Redundancy Check
**CRCU** Column Readout Control Unit
**CSA** Charge Sensitive Amplifier

**DAQ** Data Acquisition
**DIRC** Detection of Internally Reflected Cherenkov Light
**DPM** Dual Parton Model

**ECC** Error Correction Code
**EFT** Effective Field Theory
**EMC** Electromagnetic Calorimeter

**FAIR** Facility for Antiproton and Ion Research
**FIFO** First In First Out
**FPGA** Field-Programmable Gate Array
**FRS** Fragment Separator
**FSC** Forward Shashlyk-type Carlorimeter
**FTS** Forward Tracking System
**FWHM** Full Width at Half Maximum
**FZJ** Forschungszentrum Jülich

**GEM** Gas Electron Multiplier
**GPDs** Generalized Parton Distributions
**GSI** GSI Helmholtz Centre for Heavy Ion Research
**GUI** Graphical User Interface

**HESR** High-Energy Storage Ring
**HVMAPS** High Voltage Monolythic Active Pixel Sensors

**INFN** Istituto Nazionale de Fisica Nuleare

**JDRS** Jülich Digital Readout System
**JULIC** Jülich Light Ion Cyclotron

**KOALA** Key experiment fOr PANDA Luminosity determinAtion

**LCSR** Light-Cone Sum Rules
**LHC** Large Hadron Collider
**LQCD** Lattice Quantum Chromodynamics
**LVDS** Low Voltage Differential Signal

**MC** Monte Carlo
**MDT** Mini Drift Tubes
**MIP** Minimum Ionizing Particles
**MP** Micropulse
**MSB** Most Significant Bit
**MSV** Modularised Start Version
**MVD** Micro Vertex Detector

**NUSTAR** Nuclear Structure, Astrophysics and Reactions

**OPE** Operator Product Expansion

**PHSP** PHase SPace
**PID** Particle Identification

**PMNS** Pontecorvo-Maki-Nakagawa-Sakata matrix

**QCD** Quantum Chromo Dynamics
**QCDSR** QCD Sum Rules
**QED** Quantum Electro-Dynamics
**QGS** Quark-Gluon String
**QPM** Quark Potential Model

**RESR** Recuperated Experimental Storage Ring
**RICH** Ring-Imaging Cherenkov

**SLVS** Scalable Low Voltage Signal
**SODA** Synchronization Of Data Acquisition
**STT** Straw Tube Tracker

**TDAs** Transition Distribution Amplitudes
**TOF** Time Of Flight
**ToPix** Torino Pixel
**ToT** Time-over-Threshold
**TPDs** Transverse Parton Distributions

**VMC** Virtual Monte Carlo

**XYZ** exotic X, Y, Z states

# List of Figures

# List of Tables

# Acknowledgements

I would express my deep sense of thanks and gratitude to James Ritman for his great guidances. His prompt inspirations, meticulous scrutiny and scientific approach have helped me at every stage of my research. Besides extensive discussions, Jim has provided me opportunities to gain a multi-dimension development, which will be beneficial throughout my career.

I thank Tobias Stockmanns profusely for providing me necessary technical help during my research. His timely suggestions and kind supports have enabled me to complete my thesis.

Thanks to Albrecht Gillitzer and Elisabetta Prencipe for their keen interest in my research and helpful discussions.

I am thankful to all IKP colleagues in professional as well as personal matters. Special thanks go to Andreas, André, Huagen, Florian, Mei, Marius, Simone, Dariusch, Ludovico, Jennifer, Alessandra, Qiang, Artur, Frank, Günter, Rene, Michael, Daniel, Farha, Maria, Xinying, Solmaz, Alexandros, Qian and Andrew. Thanks to all for sharing a really joyful atmosphere. We have had a lot of fun at every lunch, and all group activities.

Thanks to the $\bar{\text{P}}$ANDA members for their kind help and co-operation. Thanks to Johan for his continuous support and interest in my work. Thanks to Stefano, Klaus and Ralf for their efforts in the software development and suggestions for my simulations. Thanks to Sean for useful information on the $\text{D}_\text{s}$ decay model. And all the ones I forgot to list here.

I appreciate to my dear parents for their strong supports and great love. They are my pretty sunshine from ∼8381 km afar.

Thanks for all the help, support and encouragement in accomplishing this thesis, and pleasurable company during the period.

# Curriculum Vitae

## Personal Data

Name: Lu Cao
Date of birth: June 5,1987
Place of birth: Guiyang, China

## Education

| | |
|---|---|
| 1993 - 1999 | Yuying Primary School, Guiyang |
| 1999 - 2002 | Guiyang No.19 Middle School, Guiyang |
| 2002 - 2005 | Guiyang No.1 High School, Guiyang |
| 2005 - 2009 | Physics, Southwest University, Chongqing, China<br>*Bachelor Thesis*: Inelastic Electron-Nucleon Scattering and Nuclear Structure Function |
| 2006 - 2009 | English, Southwest University<br>*Bachelor Thesis*: The Influence of Cultural Individualism-Collectivism on Cross-Cultural Communication |
| 2009 - 2012 | Theoretical Physics, Southwest University<br>*Master Thesis*: Heavy Quarkonium Properties in the Quark Model |
| 2012 - 2016 | Experimental Hadronic Physics, Ruhr-Universität Bochum<br>and Institut für Kernphysik of Forschungszentrum Jülich, Germany<br>*Ph.D. Thesis*: Simulation of the $\mathrm{D_s}$ Semileptonic Decay with the $\bar{\mathrm{P}}$ANDA Detector and Experimental Verification of the Micro-Vertex-Detector Pixel Readout ASIC with Proton Test Beam |